Constraining the properties of gas around galaxies through absorption along multiple lines-of-sight

BECKETT, ALEXANDER

Constraining the properties of gas around galaxies through absorption along multiple lines-of-sight

Alexander Beckett

A Thesis presented for the degree of
Doctor of Philosophy

Department of Physics
Durham University
United Kingdom
September 2022

Constraining the properties of gas around galaxies through absorption along multiple lines-of-sight

Alexander Beckett

Abstract

In this thesis we study the relationship between galaxies and the surrounding gas at redshifts $\lesssim 1$ using absorption spectroscopy along multiple, closely-spaced lines-of-sight. We use high-resolution UV spectroscopy of a projected quasar triplet at z ~ 1 to detect absorption due to the Lyman-α transition of neutral hydrogen across the redshift range $0 < z < 1$, as well as absorption lines attributed to numerous metal species. Alongside a variety of imaging and spectroscopic data covering foreground galaxies in this field in optical and near-infrared wavelengths, we attempt to constrain the likely origins of this absorbing gas in a range of galaxy environments.

Using our catalogue of ≈ 270 identified H I absorption systems, ≈ 150 metal line absorption systems, and ≈ 1000 galaxies with confident redshift measurements within a few Mpc of the sightlines, we apply statistical tests utilising this large sample size, and also attempt to model in detail the absorption around a smaller number of galaxies and galaxy groups.

We find that absorption is detected at a similar redshift in multiple lines-of-sight (separated by ~ 400 kpc on average) significantly more frequently than in a sample of mock absorbers with randomised redshifts. This is driven primarily by absorbers with column densities greater than $10^{14}\mathrm{cm}^{-2}$, whilst weaker absorbers do not appear in multiple sightlines more often than the random sample, suggesting that they arise in the intergalactic medium.

Using H I, a bimodality is found in the azimuthal angle distribution of galaxy-absorber pairs with impact parameters $\lesssim 300$ kpc. We attribute this primarily to minor-axis outflows and major-axis accretion. This picture is supported by the observations that absorbers near the major axis show a significant preference towards line-of-sight velocities aligned with the kinematics of the galaxy (where available), and that those near the minor axis more frequently exhibit metal absorption (most

notably O VI) at the same redshift.

By probing the gas around galaxies at multiple locations, we rule out simple disk, halo and outflow models around several isolated galaxies, and provide constraints on the velocities, opening angles or scale heights for any such structures around several additional galaxies. This can provide an additional diagnostic for helping to distinguish outflowing and infalling material in the circumgalactic medium. These simple models can plausibly fit ≈ 60 % of observed absorption within 300 $\mathrm{km\,s^{-1}}$ of our isolated galaxies.

We can also reproduce a large fraction (≈ 75 %) of absorption around pairs and groups of galaxies in this field using our 'toy' disk and outflow models, with parameters generally similar to those around isolated galaxies. However, given the large number of model parameters available in groups of galaxies, it is difficult to rule out tidally-stripped or intra-group material resulting from the interactions between group galaxies.

Combined, these results indicate that outflowing and disk-like structures containing detectable levels of neutral gas are commonplace, although not ubiquitous, around galaxies with a wide variety of properties in a wide range of environments.

Declaration

The work in this thesis is based on research carried out at the Department of Physics, Durham University, United Kingdom, under the supervision of Prof. Simon Morris, Prof. Michele Fumagalli, and Dr. Ryan Cooke. No part of this thesis has been submitted elsewhere for any other degree or qualification.

Chapters 2 and 3 of this thesis have been published in the form of a paper:

- "The relationship between gas and galaxies at z $<$ 1 using the Q0107 quasar triplet" Beckett, A.; Morris, S.L.; Fumagalli, M.; Bielby, R.; Tejos, N.; Schaye, J.; Jannuzi, B.; Cantalupo, S., MNRAS 506, 2574-2602, (Beckett et al. 2021)

Chapter 4 has has been accepted for publication in MNRAS under the title:

- "Signatures of extended disks and outflows in the circumgalactic medium using the Q0107 quasar triplet" Beckett, A.; Morris, S.L.; Fumagalli, M.; Tejos, N.; Jannuzi, B.; Cantalupo, S., (Beckett et al, 2022)

Chapter 5 has been written in the form of a paper and is in preparation for submission to MNRAS:

- "Modeling gas around galaxy pairs and groups using the Q0107 quasar triplet" Beckett, A.; Morris, S.L.; Fumagalli, M.; Tejos, N.; Jannuzi, B.; Cantalupo, S., (Beckett et al, in prep)

During this time, the author has also contributed to the publication (not included in this thesis):

- "Pair Lines of Sight Observations of Multiphase Gas Bearing O VI in a Galaxy Environment" Anshul, P.; Narayanan, A.; Muzahid, S.; Beckett, A.; Morris, S.L., MNRAS 503, 3243-3261 (Anshul et al, 2021)

Most of the work in this thesis was completed by the author, with comments and feedback provided by the listed co-authors to each publication. However, the data used in this thesis has been collected, reduced and compiled by others, as follows:

- The reduction of COS and FOS data and creation of the H I line list were mostly done by Charles W. Finn and Neil H. M. Crighton. Characterization of the H I catalogue was done by Nicolas Tejos and included in Tejos et al. (2014).

- The acquisition, reduction and galaxy redshift determination of DEIMOS data were mostly done by Neil H. M. Crighton, Jill Bechtold, Buell T. Jannuzi and Allison L. Strom.

- The acquisition, reduction and galaxy redshift determination of GMOS data were mostly done by Neil H. M. Crighton.

- The acquisition, reduction and galaxy redshift determination of CFHT-MOS data were mostly done by Simon L. Morris and Buell T. Jannuzi, as described in Morris et al. (2006).

- The above CFHT-MOS, VIMOS, DEIMOS and GMOS data were compiled into a single 'MOS' catalogue characterized by Nicolas Tejos and described in Tejos et al. (2014).

- The acquisition of the MUSE data was completed under the GTO process and led by Joop Schaye. Data reduction, source detection, redshift estimation and characterization of the resulting catalogue was done by the author.

- The acquisition of the HST/ACS imaging was led by Lorrie Straka, and reduced using standard calibration pipelines by STScI. Source detection and matching of sources to the redshift catalogue was done by the author.

Where descriptions of the data collection and reduction processes are included in published works, these are acknowledged and referenced in Chapter 2.

Acknowledgements

I would like to thank Simon Morris for his excellent support and guidance whilst supervising my PhD, for his skepticism pushing me to think critically and consider all interpretations of the data, for all the shared articles, and for the useful feedback and discussions improving my work every step of the way. Many thanks also to Ryan Cooke and Michele Fumagalli, for sharing their insightful comments, ideas and advice throughout my time at Durham. Thanks to Rich Bielby, Matteo Fossati, and Emma Lofthouse for lending me their experience, and helping me find my bearings as I started my research. I would also like to thank Tom Theuns for a wealth of insightful questions and ideas to explore, and Nicolas Tejos, who provided the foundation upon which my research is built.

I would not the person I am today without the support of teachers, mentors and friends through my formative years, so many thanks to Mr Jones and Dr Nourshargh, to Sam Cook and Pat Roche, to Kieron, Cameron, Dan, Manoj, Alex, Pat, Ching, and all of those who offered their knowledge, guidance and friendship before I arrived in Durham.

I would also not have made it through my studies without 'escaping' Durham on occasion, so a special thanks also to my hiking companions Daniel, Simon, Ben, Vikram, Chris, Jonathan, and others, who have helped me gain a wider perspective and see my problems from a different angle.

My time in Durham has been so enjoyable thanks to finding friends on the same journey, so I would like to thank Jack, Jake, Ed, Amy, Ellen, Giorgio, Vicky, Aidan, Raj, Ra'ad, Arnau, Carol, Christoph, Victor, Joaquin, Calvin, Qiuhan, Duncan, Louise, Gabriel, Nency, Lucy, Will, Annie and Daniel. Thanks for creating such a great working atmosphere, and for sharing your expertise, knowledge, and advice.

Finally, I am enormously grateful towards my parents, Paul and Juliet, and my brother Tom, for their love, support and encouragement throughout my life, and without which I would not be where I am today. Thanks for everything.

Contents

List of Figures

List of Tables

CHAPTER 1

Introduction

This thesis discusses the use of absorption spectroscopy along the line-of-sight to background sources alongside observations of intervening galaxies, in order to determine the origin and structure of the gaseous material surrounding these galaxies. In this chapter it is therefore necessary to give a brief overview of the techniques used to determine the properties of both the gas and the galaxies from observations, and place them in a wider cosmological context.

1.1 Cosmology

1.1.1 Describing the evolution of the universe

Cosmology is, in brief, studying the properties and evolution of the Universe as a whole. Our modern understanding of cosmology could be said to have begun with combining the description of how gravity affects the Universe on large scales enabled by the theory of General Relativity (GR, e.g. Einstein, 1916)[1], with the observations

[1] An English translation of several of Einstein's papers, including the 1905 and 1916 works referenced here, can be found in: The Principle of Relativity: Original Papers by A. Einstein and H. Minkowski, University of Calcutta, 1920, pp. 89-163

of recession velocities of distant nebulae (Hubble, 1929).

Using analysis of Cepheid variables, Hubble (1929) measured both the distance and recession velocity of nearby galaxies, finding a clear proportionality between these two quantities. These observations, as well as indicating that the Universe is expanding, confirmed that some nebulae were indeed galaxies outside the Milky Way.

GR provided a theory of gravity consistent with a finite and invariant vacuum speed of light, proposed earlier as part of Special Relativity (Einstein, 1905). This postulate has been tested on many occasions, most famously in the Michelson-Morley experiment (e.g. Michelson & Morley, 1887). Numerous predictions of GR have been used to confirm the veracity of the theory, including the precession of Mercury (Einstein, 1915), and deflection of light passing near the Sun (e.g. Dyson et al., 1920). More recent observations supporting GR include decaying orbits of binary stellar objects (e.g. Stairs, 2003; Jacoby et al., 2006; Falanga et al., 2015), detection of gravitational waves (e.g. Abbott et al., 2016; Krishnendu & Ohme, 2021) and the behaviour of light in the vicinity of black holes (e.g Event Horizon Telescope Collaboration et al., 2019a,b; Younsi et al., 2021).

Einstein's equations can be used to describe a Universe that is isotropic and homogeneous on the largest scales. This can then describe how the Universe evolves with cosmological time, and how this evolution depends on the mass and energy content of the Universe. The Friedmann-Lemaître-Robertson-Walker (FLRW) metric provides this description (Friedmann, 1922, 1924; Lemaître, 1931; Robertson, 1936; Walker, 1937)[2], and takes the form:

$$ds^2 = -c^2dt^2 + a^2(t)\left(\frac{dr^2}{1-kr^2} + r^2d\theta^2 + r^2sin^2(\theta)d\phi^2\right) \tag{1.1}$$

where ds represents the space-time interval, c is the speed of light, t is cosmological time, and r, θ and ϕ represent the comoving radial, axial and azimuthal spatial coordinates. In this metric, k represents the curvature of space-time as a whole (-1 if the Universe is open, 0 for a flat Universe and +1 if closed), whilst a is the

[2]English translations of Alexander Friedmann's works are available: Friedman (1999b,a).

'scale factor' of the Universe, which is a conversion factor between the comoving and physical distances between points in this metric. By convention the scale factor is defined such that a = 1 at the present time.

Modern measurements (discussed later) suggest that the Universe is indistinguishable from flat. Substituting this case into the GR field equations results in the Friedmann equation:

$$\left(\frac{\dot{a}}{a}\right)^2 = \frac{8\pi G}{3c^2}\epsilon + \frac{\Lambda}{3} \tag{1.2}$$

with G the gravitational constant, ϵ the energy density of the Universe, and Λ the 'cosmological constant'. A more detailed derivation can be found from many sources (e.g. Ryden, 2003).

The content of the Universe is generally modelled as a perfect fluid. Applying the First Law of Thermodynamics to a spherically symmetric and expanding fluid leads to:

$$\dot{\epsilon} + 3\left(\frac{\dot{a}}{a}\right)(\epsilon + p) = 0 \tag{1.3}$$

for p the pressure.

To fully solve for $a(t)$, we also need the relationship between energy density and pressure. This 'equation of state' takes the form $p = w\epsilon$, where w is usually assumed constant but can be different for different fluids. For non-relativistic matter, the pressure is negligible in comparison to energy density ($w = 0$), whilst photons do generate substantial pressure ($w = 1/3$). The cosmological constant can also be included in this total energy density, using $\epsilon = \Lambda/8\pi G$ and $w = -1$.

For each of these components with energy density ϵ_i, Equation 1.3 can be solved to recover the result:

$$\epsilon_i(a) = \epsilon_{i,0} a^{-3(1+w_i)} \tag{1.4}$$

with $\epsilon_{i,0}$ giving the energy density of each component at the present time. We use subscript r, m and Λ to denote the energy density of radiation, matter and the cosmological constant respectively.

These components are usually described as a fraction of the critical density at the present time using the notation $\Omega_{i,0} = \epsilon_{i,0}/\epsilon_{c,0}$. The critical density is the total energy density of a flat universe. From Equation 1.2:

$$\epsilon_{c,0} = \frac{3c^2}{8\pi G}\left(\frac{\dot{a}}{a}\right)_0^2 \tag{1.5}$$

Using this definition and Equation 1.4, we can then rewrite Equation 1.2 in terms of Ω:

$$\left(\frac{\dot{a}}{a}\right)^2 = \left(\frac{\dot{a}}{a}\right)_0^2 (\Omega_{r,0}a^{-4} + \Omega_{m,0}a^{-3} + \Omega_{\Lambda,0}) \tag{1.6}$$

This equation describes the evolution of the scale factor purely as a function of the relevant energy densities and the local rate of expansion at the current time, which can therefore be deduced from observations. The $(\dot{a}/a)$ parameter used in this relationship is now named for Hubble, with $H(a)$ the Hubble parameter being variable, which at the current time takes the value H_0:

$$H(a)^2 = H_0^2(\Omega_{r,0}a^{-4} + \Omega_{m,0}a^{-3} + \Omega_{\Lambda,0}) \tag{1.7}$$

The expansion of the Universe has a direct effect on photons observed from cosmological distances due to the difference in scale factor between the time at which the photon was emitted (t_e) and the time it was observed (t_o):

$$\frac{\lambda_o}{\lambda_e} = \frac{a(t_o)}{a(t_e)} \tag{1.8}$$

The cosmological component of redshift z_{cos} is then related to the scale factor at the time of emission by:

$$z_{cos} = \frac{\lambda_o - \lambda_e}{\lambda_e} = \frac{a(t_o)}{a(t_e)} - 1 \tag{1.9}$$

This can then be used to give the Hubble parameter in terms of the cosmological redshift (which outside of galaxies local to the Milky Way dominates the measured redshift over that caused by peculiar velocities):

$$H(z)^2 = H_0^2 \left(\Omega_{r,0}(1+z)^4 + \Omega_{m,0}(1+z)^3 + \Omega_{\Lambda,0}\right) \tag{1.10}$$

Estimates of the Hubble constant and relevant energy densities have been continually revised over the intervening years, but throughout this thesis (and the publications from which some sections derive) we use the recent results from the Planck satellite (Planck Collaboration, 2020): $H_0 = 67.4$ km s^{-1}Mpc^{-1}, $\Omega_{m,0} = 0.315$, $\Omega_{\Lambda,0} = 0.685$. As the radiation term drops off more rapidly than other terms, this can usually be neglected, especially at the z < 1 redshift range we primarily consider in this thesis.

1.1.2 Cosmological distances

In order to measure or estimate properties of gas and galaxies in the distant Universe, the distance to and distances between them will also be needed, for example to convert from observed brightness to galaxy luminosity. Cosmological effects such as dimming therefore need to be included in these calculations, which are described briefly here.

Using the metric given in equation 1.1, it can be shown that the radial comoving distance r is given by:

$$\begin{aligned} r &= c\int_{t_e}^{t_o} \frac{dt}{a(t)} \\ &= c\int_{a(t_o)}^{1} \frac{da}{a(t)\dot{a}(t)} \\ &= c\int_{0}^{z_{cos}} \frac{dz}{H(z)} \end{aligned} \tag{1.11}$$

Also required is the angular diameter distance D_A, used to estimate the distance Δx between two objects at similar redshifts (separated by angle $\Delta\theta$ on the sky), often the distance across a galaxy. The angular diameter distance is defined to fulfil the expected relation $\Delta x = D_A \Delta\theta$, but is also related to the comoving distance by the FLRW metric:

$$\begin{aligned} \Delta x &= ar\Delta\theta = D_A\Delta\theta \\ D_A &= ar \\ D_A &= \frac{r}{1+z} \end{aligned} \tag{1.12}$$

Finally, the luminosity distance takes into account the energy loss of photons over cosmological distances due to their redshift. The change in scale factor affects both the wavelengths and time intervals of emitted photons when they are detected at a distance r from the source, introducing a factor of a^2 to the incident flux:

$$\begin{aligned} F &= \frac{L}{4\pi D_L^2} = \frac{La^2}{4\pi r^2} \\ D_L &= \frac{r}{a} = r(1+z) \end{aligned} \tag{1.13}$$

These distance measures allow conversion between apparent and physical sizes and luminosities of galaxies once redshift measurements are obtained.

1.2 Galaxies

Once galaxies were known to be separate collections of stars beyond the Milky Way, with distances measured using 'standard candles' such as Cepheid variables (e.g. Leavitt & Pickering, 1912; Hubble, 1929) and later Type 1a supernovae (e.g. Phillips, 1993; Riess et al., 1998), their properties could be studied in detail. Although some information can be gleaned from broad-band imaging, many galaxy properties are inferred through their spectra.

It is important to note that, although the study of galaxies makes up a large part of astronomy, the term is often not well-defined (see e.g. Forbes & Kroupa, 2011). Whilst a galaxy is considered to be a gravitationally-bound collection of stars, gas, dust and dark matter, the quantity of each of these components required to constitute a galaxy is not necessarily agreed-upon. For example, globular clusters could fit this definition, although they generally contain little dark matter, and possible dark

galaxies (e.g. Cantalupo et al., 2012) would contain few stars, but larger quantities of gas and dark matter. In this thesis, galaxies are detected through their spectra, tracing the stellar and gaseous components, so it is useful to define galaxies using their luminosity. We can therefore define a galaxy as a gravitationally bound system, with a spectrum consistent with stars and/or gas, that is more luminous than most globular clusters ($\gtrsim 10^6\ L_\odot$, e.g. Baumgardt & Hilker 2018).

1.2.1 Galaxy spectra

Stars emit light at wavelengths approximately following a black-body curve. The continuum emission seen in galaxy spectra is produced by a large number of stars covering a range of masses and temperatures. The brightness and slope of the continuum can be used to infer the masses and ages of these stellar populations.

Stellar atmospheres, being cooler than the interiors of stars, impose absorption features on galaxy spectra. In the visible wavelength range, the most common features are the Calcium H and K Lines, (at 3969 and 3934 Å respectively, which contribute to a large 'break' near 4000 Å, the D4000 break) and the Balmer break in Hydrogen (at 3646 Å).

Radiation from interstellar gas also adds emission lines to the galaxy spectrum. At low redshifts, this generally includes the Hα (6563 Å) and Hβ (4861 Å) lines, as well as [O II](e.g. 3727 Å) and [O III](e.g. 4959, 5007 Å) 'forbidden' lines.

Both emission and absorption features arise from transitions in quantum energy levels in the atoms, ions and molecules that make up the stars and gas in galaxies. The discrete energy difference between the two energy levels leads to a clear emission or absorption line in the spectrum at the wavelength corresponding to a photon of that energy.

The observed wavelength of a particular transition therefore indicates the redshift, and by extension distance (see Section 1.1), of the galaxy. We can then convert observed fluxes at different wavelengths into intrinsic galaxy luminosities in both the continuum and the spectral lines, and thereby infer several other galaxy properties. Figure 1.1 shows two example galaxy spectra from the Sloan Digital Sky

Survey (SDSS[3]), illustrating one galaxy spectrum dominated by absorption features and another dominated by emission features. These clearly demonstrate the main D4000 break, as well as major emission lines at visible wavelengths.

It is important to note that dust in galaxies often has a substantial effect on the spectrum through absorbing and scattering photons. Shorter wavelengths are preferentially scattered and absorbed, with absorbed energy often later radiated in the infrared. The effect of dust can in some cases be mitigated by using observables that are not modified by the dust (such as line ratios for lines at similar wavelengths), or estimated through various means such as direct far-infrared observations (e.g. Berta et al., 2016) or ratios of lines produced by the same element at different wavelengths (often the Balmer decrement, the ratio between Hα and Hβ, e.g. Groves et al. 2012).

1.2.2 Galaxy properties

Once the redshift is known and effects such as dust reddening are taken into account, many properties of galaxies can be inferred from the spectra. We now briefly describe some of these properties that we utilize in this thesis.

Stellar mass

In order to estimate the total galaxy stellar mass from its spectrum, the galaxy mass-to-light ratio needs to be measured, requiring knowledge of the contribution to the continuum from stars of different masses. This is generally done using stellar population synthesis models (SPS, e.g. Bruzual & Charlot, 2003), in which the star formation rate over time alongside an initial mass function (the probability distribution of stellar masses at which stars form, e.g. Salpeter 1955; Chabrier 2003) provide a model of the number of stars of different masses and ages in the galaxy. Our knowledge of stellar physics allows spectra of these stars to be generated, and then combined into a model galaxy spectra. Fitting this to the observed galaxy spectra constrains the total mass of stars in the galaxy.

[3]retrieved using the SDSS 'skyserver' portal: http://skyserver.sdss.org/dr17/

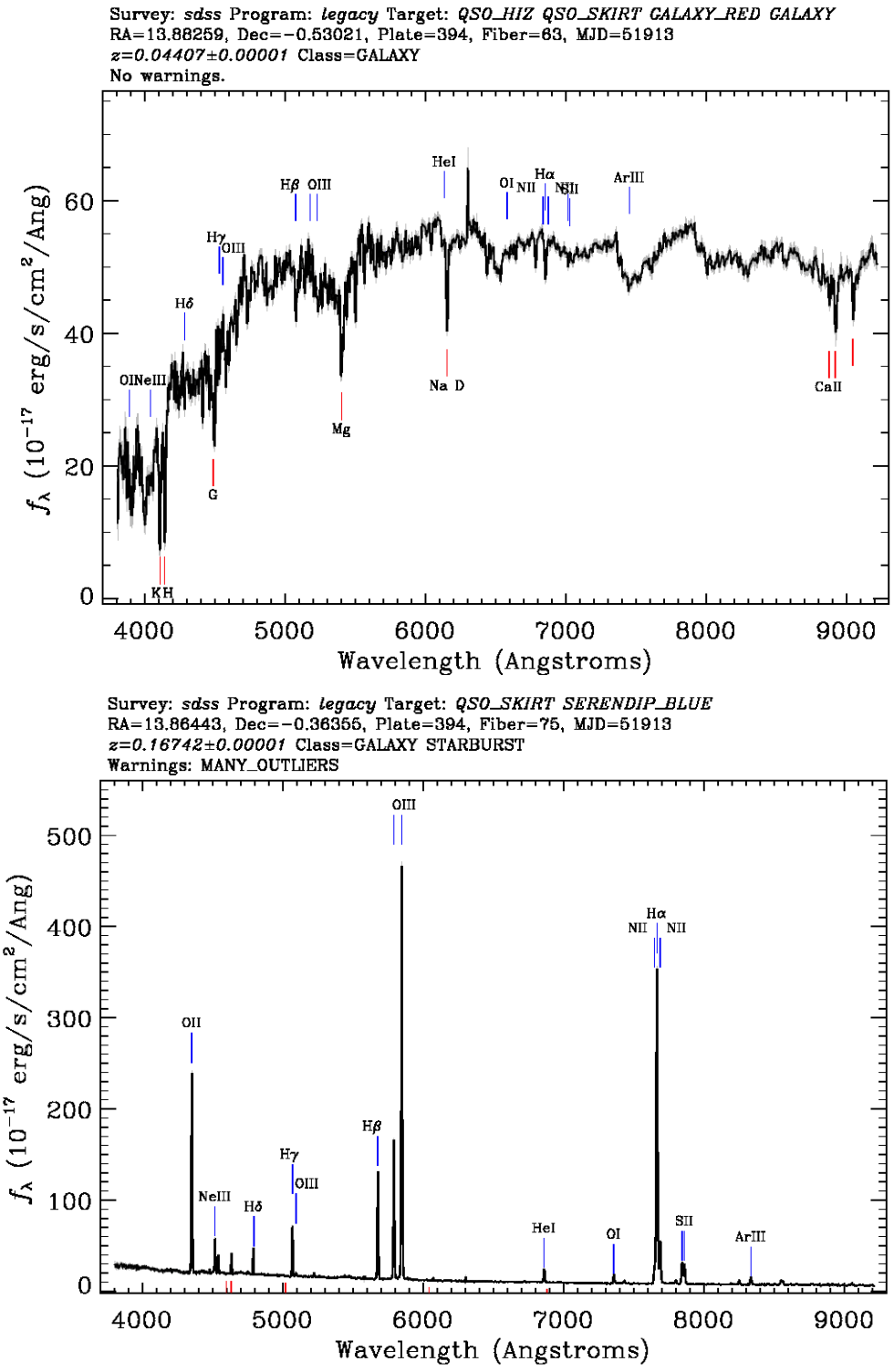

Figure 1.1: Two example galaxy spectra from the SDSS survey, illustrating the differences between absorption-line-dominated (top) and emission-line-dominated (bottom) galaxies. Both galaxies are at low redshift, with major emission and absorption features labelled.

In many studies, time is saved by producing a simpler calculation that approximates the results from SPS models (e.g. Bell et al., 2003; Johnson et al., 2015), usually as a function of the brightness and colour in specific wavelength bands. (This can therefore be used with photometric measurements if galaxy spectra are not available.)

Star-Formation rate

Emission lines are often produced by recombination, as ions and electrons recombine in ionized gas, as well as in collisions. As gas is generally highly ionized only by nearby stars with strong emission at energies greater than the ionization energy (e.g. Strömgren, 1939), the gas emission traces blue stars, which tend to be both massive and short-lived. Emission lines are therefore useful as a tracer of recent star formation within the galaxy. The lifetimes of these stars are sufficiently short that most studies treat emission line luminosity as a direct proxy for the current star-formation rate (SFR) of the galaxy (e.g Kennicutt, 1998; Kewley et al., 2004). Whilst the nuclei of active galaxies (AGN) also exhibit strong emission lines, these are usually much broader so can easily be distinguished from those produced by star-formation. Where the lines are not broadened along the line-of-sight, we can discriminate between emission lines produced by AGN and star-formation using line ratios sensitive to the incident radiation (see e.g. Baldwin et al. 1981; Kewley et al. 2019).

Absorption features in galaxy spectra are often produced by stellar atmospheres. As well as absorption lines, this includes 'breaks', such as the D4000 and Balmer breaks, where the continuum emission is substantially lessened for a large wavelength range blueward of a specific wavelength. In non-star-forming galaxies, bluer stars, which die earlier than red stars, are not replaced. Therefore these breaks generally become stronger over time. Breaks can therefore provide an indication of time since the most recent star formation in that galaxy (e.g. Bruzual A., 1983; Bruzual & Charlot, 2003; Kauffmann et al., 2003).

Kinematics

Traditionally, galaxy spectra have been obtained using long slits, which after dispersing through a grating produce 2D images with axes representing wavelength and position along the slit. Using multiple slits in a single observation is possible, but the proximity of multiple slits is often limited by the design of the instrument. In this case, estimates of galaxy rotation velocities were generally only obtained along this slit, although could sometimes be obtained using multiple slits for a single galaxy. More recently, integral field units such as the Multi-Unit Spectroscopic Explorer (MUSE, e.g. Bacon et al., 2010) allow spectra to be obtained individually for each spatial pixel (spaxel) of an image, often on scales smaller than one arcsecond. This produces spectra at tens or even hundreds of locations within a galaxy, and makes determining the magnitude and direction of galaxy velocities far more straightforward. Using integral field units (IFUs) can also reveal any additional features in the galaxy velocities, such as distortions caused by galaxy interactions.

1.3 Observing gas

In addition to galaxies, other sources were found with substantial redshifts, most notably quasars (e.g Matthews & Sandage, 1963), which are usually seen through emission from black-hole accretion disks in distant galaxies. Their spectra exhibit absorption features at various redshifts that would require enormous peculiar velocities if associated with either the quasar or the Milky Way (e.g. Bahcall & Salpeter, 1966). These absorbers were therefore expected to reside in intergalactic space, and it was hypothesised that this gas was found in extended halos around galaxies far larger than the visible galaxy (Bahcall & Spitzer, 1969). We show a schematic illustrating this process in Figure 1.2. Measurements of the state of this gas, such as its densities, temperatures and metallicities, are required to understand the origins of this gas and its effects on galaxy evolution.

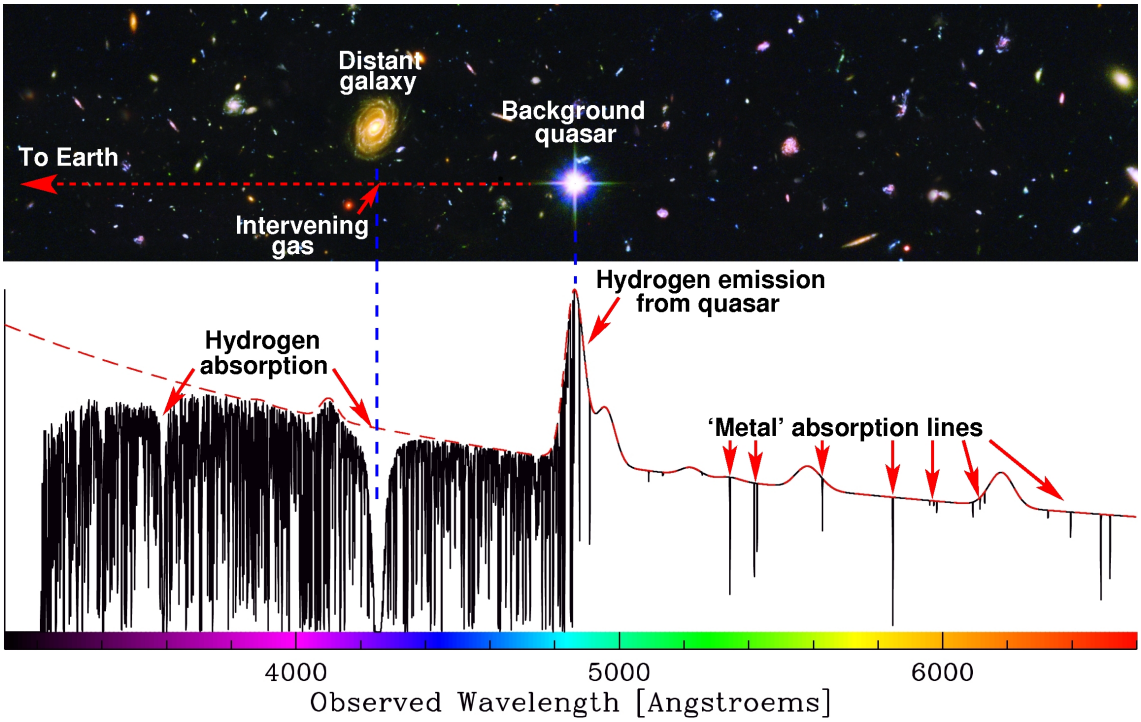

Figure 1.2: Schematic illustrating the quasar absorption technique for detecting gas along the line-of-sight. Neutral hydrogen along the sightline imposes a 'forest' of absorption lines on the quasar spectra at redshifts blueward of the quasar Lyα emission. We therefore observe lower flux (black line) than would be expected in continuum and emission from the quasar (red line). Galaxies near the line-of-sight tend to impose stronger absorption features (e.g. at the blue line), and also a range of metal absorption lines. Copyright Michael Murphy.

1.3.1 Detecting intergalactic gas

Absorption features in the spectra of background sources, usually quasars, remains our most sensitive probe of intergalactic gas. Its low density means that emission from this gas is difficult to detect, especially around galaxies at high redshifts. The sensitivity of absorption measurements is affected less strongly by the gas density, and is in principle affected only by the flux in the background spectrum, maintaining consistent sensitivity across a range of wavelengths (and therefore redshifts).

Many absorption studies use the Lyman-α transition for analysis of circumgalactic and intergalactic gas. This has a rest-frame wavelength of $\approx$1216 Å, and therefore lies in the far-ultraviolet part of the spectrum at low redshifts. This is not visible from the surface of the Earth, so requires space telescopes in order to observe.

Identifying absorption features due to intergalactic gas requires eliminating ab-

sorption due to the much higher column densities of material found around the quasar itself, and gas in and around the Milky Way. In most cases, reasonable confidence in a line identification requires multiple absorption features in the spectrum at the same redshift. We also note that, as gas redshift measurements are a combination of cosmological redshift and peculiar velocity, the location of the gas along the line-of-sight and its velocity relative to the Hubble Flow are degenerate.

There is also the further disadvantage of probing only a pencil-beam through the gas (in most cases), rather than detecting gas over a larger area, due to the sparsity of background sources bright enough to obtain sensitive measurements. However, the high sensitivity, even at high redshifts, means that absorption is still commonly used. It is therefore necessary to extract as much information on the gas properties as possible from the absorption line profiles observed.

1.3.2 Absorption-line profiles

Numerous physical properties of the absorbing gas contribute to its line profile. Firstly, the properties of the transition itself affect the line width (known as 'natural' broadening). The uncertainty principle relates a finite lifetime of an excited quantum state with a finite uncertainty in the transition wavelength. This produces a Lorentzian profile with a finite width which can be measured in the laboratory.

Second, the thermal velocities in the gas along the line-of-sight also broaden the line profile. Through consideration of the statistical mechanics of a gas, it can be shown that these line-of-sight velocities follow a Maxwell-Boltzmann distribution, and in turn that the broadened line has a Gaussian profile with standard deviation:

$$\sigma = \sqrt{\frac{k_B T}{m}} \tag{1.14}$$

for m the mass of each absorbing ion and T the temperature of the gas. We often define the Doppler parameter (or Doppler width) as $b = \sqrt{2}\sigma$.

A third source of broadening is the collisions between gas particles. These collisions reduce the expected lifetime of the excited state, and therefore increase the width of the Lorentzian profile discussed for natural broadening.

Any turbulent motion in the gas can have an additional broadening effect. This is usually assumed to be Gaussian and included in the measurement of Doppler width:

$$b = \sqrt{\frac{2k_B T}{m} + b_{turb}^2} \tag{1.15}$$

These sources of broadening therefore produce a Voigt line-profile, which is a convolution of Lorentzian and Gaussian profiles.

We note that the expansion of the Universe itself can have an effect on the shape of the line, but this is usually only relevant for extremely underdense material and will not contribute significantly to the line profiles we analyse in this thesis.

Finally, the shape of the line is also affected by the instrument itself, with a convolution between the intrinsic shape of the line and the instrumental line-spread-function resulting in the line profile observed in the data.

1.3.3 Gas properties & the curve of growth

For most low-density absorption, gas temperature is the dominant broadening factor, so the line profile is approximately a Gaussian with a Doppler parameter indicating that temperature.

Unfortunately the lack of knowledge about the gas distribution along the line-of-sight makes it impossible to determine the gas density itself from a single absorber (although the presence of multiple absorbers may constrain the density to some extent). Instead the absorption profile only reveals the gas column density, the total summed density per unit area along the line-of-sight.

The properties of the transition itself are necessary to convert between a column density (as a function of wavelength) and the line profile produced. We define an absorption cross-section σ_{abs} as a function of wavelength, representing the probability of an absorption event as an effective area of each gas particle at that wavelength. This depends on the 'oscillator strength' of the transition (f_{osc}, a dimensionless parameter indicating the likelihood of the transition based on the quantum mechanics of the two energy levels, measurable in the laboratory), and how the line is broadened

(the Voigt profile $\phi(\lambda)$ resulting from the mechanisms discussed above).

$$\sigma_{abs}(\lambda) = \frac{\pi e}{m_e c} f_{osc} \phi(\lambda) \tag{1.16}$$

This can then be used to measure an optical depth ($\tau(\lambda)$), which is the expected number of interactions a typical photon of that wavelength will experience passing through the gas.

$$\tau(\lambda) = N\sigma_{abs}(\lambda) = \frac{\pi e}{m_e c} N f_{osc} \phi(\lambda) \tag{1.17}$$

This is directly related to the fraction of flux that is transmitted and absorbed by the gas, by $F_{obs} = F_c e^{-\tau}$ (for F_{obs} and F_c the observed and continuum flux levels), and therefore reproduces the absorption profile caused by the intervening material.

Note that the overall strength of an absorption feature is often stated using its equivalent width (W). This describes the width of an absorption feature in which the same flux is absorbed but has a perfect 'top-hat' profile.

$$\begin{aligned} W &= \int_{\lambda_1}^{\lambda_2} \left(1 - \frac{F_{obs}(\lambda)}{F_c(\lambda)}\right) d\lambda \\ &= \int_{\lambda_1}^{\lambda_2} \left(1 - e^{-\tau(\lambda)}\right) d\lambda \end{aligned} \tag{1.18}$$

Given that $\tau(\lambda)$ depends on a Voigt profile with Gaussian and Lorentzian components, the dependence of the measurable equivalent width on the gas column density is a complex one. This relationship is known as the 'curve of growth' and consists of three main regimes.

Firstly, at low densities where $\tau << 1$, the integrand $1 - e^{-\tau(\lambda)}$ can be approximated by $\tau(\lambda)$, so $W \propto N$. We can also usually neglect collisional broadening at these densities, so the line profile becomes a Gaussian with Doppler width primarily determined by temperature. Most absorption caused by circumgalactic gas is in this 'optically thin' regime, and thus the Doppler parameters fit to the observed absorption are a useful indicator of the gas temperature.

At higher column densities and optical depths ($\tau \sim 1$) neither the Gaussian nor

Lorentzian contributions to the line profile are dominant, so both must be taken into account. The relationship between W and N is much flatter, making it more difficult to determine the column density from observations. Furthermore, this relationship also has a strong dependence on the line width $W \propto b\sqrt{ln(N/b)}$ (e.g. Draine, 2011), with this degeneracy further reducing the accuracy with which the column density can be measured. In some cases, it is possible to use weaker transitions to estimate the line width and thereby break this degeneracy. However, this depends on the properties of the observational data, such as the wavelength coverage including a suitable alternative transition.

For extremely saturated, optically thick lines ($\tau >> 1$), the Lorentzian profile dominates the overall line shape. In this scenario, $W \propto \sqrt{N}$, and the column density can once again be reliably determined.

We illustrate some model Lyα absorption profiles in Figure 1.3, showing the saturation of an absorption line as column density increases alongside the resulting optical depth. This covers the approximate range of column densities considered in this thesis.

For H I observations using the Lyα transition, lines begin to saturate around column densities of $10^{14.5}\,\mathrm{cm}^{-2}$, indicating the transition between the linear and 'flat' portions of the curve-of-growth. The Lyman break, occurring at ≈ 912 Å in the rest frame, becomes detectable near $10^{17}\,\mathrm{cm}^{-2}$, and can be used to estimate column densities smaller than that at which the damped wings become measurable near $10^{18.5}\,\mathrm{cm}^{-2}$, and dominant near $10^{20}\,\mathrm{cm}^{-2}$. For this reason, high-column-density absorption systems can be called Lyman Limit Systems (LLSs) above $10^{17}\,\mathrm{cm}^{-2}$ and damped Lyman Alpha Systems (DLAs) above $2 \times 10^{20}\,\mathrm{cm}^{-2}$ (e.g. Wolfe et al., 2005). Systems of slightly lower column density than these thresholds may also be called partial Lyman Limit Systems (pLLSs, $\sim 10^{16} - 10^{17}\,\mathrm{cm}^{-2}$) and sub-Damped Lyman Alpha Systems (sub-DLAs, $\sim 10^{18} - 10^{20}\,\mathrm{cm}^{-2}$).

1.3.4 Metals & ionization models

Although a single absorption feature only reveals the column density and temperature (if optically thin), in many observations transitions from several ions are avail-

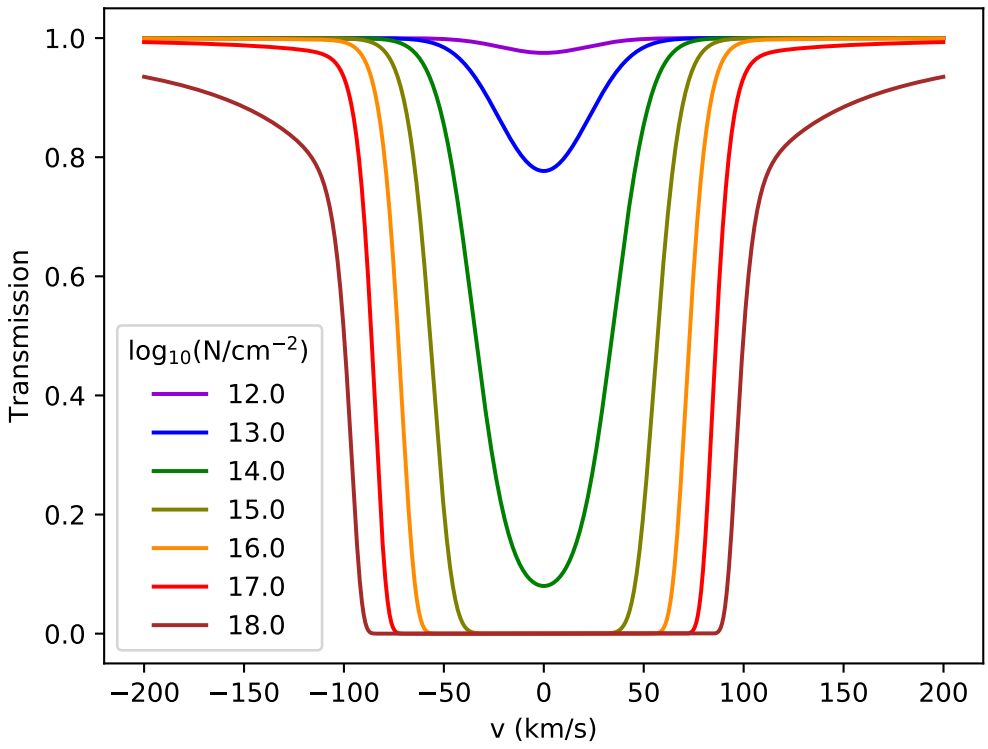

Figure 1.3: Model Lyα absorption profiles for a range of H I column densities, covering the three main regimes of the curve-of-growth.

able, enabling constraints on metallicities, densities, and ionization states.

Two metal ions commonly used are Mg II, a low ion probing cool ($\lesssim 10^5$K) gas using a near-UV doublet (2796 and 2802 Å), which is therefore accessible to ground-based observations at a lower redshift than the Lyman lines of H I, and O VI, producing a doublet at a wavelength not too distant from Lyα (1031, 1037 Å), a higher ion probing warmer material. Higher ions tend to produce transitions in the X-ray wavelength band, and are therefore not accessible to UV observations.

The presence of multiple ions allows constraints on the metallicity of the gas, as well as its ionization state and the mechanism(s) behind that ionization. Most models assume that the gas is in equilibrium, driven by photoionization (PIE models) or collisional ionization (CIE models). PIE models are generally more useful for low ions, and use an assumed incident radiation field to estimate ionization fractions for each element, and therefore the metallicity (e.g. Bergeron, 1986; Lehnert et al., 2013; Fumagalli et al., 2017), often using radiative transfer codes such as CLOUDY (Ferland et al., 2017). CIE models are more often used for high ions, where the ionization fractions are determined by the gas temperature (e.g. Gnat & Sternberg, 2007). These models are unlikely to fully represent the state of the gas, with some models combining photo- and collisional ionization, and others considering non-equilibrium states involving shocks and turbulent mixing among other processes (e.g. Heckman et al., 2002; Gnat & Sternberg, 2009).

Although such models do not fully capture the complex physics involved, the approximations provide useful constraints on the gas properties.

1.4 Cosmological structure

1.4.1 Dark matter

Observations over the past century have provided several lines of evidence that the visible matter in the Universe makes up only a small fraction of its mass. These observations include large velocity dispersions of cluster galaxies found by Zwicky

(1933)[4], flatter rotation curves than expected for spiral galaxies (e.g Babcock, 1939; van de Hulst et al., 1957; Rubin et al., 1978; Persic et al., 1996), gravitational lensing in galaxy clusters (e.g. Clowe et al., 2006), and the power spectrum of the Cosmic Microwave Background (CMB, e.g. Komatsu et al., 2011; Planck Collaboration, 2020). Although some fraction of this may be material that is simply not bright enough to be visible (e.g. gas, dust, faint stars), results from both Big Bang Nucleosynthesis and the Cosmic Microwave Background indicate that most of this 'dark matter' is non-baryonic (e.g. Schramm, 1998; Planck Collaboration, 2020).

Whilst these varied lines of evidence mean that the dark matter model is a well-supported one, direct detection of dark matter particles remains elusive (e.g. Tanabashi et al., 2018), allowing for the possibility of various modified gravity models (in which the evidence stated above is due to gravity acting differently on the largest scales). However, these alternative models are rarely able to reproduce the sensitive measurements within the solar system and simultaneously match cosmological observations on larger scales (e.g. Koyama, 2016).

The shape of the galaxy rotation curves suggests that dark matter forms halos around galaxies. As the mass of dark matter dominates over that from baryonic matter, density fluctuations of dark matter are expected to be the 'seeds' from which galaxies could grow, accreting dark and baryonic matter from less-dense regions of space (e.g. Press & Schechter, 1974; Rees & Ostriker, 1977), and then merging to form larger galaxies and structures (e.g. Blumenthal et al., 1984). This model requires that the dark matter is primarily 'cold' (massive and non-relativistic). The cosmological paradigm in which this cold dark matter and the cosmological constant (dark energy) dominate is known as ΛCDM.

This collapse forms a region of space which is gravitationally bound and no longer expands in line with the Friedmann equations. Within this region the virial theorem (kinetic energy = -0.5 × potential energy) can be said to apply. By convention, the size of such a collapsed region is usually given as that within which the average density is 200 times the critical density.

[4]English translation by Andernach & Zwicky (2017)

$$\begin{aligned} \rho(r < r_{vir}) &= 200 \times \frac{3H(z)^2}{8\pi G} \\ \rho(r < r_{vir}) &= \frac{3M}{4\pi r_{vir}^3} \\ r_{vir} &= \left(\frac{GM}{100H(z)^2}\right)^{1/3} \end{aligned} \tag{1.19}$$

This is the virial radius, denoted r_{vir} or r_{200}. We then also define a virial mass, which is the total mass contained within r_{vir}, and virial velocity, which is the circular velocity at r_{vir}. The virial radius is also often used to mark the 'boundary' between the circumgalactic medium of the galaxy (CGM, e.g. Tumlinson et al., 2017) and the intergalactic medium (IGM), although galaxies clearly influence the surrounding gas to larger scales, and a limit of 2 r_{vir} may be more appropriate (e.g. Wilde et al., 2021).

In order to study the outer regions of galaxies, as well as any material surrounding galaxies or interactions between galaxies, the mass of the dark matter component must be taken into account. This 'halo mass' is difficult to observe directly, although it can be estimated using gravitational lensing (e.g Guzik & Seljak, 2002; Mandelbaum et al., 2006) or by tracing the potential well using satellite galaxies or stars (e.g Conroy et al., 2007). Most halo mass estimates are now made using an 'abundance matching' technique (e.g. Berlind & Weinberg, 2002; Behroozi et al., 2010), matching the most common galaxy stellar masses to the most common halo masses predicted using a cosmological model.

This process can cover a far wider range of galaxies than direct measurements, but also reproduces results from large galaxy surveys (e.g. Moster et al., 2010). It is important to note that the ratio between stellar and halo masses is not constant (e.g. Girelli et al., 2020), but that the stellar mass is a smaller fraction of the halo mass at both large and small masses. This is generally found to be due to differences in the efficiency with which galaxies turn their baryon content into stars, rather than in the ratio of their baryonic and dark matter components.

It is therefore suggestive of various forms of feedback, in which gas within the galaxy is either heated such that it can no longer cool and form stars, or expelled

from the galaxy entirely. Low-mass galaxies have smaller potential wells, such that the shocks produced by supernovae can more easily drive gas out of the galaxy and exceed escape velocity (e.g. Dekel & Silk, 1986; Schroetter et al., 2019). High-mass galaxies are more likely to host AGN, which also heat the gas and drive far stronger winds expelling baryons from the galaxy (e.g. Harrison et al., 2018; Laha et al., 2021).

In both cases this gas, having been driven out of the central galaxy, may be visible within the galaxy halo, and makes up part of the circumgalactic medium we discuss in this thesis.

1.4.2 Galaxy environments

Large galaxy surveys reveal a 'cosmic web' throughout the Universe, consisting of galaxy clusters in the densest regions of space, connected by filaments and sheets, surrounding underdense regions known as voids (e.g. Bond et al., 1996).

Gas and galaxy properties are found to vary between these different environments, with, for example, group and cluster galaxies generally exhibiting lower star-formation (e.g. Peng et al., 2010; Wetzel et al., 2013; Jian et al., 2017; Kuschel et al., 2022), and clusters exhibiting much larger quantities of hot, X-ray-emitting gas (e.g. Sarazin, 1986).

Closely-spaced galaxies are also likely to be interacting, with tidal interactions producing streams of stars and gas visible around the Milky Way (e.g. Mathewson et al., 1974; Lynden-Bell & Lynden-Bell, 1995) and other nearby galaxy groups (e.g. M81/M82, Sorgho et al., 2019). Therefore discussion of gas around galaxies will necessarily need to take into account the galaxy environment and its location within the cosmic web.

1.5 Studies of the gas around galaxies

1.5.1 Observations

Whilst this thesis primarily focuses on measuring CGM properties using absorption features in quasar spectra, we also briefly note that various methods are used to detect and characterize the CGM and IGM.

Although quasars, due to their high redshift and luminosity, represent a large fraction of absorption-line studies, other objects can also be useful as background sources. If sufficiently bright, background galaxies can play a similar role, either in detecting gas around other galaxies along the sightline (e.g. Steidel et al., 2010; Chen et al., 2020b), or the CGM of the same galaxy (down-the-barrel observations, e.g. Martin et al., 2012; Rubin et al., 2012). As galaxies are much more common than quasars, this can provide much larger sample sizes, but they are usually fainter so this often comes at the expense of sensitivity in the spectra. Down-the-barrel observations can unambiguously distinguish between infalling and outflowing structures, but then provide no indication of the distance between the gas and the galaxy. Alternatively, galaxy spectra can be stacked (e.g. Roberts-Borsani et al., 2020; Muzahid et al., 2021), greatly increasing sensitivity but averaging over any differences in the properties of the stacked spectra.

Additionally, it is sometimes possible to take advantage of gravitational lensing, which produces arcs behind foreground structures. This therefore probes the gas around foreground galaxies in a range of spatial locations (and the image may also be magnified to boost the signal-to-noise). This can help to reveal how the gas properties change with location relative to the central galaxy (e.g. Lopez et al., 2018, 2020; Tejos et al., 2021b), mostly on scales of a few kpc to tens of kpc. The afterglows of gamma-ray bursts (GRBs) have also recently been utilized as background sources (e.g. Gatkine et al., 2019).

CGM emission, as discussed briefly in Section 1.3.1, is usually less sensitive than absorption at low densities and large distances. However, integral-field units have made it possible to detect emission from all locations around a galaxy with a single observation, which has been used in recent studies (e.g. Finley et al., 2017;

Burchett et al., 2021; Leclercq et al., 2022). Cooler gas with molecular lines may also be detected in emission or absorption by radio and sub-mm telescopes such as ALMA (the Atacama Large Millimeter Array, e.g. Péroux et al., 2019). The 21cm transition of neutral hydrogen is often targeted for studying the inner CGM, where column densities are sufficiently high (e.g. Pisano, 2014; de Blok et al., 2014; Das et al., 2020). Recently, the properties of Fast Radio Bursts (FRBs) have been used to study the IGM, with their dispersion dependent primarily on the total column density of electrons along the line-of-sight (e.g. Macquart et al., 2020).

1.5.2 Simulations

Simulations of various aspects of the Universe provide useful tools for isolating the effects of physical processes, and hence the physics underlying our observations.

From initial N-body, dark-matter-only simulations (e.g. Efstathiou & Eastwood, 1981), considering only gravitational forces between thousands of dark matter particles in order to study the formation of the cosmic web from initial density perturbations, some simulations have evolved to capture a wide range of processes over a large region of the Universe, whilst others focus on particular aspects of much smaller systems (e.g. a single galaxy or group).

Advances in both computing power and numerical techniques enable larger numbers of particles to be simulated, and hence either improved resolutions or larger volumes. This in turn allows smaller-scale physical processes to be simulated directly, or enables simulations covering a larger and more representative sample of the Universe. The addition of baryons to simulations requires the implementation of more complex physics, including radiative transfer, gas pressure and shocks.

Major cosmological simulations of recent times include the EAGLE project (Evolution and Assembly of GaLaxies and their Environments, Schaye et al., 2015) and IllustrisTNG (Weinberger et al., 2017; Pillepich et al., 2018), with other simulations focusing on feedback between galaxies and their surroundings including the FIRE simulations (Feedback in Realistic Environments, Hopkins et al., 2014). Zoom-in simulations such as Auriga (Grand et al., 2017) are also useful, although these may not fully capture the effects of the environment on the gas around any galaxy. These

codes utilize a range of methods to simulate the properties and motion of gas and dark matter cells or particles over cosmological time. For example, EAGLE uses smoothed-particle hydrodynamics (SPH), an evolution of N-body simulations with several improvements in efficiency such as tree methods (e.g. Rosswog, 2009), whilst TNG uses a 'moving mesh' method where properties are evaluated at locations moving with the flow of matter.

Despite huge improvements over recent decades, the resolution of these simulations remains limited, and is usually varied with density in order to provide better resolution in dense environments such as galaxy centres. The results of the simulations therefore depend on 'sub-grid' calculations to parameterize effects that occur on smaller scales than the resolution. These simulations are generally calibrated against a relatively small number of observables, such as the galaxy stellar mass function, and can then be used to predict the results of numerous other observations.

Unfortunately for those studying the CGM and IGM, it is not generally possible to provide a simulation that covers both the stellar feedback produced by supernovae (on sub-pc scales) and the large-scale effects such as interactions between galaxies occurring on scales of tens of kpc. It is not yet clear what resolution is required to accurately model the CGM (e.g. van de Voort et al., 2019), so simulated CGM/IGM properties continue to depend substantially on the sub-grid models used by the different simulations.

Despite this, they can still guide us towards understanding the effects on the CGM caused by various physical processes. Recent examples include strong AGN feedback reducing the mass in the CGM (Davies et al., 2021), and possible inclusion of cosmic rays in the driving of CGM outflows (e.g. Hopkins et al., 2021).

1.6 Thesis motivation and structure

With observations in emission limited by the sensitivity of current instruments to relatively large densities (and therefore small distances from the central galaxy), absorption studies limited to usually only a single line-of-sight through the gas sur-

rounding any individual galaxy, and simulations often limited by resolution, identifying outflowing and accreting structures remains difficult, especially at large radii.

This difficulty in identifying disks and outflows means that questions remain over what fraction of the gas observed around galaxies is due to this material, how far from galaxies these structures extend, and how these extents are affected by galaxy properties and environments. With most disks and outflows probed in only one location, it is also difficult to determine how the gas properties in these structures (e.g. temperature, metallicity) vary with distance from the galaxy, and the properties of the structures themselves (e.g. outflow opening angles, disk thicknesses).

Although simulations provide some indications of expected answers to these questions, observations currently provide few constraints. These answers would improve our understanding of the processes involved in stellar feedback, and hence how star formation in galaxies evolves.

In this thesis we utilize a rare alignment of three quasars with small projected separations on the sky. This field, the Q0107 system, features sensitive spectra covering transitions such as Lyα along all three lines-of-sight, and a variety of deep galaxy observations. In addition to a large sample of galaxy-absorber pairs from $\lesssim$ 10 kpc to several Mpc, these data provide an opportunity to test models of CGM structures with stronger constraints than are possible in most transverse absorption studies. Probing the same disk or the same outflow in multiple locations can also allow us to estimate parameters such as rotation/infall velocities and outflow opening angles more accurately than would otherwise be possible.

This work has resulted in the production of three papers: Beckett et al. (2021) (Paper 1), Beckett et al. 2022 (accepted, Paper 2); and Beckett et al. 2022b (in prep, Paper 3). The structure of the thesis is as follows:

- In Chapter 2 (derived from Paper 1, Section 2), we describe the data available covering the Q0107 field. This includes the data collection and reduction methods, and the process by which we compiled a single galaxy catalogue and a single absorption-line catalogue for this system. Some statistical properties of the sample are also discussed.

- Chapter 3 (reproduced from the remainder of Paper 1) discusses several tests of the sample as a whole. These include a comparison between the frequency of absorber coincidences (where multiple lines-of-sight feature absorption at a similar redshift) in the real Q0107 data and a random distribution of absorbers, and a check for bimodality in the azimuthal angle of detected galaxy-absorber pairs. We also apply these tests to samples split by absorber column density, galaxy star-formation rate, and galaxy environment.

- In Chapter 4 (derived from Paper 2), we describe toy models for disk and outflow structures in the CGM, producing synthetic absorption spectra which can be compared with the features seen in the observations. We apply these models to isolated galaxies in our sample to determine whether such structures can plausibly explain much of the absorption seen around galaxies. This can also constrain some of the parameters of the models (e.g. outflow opening angle, disk thickness), and include detection of both structures around the same galaxy, indicating gas recycling.

- Chapter 5 (also reproduced in Paper 3) extends this modelling to galaxies in pairs and groups, in an attempt to determine to what extent these infalling and outflowing structures are affected by galaxy interactions. We also consider alternative models for absorption in galaxy groups, such as tidally-stripped streams and an intra-group medium.

- Finally, Chapter 6 summarizes our key results and briefly discusses possible future projects that could extend and improve upon this work.

CHAPTER 2

Observations

In this chapter we describe the observational data covering the Q0107 system. This consists of three bright quasars at z $\approx$ 1, and we summarize some of their properties in Table 2.1. Due to their brightness and location near to the celestial equator, these quasars and the surrounding field can be observed using most ground- and space-based telescopes. We have therefore been able to obtain high-fidelity spectroscopy of all three lines-of-sight, as well as deep imaging and spectroscopy providing properties of intervening galaxies. This was collated into a single catalogue of absorption features in the QSO spectra, and a single galaxy catalogue.

This chapter is reproduced from Section 2 of Beckett et al. (2021), hereafter Paper 1, but as this dataset was also used in the other work that makes up this thesis, we discuss it separately here.

Table 2.1: Coordinates, redshifts and R-band magnitudes of the three quasars making up the Q0107 triplet. (Reproduced from Crighton et al. 2010)

Object	RA (J2000)	Dec (J2000)	Redshift	R-mag
Q0107-025 A	01:10:13.14	-2:19:52.9	0.960	18.1
Q0107-025 B	01:10:16.25	-2:18:51.0	0.956	17.4
Q0107-0232 (C)	01:10:14.43	-2:16:57.6	0.726	18.4

2.1 Data

Our dataset consists of Hubble Space Telescope (HST) spectra of the three quasars using the Cosmic Origins Spectrograph (COS) and Faint Object Spectrograph (COS), and galaxy surveys from the Visible Multi-Object Spectrograph (VIMOS), Deep Imaging Multi-Object Spectrograph (DEIMOS), Gemini Multi-Object Spectrograph (GMOS) and the multi-object spectrograph on the Canada-France-Hawaii Telescope (CFHT-MOS), supplemented by HST R-band imaging and two MUSE fields. In this section we describe the reduction processes for each of these observations and the compilation of the results into our final catalogues of galaxies and absorbers, which are then used in Chapters 3-5.

2.1.1 IGM data

The UV spectra of the quasars were taken by the Cosmic Origins Spectrograph (COS, Green et al., 2012) and Faint Object Spectrograph (FOS) on the Hubble Space Telescope. The COS spectra were observed in 2010-11 (program GO11585, PI: Neil Crighton), using the G130M and G160M gratings, with a FWHM of 0.07–0.09Å, and a signal-to-noise ratio (SNR) per pixel of 7–9. These complement longer-wavelength FOS data described in Young et al. (2001). The observations are detailed in Table 2.2. The G130M and G270H gratings were not used for QSO-C, due to the Lyman Limit of a sub-damped Lyman-α system in the sightline and the lower redshift of this quasar respectively. These observations cover Lyα in COS from $z = 0$ (or the Lyman Limit in the case of QSO-C) to $z \approx 0.45$, and in FOS from 0.45 to the redshift of the quasar.

We use the line catalogue from Tejos et al. (2014) (hereafter T14, also used by Finn et al. 2016). They provide a more detailed description of the reduction process with further references, but we summarise it here. Individual exposures from COS were downloaded from the Space Telescope Science Institute (STScI) archive and reduced using CALCOS v2.18.5.

T14 performed their own background smoothing procedure masking out portions of the spectra affected by strong geocoronal emission lines (namely the Lyα and

Table 2.2: Summary of the QSO spectra used to generate the absorption-line catalogue. Columns are: (1) The QSO featured in the spectrum; (2) the spectrograph used; (3) the grating used; (4) the wavelength range for which this instrument and grating provides the spectrum; (5) the full width at half-maximum of the line-spread function of the spectrograph; (6) dispersion of the spectrum; (7) average signal-to-noise across the wavelength range given; (8) exposure time of the observations; (9) HST program ID of the observations.

QSO	Instrument	Grating	Wavelength Range (Å)	FWHM (Å)	Dispersion (Å/pix)	SNR (per pix)	Exposure Time (h)	Prog ID
(1)	(2)	(3)	(4)	(5)	(6)	(7)	(8)	(9)
Q0107-025A	COS	G130M	1135-1460	0.07	0.01	9	7.8	11585
	COS	G160M	1460-1795	0.09	0.01	8	12.3	11585
	FOS	G190H	1795-2310	1.39	0.36	28	7.5	5320, 6592
	FOS	G270H	2310-3277	1.97	0.51	32	2.4	6100
Q0107-025B	COS	G130M	1135-1460	0.07	0.01	9	5.9	11585
	COS	G160M	1460-1795	0.09	0.01	7	5.9	11585
	FOS	G190H	1795-2310	1.39	0.36	28	1.8	5320, 6592
	FOS	G270H	2310-3277	1.97	0.51	32	1.8	6100
Q0107-0232 (C)	COS	G160M	1434-1795	0.09	0.01	7	23.2	11585
	FOS	G190H	1795-2310	1.39	0.36	18	9.1	11585

O I 1302,1306 Å lines) and pixels with bad data quality flags. The error array was calculated in the same way as in CALCOS, but using the new background estimation, interpolated across the masked-out regions. Each spectrum was then flux calibrated using sensitivity curves provided by STScI.

Co-alignment was performed by cross-correlating strong galactic absorption features. Pixels with bad data quality flags were then excluded, whilst pixels with warning flags were halved in weight, before fluxes were re-binned to have a constant spacing equal to the dispersion of the grating. Co-addition was weighted by exposure time, and was followed by re-binning on a linear scale sufficiently narrow to ensure Nyquist sampling[1] across the entire wavelength range (0.0395 Å per pixel).

Individual exposures from FOS were downloaded from the STScI archive and reduced using the standard CALFOS pipeline. Wavelength corrections given by Petry et al. (2006) were applied to each individual exposure. The shortest wavelength region of the FOS G190H settings overlap with the longest wavelength COS settings, and T14 confirmed that the wavelength scales in these overlapping regions were consistent between the two instruments. All individual exposures were then combined together, resampling to a common wavelength scale of 0.51 Å per pixel.

T14 then estimated the continuum of each spectrum using a semi-automated method. They split the spectrum into 'chunks' of ≈ 12 Å (blueward of QSO Lyα emission, longer chunks at longer wavelengths), fit a straight line through the points within each chunk (iteratively removing outliers until convergence), then fit a cubic spline to give a smooth result. They checked the resulting continuum 'by eye' to ensure a reasonable fit (see their Figure 1).

VPFIT (Carswell & Webb, 2014) was used to estimate redshifts, column densities and Doppler parameters for each identifiable absorption system. The H I systems were assigned a flag ('a', 'b' or 'c') based on the number of absorption lines observed and the signal-to-noise in the column density estimate:

(a): At least two Lyman transitions observed with log(N) estimates at least 30 times their uncertainty

[1]Usually 2 pixels per resolution element, although this is not well-defined for the non-Gaussian line-spread function of COS. Here the FWHM is used to estimate the required sampling.

(b): Only Lyα observed with log(N) estimate at least 30 times its uncertainty

(c): log(N) estimate less than 30 times its uncertainty

Only those with 'a' and 'b' flags are included in our analysis. The distribution of H I column densities is consistent (using results from Keeney et al. 2012, as discussed in Figure 5 and Section 4.5 of T14) with a 3σ detection limit estimate of $\sim 10^{13}\text{cm}^{-2}$ in the COS spectra and $\sim 10^{13.5}\text{cm}^{-2}$ in the FOS spectra. Our catalogue should therefore be complete above this column density, with the exception of unresolved blended systems more likely to be found in the lower-resolution FOS spectra. We incorporate the differing detection limits of the COS and FOS gratings into our analysis in Section 3.2, and check for any resulting redshift bias throughout this work.

The catalogue contains 430 absorption systems, of which 272 are H I. Most of our discussion focuses on these H I absorbers, although metals are briefly discussed in Section 3.3.2 and where observed in Chapters 4 and 5.

2.1.2 Galaxies

The galaxy data used in this study comes from a number of different surveys. The catalogue is based on that used in T14 and F16, with spectra from VIMOS, DEIMOS, GMOS and CFHT-MOS observations (referred to as MOS data throughout). More recent observations using the Multi-Unit Spectroscopic Explorer (MUSE, Bacon et al. 2010) on the Very Large Telescope (VLT) are added to this catalogue. Table 2.3 summarises the number of spectra taken in each of these observations. Additionally, HST imaging is used to determine position angles and inclinations of galaxies with identified redshifts. These observations and the associated data reduction are discussed below. Figure 2.1 shows the magnitude and impact parameter distributions of the MOS and MUSE surveys, whilst their projected extent on the sky is illustrated in Figure 2.2.

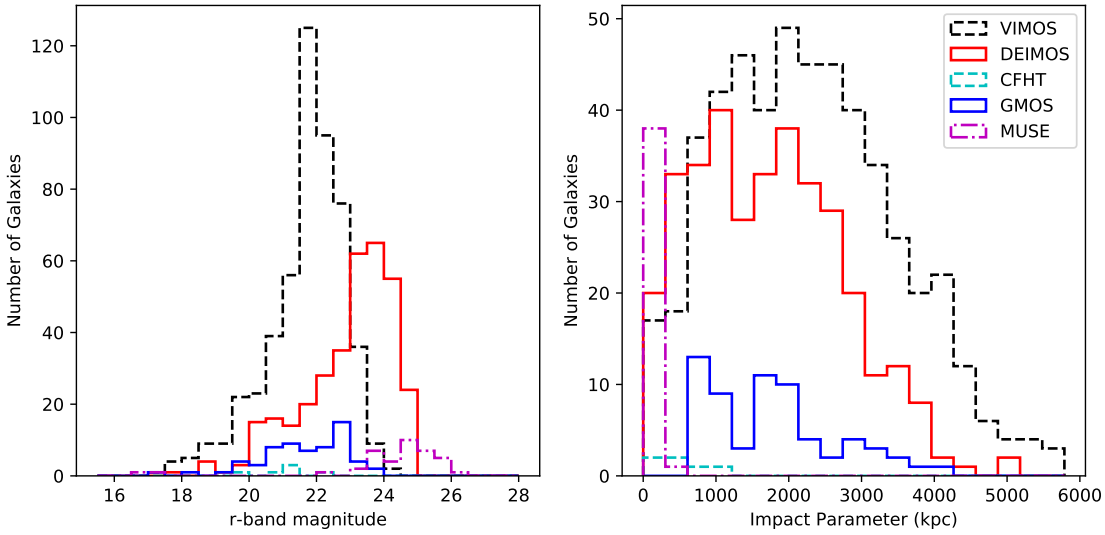

Figure 2.1: The magnitude and impact parameter distributions of galaxies in our catalogue, divided by the instrument used to obtain the galaxy spectrum, illustrating the depth and area of each observing program. Objects observed by multiple MOS instruments are shown only in the instrument with the best redshift flag (these flags are described in Section 2.2), or the best resolution if flags are equal. The MUSE objects shown are all new detections not featuring in the MOS surveys. *Left:* The apparent magnitude distribution of the galaxy samples, using the SDSS r-band in bins of 0.5-magnitude width. *Right:* The impact parameter from each galaxy to the nearest of the three quasars.

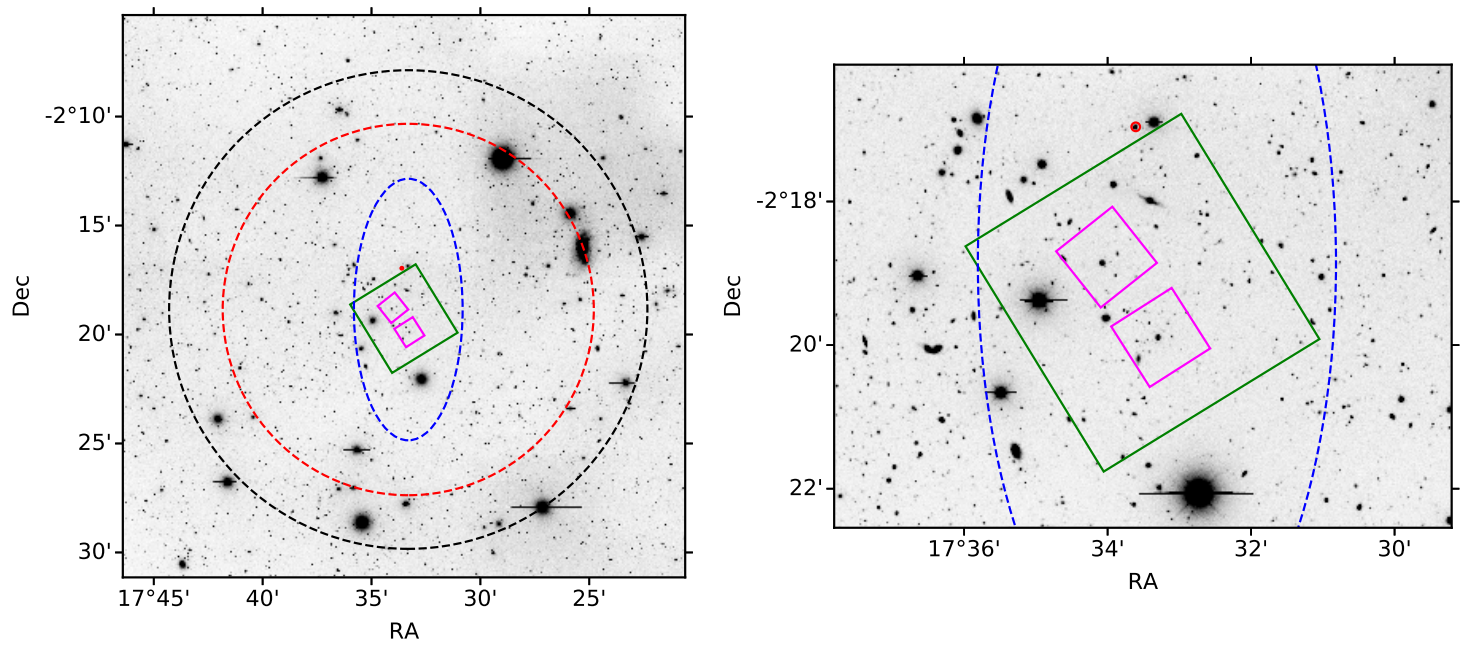

Figure 2.2: The layout of the surveys used in this study. The background image was taken with the Mayall 4-metre Telescope at the Kitt Peak National Observatory. The dashed lines enclose the approximate regions covered by the MOS surveys, with VIMOS, DEIMOS and GMOS shown in black, red and blue respectively. The solid green square shows the region covered by HST imaging, whilst the smaller magenta squares show the MUSE fields centered on QSOs A and B. QSO-C lies inside the small red circle just outside the northern edge of the HST field. The left panel shows the full extent of the galaxy surveys, and the right panel more clearly shows the region close to the lines-of-sight.

Table 2.3: Summary of the galaxy spectra used in the catalogue. Columns are: (1) instrument used; (2) number of spectra taken (including duplicates); (3) number of unique objects observed by that instrument; (4) number of objects for which that instrument provides the reference spectrum and redshift; (5) number of objects for which we have estimated a redshift using MARZ (used to estimate redshift uncertainties as described in Section 2.2); (6) approximate FWHM of the line-spread function in km/s; (7) the program ID of the observations. The instrument with the highest confidence flag is used in the catalogue; if multiple instruments have the same flag, then the best resolution is used.

Instrument (1)	N spectra (2)	N unique (3)	N cat (4)	N marz (5)	FWHM (km/s) (6)	Prog ID (7)
VIMOS	935	757	746	436	1500	086.A-0970, 087.A-0857
DEIMOS	642	543	487	286	60	A290D
GMOS	210	196	112	107	470	GS-2008B-Q-50
CFHT-MOS	30	29	20	9	400	
MUSE	140	140	59	67	120	094.A-0131

MUSE

Information on the kinematics of galaxies close to the quasar lines-of-sight can be extracted from MUSE data. During 2014, the MUSE GTO team took eight exposures covering $1' \times 1'$ fields of view around both QSO-A and QSO-B (program ID 094.A-0131, PI Schaye), totalling two hours for each quasar. This produces a 3D datacube, with a spectrum in each $0.2'' \times 0.2''$ 'spaxel' from 4750 to 9350 Å. These deliver seeing of $0.96''$ for QSO-A, and $0.82''$ for QSO-B. In the spectral direction, the datacube has a FWHM of $\approx$2.7 Å.

The reduction of these data follows a similar process to Fumagalli et al. (2016, 2017); Fossati et al. (2019b); Lofthouse et al. (2020); Bielby et al. (2020). MUSE ESO pipeline routines were used to remove bias, apply flat-fielding, and calibrate astrometry and wavelength for each exposure. The 'scibasic' and 'scipost' pipeline routines combine the IFUs for each exposure, resampling using a drizzle algorithm onto a 3D grid, as well as correcting for telluric absorption using sky continuum and sky line models produced using the darkest pixels in the exposure. Exposures can be aligned using point sources to produce a reasonable combined datacube, but this process generally leaves sky line residuals as well as uneven illumination across the field (e.g. Bacon et al., 2017).

Further corrections were applied using the CUBEX package (S. Cantalupo, in prep). We use two main routines from this package (Cantalupo et al., 2019). CubeFix performs a renormalization on each IFU, stack, and 'slice' (similar to a single slit), making the background as flat as possible across the MUSE field-of-view and wavelength range, and removing the 'chequered' pattern that often afflicts images reduced solely using the ESO pipeline. CubeSharp provides a flux-conserving sky subtraction, using the empirical shape of sky lines to calculate a line-spread function. Within each spatial pixel, flux is then allowed to move between neighbouring spectral pixels to best match the LSF, allowing the sky lines to be more accurately removed whilst conserving total flux. CubeFix and CubeSharp are run twice on each exposure, the results of the first run allowing better masking of sources in the second run. This further ensures that fluxes are not overcorrected and preserves the source flux as well as possible.

Table 2.4: Objects detected in the MUSE fields by the MARZ flag assigned. The flag 2-4 galaxy detections are those added to the galaxy sample used for this study.

Flag	Descriptor	N
4	highly confident	24
3	good	21
2	possible	22
1	unknown	39
6	artefacts/stars	32
	QSOs	2
2-4	galaxy detections	67
	total	140

A 3σ clipping is then used, combining the exposures using mean statistics. This combined cube is then used to mask sources for a final run of CubeFix and CubeSharp. Using this package greatly reduces sky and flat-field residuals, although some residuals remain visible towards the red end of the MUSE spectra.

Objects in the MUSE fields were identified using SExtractor (Bertin & Arnouts, 1996) on the white-light image. We produced 1D spectra by summing the flux within the SExtractor aperture.

We then estimated redshifts using the MARZ software (Hinton et al., 2016), with additional galaxy templates provided by Matteo Fossati (described in Fossati et al. 2019b, created using Bruzual & Charlot 2003 stellar population models). MARZ identifies the five redshift/template combinations producing the best cross-correlation between the observed spectrum and the template. We then chose the most likely of these based on the features fitted. Objects identified by SExtractor that are much smaller than the point-spread function ($\approx$1", 5 pixels) can be excluded as artifacts, and other objects are best fit by a stellar template instead of a galaxy template. The remaining objects have been assigned a confidence flag between 1 (redshift unknown) and 4 (highly confident) based on the spectral features visible at the redshift given by the best-fit result from MARZ. 67 galaxies were assigned a flag > 1, and are therefore used in this study. The number of objects with each confidence flag is shown in Table 2.4.

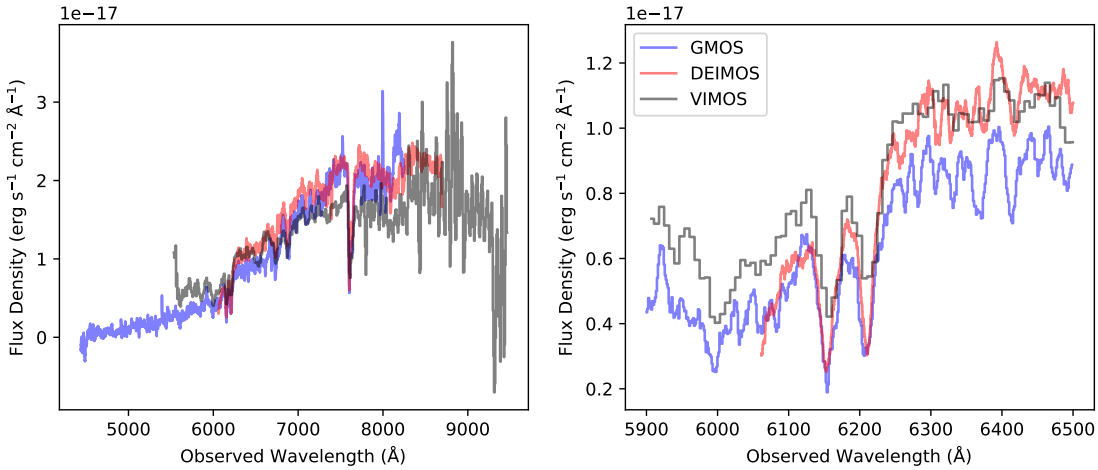

Figure 2.3: Example spectra of a galaxy observed in VIMOS, GMOS and DEIMOS. The left panel shows the full spectrum highlighting the different wavelength ranges covered, whilst the right panel centers on the Ca K & H absorption features. This galaxy is at z $\approx$ 0.56, has luminosity close to $L_\star$, and is classified as non-star-forming. We smooth over a 3 Å kernel to improve visibility.

MOS

The MOS galaxy data is the subset of the catalogue from T14 that covers the Q0107 field, consisting of spectra from CFHT-MOS, VIMOS, DEIMOS and GMOS. Many objects in the catalogue were observed multiple times, either by the same instrument or by multiple instruments. One example is shown in Figure 2.3. The data are described briefly here. T14 and references therein describe the data collection and reduction processes in more detail.

CFHT-MOS

The multi-object spectrograph on the Canada-France-Hawaii Telescope (CFHT-MOS) (Le Fevre et al., 1994) was used for observing runs in 1995 and 1997 by Morris & Jannuzi (2006). The Q0107 field was observed on the 29th and 30th July 1995, producing 30 galaxy spectra (one object observed twice, so 29 objects). The observation and reduction are described in more detail in the above paper.

The observed spectra were bias-subtracted using IRAF, and bad pixels were interpolated over. Cosmic rays were removed by comparing multiple exposures using the same mask. Sky subtraction used adjacent regions of the slit, whilst wavelength

calibration used an arc frame obtained whilst pointing towards the same region of sky (to minimize the effects of instrument flexure). Flux calibrations used a nearby standard star.

Only nine of the galaxies observed by CFHT-MOS also feature in any of the other MOS surveys. We therefore cannot confidently determine whether any systematic offset in wavelength/redshift affects these observations. The MOS catalogue did not include redshift confidence flags for these objects.

VIMOS

The VIMOS data (LeFevre et al., 2003) used a low-resolution (R $\approx$ 200) grism, giving 935 spectra with coverage between 5500 and 9500 Å (programs 086.A-0970, PI:Crighton; and 087.A-0857, PI: Tejos). The data were reduced using VIPGI (Scodeggio et al., 2005). Wavelength corrections were made using both lamp frames and skylines, whilst flux calibration used a standard star. We note that these data were taken shortly before the VIMOS charge-coupled devices (CCDs) were updated in August 2010, and are unfortunately affected by fringing effects at wavelengths $\gtrsim$7500 Å.

Redshifts were estimated using cross-correlation between the observed spectra and SDSS templates. These redshifts were then manually assigned a confidence flag (a: secure, b: possible, c: uncertain), where secure redshifts required at least three spectral features. The redshifts of all MOS objects in the Q0107 field were then adjusted to match the DEIMOS frame (as DEIMOS has the best resolution of the MOS instruments used), based on the objects observed by VIMOS and DEIMOS. The magnitude of this shift was $\Delta z \approx 0.0008$, or 120-240 km s^{-1} (see T14 for details).

DEIMOS

The DEIMOS (Faber et al., 2003) settings give a much better resolution (R $\approx$ 5000) and substantially deeper data but over a smaller field, covering the 6400-9100 Å range for 642 objects (taken in 2007-08, program A290D, PIs: Bechtold and Jannuzi). Redshifts were obtained from the DEEP2 data reduction pipeline (Newman et al., 2013), which applied all necessary de-biasing, flat-fielding, wavelength and

flux calibration, and heliocentric corrections. The DEIMOS redshift confidence was measured in the pipeline using four categories (1: not good enough, 2: possible, 3: good, 4: excellent), which were reassigned to match the three categories above (1 to c, 2 and 3 to b, 4 to a) when added to the catalogue.

GMOS

GMOS (Davies et al., 1997) was used in 2008 on this field (program GS-2008B-Q-50, PI: Crighton), with an intermediate resolving power (R $\approx$ 640) and a slightly bluer wavelength range of 4450–8250 Å.

Each spectrum consists of three 1080s exposures, dithered in wavelength to allow removal of bad pixels. IRAF was used to calibrate fluxes and wavelengths, using arc frames and a standard star taken contemporaneously with the science exposures.

210 redshifts were estimated using the same method as for VIMOS data, although the shift needed to match the DEIMOS frame was smaller, only $\Delta z \approx 0.0004$ or 60-120 km s^{-1}.

2.2 Combined galaxy catalogue

In order to combine spectra from the multiple instruments previously described into a single galaxy catalogue for this field, we need to match objects observed by multiple instruments in order to remove duplicates, as well as ensure that the galaxy properties we utilise in our analysis are measured consistently. We use photometry and astrometry from the Sloan Digital Sky Survey source catalogue (SDSS, Albareti et al. 2017) as an anchor, as the SDSS catalogue includes close to half of the MOS objects, and 14 of the MUSE galaxies.

Astrometry

In order to remove duplicates and select a single spectrum from which to derive the properties of each galaxy, we matched the coordinates of objects observed by multiple MOS instruments to those observed in SDSS. With the exception of CFHT, all instruments had sufficient cross-matches within 1" to confirm that the astrometry

is consistent between the MOS instruments, and required an offset of less than 0.5" to match SDSS. The same process applied to the MUSE astrometry revealed a similar ≈ 1" offset for both fields, which were corrected separately.

The astrometry of both the MOS and MUSE catalogues were adjusted to match SDSS, to ensure objects appearing in both catalogues were correctly paired. 28 objects were found to match within 1" after the correction to SDSS, and no additional matches within 2". Due to the larger number of objects, the offset between MOS and SDSS is more accurately determined than that for MUSE, so the corrected MOS coordinates are used for the objects appearing in both catalogues.

Magnitudes

R- and I- band magnitudes included in the MOS catalogue are systematically shifted to match the r- and i- band SDSS magnitudes, using the Lupton (2005) transformations[2]. Magnitudes for MUSE-only objects were estimated by integrating the spectrum through the SDSS r- and i- filters. The corrected MOS magnitudes were preferred for objects appearing in both MOS and MUSE catalogues, and the differences were approximately consistent with the uncertainties provided.

The survey depths are limited by the original target selections, at R $\approx$ 23.5, 24 and 24.5 for VIMOS, GMOS and DEIMOS respectively. As shown in Figure 8 of T14, the success rate of assigning redshifts to objects in the Q0107 field is $\gtrsim 80\%$ to a depth of R=22 in both VIMOS and DEIMOS, with the deeper DEIMOS data showing $\gtrsim 60\%$ success to R=24.

We do not detect any significant variation in the depth of the MOS data within the HST field, although the small number of MUSE galaxies extend to fainter objects. Any variation in depth across the field does not have a significant effect on our results, as we retain the same selection for our analysis in Section 3.2, and our Section 3.3 and 3.4 use the much smaller HST field. The models utilized in Chapters 4 and 5 also focus in galaxies within the HST field.

[2] `https://www.sdss.org/dr16/algorithms/sdssubvritransform`

Redshifts

Calculations of relative velocities between galaxies and absorbers require that there are no systematic shifts between their redshifts. We therefore compared redshifts to ensure that all of our galaxy samples are in the same frame as the absorption features.

The separate MOS samples from T14 have already been corrected to a single frame, described in the section for each instrument. We therefore first check that this galaxy frame is the same as the frame in which the absorber redshifts are measured. One test of this is to calculate the difference in redshift between galaxy–absorber pairs. At the scales on which galaxies and absorbers are correlated, this should produce a signal that is symmetric about zero (velocity offsets e.g. outflows should average to zero over a large sample), as presented by Rakic et al. (2011). If the signal is offset, that suggests a shift is needed to bring all the redshifts into the same frame.

We find no such shift when pairing high column density H I absorbers (N(H I) $> 10^{14}$ cm^{-2}) with galaxies within 2.5 Mpc of at least one sightline, both from the T14 catalogues. We fit a model consisting of a Gaussian plus constant offset to the velocity distribution of these pairs, these two components representing associated absorbers with small velocity differences, and unconnected absorbers with uniformly distributed velocity differences.

As most possible pairs lie in the uniform distribution, a velocity cut is needed to centre the fit close to zero, and avoid noise in this distribution dominating over the Gaussian peak (i.e the Gaussian component of the fit jumps to a nearby 'noise spike' rather than the peak of associated galaxy–absorber pairs). The fit varies with the velocity used for this cut, but the centroid of the Gaussian component remains within $\pm$10 km s^{-1} for cuts smaller than 5000 km s^{-1}. Therefore the galaxies and absorbers provided by T14 can be taken to lie in the same frame to better than 10 km s^{-1} precision. We similarly confirm that the separate samples for each instrument in the T14 catalogue are each consistent with this frame.

A small offset can be found if weaker absorbers are used or galaxies with a larger impact parameter are included, as well as if a larger velocity cut is used. These are

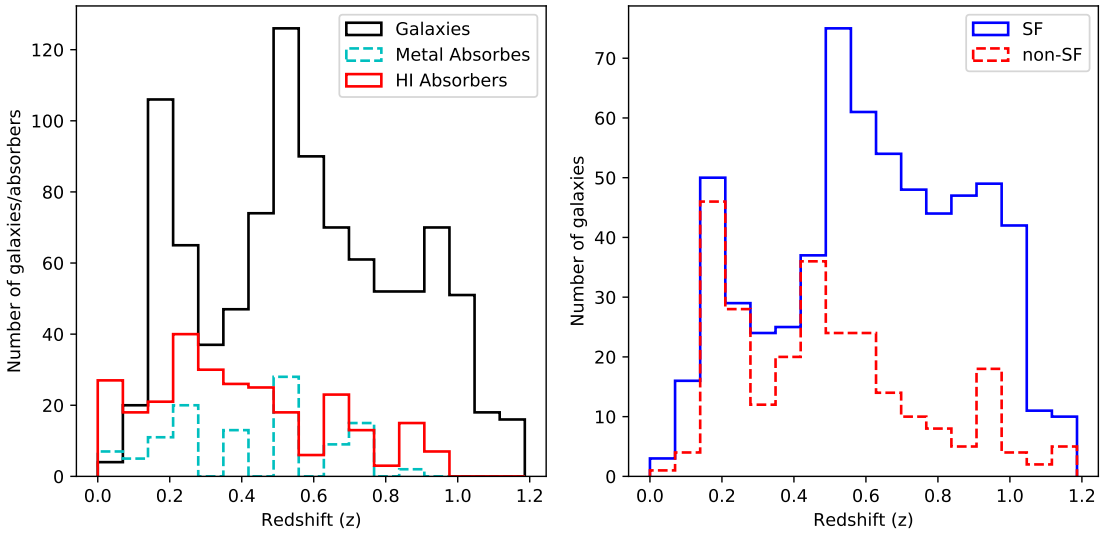

Figure 2.4: The redshift distributions of galaxies and absorbers in our catalogue. *Left:* The redshift distributions of the galaxy and absorber samples. *Right:* The redshift distributions of the star-forming and non-star-forming galaxies in our sample.

less likely to be physically connected, so introduce noise that dominates over the peak. We therefore do not attempt to correct for any such spurious offset.

We then add the MUSE observations. The distribution of velocity differences between MOS and MUSE observations of duplicate objects showed that the MUSE objects required a further shift of 30 km s^{-1} in order to match the frame of the MOS catalogue.

We note that, although the redshifts of galaxies and absorbers are in the same frame, the overall redshift distributions are not similar, as seen in the left panel of Figure 2.4. Therefore the redshift distribution of galaxy–absorber pairs is not uniform, and the redshift distributions of galaxy–absorber pairs with different properties (e.g. those involving star-forming galaxies vs those involving non-star-forming galaxies) will also differ. Any such differences need to be considered when analysing the results of this work.

Redshift uncertainties

Redshift uncertainties for the MOS objects are based on those with multiple spectra. We attempted to fit all MOS spectra using the MARZ code used earlier to

Table 2.5: Comparison of the measured velocity differences between objects measured twice by the same MOS instrument. We show the lowest-confidence flag assigned to spectra of each object from each instrument, and consider the distribution of velocity differences of each sample. Redshifts and flags shown are those assigned using the MARZ software (flags from 1 being 'unknown' to 4 being 'highly confident'), and we also show the flags given by the T14 catalogue to which the MARZ flags are matched. A velocity cut of 2000 km s^{-1} was used to remove pairs of observations for which the velocity difference is due to a different identification of spectral features. The cut affects only a small number of 'flag 2' objects. The number removed by this cut is shown in brackets. σ is the standard deviation of the velocity differences, which can be adopted as the uncertainty on any individual redshift measurement within that sample.

Intstruments	Flags	N	σ (km/s)
VIMOS	3, 4 (a)	29	120
	2 (b)	69 (6)	190
DEIMOS	3, 4 (a)	23	26
	2 (b)	40 (3)	47
GMOS	3, 4 (a)	4	44
	2 (b)	5	48

obtain redshifts from MUSE. For objects with multiple spectra from the same instrument, the redshift differences could be compared. The width of the distribution of velocity differences for each instrument provides an estimate of the uncertainty in the redshift of objects observed by that instrument. These are given in Table 2.5, where σ is adopted as the uncertainty for all objects in the T14 catalogue with the confidence flag shown in brackets. As redshifts with poorer confidence flags are generally identified using fewer features, we assign a larger redshift uncertainty to these b-flag galaxies. Whilst the GMOS sample size is very small, the relative values of the three instruments are consistent with the resolutions given in Table 2.3, so we adopt these uncertainties.

Our MUSE observations contain no duplicates, so this method cannot be used to estimate uncertainties on their redshifts. As MUSE has a higher resolution than GMOS, but lower than DEIMOS, we take the GMOS values as (likely somewhat conservative) estimates of the velocity errors for MUSE galaxies with the same confidence flags.

In order to directly compare the flags assigned for objects with MOS and MARZ

redshifts (a–c in the catalogue, 4–1 in MARZ), flag 'a' objects were numbered 3.5, 'b' to 2.5 and 'c' to 1.5. Redshifts quoted in our final catalogue are those with the highest flag.

Finally, the MARZ flags were reassigned to match those from the MOS catalogue: 1 to c, 2 to b and 3 & 4 to a. This produces our final catalogue of 1424 galaxies, of which 1026 have 'a' or 'b' flags and are used in the following analyses. Their locations in space and redshift are shown in Figure 2.5.

Spectral classification

We divide our galaxy sample into 'star-forming' and 'non-star-forming' galaxies. We maintain the classifications used in T14 for the MOS galaxies (see their section 5.1) and apply similar criteria for dividing the MUSE galaxies. Namely, those galaxies best fit by a star-forming template (e.g. 'late-type', 'starburst' or 'star-forming' templates) are classified as star-forming, and those fit by a passive template (e.g. 'passive', 'early-type' or 'absorption galaxy' templates) are classified as non-star-forming.

These templates differ primarily due to the presence of emission lines, so this classification is denoting galaxies with measurable emission lines as star-forming, and those without as non-star-forming.

We also estimate the star-formation rates by directly fitting the Hα and [O II] emission lines, and additionally estimate stellar masses in order to derive specific star-formation rates. We use the Kennicutt (1998) and Kewley et al. (2004) calibrations to convert line luminosity to SFR for Hα and [O II] respectively. We assume 1 magnitude of extinction at Hα (Charlot et al., 2002), and use the Calzetti et al. (2000) curve to estimate extinction at [OII]. The predicted wavelength of at least one of these emission lines is available for $\approx 90\%$ of galaxies with well determined redshifts. Stellar masses are estimated using the relationship given in equations 1 and 2 of Johnson et al. (2015), which represent a fit to the stellar mass to r-band light ratio obtained from low-redshift galaxies in the NASA-Sloan atlas. These NASA-Sloan masses were determined by fitting spectra to stellar population models based on those in Bruzual & Charlot (2003).

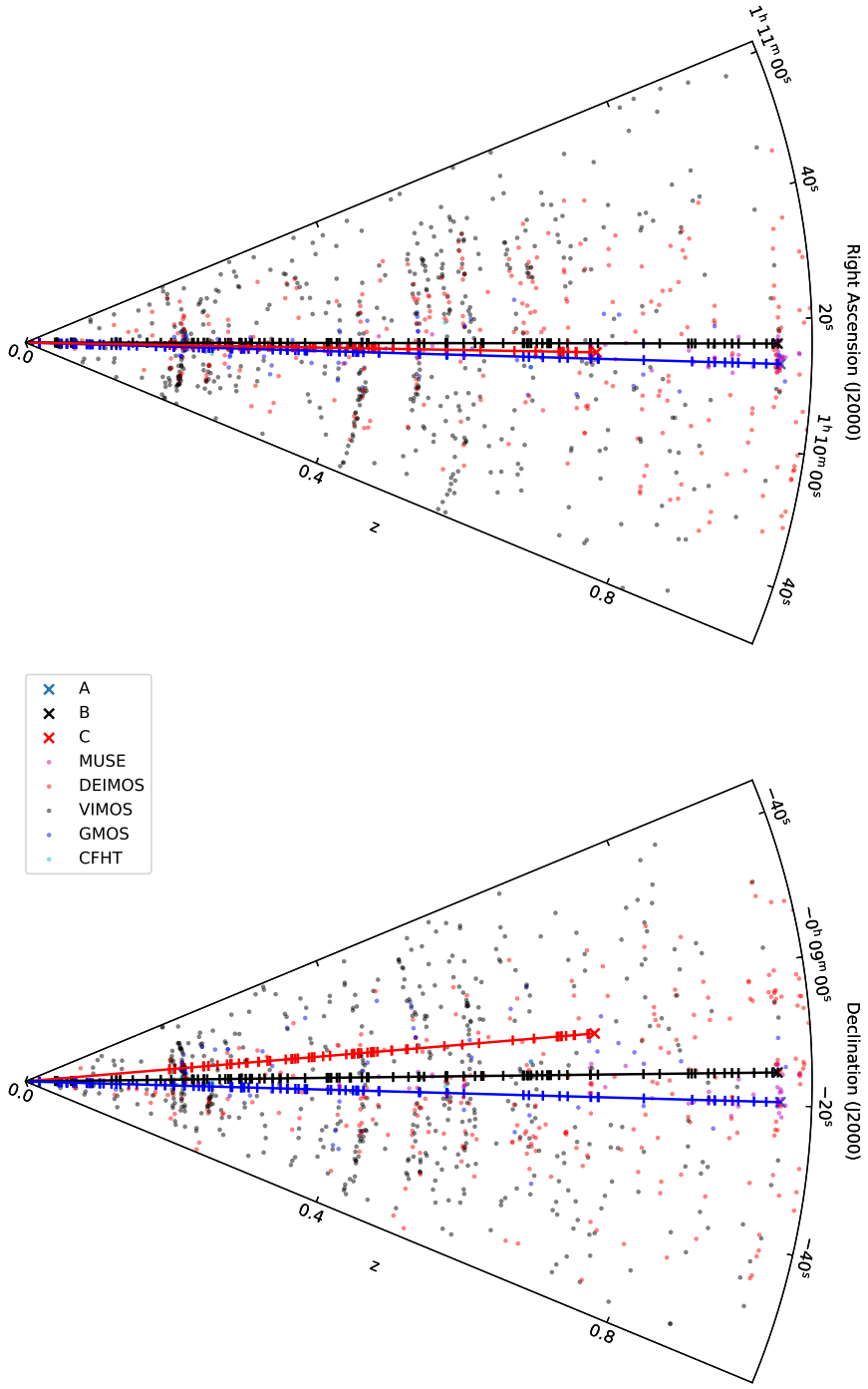

Figure 2.5: The distribution of galaxies and H I absorption features in the sample, plotted in redshift and right-ascension (top) or declination (bottom). Solid lines show the lines-of-sight to the three quasars, with HI absorption shown as tick marks. Points are galaxies coloured by observed instrument. Note that the angles are massively expanded, so arc-like features likely correspond to galaxy groups.

We find that a cut at a specific star-formation rate of 0.02 Gyr^{-1} correctly identifies $\approx 75\%$ of both samples. Our stellar mass and SFR estimates are illustrated in Figure 2.6. However, these estimates have substantial measurement and systematic uncertainties, so we primarily use the classification described above, in which galaxies are denoted as 'star-forming' (SF) or 'non-star-forming' (non-SF) based on the template fit.

These subsamples of SF and non-SF galaxies show no substantial bias in their impact parameter distributions or mass distributions. It must be noted that there is a small excess of star-forming galaxies at the smallest impact parameters ($<$ 200 kpc), due to the ease of finding emission lines using the MUSE datacubes. The SF and non-SF samples also feature slightly larger low-mass and high-mass tails respectively in their mass distributions, but both of these biases affect a small number of galaxies. We confirm throughout that these have no substantial effect on our results by re-running our tests with samples excluding the MUSE galaxies and samples excluding the tails of the mass distribution, obtaining similar results.

However, there is a substantial bias in redshift, with SF galaxies preferentially featuring at higher redshifts than non-SF galaxies, as seen in the right panel of Figure 2.4. This is likely a combination of real redshift evolution (higher cosmic star-formation rates at higher redshift, e.g. Madau & Dickinson 2014) and observational effects (higher signal-to-noise is required to confirm the redshifts of galaxies without emission lines), and must be taken into account when comparing the CGM/IGM around galaxies in these samples.

2.2.1 HST imaging

In addition to the spectroscopic data, we also use high-resolution imaging of the field to constrain galaxy morphologies and orientations. We use publicly available Hubble Space Telescope imaging of this field (Program ID: 14660, PI Straka), obtained through ACS (Ryon, 2019) and the F814W filter. This consists of four exposures totalling 2171 seconds.

It must be noted that one of the exposures was affected by an unidentified bright object moving across the field, leaving an artefact in the final combined image.

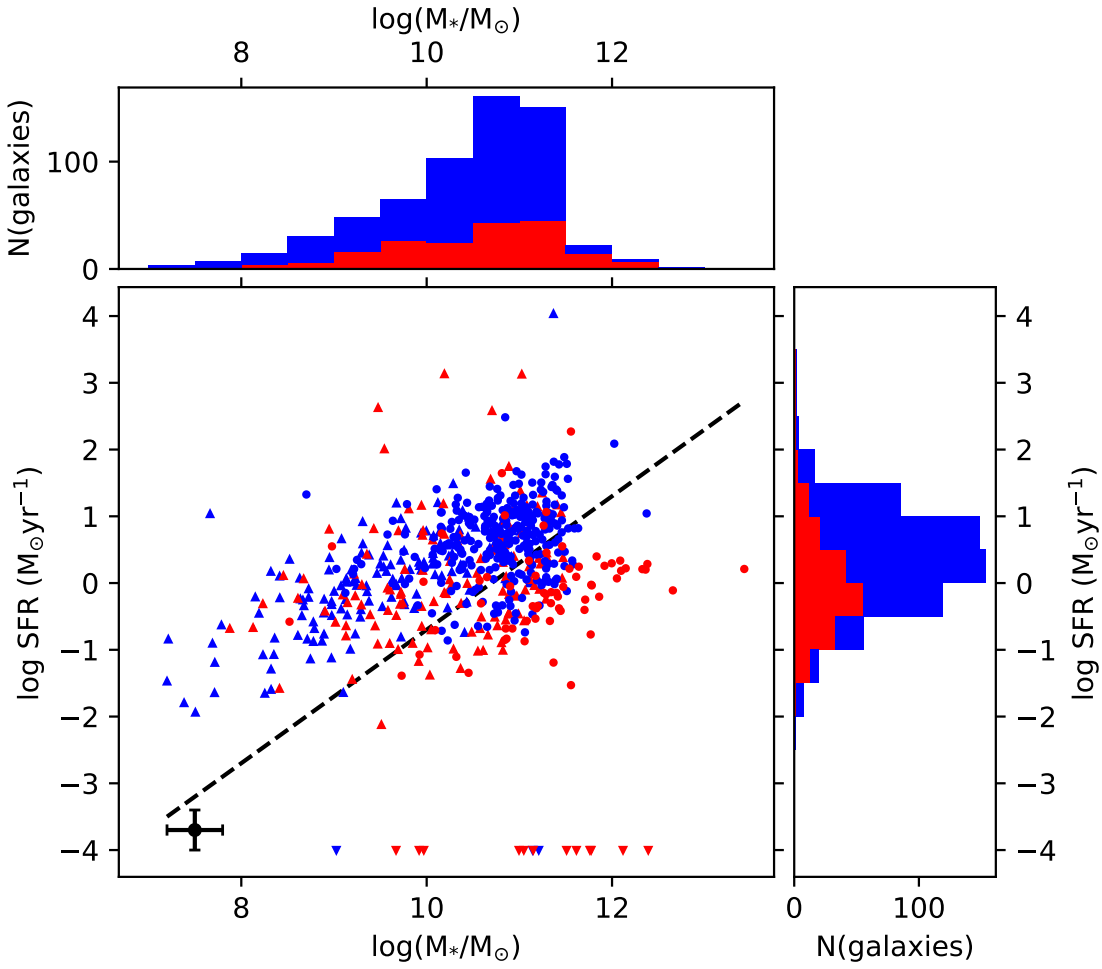

Figure 2.6: The star-formation rate against stellar mass for our galaxy sample. Star-formation rates are calculated using the [OII] or Hα emission lines, shown in circles and upward-pointing triangles respectively. The downward-pointing triangles at the bottom of the figure show the masses of galaxies for which the line fit was unable to produce a result. (These are excluded from both projected histograms.) The blue points and histograms denote galaxies classified as 'star-forming' using the template fits, whilst the red points were classified as 'non-star-forming'. The black point in the lower-left shows the median uncertainty in each axis, although the non-star-forming galaxies exhibit systematically larger uncertainty in SFR. The dotted black line is the 0.02 Gyr^{-1} cut in sSFR that best reproduces our template classification. Most of the outlying objects with SFRs substantially higher than most galaxies of similar mass are due to the spectrum at the expected wavelength of the emission line being contaminated by sky lines or the fringes seen in the VIMOS spectra at red wavelengths.

However, we only use the HST imaging to study the morphology of galaxies in this field, so this artifact does not substantially affect our results.

Galaxies were identified using SExtractor, then matched to the coordinates of objects in the MOS/MUSE combined catalogue. No systematic offset was found, so objects within 1" were matched, as above.

We run GALFIT (Peng et al., 2002), which uses chi-squared minimization algorithms to produce a best-fitting 2D model of a galaxy. We initially fit a Sersic disk to every galaxy found in both our redshift catalogue and the HST image, using SExtractor results as initial guesses for the fit, and then introduce additional components where necessary to find a reasonable fit. This provides improved position angles and inclinations, taking full account of the point-spread function of the image and reducing the average uncertainty by a factor ≈ 3 relative to the position angles produced by SExtractor.

We again assign quality flags to the GALFIT results (1: good fit by eye and no clear structure remains in residuals, 2: good by eye, 3: possible, 4: clearly a poor fit), allowing poorly constrained results to be excluded. Flag 4 objects are excluded from all results, but galaxies near to face-on that were fit successfully are included despite large position angle uncertainties. This returns 109 galaxies with position angles constrained by GALFIT and a counterpart in our spectroscopic survey, of which 72 also have well-constrained redshifts ('a' or 'b' flags). We illustrate examples of this fitting in Appendix A.

CHAPTER 3

Statistical properties of detected CGM/IGM absorbers

In this chapter we discuss several tests used to determine the size scales and structures of the CGM and IGM around galaxies in the Q0107 field through the statistics of our large galaxy and absorber samples. This work has been published in Beckett et al. (2021), which we refer to as Paper 1 throughout this thesis.

3.1 Background

Galaxies follow a large-scale filamentary structure throughout the Universe, known as the cosmic web (Bond et al., 1996), formed by the gravitational accretion of gas towards the potential wells of dark matter around initial overdensities, as has been modelled in dark-matter-only simulations for decades (e.g. Klypin & Shandarin, 1983; Springel et al., 2005). Once stars and galaxies form, this accretion from the intergalactic medium (IGM) towards galaxies becomes affected by complex baryonic physics, including stellar and AGN feedback (e.g. van de Voort et al., 2011; Nelson et al., 2019; Mitchell et al., 2020b). Simulating these effects on a range of scales from sub-parsec-scale supernovae to megaparsec-scale gas flows around clusters necessitates sub-grid models which require constraints from observations.

Such constraints are necessary for studies of galaxy evolution, as exchanges of material between galaxies and their environments play an important role in regulating star formation (e.g. Kereš et al., 2005; Schaye et al., 2010; Davé et al., 2012; Lehnert et al., 2013; Somerville et al., 2015; Salcido et al., 2020). Gas outside of galaxies is believed to contain a substantial fraction of the baryons in the Universe (e.g Fukugita et al., 1998; Behroozi et al., 2010; Werk et al., 2014), so any census of baryons used to constrain cosmological parameters must consider the state of the gas around galaxies (usually by modelling the ionization state of the gas based on absorption spectra, e.g. Shull et al. 2012, although recent methods using fast radio bursts account for all ionized baryons, e.g. Macquart et al. 2020). The dynamics of galaxies are also strongly linked to the state of the surrounding gas through the transfer of angular momentum (e.g Pichon et al., 2011; Stewart et al., 2017; DeFelippis et al., 2020). Therefore, observational insights into the distribution of baryons around galaxies can not only inform our understanding of the gas itself, but also stellar processes within galaxies and their effects on galaxy formation and evolution.

Outside the local environment, most observations of the gas around galaxies are made by identifying absorption features in the spectrum of background sources, usually quasars. These features can probe neutral gas, most commonly using H I (e.g. Morris et al., 1991; Lanzetta et al., 1995; Chen et al., 1998; Adelberger et al., 2003; Tumlinson et al., 2013; Rakic et al., 2013; Heckman et al., 2017; Chen et al., 2018), especially since the Hubble Space Telescope has allowed the Lyman-α transition to be observed at low redshifts. Other studies use low ions such as Mg II to probe cool ($\sim 10^4$ K) gas (e.g. Bergeron, 1986; Bergeron & Boissé, 1991; Bouché et al., 2006; Nielsen et al., 2013; Schroetter et al., 2016; Ho et al., 2017), or search for highly-ionized material (e.g. Bergeron et al., 1994; Tripp & Savage, 2000; Cen et al., 2001; Tumlinson et al., 2011; Turner et al., 2014; Finn et al., 2016; Werk et al., 2016; Nicastro et al., 2018; Bielby et al., 2019) through transitions from ions such as O VI to O VIII. This variety of observed ions found in sightlines probing the gas near to galaxies suggests that it has a complex, multi-phase structure (e.g. Veilleux et al., 2005; Werk et al., 2013; Mathes et al., 2014; Péroux et al., 2019; Chen et al., 2020a).

Galaxy-scale outflows are observed in emission (e.g. Bland & Tully, 1988; Finley

et al., 2017; Burchett et al., 2021) and absorption (e.g. Grimes et al., 2009; Turner et al., 2015; Lan & Mo, 2018; Schroetter et al., 2019), their multi-phase nature indicated by a range of diagnostics from low ions (tracing cool gas, e.g. Concas et al. 2019), to X-ray-emitting hot gas (e.g. Lehnert et al., 1999). These are consistent with stellar feedback, in which supernovae and stellar winds drive material out of the galaxy (e.g. Chevalier & Clegg, 1985; Heckman et al., 1990) to distances of several tens of kiloparsecs. Cosmological simulations also find these winds, and can produce the multi-phase biconical outflows observed despite isotropic injection of energy and momentum (e.g. Nelson et al., 2019; Mitchell et al., 2020a). Hopkins et al. (2021) also find that the addition of cosmic rays to the outflow-driving mechanism may allow such flows to reach megaparsec scales.

There are several lines of evidence suggesting that substantial gas accretion occurs onto galaxies from the surrounding medium, including the metallicities of dwarf stars (e.g. Casuso & Beckman, 2004), the short depletion timescales of star-forming galaxies (e.g. Freundlich et al., 2013; Scoville et al., 2017), and the declining H I density of the Universe over time (e.g. Neeleman et al., 2016). Evidence for this accretion is found in 'down-the-barrel' observations (using the host galaxy as the background source) where absorption line profiles indicate gas flows towards the galaxy (e.g Martin et al., 2012; Rubin et al., 2012). Observations in Mg II have long suggested that the gas shows strong rotation, often with an in-falling velocity component (e.g Charlton & Churchill, 1998; Steidel et al., 2002). When this is compared to the rotation curves of galaxies, often using integral field units such as MUSE, most find that absorbing gas close to the major axis of a galaxy preferentially shows co-rotation in both Mg II (e.g. Ho et al., 2017; Martin et al., 2019b; Zabl et al., 2019) and H I (e.g French & Wakker, 2020), particularly within 100 kpc. However, this co-rotation is not always apparent when extending to weaker absorbers or larger impact parameters (e.g. Dutta et al., 2020).

This 'galactic fountain' model, consisting of minor axis outflows and major axis co-rotating accretion, can explain the bimodality in position angle found in the MEGAFLOW survey (Schroetter et al., 2016; Zabl et al., 2019; Schroetter et al., 2019). It is also supported by cosmological simulations, for example the FIRE

simulations (Hafen et al., 2019, 2020) produce galaxies around which the gas around galaxies is a mixture of material ejected from the galaxy interstellar medium (ISM) in winds, and material accreted from the IGM. Much of this material then accretes onto the central galaxy. However, this model would predict generally lower metallicities along the major axis, which has not been detected in recent H I observations (Pointon et al., 2019; Kacprzak et al., 2019), and Mg II observations often do not find a significant bimodality in position angle (Dutta et al., 2020; Huang et al., 2021). How frequently these structures form, and to what extent, therefore remains uncertain.

Whilst a galactic fountain can reproduce many observations of the gas close to galaxies (the circumgalactic medium, or CGM; see Tumlinson et al. 2017 for a recent review), studies of the correlation between gas and galaxies show transverse correlation lengths of 2–3 Mpc at $z < 1$ (Tejos et al., 2014; Finn et al., 2016). On these scales the interactions between galaxies are expected to have a significant effect on the structure of the CGM/IGM (e.g Fossati et al., 2019b; Dutta et al., 2020). Intra-group material can be observed in absorption, that can not easily be assigned to an individual galaxy (e.g. Péroux et al., 2017; Bielby et al., 2017; Chen et al., 2020a). We expect interactions in groups and clusters to build up pressure-confined tidal debris, visible across a range of column densities (Morris & van den Bergh, 1994). This is clearly visible in H I maps of the Magellanic Stream (e.g. Mathewson et al., 1974; Nidever et al., 2008) and the M81/M82 group (e.g. Croxall et al., 2009; Sorgho et al., 2019), as well as Hα and occasionally [O III] emission in dense environments (e.g Fumagalli et al., 2014; Johnson et al., 2018; Fossati et al., 2019a).

Absorption, especially in Lyα, is our most sensitive probe of the CGM and IGM, but it is in most cases limited to a single pencil-beam sightline through the CGM of any individual galaxy. This makes it difficult to directly constrain the size scales and structures in the CGM, although some studies have stacked large samples together attempting to infer these properties (e.g Chen, 2012; Turner et al., 2014).

Additional information can be extracted using multiple sightlines probing the CGM of an individual galaxy. Bowen et al. (2016) take advantage of the large angle subtended by relatively nearby haloes, such that the halo is pierced by a number of

QSO sightlines, finding the gas surrounding NGC 1097 to have a disk-like structure with rotating and in-falling velocity components. Similarly Keeney et al. (2013) find the absorption in three sightlines around a nearby galaxy to be consistent with a 'galactic fountain'. Gravitational lensing produces multi-sightline systems, through multiple images (e.g Smette et al., 1992; Rauch et al., 2002; Chen et al., 2014; Zahedy et al., 2016), and extended arcs that can be considered as multiple closely-spaced lines-of-sight (e.g. Lopez et al., 2018, 2020). It is also possible to use bright background galaxies as sources (which may also be extended), as an alternative or in addition to quasar sightlines (e.g. Adelberger et al., 2005; Steidel et al., 2010; Cooke & O'Meara, 2015; Rubin et al., 2018; Fossati et al., 2019b; Zabl et al., 2020).

This study focuses on the Q0107 system, a quasar triplet at z $\approx$ 1: LBQS 0107-025A, LBQS 0107-025B, and LBQS 0107-0232, hereafter denoted A, B, and C. Table 2.1 summarizes some of the main parameters of this system. This allows multiple sightlines to be probed through the CGM/IGM around galaxies in this field, separated by hundreds of kpc.

As the only known, bright, low-redshift quasar triplet, this system has been the focus of many studies. Dinshaw et al. (1997) observed A and B, finding 5 absorption systems that cover both sightlines, and 6 limited to a single sightline. Using a maximum likelihood analysis, they concluded that their data was best explained by randomly inclined disks approximately 1 Mpc in radius. Young et al. (2001) complemented this with analysis of the likelihood of individual multi-sightline absorption systems, and found that matches involving stronger absorption features tended to have smaller velocity separations. Coincidences of absorption between the sightlines also occur more frequently among high-column-density absorbers, as found by Petry et al. (2006).

A later study by Crighton et al. (2010) (hereafter C10) used improved QSO spectra, including QSO-C, in addition to galaxy data from CFHT-MOS, to extend these results. They observed a highly-significant excess of absorption systems covering all three sightlines over an ensemble of randoms, providing clear evidence that gas and galaxies are associated on scales of hundreds of kpc. Additionally, galaxies and groups of galaxies could be associated with multiple absorbers, allowing the struc-

ture of the gas to be analysed in individual systems (although we defer an updated analysis of these systems to a later paper, focusing here on the statistical properties of our samples).

Ionization modelling was used by Muzahid (2014) to study one example in this field at z $\sim$ 0.22, using the presence of O VI in sightlines A and B to estimate the radius of the CGM as 330 kpc, and therefore detect both the warm and cool CGM of an $L_\star$ galaxy.

This field was also included in a study of galaxy–absorber cross-correlations covering six independent fields by Tejos et al. (2014) (hereafter T14) and another using 50 fields by Finn et al. (2016) (F16). Their galaxy catalogue forms the basis for the galaxy data used in this work.

In this study we present an updated analysis on the Q0107 triplet, using a much larger sample of galaxies extending to fainter magnitudes, in addition to Hubble Space Telescope imaging providing improved morphologies, and MUSE fields providing kinematics on a subsample of galaxies close to the A and B sightlines. We use this data to examine the CGM/IGM on large scales, where the improved imaging allows us to constrain the extent of the 'galactic fountain' and the larger galaxy samples allow us to study the presence of absorption features covering multiple sightlines around galaxies of different properties.

In Section 2.1 we describe the quasar spectra and galaxy survey used to produce our catalogues of absorption features and galaxies. Section 3.2 discusses our test for correlated absorption between the three sightlines. Section 3.3 gives results from studying the relationship between absorption properties and the position angles of nearby galaxies, whilst in Section 3.4 we use the MUSE data to identify co- and counter-rotation among material close to the major axis of galaxies. In Section 5.6 we discuss the consequences of our results and how future work can further progress our understanding.

We use the cosmology from Planck Collaboration (2020) throughout, with $\Omega_m = 0.315$ and $H_0 = 67.4$ km s^{-1} Mpc^{-1}, and quote physical sizes and distances unless otherwise stated.

3.2 Coherence between sightlines

One unique test allowed by the configuration of multiple lines-of-sight is to compare the absorption seen across multiple sightlines at the same redshift. Both Dinshaw et al. (1997) and Crighton et al. (2010) (C10) attempted to estimate the scale size of absorbers using the numbers of coincidences (where absorption was identified at multiple redshifts) and anti-coincidences (where detection of absorption in one sightline was not matched in the other(s)). We can therefore use our larger sample to both review the results from these papers, demonstrating that absorption is often correlated on the 400-1200 kpc scales separating these sightlines, and to split the sample, allowing us to study how these coincidences are affected by the properties of the absorption and of nearby galaxies.

3.2.1 Random absorbers

In order to test the significance of the correlations between sightlines, we must compare the observed distribution to the number expected if there were no physical connection between the observed gas and galaxies. For this reason, we have generated 5000 sets of randomly distributed absorbers, using a method similar to that used in T14, as follows:

i) Calculate the signal-to-noise per resolution element for each QSO spectrum.

ii) Convert this to a minimum rest-frame equivalent width for the absorption feature as a function of redshift. The detection limits for QSO-A are shown as an example in Figure 3.1.

iii) For each real absorption feature, find the allowed region in redshift space for which the EW of the real absorber is larger than the minimum, and is not covered by galactic absorption.

iv) Distribute absorbers randomly through the allowed region, giving the random absorber the same properties as the original observed absorption feature.

In order to maintain the approximate redshift/wavelength distribution of absorbers, we restrict each randomized absorber to the same grating as the observed

absorber from which we derived its properties. We describe this process in more detail in Appendix B.2.

3.2.2 Absorber-Galaxy groups

In order to associate galaxies and absorbers, we use two different grouping algorithms in this section, similar to those used in C10. The first is a nearest-neighbour algorithm, which simply takes the nearest absorber (in velocity) to each galaxy in each sightline.

The second method is a velocity-cut around each absorber/galaxy, in which we consider all absorbers/galaxies within that velocity window as associated with that absorber/galaxy.

Galaxies must be within 2.5 Mpc of at least one of the sightlines in order to be included, and have a redshift flag of 'a' or 'b'. These restrictions remove the galaxy-absorber pairs with the largest separations (and are therefore the least likely to be physically connected), as well as those with poorly-determined redshifts.

3.2.3 Results

In the series of Figures 3.2, 3.3 and 3.4, three plots are shown for each set of constraints applied to the samples, each with three panels. The top three panels show the velocity difference between each galaxy and its nearest-neighbour absorber in each sightline. The histogram shows the distribution of real velocity differences, with the black points giving the median number of galaxies in each bin in the random sets, and the cyan points showing the 99th percentile. Thus, the level of the histogram in relation to the points shows the excess of galaxy-absorber separations in that 100 km s^{-1} bin over the expectation if the absorber redshifts were randomly distributed. Note that, as the total number of galaxies is the same, any excess in bins with small velocity difference must be accompanied by a deficit in other bins.

The middle set of three panels shows the number of galaxies around which at least 1, at least 2, or all 3 sightlines contain H I absorption within the 500 $\mathrm{km\,s^{-1}}$ cut in velocity. The histogram shows the distribution of the random sets, with the

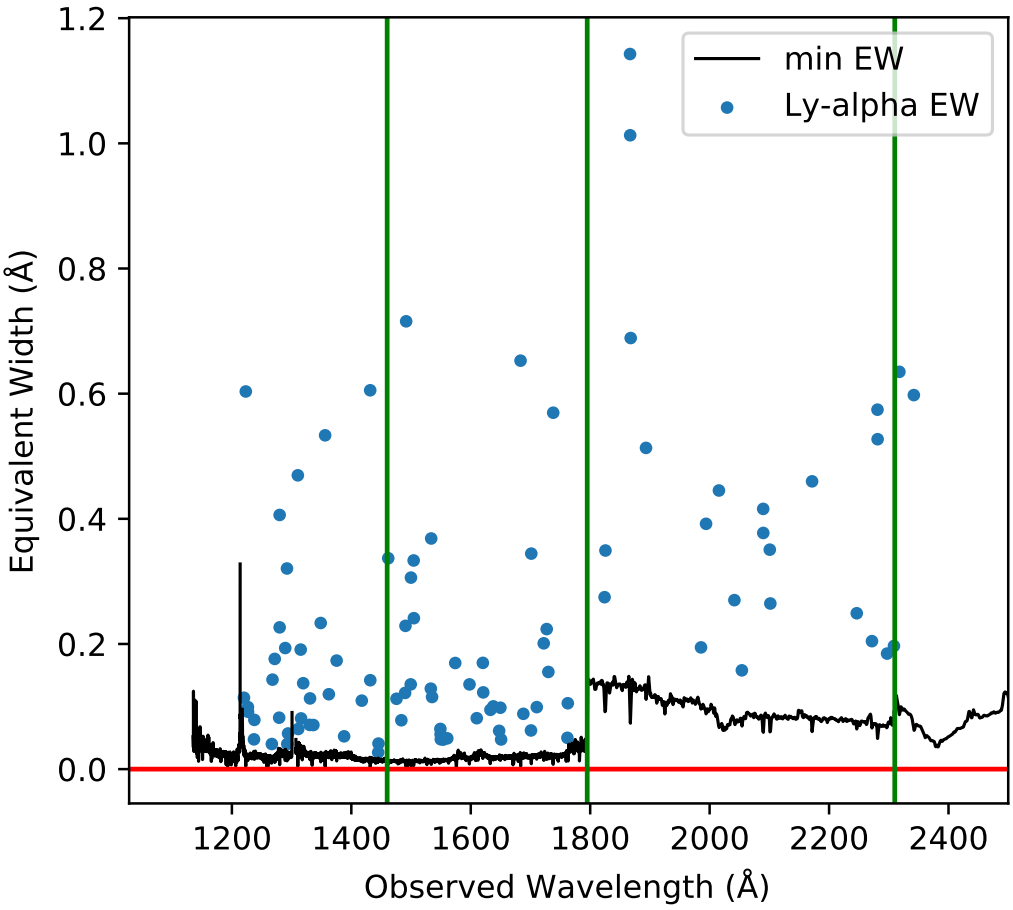

Figure 3.1: The estimated minimum rest-frame equivalent width detectable in the COS and FOS spectrum of QSO-A. The calculation is described in the text, SNR is calculated using the continuum estimate and the instrumental noise, with the FWHM taken from Table 2 in T14 for each grating. A significance limit of 3 is used. The observed H I absorbers from the catalogue are scattered on the plot, assuming that the Ly-α line was observed. The vertical green lines divide the different gratings used in the spectrum, which therefore have different signal-to-noise and FWHM.

black vertical line giving the mean value. The red vertical line shows the number of galaxies found in the real system. In the top-right of each panel we also give the percentage of random sets for which the number of galaxies found with absorption in 1, 2 or 3 sightlines is greater than or equal to the number seen in the real Q0107 system, and the significance of the difference from the mean (in units of the standard deviation of the random distribution). Therefore panels in which the red line lies to the right of the histogram show that there are more galaxy–absorber groups in the real Q0107 system than in the random distributions.

The final panels show the number of H I absorber groups for which absorption within the velocity window is found in precisely 1, 2, and 3 sightlines. The layout of the plot is as described above, with the percentage of random sets containing at least as many absorber groups as the real system given alongside the significance of the difference. The uppermost of these three panels often shows the real system having fewer single-LOS absorber groups than the random distribution, as the real absorbers are more likely to form coherent structures across multiple lines-of-sight, and be more clustered along any one line-of-sight.

These figures are intended as a direct comparison with those in C10. However, with the much larger samples now available, it is possible to obtain results from subsamples of galaxies and absorbers. These include separating star-forming from non-star-forming galaxies, and dividing absorption systems into low- and high-column-density samples. This allows testing of numerous models of the links between the galaxies and surrounding gas, as described below.

Full sample

Figure 3.2 shows the results from the full sample, in which we consider all observed H I absorption systems, and all galaxies with 'a' and 'b' redshift flags within 2.5 Mpc of a sightline. The top panels show the velocity difference between each galaxy and its nearest-neighbour absorber in each sightline. For each sightline, the number of galaxies with absorption within 100 km s^{-1} (the innermost bin) is above the 99th percentile of random absorber sets, and remains consistently above the median out to 400 km s^{-1}. This suggests that most of the physical associations between galaxies

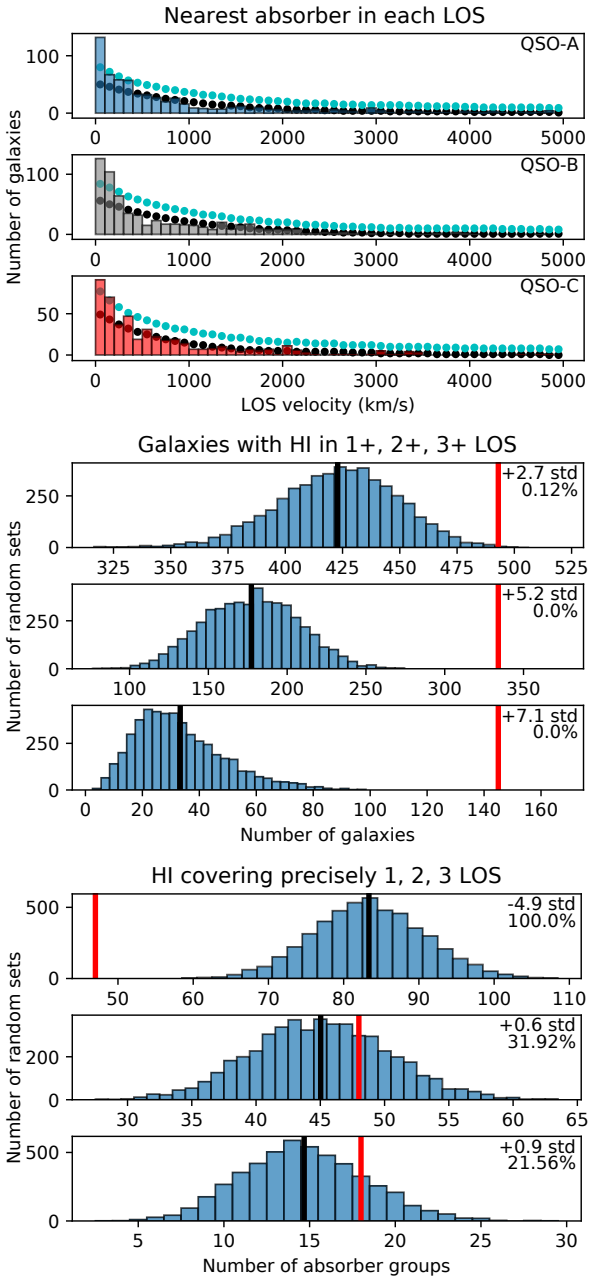

Figure 3.2: Nearest-neighbour and velocity-window groups using the **full sample**, as described in Section 3.2.3. These compare the absorbers in the real Q0107 sightlines with the ensemble of randomly distributed absorber sets, showing line-of-sight velocity distances between galaxies and absorbers, number of galaxies with associated H I in one or more lines-of-sight, and number of absorber groups covering one or more lines-of-sight. Features are identical to those in Figures 3.3 and 3.4, and are described in detail in Section 3.2.3 of the main text. *Top 3 panels:* The nearest absorber to each galaxy in each sightline. *Middle 3 panels:* The number of galaxies around which absorption is seen within 500 km s^{-1} in at least one, at least two and all three sightlines. *Lower 3 panels:* The number of absorber groups covering precisely 1, 2 and 3 sightlines within 500 km s^{-1}.

and absorbers occur with smaller velocity differences. For most of this work, we use a velocity cut of 500 km s^{-1}, thus capturing most of the likely galaxy–absorber groups whilst minimizing the noise from unrelated pairs. This is also directly comparable to the grouping used by C10.

The middle panels shows the number of galaxies for which absorption systems are found in at least 1, at least 2, and all three sightlines within the 500 km s^{-1} window. In each case significantly more galaxies have absorption in the real Q0107 field than expected from the systems with randomly generated absorbers. Only six of the 5000 random distributions show as many galaxies with associated absorption, and no set of randoms has as many matches between a galaxy and multiple absorbers as the real Q0107. The significance of the excess also increases with the number of sightlines covered. This is similar to the results of P06 and C10 (their figure 16), in which there is a significant excess of galaxies associated with absorbers on these scales. The larger sample of absorbers and galaxies in this study has allowed a higher confidence level to be reached.

The lower panels show the number of absorber groups covering one, two and three sightlines respectively. As in C10 (the lowest panel of this plot is directly comparable to the middle panel of their figure 7) the number of triple-absorber groups is larger in the real system than in most sets of randoms. However, the excess is less significant here, with $\approx 22\%$ of random sets showing more triples (as compared to $\approx 11\%$ in the C10 results). This may be due to the improved sensitivity to low-column-density absorption. This observed absorption across all three sightlines within a small velocity window supports the idea that the gas is found in structures at least 500-1000 kpc in extent (the distances between the sightlines).

Column density

We then extend this test by cutting the absorber sample by column density, using a cut of $N(\mathrm{H\,I}) = 10^{14}$ cm^{-2} identical to that used in T14, and perform this analysis on both the high- and low-column density samples. Figure 3.3 compares the results obtained from these two samples, with the left column giving results from the high-column-density sample, and the right column showing the low-column-density

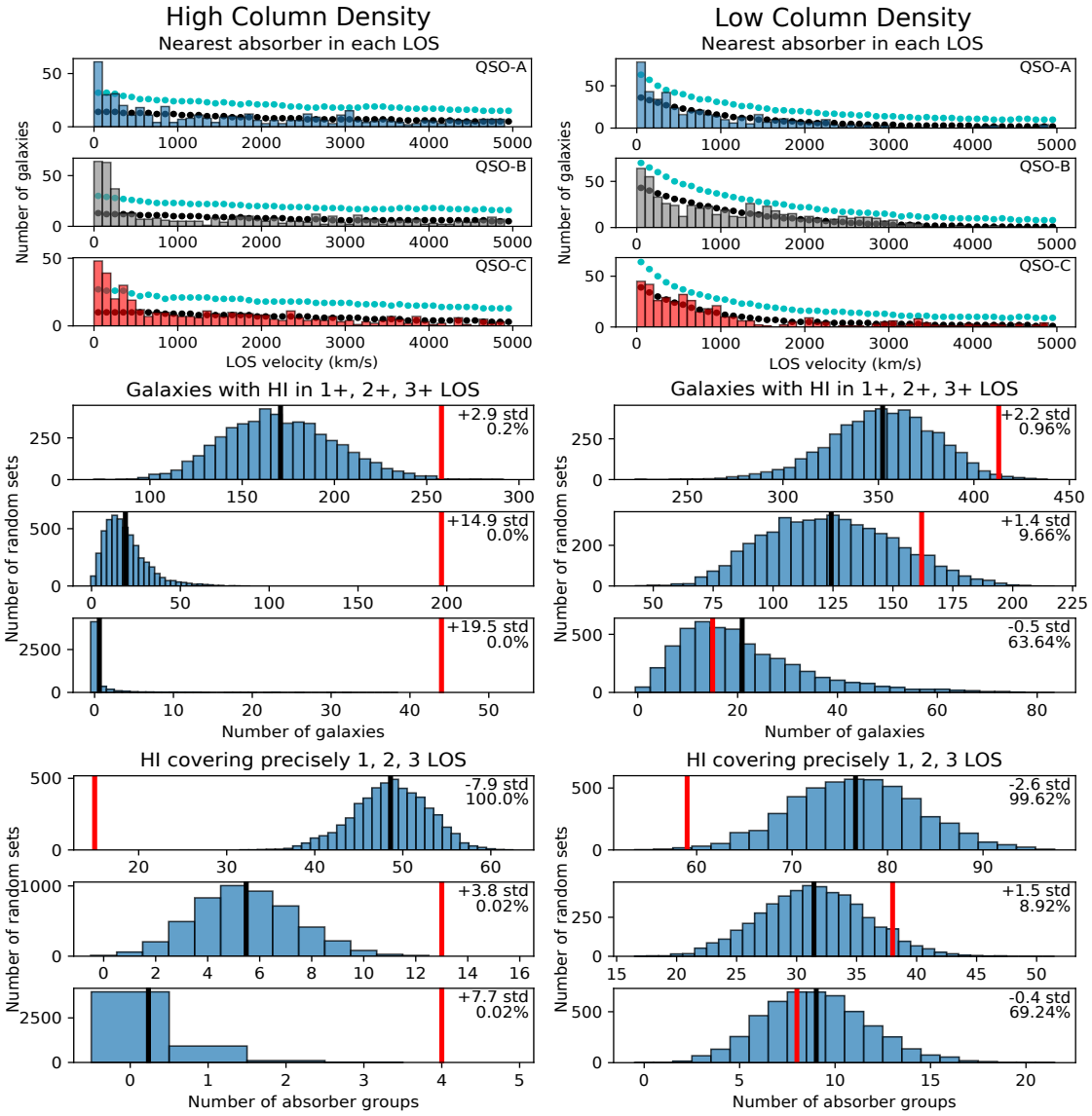

Figure 3.3: Comparison between the real Q0107 system and the ensemble of randomly distributed H I absorber sets, using the **column density cut**, as described in Section 3.2.3. We show galaxy and absorber groups involving galaxies with 'a' or 'b' redshift flags within 2.5 Mpc of at least one line-of-sight, considering only high-column-density ($N(H\,I) > 10^{14}$ cm^{-2}) absorbers in the left column, and lower-column-density absorbers in the right column. The features shown are identical to those in Figures 3.2 and 3.4, detailed in Section 3.2.3 of the main text. *Top 3 panels:* The nearest absorber to each galaxy in each sightline. *Middle 3 panels:* The number of galaxies around which absorption is seen within 500 km s^{-1} in at least one, at least two and all three sightlines. *Lower 3 panels:* The number of absorber groups covering precisely 1, 2 and 3 sightlines within 500 km s^{-1}.

sample.

Using these constraints, the nearest-neighbour results (top) show a much clearer excess of galaxy-absorber pairs in the innermost velocity bins when only high-column-density absorbers are considered, substantially above the 99% level in all three sightlines. In the low-column-density case, the excess of small-velocity pairs is below the 99% level in two of the sightlines.

The excess of galaxies with associated absorption is more significant in the high-density sample (middle-left) than the low-column-density sample (middle-right). Indeed, there is no significant excess of galaxies with absorption in multiple sightlines in the low-density case. Similarly, the significance of the excess of real absorber triples is greater in the high-column-density case (bottom panels), and the low-column density observed coincidences are also consistent with the randomly generated sample.

These results confirm previous observations that high-column-density gas preferentially resides close to galaxies, in the CGM or intra-group medium, whereas the excess of low-column-density absorption around galaxies is less significant, suggesting these absorbers occur in the IGM. As only four absorber groups exist with high-column-density absorption in all three lines-of-sight, and these lie at the same redshift as more than 40 galaxies, these triplets correspond to galaxy overdensities.

That low-column-density absorption is not found in multiple sightlines at a significantly higher frequency than in the random distribution may also indicate that these weak absorbers do not often form Mpc-scale structures.

These results are consistent with those in T14, in which the correlation function between weak absorbers and galaxies suggests that they do not trace the same dark matter distribution, and the low auto-correlation between low-column-density absorbers indicates that they rarely form large structures. Burchett et al. (2020) suggest that these column densities should be tracing the outer regions of filaments, as well as some overdensities in voids. This could lead to detection in two sightlines if the filament is aligned across two sightlines, but is unlikely to produce triplets, a possible explanation for the $\sim 1.5\sigma$ excess of low-column-density, two-sightline detections.

We also repeated this test after randomly discarding low-column-density ab-

sorbers until the sample sizes of high- and low- density absorption features were of equal size. There were no significant differences in the results, confirming that the greater excess seen in the high-column-density case is not merely an effect of the larger sample size. Due to the higher detection limit in the FOS spectra, there is also a difference in redshift between the low- and high-column-density absorbers, with low-column-density systems rarer at $z \gtrsim 0.48$ (median redshift of low- and high-column-density absorbers 0.32 and 0.52 respectively). However, the results are similar if we only include absorbers found in the COS spectra. Redshift evolution of the IGM is found to be slow at $z \lesssim 1$ (e.g Kim et al., 2020), so no substantial difference is expected.

Star formation

Another cut was made on the star-formation of galaxies in the sample (using the star-formation class for each galaxy defined in Section 2.2). Figure 3.4 shows these results. The excess of groups in the real system is more significant in the star-forming case (lower-left) than the non-star-forming case (lower-right). This can also be seen in the nearest-neighbour matching (upper-left and upper-right), in which the excess of galaxies in the innermost bins is greater in the star-forming sample.

These results show absorption is more likely to be detected around star-forming galaxies on scales of hundreds of kpc. This is similar to the results from (Chen & Mulchaey, 2009), in which the correlation between Lyα absorbers and galaxies is stronger among emission galaxies than absorption galaxies. Our results are generally consistent with those in T14, despite the different approach. They do not find a significant difference in the correlation slope or length between the strong-H I/SF-galaxy and strong-H I/non-SF-galaxy cross-correlations. However, they show that the strong/SF results are consistent with linearly tracing the same dark matter distribution, whilst the strong/non-SF results are not, due to the greater auto-correlation between non-SF galaxies. Therefore the probability of finding a strong H I absorber near a non-SF galaxy is lower than that of finding a strong H I absorber near a SF galaxy, in agreement with our results.

Whilst the star-forming galaxies in our sample are more likely to be surrounded

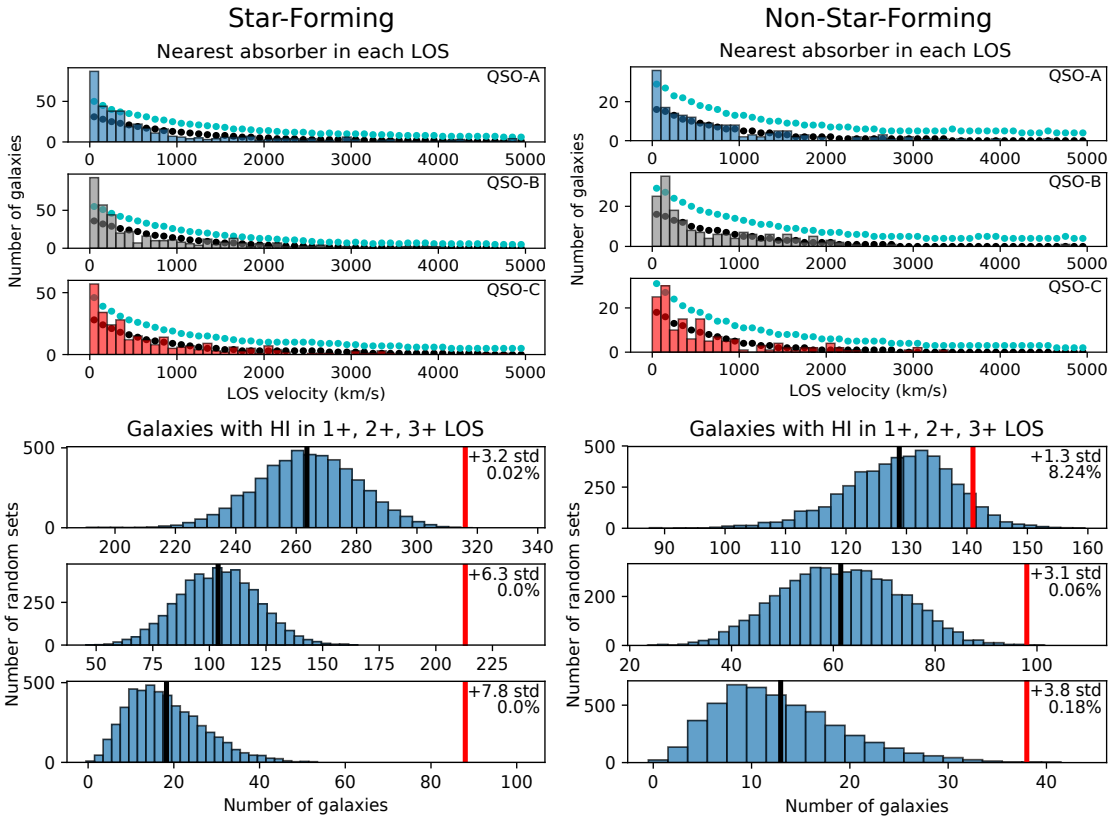

Figure 3.4: Nearest-neighbour and velocity-window groups using the **star-formation cut**, as described in Section 3.2.3. These compare the the real Q0107 system with the ensemble of randomly distributed absorber sets, showing line-of-sight velocity distances between galaxies and absorbers, number of galaxies with associated H I in one or more lines-of-sight, and number of absorber groups covering one or more lines-of-sight. Features are identical to those in Figures 3.2 and 3.3, and are described in detail in Section 3.2.3 of the main text. *Top 3 panels:* The nearest absorber to each galaxy in each sightline. *Lower 3 panels:* The number of galaxies around which absorption is seen within 500 km/s in at least one, at least two and all three sightlines. The absorber-only groups are omitted as these are not affected by the cut, so the results are the same as in the lower panel of Figure 3.2.

by detectable levels of H I gas, it is difficult to determine the cause of this. We note that excess absorption within the virial radius is not sufficient to explain the excess of two- and three-sightline absorption, as the distance between the sightlines is larger than the virial radius for most of our galaxies.

There are suggestions from simulations that stellar-feedback-driven outflows may extend to and beyond the virial radius (e.g. DeFelippis et al., 2020; Mitchell et al., 2020a; Hopkins et al., 2021), so their presence around star-forming galaxies could lead to the observed absorption. If outflows make a substantial contribution to this excess absorption, we may expect to see a broader distribution of galaxy-absorber velocity offsets in the SF sample, arising from the line-of-sight component of the outflow velocity (see e.g. Chen et al., 2020b). This broader distribution is not seen in our data, which would suggest that outflows do not make a large contribution on these scales. However, there are potential redshift errors in the VIMOS galaxies in the same 100–200 km s^{-1} regime as the likely outflow velocities (see Table 2.5), which could similarly broaden the distribution. We further discuss the presence of outflows in Section 3.3.

We consider the environments in which the SF and non-SF galaxies are likely to be found. Non-SF galaxies are more likely to reside in groups (41% of non-SF and 32% of SF galaxies lie in groups of five or more galaxies, using the friends-of-friends algorithm described in Appendix B.1), as expected due to quenching when galaxies fall into larger haloes (e.g. Wetzel et al., 2013). As these groups will often correspond to larger overdensities in the cosmic web than single galaxies, we may expect increased incidence of H I absorber groups around non-SF galaxies, the opposite effect to that observed. However, the higher virial temperatures of group haloes would lead to a suppression of neutral hydrogen, possibly negating this effect.

We also consider the effects of biases in our sample selection (as discussed in Section 2.2). Firstly, to remove any effects of having a larger star-forming than non-star-forming sample, the analysis was rerun after randomly discarding star-forming galaxies until the sample sizes were identical, and the significance of the excess in galaxy-absorber groups was only marginally reduced in each case. Whilst there are small biases in the mass and impact parameter distributions of the two samples, a

Kolmogorov-Smirnov (K-S) test cannot distinguish them at the 5% level, and they appear localised to the mass tails and the smallest impact parameters (i.e. the MUSE fields). Removing the mass tails and/or MUSE-only galaxies again slightly reduces the significance of the excess, but does not substantially affect the comparison.

The bias of SF galaxies towards higher redshifts does appear to have an effect, but this is found to be primarily due to the absorber selection function removing lower column density absorbers at higher redshifts (as seen in Figure 3.1). If only high-column-density absorbers are considered, no substantial difference between high-z and low-z coherence is found, but there remains a larger excess of absorption around star-forming galaxies than non-star-forming galaxies.

The difference between our SF and non-SF samples is therefore unlikely to have arisen from any sample biases, and instead does indicate that star-forming galaxies are more likely than quiescent galaxies to exhibit H I absorption covering single and multiple lines-of-sight.

3.3 Galaxy orientations

As described in Section 2.1.2 and shown in Figure 2.2, we have obtained MUSE data for the $1' \times 1'$ fields around QSOs A and B, in addition to high-resolution HST imaging of a larger field (but not extending as far as QSO-C). We used GALFIT (Peng et al., 2002) to determine the position angles of galaxies in the HST field, as described in Section 2.2.1. This allows galaxy–quasar pairs in which absorption is detected (and those where it is not) to be shown as a function of position angle and impact parameter. We can then determine whether absorption lies preferentially along the major or minor axis of the galaxy, and identify possible co-rotating material and polar outflows.

The MEGAFLOW survey mostly covered impact parameters out to ~ 100 kpc using Mg II, focusing their selection on sightlines with high-equivalent-width absorbers in their SDSS spectra (Schroetter et al., 2016). They find a clear bimodality in position angle, with more absorbers found along both the major and minor axes, identified with discs and outflows respectively. It must be noted that they remove

absorbers found with three or more nearby galaxies, and assign a single galaxy to the absorber in cases with two nearby galaxies.

Similarly, Bordoloi et al. (2011) and Bordoloi et al. (2014) look for Mg II around zCOSMOS galaxies, finding strong minor-axis absorption attributed to outflows that is much stronger than the major-axis absorption, and an increasing outflow equivalent width with host galaxy SFR. They only find this for impact parameters $\lesssim$ 50 kpc, but also include group galaxies in their analysis, obtaining results consistent with a superposition of outflows from group members.

On the other hand, Dutta et al. (2020) find that their sample, primarily consisting of Mg II absorption at larger impact parameters, does not show such a bimodality (a similar result is found by Huang et al., 2021), nor can their measurements in group environments be fully explained by a superposition of absorption from individual group members. This suggests that, at least in Mg II, the disk/outflow dichotomy does not extend to scales much beyond $\sim$ 50 kpc.

This appears in contrast to some recent models. For example, Hopkins et al. (2021) find that their simulations (based on the FIRE simulations, with the addition of cosmic ray effects) can allow biconical outflows to reach megaparsec scales. Outflows in the EAGLE simulations are also seen to maintain their bi-directional structure to at least the virial radius of $\sim 10^{12}$ $M_\odot$ halos (Mitchell et al., 2020a), whilst Illustris also features hot outflowing material and cool co-rotating material along the minor and major axes out to close to the virial radius (DeFelippis et al., 2020).

Using H I absorption from lines-of-sight with no pre-selection allows an unbiased sample to extend to larger impact parameters than most Mg II studies. When considering galaxies in groups, we avoid artificially selecting the associated galaxy to each absorber, instead including all galaxy–absorber pairs within the 500 km s^{-1} cut. We test for this bimodality in position angle for the galaxy–absorber pairs in our sample using the Hartigan dip test (Hartigan & Hartigan, 1985), which calculates the likelihood of observing the 'dip' in the sample histogram if the underlying distribution is unimodal. As in Section 3.2, we also compare the results when the sample is split into complementary subsamples such as high- and low-column-density

absorbers, and star-forming and non-star-forming galaxies.

3.3.1 Hydrogen

The results from applying this test to the distribution of galaxy–absorber pairs involving H I absorption are summarized in Table 3.1. Where the sizes of the complementary samples (paired using horizontal lines in the table) are substantially different, we randomly discard detections from the larger sample until the sizes match in order to perform a fair comparison. We repeat with 100 random samples and take a median, giving the results in brackets.

Full sample

Figure 3.5 shows the position angle against impact parameter for the full sample of galaxies and absorbers, associating each galaxy with all absorbers within 500 $\mathrm{km\,s^{-1}}$. Non-detections are shown on the scatter plot, but only the position angles and impact parameters of detected absorption are included in the histograms. There is a visible bimodality, and the dip test finds a significant result, returning a p-value of 0.025. This reproduces in H I the bimodality obtained using Mg II in Zabl et al. (2019) and Martin et al. (2019b), although extending to larger impact parameters, suggesting that some fraction of our observed H I is tracing the same outflowing and accreting material. We note that the major axis absorption we observe covers position angles $\lesssim 40°$. It is not simple to distinguish between a thin disk viewed at moderate inclination angles, and a thicker 'wedge' of material.

Some studies (e.g Tempel & Libeskind, 2013; Zhang et al., 2015) suggest that galaxy spins are preferentially aligned with or perpendicular to the surrounding large-scale structure. Observing the cosmic web around these galaxies, as traced by H I, could produce a bimodality. This alignment is a weak effect (in Tempel & Libeskind 2013, galaxies are a maximum of $\approx 20\%$ more likely to be aligned over a random distribution), so unlikely to fully explain our stronger observed bimodality.

The overall position angle distributions of galaxies and galaxy-sightline pairs are consistent with uniform, with neither the dip test nor a K-S test against a uniform distribution showing a significant result. Therefore our bimodality is not due to an

inherent alignment between galaxies in our sample. It is instead most likely due to the inflow/outflow dichotomy discussed above.

Galaxy groups

Cutting the sample to only include galaxies in groups of five or more decreases the significance of the bimodality to $\approx 10\%$, whereas no bimodality is seen among the non-group galaxies (using the friends-of-friends algorithm described in Appendix B.1).

The significance of the bimodality is expected to be reduced in galaxy groups. If the gas is primarily a superposition of outflows and/or accretion from individual galaxies, the signal would still be partially masked by other galaxies being paired with the same absorber. If the gas does not form these structures within most groups, and instead forms an intra-group medium not attributable to a single galaxy, this bimodality should not be visible.

The bimodality we see in the in-group sample is not significant at the 5% level, and the significance is further reduced when galaxy-absorber pairs are randomly discarded until the group and non-group samples contain the same number of pairs. Our results are consistent with the difference in the p-values shown in Table 3.1 being primarily due to sample size, as neither sample shows a significant bimodality at the 5% level, yet the combined sample does. A K-S test also fails to find a significant difference between the position angle distributions of galaxy-absorber pairs of these two samples.

No significant effect on the bimodality or the position angle distribution is found when using shorter linking lengths, when adjusting the minimum number of galaxies needed to constitute a group between three and five, or when splitting the non-group galaxies into those with no detected neighbours and those with 1-3 neighbours.

Impact parameters

When the sample is cut to absorber-galaxy pairs with an impact parameter of less than 500 kpc, the bimodality remains strong, a Hartigan dip test returning a significance of 3%, whereas the pairs with an impact parameter larger than 500 kpc

exhibit no significant bimodality. The difference between the large- and small- impact parameter results may suggest that the model of minor axis outflow and major axis accretion can extend well beyond the ~ 100 kpc observed in the MEGAFLOW results (Schroetter et al., 2016). We confirm that this bimodality is not entirely driven by galaxy-absorber pairs on small scales, obtaining a significant result from pairs with impact parameters of 200–500 kpc.

This is further illustrated in Figure 3.6, in which the galaxy-absorber pairs are binned by position angle and impact parameter. For the two innermost bins in impact parameter (< 500 kpc), the 30-60° bin has a clear lack of absorption relative to the major axis and minor axis bins. The third radial bin ($\approx$ 500-750 kpc) does not show this bimodality, suggesting that IGM absorption or other structures such as group material form the dominant component at this scale. Beyond this distance, the sample size is very small. We note that few conclusions can be drawn from the radial distribution, as this depends primarily on the geometry of the sightlines and redshift surveys. (The apparent 'edge' at ≈ 750 kpc is an artifact of this layout, as this is roughly the maximum distance from the A and B sightlines to the edge of the HST imaging. Most galaxy–absorber pairs beyond this distance involve absorption in sightline C.)

Column densities

Cutting to column densities N(H I) $> 10^{14}$ cm^{-2} improves the significance of the bimodality to better than 1%, as shown in Figure 3.7, whereas no clear bimodality is found for the low-column-density absorbers. These two subsamples show the strongest and weakest bimodalities according to the dip test results, suggesting that high-column-density gas is preferentially found in these putative inflows and outflows. This likely captures much of the same physics as the variation with impact parameter, as high-column-density absorbers are generally found closer to galaxies, for example in Chen (2012) and Keeney et al. (2017). Wilde et al. (2021) find that the probability of finding H I above our column density threshold around a galaxy drops to 50% at impact parameters of ≈ 300 kpc, similar to the extent of our bimodality.

Table 3.1: Summary of constraints applied to the sample and resulting bimodalities in the position angle distributions of galaxy–H I absorber pairs. Columns show: (1) The subsample used; (2) the number of possible galaxy–sightline pairs, accounting for the reduced redshift range for which QSO-C can be observed as well as the additional constraints; (3, 4) the number of galaxy–sightline pairs with and without observed H I absorption within $\Delta v < 500$ km s^{-1}, and (5) the p-value obtained from a Hartigan dip test applied to the position angle distribution of galaxy–absorber pairs with detected absorption. Where the sizes of complementary samples are substantially different, we randomly discard detected galaxy-absorber pairs from the larger sample until the sizes match, repeating 100 times and showing the average result in brackets.

Constraint (1)	Pairs (2)	Det (3)	Non-Det (4)	P-value (5)
Full Sample	289	242	47	0.025
In-Group	190	173	17	0.091(0.281)
Non-Group	99	69	30	0.511
r < 500 kpc	154	137	17	0.031
r > 500 kpc	152	105	47	0.185
r < 300 kpc	93	81	12	0.030
r > 300 kpc	208	161	47	0.399(0.393)
200 < r < 500 kpc	101	84	17	0.033
High-N(H I)	245	128	117	0.009
Low-N(H I)	229	114	115	0.709
Star-forming	187	155	32	0.123(0.224)
Non-SF	83	73	10	0.284

As discussed in Section 3.2.3, the high- and low-column density samples have different redshift distributions, but this does not have a substantial impact on the results. We confirm that the bimodality is retained for the high-column-density absorbers in the COS gratings, removing the FOS absorbers at higher redshifts where low-column-density absorbers are not detected (p=0.018).

Star formation

We also consider the bimodality around star-forming and non-star-forming galaxies. Neither subsample shows a significant bimodality in position angle of absorption (p-values 0.12 and 0.28 respectively). This appears to be primarily due to the sample sizes. When star-forming galaxies are randomly discarded from the sample until the number of detections around the star-forming and non-star-forming galaxies are equal, the resulting p-values are similar between the two samples. A K-S test also fails to find a significant difference between the position angle distributions of absorbers around star-forming and non-star-forming galaxies.

It is expected that more strongly star-forming galaxies are likely to have stronger outflows (e.g. Mitchell et al., 2020a). Our star-forming classification may be including many galaxies with SFRs too small to launch large-scale outflows, thus reducing the strength of the observed bimodality. We attempt to test this by applying a cut in sSFR (using the estimates described in Section 2.2) instead of our binary classification. This results in a bimodality significant at the 5% level in the strongly star-forming sample when using a threshold between ≈ 0.05 and 0.1 Gyr^{-1}. Higher thresholds leave the star-forming sample too small to obtain a significant result, and lower thresholds give similar results to our original classification. Figure 3.8 shows this bimodality for absorption around galaxies with sSFR > 0.05 Gyr^{-1}.

This can be discussed in the context of the star-formation comparison in Section 3.2.3. Whilst our sSFR estimates have high uncertainties, our finding that more strongly star-forming galaxies show a stronger bimodality is likely an indication that stellar-feedback-driven outflows are a contributor to this bimodality we observe in the position angle distribution of H I absorbers around galaxies on scales $\lesssim 300$ kpc. Our result that outflows on these scales are not evidenced by a bimodality

around our more inclusive sample of star-forming galaxies, yet larger-scale coherent structures are observed (on the 500-1200 kpc scales probed by coincidences between the lines-of-sight), suggests that these larger-scale structures are not primarily a result of outflows, but are instead a consequence of the environment around these galaxies.

Inclination

We note that when an inclination cut of $i > 40°$ (identical to that used in the MEGAFLOW survey, Zabl et al. 2019) is used to remove face-on galaxies for which the major and minor axes cannot easily be distinguished, the same subsamples show significant bimodalities at the 5% level as those in Table 3.1. For randomly oriented galaxies, $\cos(i)$ is expected to be uniform, so the distribution of inclinations is not uniform, but is instead suppressed at low inclinations (face-on galaxies). This leads to only 8 of the 72 galaxies considered throughout this section having inclinations less than 40°, so it is unsurprising that the results do not change. We also note that a small number of galaxies, although fit well by the GALFIT modelling, have large uncertainties on their position angle (5 have position angle uncertainties $> 20°$). Excluding these galaxies also has no effect on which subsamples show bimodalities significant at the 5% level.

We briefly consider variation with inclination, by dividing the $i > 40°$ sample into two bins of $40° < i \leq 65°$ and $65 < i \leq 90°$ (which contain 39 and 25 galaxies respectively). Neither sample shows a clear bimodality, and both are consistent with the overall distribution using the K-S test. Interestingly, the two bins are not consistent with each other ($p \approx 0.04$). This appears to be mostly driven by galaxy–absorber pairs with impact parameters in the 250-500 kpc bin.

We find that 26 of the 39 pairs in this impact parameter range involving galaxies with $40° < i \leq 65°$ have position angles 0-30° (near the projected major axis), whilst 14 of the 23 pairs involving $i > 65°$ galaxies have position angles of 60-90° (near the minor axis). Whilst these sample sizes are relatively small, this perhaps supports the presence of a disk-like structure along the major axis with a small cross-section when viewed close to edge-on.

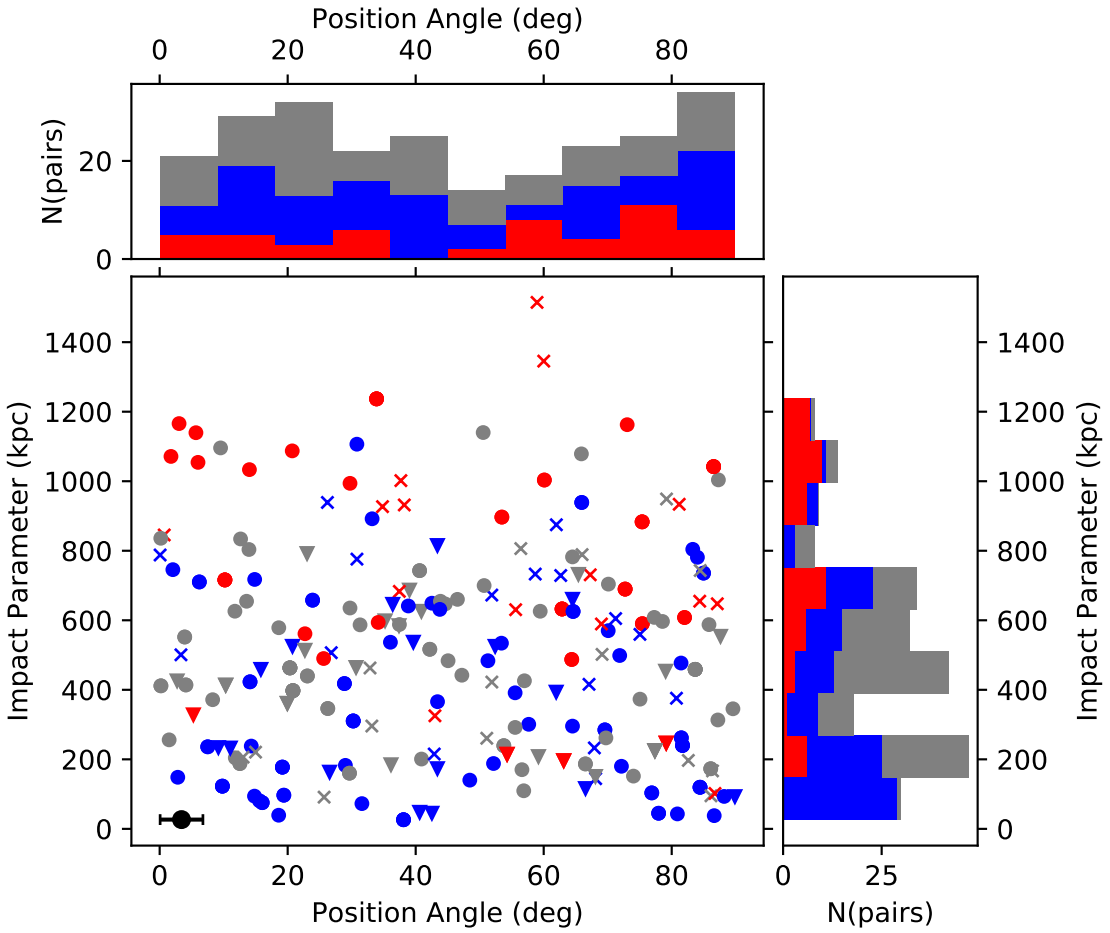

Figure 3.5: The position angle and impact parameter distributions of galaxy-absorber pairs involving H I absorption features around all galaxies in the sample for which position angles were measured. Position angles close to 0° represent absorption found close to the projected galaxy major axis, whilst those close to 90° show absorption found near the minor axis. Points are coloured by quasar sightline (A, B and C shown in blue, grey and red respectively), using triangles for galaxies in groups of five or more galaxies and circles for non-group galaxies, and non-detections are marked with crosses. Only the detected absorbers are included in the histograms. The bars on the black point in the lower-left are illustrative of the median error in each axis.

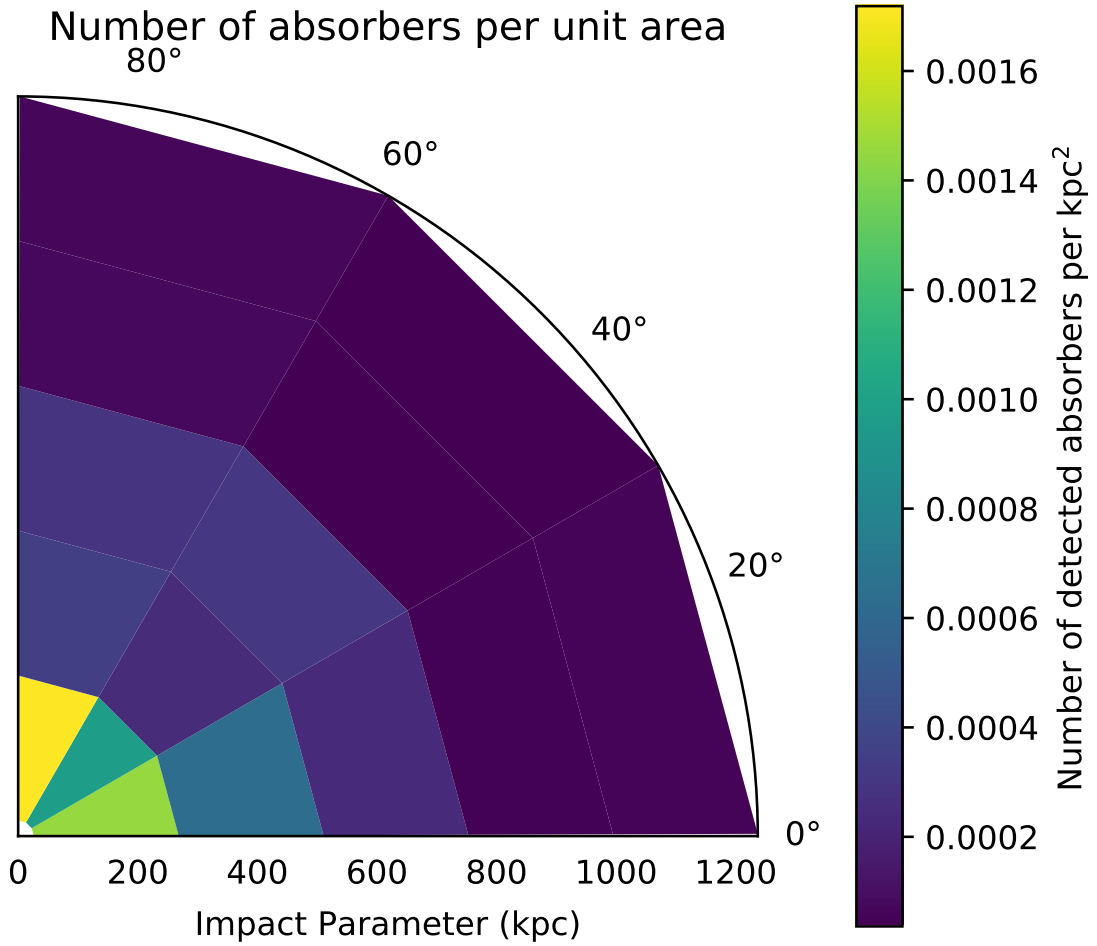

Figure 3.6: The position angles and impact parameters of H I absorbers detected around galaxies, shown in bins of $\sim$ 250 kpc $\times$ 30°. In this representation the galaxy major axis lies along the x-axis. Colour scale shows number of detections per projected kpc^2. Note that the radial distribution is determined primarily by the geometry of the survey: with QSOs A and B lying near the centre of the HST field, and QSO-C outside the field, only absorbers in the line-of-sight to QSO-C can be found beyond 800 kpc.

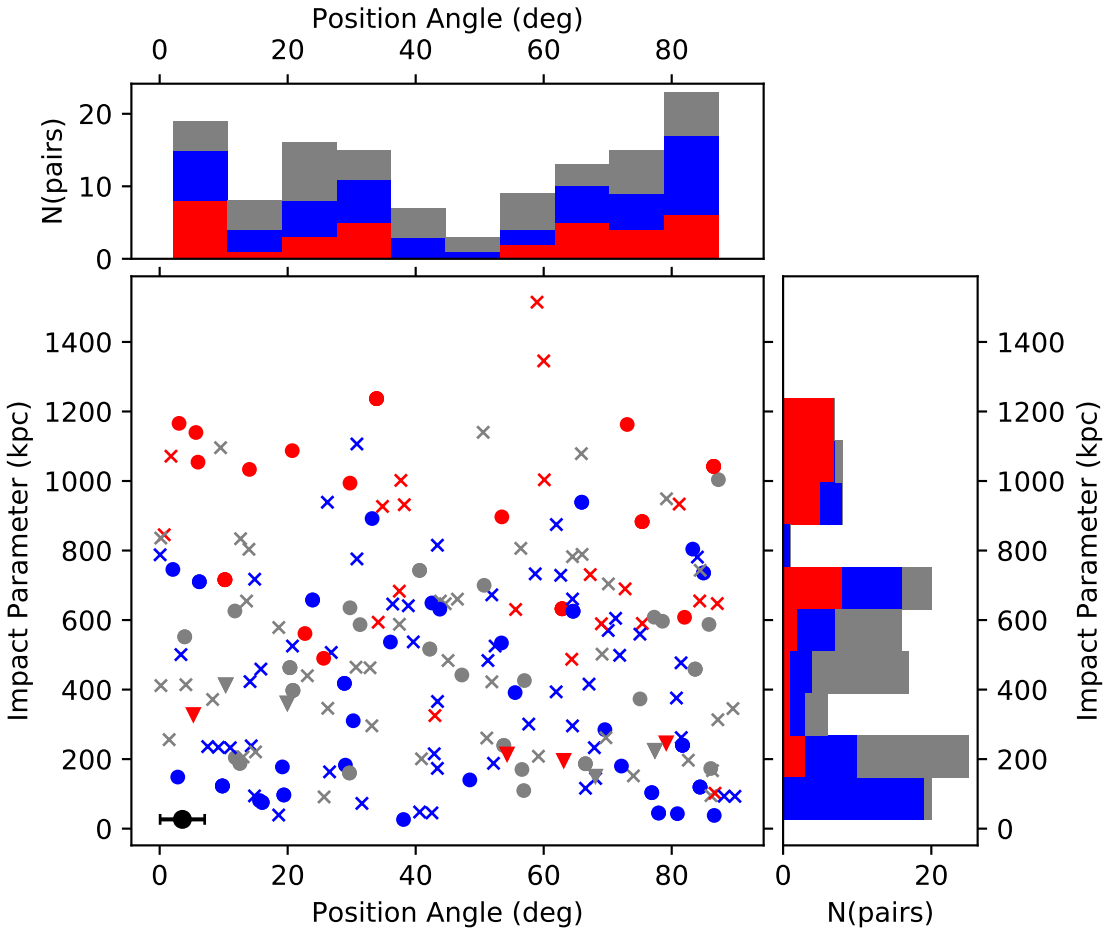

Figure 3.7: The position angle and impact parameter distributions of galaxy-absorber pairs involving H I absorption features with column densities N(H I) > 10^{14} cm^{-2}. Features are as in Figure 3.5.

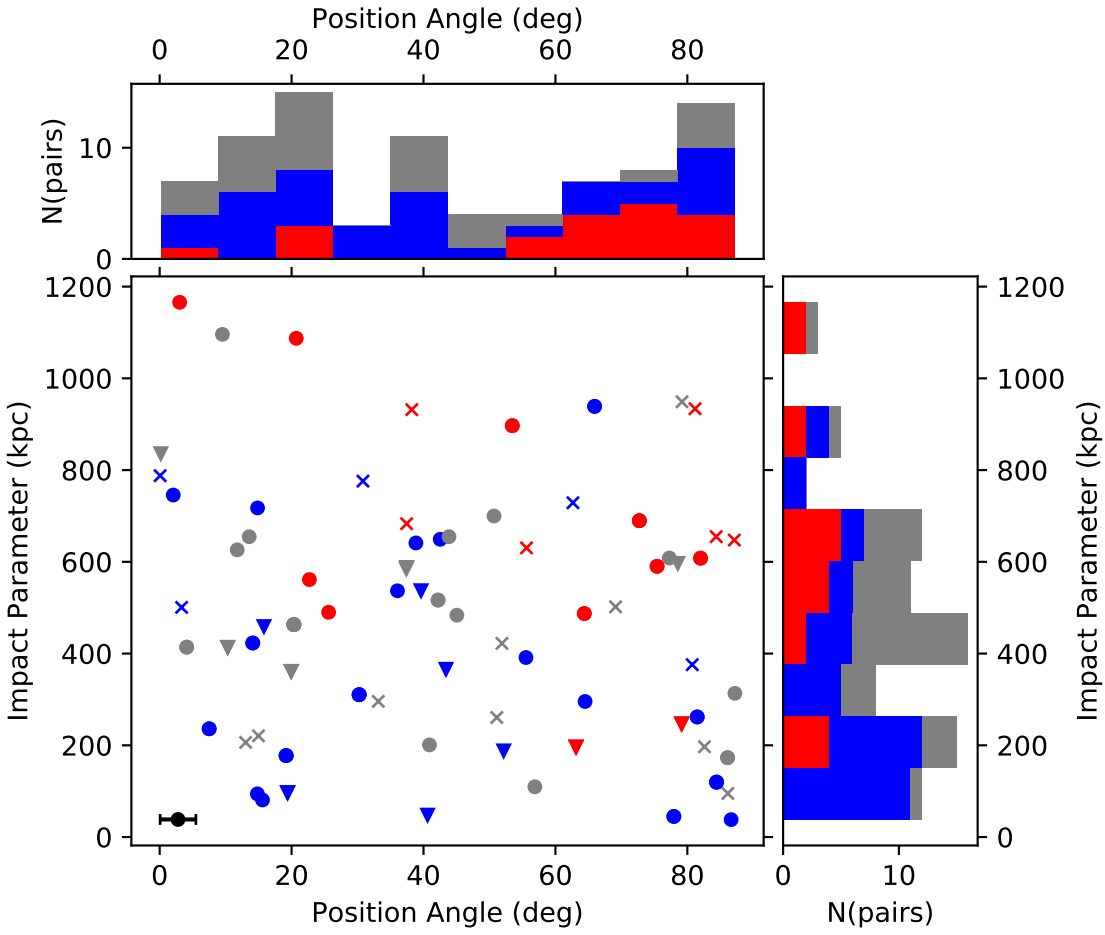

Figure 3.8: The position angle and impact parameter distributions of galaxy-absorber pairs involving galaxies with sSFR $> 0.05\,\mathrm{Gyr}^{-1}$. Features are as in Figure 3.5.

Closest galaxies

We note that if we reduce our sample to only the closest galaxy in impact parameter to each absorber (within the 500 km s^{-1} cut), the bimodality becomes somewhat stronger, with significance improving from $\approx 2.5\%$ to $\approx 1.0\%$. This will capture the physical origin of the absorbing material in many cases, but does not appear to in all cases, as the galaxy-absorber pairs removed do themselves show some hint of bimodality (with a significance of $\approx 7\%$). Splitting the sample of galaxy-absorber pairs involving only the closest galaxy produces results similar to those in Table 3.1, with no sub-sample crossing the 5% threshold. We do not take this approach through our earlier analysis as the cut appears to remove some physical associations and substantially reduces the sample size in some cases. This makes detecting a bimodality more difficult, especially in the in-group, SF and non-SF sub-samples.

3.3.2 Metals

We briefly discuss here the presence of metals in our absorption-line sample. Lines in the spectra exist that are identified with numerous ions, including C I-C IV, Si II, Si III, O I-O IV and O VI. Only O VI forms a significant sample, with 34 lines identified across the three spectra.

Figure 3.9 shows the resulting distribution of position angles and impact parameters. The bimodality is again visible by eye, and statistically significant ($p \sim 0.009$ from the Hartigan dip test). We also show a polar histogram illustrating this in Figure 3.10. It must be noted that all non-group detections occur at impact parameters of less than 350 kpc (postage-stamp images of the 6 non-group galaxies with detected O VI absorption are shown in Appendix A). This is comparable with the results from Bielby et al. (2019), in which all O VI absorption was accompanied by at least one galaxy within 350 kpc. It may also be suggested that the minor-axis 'peak' is stronger relative to the major-axis than in the H I figures. This is in general agreement with the results from Kacprzak et al. (2015), in which a bimodality is also found around isolated galaxies, with higher O VI equivalent widths along the minor axis.

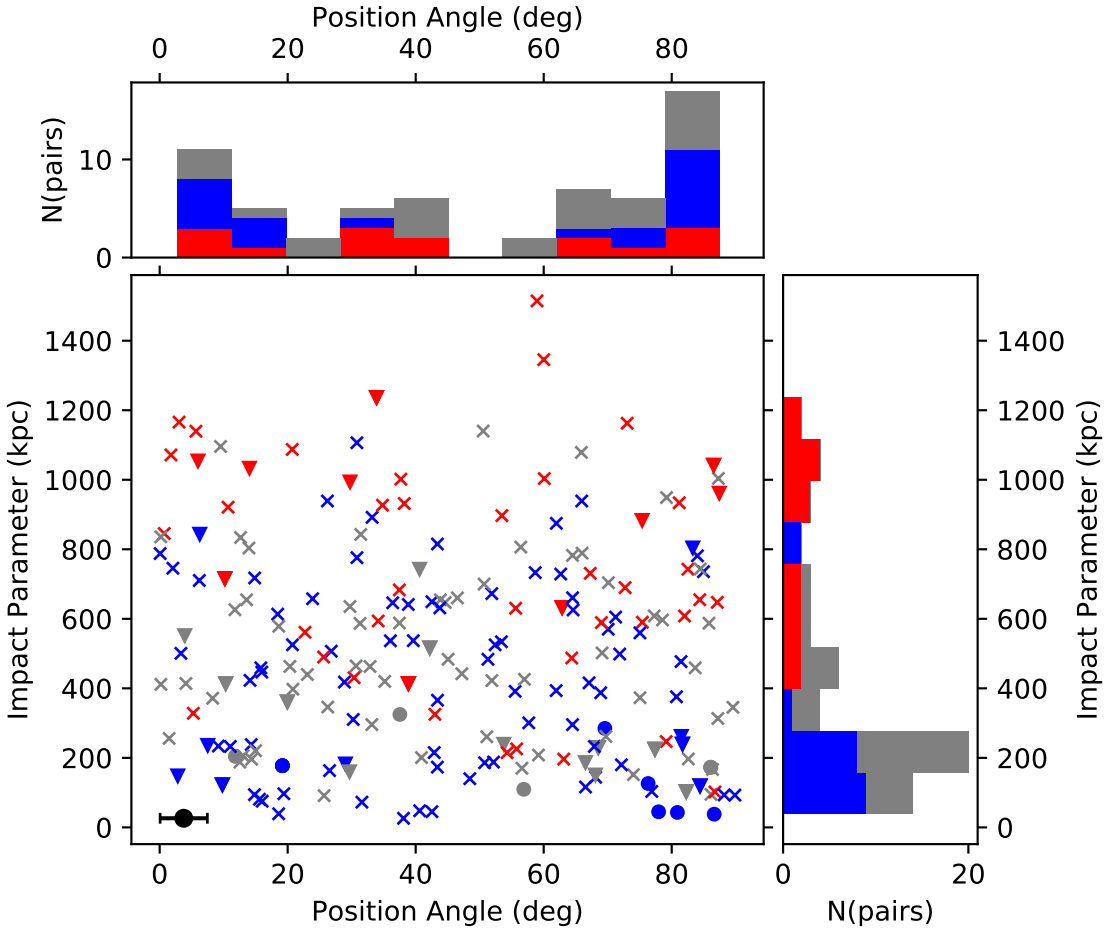

Figure 3.9: The position angles and impact parameters of detected O VI absorption features around all galaxies with measured position angles. Features shown are as in Figure 3.5.

We also compare the column-density distributions of O VI detections in galaxy groups with those not in groups. A K-S test indicates that these distributions are likely different (98% confidence), with a substantial number of in-group absorbers observed with lower column density.

This is again consistent with the disk/outflow model at small scales, whereas all metal absorbers found at large impact parameter from galaxies occur in groups. This could be due to absorber-galaxy pairs involving an absorber associated with a different (possibly undetected) galaxy in the same group, virialized gas within the group halo, or due to tidal and intra-group material within the group. Whilst observations of this material in emission (e.g Fossati et al., 2019a) allow us insight into the structure of this material on small scales, the lower column densities found

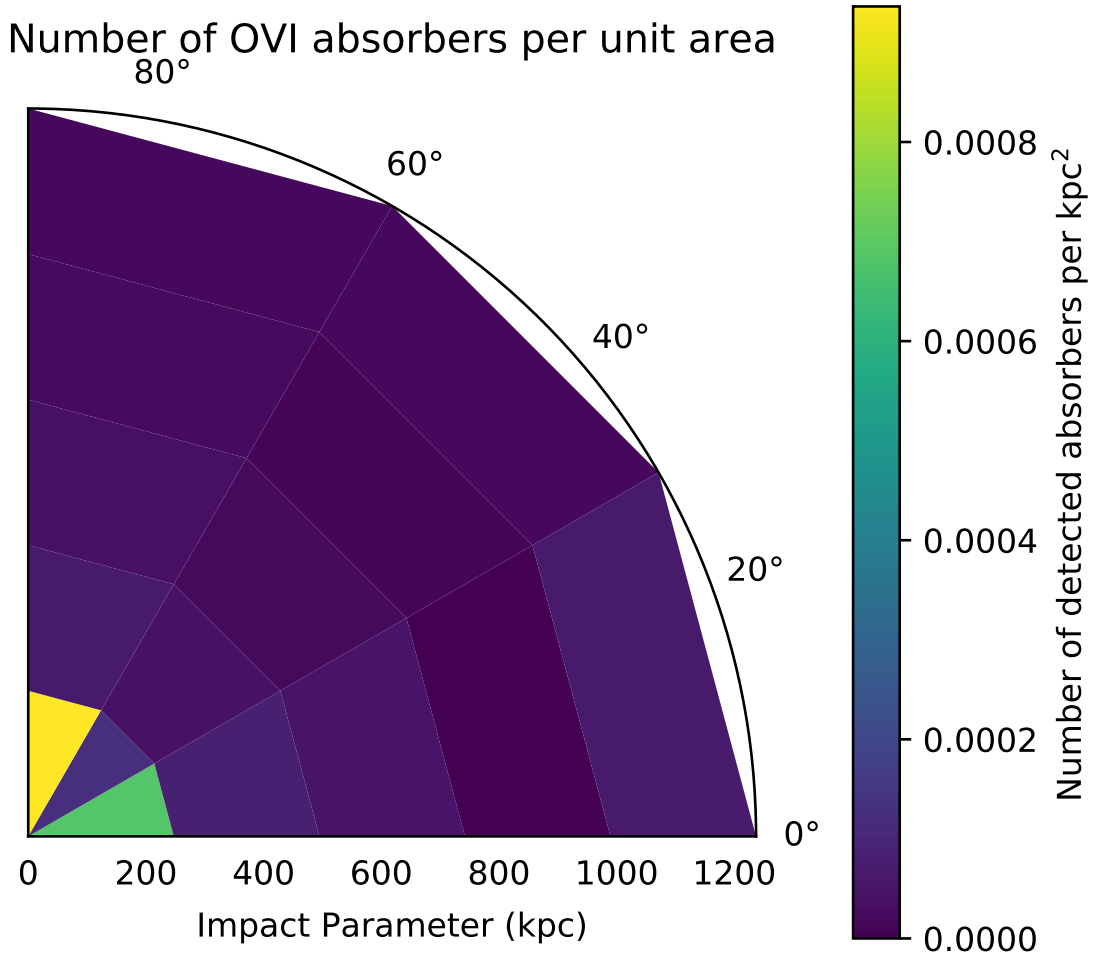

Figure 3.10: Polar representation of the position angles and impact parameters of detected O VI absorption features around all galaxies with measured position angles. Features shown are as in Figure 3.6.

on larger scales cannot easily be probed in this way. Morris & van den Bergh (1994) found that tidal absorbers extending to 1 Mpc radius would be consistent with observations. Unfortunately, this is approximately the limit of impact parameters for which position angles are available, so we cannot test whether this O VI extends to larger radii.

Oppenheimer et al. (2016) predict that the presence of O VI should be suppressed in group haloes due to a higher virial temperature than $L_\star$ galaxy haloes, reducing the fraction of O VI in favour of higher ions. A similar suppression is found in Wijers et al. (2020) for high-mass haloes.

Alternatively, observations and radiative transfer modelling from Werk et al. (2014) suggest that the warm gas phase is not supported hydrostatically in $L_\star$ galaxies, favouring a galactic 'fountain' over a virialized halo. The strong bimodality we observe in our data favours the galactic fountain for non-group galaxies. That the scale of O VI in non-group galaxies is similar to the extent of the observed bimodality in H I also supports the existence of such fountains extending to ∼300 kpc. The apparent shift in the ratio between the major- and minor-axis peaks, towards the minor axis, further fits this picture, with warmer, higher-metallicity outflows exhibiting more O VI than cool accreting flows.

However, our sample contains relatively few isolated $L_\star$ galaxies (see Figure 3.12), with most substantially smaller or lying in groups of galaxies. Either case moves the virial temperature of the halo away from the $\sim 10^{5.5}$K at which O VI is most prominent, making these virialized haloes harder to observe. Therefore, whilst a basic model without such haloes is consistent with the data, producing O VI from fountains and group interactions, we cannot rule out their presence. With our small number of isolated $L_\star$ galaxies, we cannot detect any 'peak' in absorber number or column density around $L_\star$ galaxies.

We also note that there are four redshifts at which O VI absorption occurs in two sightlines within 500 km s^{-1}, with no three-sightline O VI systems. In one of these systems, both sightlines featuring O VI lie within 30° and 200 kpc of the minor axis of an isolated 1.5 $L_\star$ galaxy. The other three systems exist in galaxy groups, where it is difficult to distinguish between tidal debris, virialized haloes, and warm

outflows. More detailed ionization modelling of the absorption in two of these groups are described in Muzahid (2014) and Anshul et al. (2021).

3.3.3 Comparison between major and minor axes

We now compare the properties of absorption along the major- and minor- axes. We take two samples of galaxy-absorber pairs, with position angles $< 40°$ and $> 50°$ respectively. We remove face-on galaxies by requiring a galaxy inclination of $> 40°$ and impose a 500 kpc maximum impact parameter to focus on the regions in which the bimodality is significant[1]. This returns 67 galaxy–H I pairs in each sample.

A K-S test reveals no difference between the column density or Doppler width distributions of these two samples. We also compare the galaxy–absorber velocity offsets around moderately inclined and edge-on galaxies ($40 - 65°$ and $> 65°$ inclination respectively), finding no significant difference. If our observed position angle distribution is primarily due to major axis co-rotation and minor axis outflows, we may expect to see a wider velocity distribution along the minor axis of moderately inclined galaxies and the major axis of edge-on galaxies, due to the larger line-of-sight velocity components. This is not observed in our data, although the further split results in a small sample size.

However, 14 of the major-axis absorbers have associated O VI, whilst 28 of the minor-axis absorbers show this association (a difference of $\approx 2.1\sigma$ assuming Poisson statistics). A similar ratio is found when using a 300 kpc maximum impact parameter. This difference in O VI incidence is found in Kacprzak et al. (2015) and Kacprzak et al. (2019), but is attributed to a higher H I column density rather than metallicity differences. We do not find any significant increase in H I column density along the minor-axis, so the increased O VI found near the minor-axis may be due to more warm-hot material than in the absorbers found near the major axis.

[1]These cuts in inclination and azimuthal angle cover an identical region to the MEGAFLOW survey for the major axis sample (Zabl et al., 2019), whilst the slightly larger region along the minor axis is used both for symmetry and to produce a sample of identical size. The major axis cut is also identical to that shown in Figure 3.11, although we do not require observed kinematic data in this case.

3.4 Kinematics

We attempt to determine whether the major-axis population discussed above is indeed the same co-rotating material identified in Mg II (e.g Zabl et al., 2019), as well as found in simulations (e.g Huscher et al., 2021; DeFelippis et al., 2020). We compare the velocity offsets between galaxies and H I absorbers found near to their major axes with the stellar rotation of the galaxies determined from emission lines in the MUSE data.

We use Astropy (Astropy Collaboration et al., 2018) to fit Gaussian line profiles to each spaxel within the aperture defined by SExtractor. In the case of [O II], we fit a double Gaussian with equal line width and redshift-dependent difference in central wavelength, and an intensity ratio between 0.1 and 10 to avoid fitting unphysically large or small values. We use kinematic maps from [O II] 3727, [O III] 5007 and Hα 6563, and generally consider the strongest line available for each galaxy.

We consider galaxies in which a velocity gradient is visible in the MUSE data. For comparison with Zabl et al. (2019) we only consider galaxies with inclinations above 40°, and position angles on the sky below 40°, although all galaxies with observed velocity gradients already fit this inclination constraint. A velocity window of 500 km s^{-1} is used, as we showed in Section 3.2.3 that this includes most of the associated absorption whilst reducing the noise from unassociated IGM absorbers. The position angles and inclinations of the resulting subsample are shown in Figure 3.11, whilst the locations of the galaxies in redshift-luminosity space are shown in Figure 3.12.

Using the position angle found from GALFIT as described in Section 2.2.1, we divide the galaxy into two regions, one each side of the projected minor axis. The median velocity of spaxels within each region then gives a redshifted and a blueshifted region. We then compare this to the velocity difference between the galaxy and absorber to identify possible co-rotation. As the subsample is small (22 galaxies with velocity gradients, of which 15 feature major-axis absorption), we also confirm by eye that this algorithm produces the correct result.

We first consider only galaxies not lying within groups of five or more galaxies, as any co-rotating structures are less likely to be disturbed by galaxy interactions

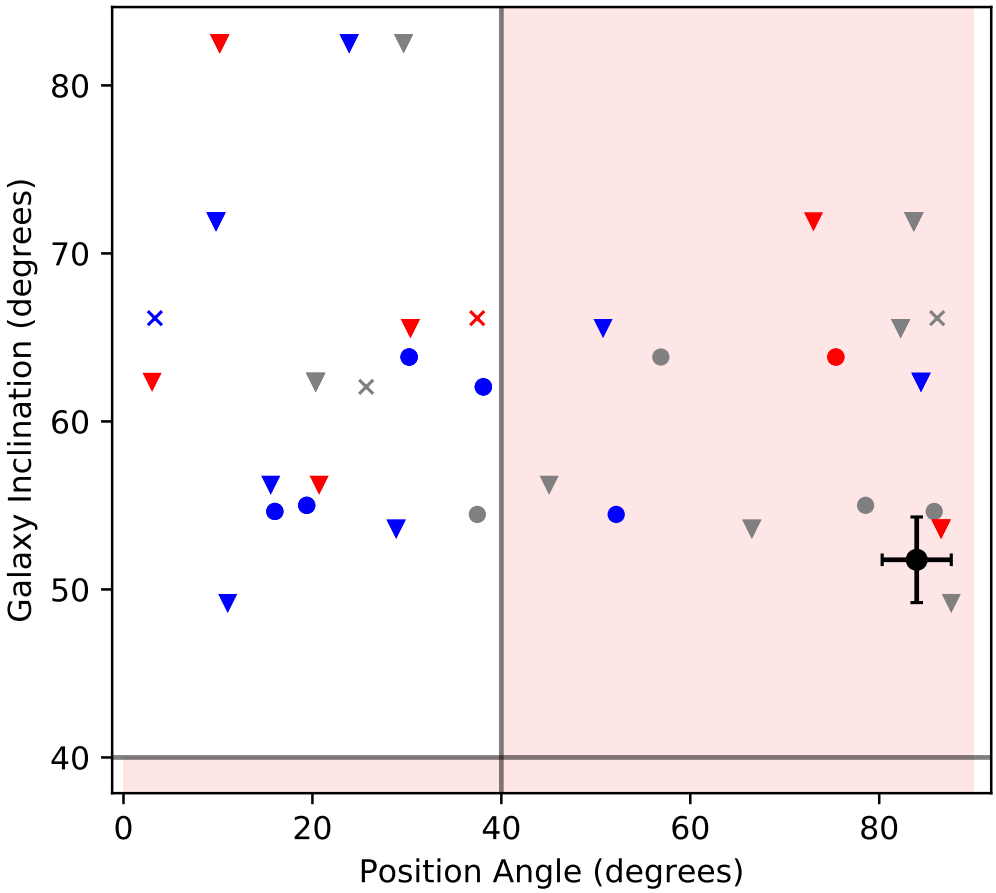

Figure 3.11: The position angles and inclinations of absorption features around galaxies with observed velocity gradients in MUSE (using any emission line). This selection introduces the strong bias against face-on galaxies seen in the figure. We cut by inclination and position angle at 40° as described in the text, in order to identify candidate co-rotating material (unshaded region). Points are coloured by quasar sightline (A in blue, B in grey, C in red). Galaxies in groups are marked with triangles and non-detections are marked with crosses. The bars on the black point in the lower-right are illustrative of the median 1-σ uncertainty in each axis.

in these cases. The magnitude and direction of the velocity offset relative to the rotation of the galaxy for each system is illustrated in Figure 3.13. All five of the galaxy–absorber pairs meeting the above constraints and not within groups show absorption offset in the same direction as the galaxy rotation. The probability of all five absorbers that are not consistent with zero (within 1σ) being offset in the same direction if the direction is random is 3%. A weighted mean of the velocity differences also gives a significant result (105 ± 40 km s^{-1}). We note that where multiple absorption components are observed in the same spectrum within 500 km s^{-1} of one of these galaxies, each component is counted separately and shown separately in the figures.

When galaxies in groups are also included, the major-axis H I absorption still shows a tendency to align with the galaxy rotation when using a weighted mean (Figure 3.14), with a $\approx 2.5\sigma$ result of (74 ± 27) km s^{-1}. The binomial calculation returns a p-value of 0.3 (the probability that at least 8 of the 13 absorber velocities not consistent with zero would be aligned with the galaxy rotation if there were no physical link between the galaxy and absorber).

Whilst the tendency for line-of-sight velocities of gas along the major axis to be aligned with the galaxy rotation would be expected given the rotating disk model, the sample size is too small to draw strong conclusions. Both of the non-group sightlines more than 100 kpc from the galaxy exhibit this alignment well beyond the virial radius of the galaxy, whereas studies such as MEGAFLOW (Zabl et al., 2019) and others (e.g. Bouché et al., 2016; Diamond-Stanic et al., 2016; Ho et al., 2017) only show co-rotation out to tens of kpc. In our small sample this can be explained by coincidence, but such alignment is thought to be a result of coherent accretion over Gyr timescales, due to the location of the galaxy within the cosmic web, transferring angular momentum from the gas to the central galaxy (e.g Danovich et al., 2015; Stewart et al., 2017). DeFelippis et al. (2020) find, in Illustris TNG simulations, that this major-axis co-rotating material often extends in a much thicker 'wedge' out to $\sim 0.75\ R_{\rm vir}$ for sub-$L_\star$ galaxies. However, Huscher et al. (2021) use the EAGLE simulations and study larger $\approx L_\star$ galaxies, finding substantial rotation only to $\approx 0.3R_{\rm vir}$ in cool gas at $z = 0$. Any attempts to constrain the extent of this material

through observations will require detections of absorption with impact parameters of 100–300 kpc from isolated galaxies, which our sample lacks. The sample of French & Wakker (2020) does contain H I absorption in this range, but they do not detect a significant preference for co-rotation beyond $\approx$ 100 kpc.

The less-clear alignment in galaxy groups is consistent with models suggesting interactions between galaxies are the origin of most strong H I absorbers in these environments (e.g Morris & van den Bergh, 1994), as the velocities of such tidal material would be more strongly affected by the relative velocities of the galaxies at large impact parameters. The velocity offsets between galaxies and absorbers are generally within the velocity dispersion of the observed galaxies.

3.5 Chapter summary & conclusions

In this study we take advantage of multiple observing campaigns, resulting in a deep, dense galaxy survey covering the field around a unique quasar triplet, to examine the geometry and extent of gas flows in the CGM and IGM on larger scales than most CGM studies.

We find that:

i) The H I absorbing gas is often found in structures several hundred kpc in extent, as observed in absorption lines visible in multiple lines-of-sight at the same redshift. These structures traced by H I over all column densities are more likely to match those traced by galaxies and high-column-density absorbers (N $> 10^{14}$ cm^{-2}). We do not find significant evidence that H I absorbers with lower column densities form structures reaching this extent. It is not clear whether these are arising from smaller overdensities in galaxy voids, or forming filaments, most of which are not aligned such that they cover multiple sightlines. A larger number of background sources would be needed to confirm this through absorption measurements.

ii) Galaxy–absorber pairs with H I absorption exhibit a significant bimodality in position angle for impact parameters up to $\approx$ 300 kpc, possibly evidence that

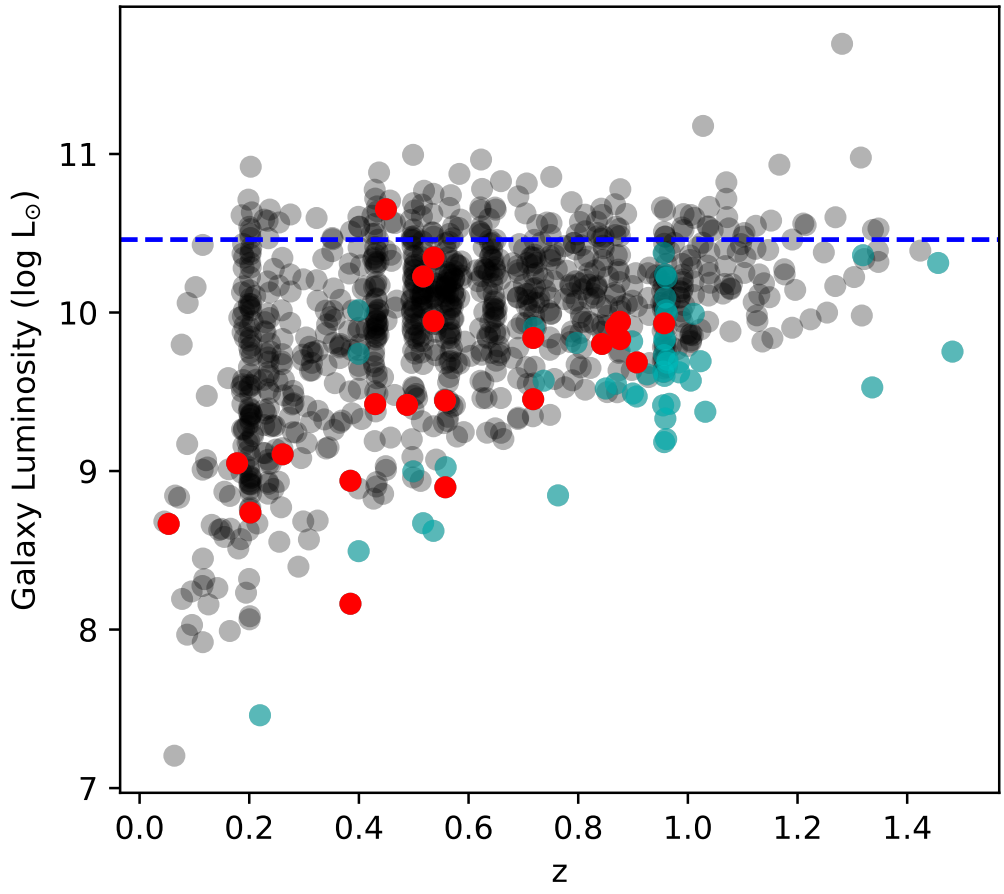

Figure 3.12: The r-band luminosities of observed galaxies as a function of redshift. Red points illustrate objects in which a velocity gradient is observed in MUSE. Cyan points show other galaxies within the MUSE fields. The horizontal dashed line represents an estimate of $L_\star$, as given by Montero-Dorta & Prada (2009) for $z \lesssim 0.2$. ($L_\star$ does vary over the given redshift range, but this is expected to be less than a factor of two, e.g. Gabasch et al. 2006, so is not shown.)

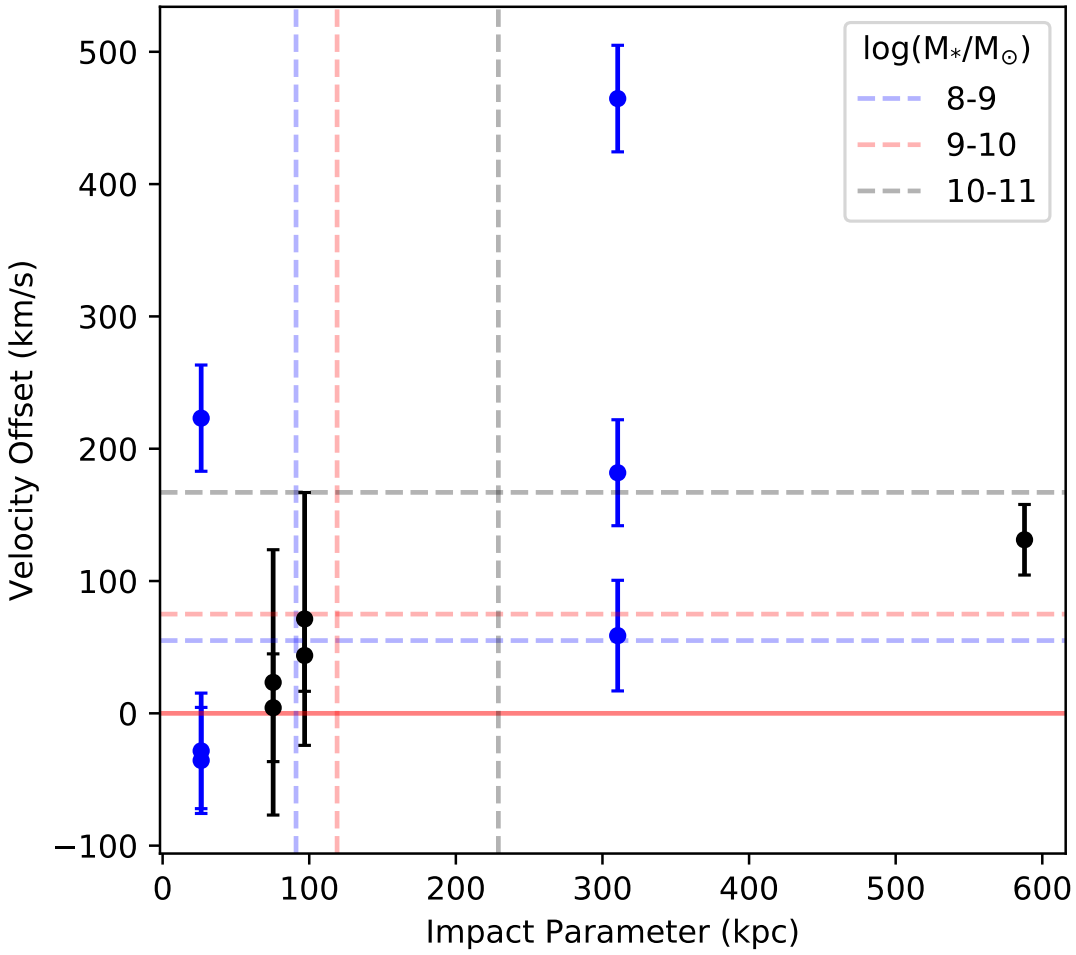

Figure 3.13: The impact parameter and line-of-sight velocity difference between galaxies and absorbers in the major-axis subsample described in Section 3.4, showing only non-group galaxies. The sign of the velocity difference is chosen to reflect alignment (positive) between the angular momenta of the galaxy and gas, with the red solid line indicating zero offset. Uncertainties in velocity offset are the redshift measurement errors for the galaxy and absorber added in quadrature. Points are coloured by galaxy stellar mass, with galaxies of between 10^8 and 10^9 $M_\odot$ shown in blue, 10^9-10^{10} $M_\odot$ in red, and 10^{10}-10^{11} $M_\odot$ in black. The dashed horizontal and vertical lines show the median virial velocities and radii for galaxies within each bin across our full galaxy survey

.

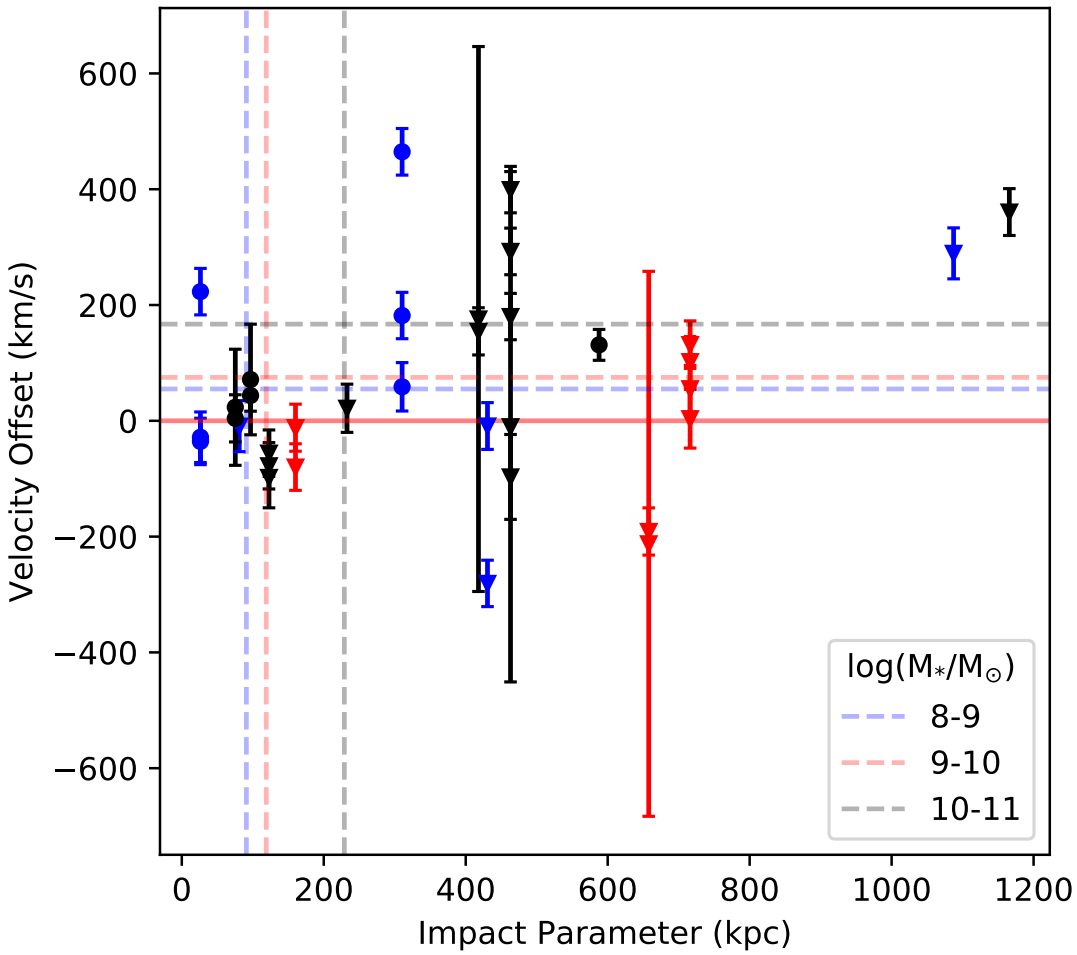

Figure 3.14: The impact parameter and line-of-sight velocity difference between galaxies and absorbers in the major-axis subsample described in Section 3.4, as in Figure 3.13 but including group galaxies. Galaxies in groups are shown with triangles, those not in groups are shown with circles. Points are coloured by galaxy stellar mass. Median virial velocities and radii do not consider other galaxies in the group that may be sharing the same halo.

outflows and extended disks reaching these scales are common. However, we do not find that H I absorbers near the minor axis have significantly higher Doppler widths than those on the major axis, nor do they show smaller velocity offsets around edge-on galaxies for which a putative outflow should not have a large line-of-sight velocity component. We therefore cannot rule out alternative hypotheses for this bimodality, such as preferential alignment between galaxies and large-scale structure.

iii) H I absorbers found close to the minor axis of a galaxy are twice as likely to have associated O VI absorption as those found close to the major axis. The position angle distribution of O VI shows a clear bimodality, weighted towards the minor axis more than H I, supporting models in which O VI is primarily observed in galactic winds. O VI around isolated galaxies is far more limited in extent than H I, with no isolated galaxies featuring O VI absorption beyond 400 kpc. We also see O VI in galaxy groups, but cannot currently distinguish between virialized halo gas, tidal debris, and outflows/halo gas from other galaxies in the same group.

iv) The line-of-sight velocities of H I absorption found near the major axis of a galaxy show a significant tendency to align with the galaxy rotation, suggesting a strong coupling between the angular momentum of the CGM and galaxy (as found by e.g. DeFelippis et al., 2020; Huscher et al., 2021).

v) Star-forming galaxies are more likely to trace the same structures as H I seen in multiple sightlines. Our star-forming sample does not exhibit the bimodality in position angle that could be indicative of accreting and outflowing material, but this bimodality is apparent when using a more restrictive 'strongly-star-forming' sample. This suggests that this inflow/outflow dichotomy contributes to the overall bimodality seen on scales $\lesssim 300$ kpc, although is not ubiquitous among star-forming galaxies, and that the excess absorption seen on larger scales is primarily due to environmental effects (although the redshift biases of our star-forming and non-star-forming samples may also contribute).

This study illustrates some of the ways in which multiple sightlines can be used

to probe the structure of the gas around galaxies. In future work we will also study the absorption around individual galaxies and galaxy groups probed by these quasar lines-of-sight, where knowledge of absorption at multiple impact parameters and position angles around the same galaxy will enable us to test a range of models. Similar methods applied to mock lines-of-sight through simulations may provide further insights into the processes behind these results.

Whilst Q0107 is one of very few systems for which these techniques can currently be used, the prospects at higher redshift are much improved. The ELT will allow far deeper galaxy surveys, enabling high-redshift galaxies to be used as background sources (e.g. Japelj et al., 2019), and improving on current studies that have poor signal-to-noise (e.g Lee et al., 2018) or stack observations to improve the sensitivity (e.g Chen et al., 2020b). This progresses the field towards full tomography, in which numerous sightlines can probe a variety of scales throughout the same structures, and improve upon the usual pencil-beam observations of the IGM.

Similarly, observations of emission in H I 21cm rarely reach detections of material in the $10^{13} - 10^{16}$ cm^{-2} regime covered here, but the Square Kilometre Array will likely be able to reach sensitivities of 10^{15} cm^{-2} (Popping et al., 2015), sufficient to begin detecting the denser filaments of the cosmic web, and allowing study of the interaction between the CGM galactic fountains, the tidal material produced in galaxy groups, and the large-scale cosmic web.

CHAPTER 4

Testing models of CGM structure around isolated galaxies

In this chapter we attempt to model the absorption around isolated galaxies using simple halo, disk and outflow models. This chapter has been written in the form of a paper, which has been accepted for publication in MNRAS and is referenced as Paper 2 throughout.

4.1 Introduction

The circumgalactic medium (CGM) is the reservoir of gas surrounding galaxies. Consisting of material outside the galaxy itself, but within its dark matter halo, it is often defined as extending to the virial radius (e.g. Tumlinson et al., 2017). Observations using absorption in the line-of-sight to background sources (often quasars) have long been used to study the gaseous halos around intervening galaxies and the surrounding intergalactic medium (e.g. Bahcall & Spitzer, 1969; Bergeron, 1986; Bergeron et al., 1994; Weymann et al., 1998; Adelberger et al., 2005; Prochaska et al., 2011; Kacprzak et al., 2012b; Rubin et al., 2018; Pointon et al., 2019; Wilde et al., 2021; Dutta et al., 2021). The wide variance of absorber properties indicate a complex, multi-phase medium (e.g. Tripp et al., 2008; Werk et al., 2013; Mathes

et al., 2014; Péroux et al., 2019; Chen et al., 2020a), but most of these studies can probe only a single line-of-sight through the CGM of any one galaxy, preventing detailed study of the CGM of each galaxy and limiting these works to statistical properties of a sample of galaxy–sightline pairs. More information can be obtained by using multiple lines-of-sight where possible, although this requires rare cases with multiple closely-spaced quasars (e.g. Fossati et al., 2019b; Maitra et al., 2019), sufficiently bright background galaxies (e.g. Zabl et al., 2020), multiply-lensed quasars (e.g. Zahedy et al., 2016; Okoshi et al., 2021), or gravitational arcs (e.g. Lopez et al., 2018, 2020; Tejos et al., 2021b; Mortensen et al., 2021).

The evolution of galaxies is strongly linked to the state of the CGM, with models suggesting that material ejected from the galaxy in stellar-wind-driven and AGN-driven outflows alongside material accreting onto the central galaxy regulates its star formation (e.g. Lehnert et al., 2013; Somerville et al., 2015; Salcido et al., 2020). This exchange of material also transfers angular momentum between the galaxy and its CGM (e.g. Brook et al., 2012; Stewart et al., 2017; DeFelippis et al., 2017, 2020), which likely affects galaxy morphologies (e.g. Swinbank et al., 2017).

At distances of tens of kpc, observations of the cool gas in the $z \lesssim 1$ CGM often find a bimodality in the distribution of azimuthal angles, identified with outflows near to galaxy minor axes, and rotation and accretion along the major axis (e.g Bouché et al., 2012; Kacprzak et al., 2012b; Zabl et al., 2019; Beckett et al., 2021). This difference in gas properties found at different azimuthal angles is also reproduced by many simulations (e.g. DeFelippis et al., 2020; Péroux et al., 2020; Hopkins et al., 2021).

Emission-line kinematics provide evidence for minor axis outflows, with early Hα measurements of the wind from the nearby M82 (e.g. Bland & Tully, 1988; Lehnert et al., 1999) and other nearby galaxies (e.g. Heckman et al., 1990), as well as more recent studies (e.g. Wang et al., 2020) and metal-line emission using integral field units such as MUSE and KCWI (e.g. Finley et al., 2017; Burchett et al., 2021; Zabl et al., 2021b). Transverse and down-the-barrel absorption measurements also indicate cool outflowing material in transitions from H I and low metal ions such as Na I and Mg II (e.g. Lan & Mo, 2018; Concas et al., 2019; Schroetter et al., 2019).

Despite differing methods of energy injection representing stellar and AGN feedback, bi-conical outflows near the galaxy minor axis are found in many simulations, including EAGLE (e.g. Mitchell et al., 2020a), Illustris TNG50 (e.g Nelson et al., 2019) and FIRE-2 (e.g. Hopkins et al., 2021).

Near the major axis, evidence for co-rotation has been found using a similarly wide range of diagnostics, including absorption in H I (e.g. Bouché et al., 2016; French & Wakker, 2020) and Mg II (e.g. Charlton & Churchill, 1998; Steidel et al., 2002; Ho et al., 2017; Martin et al., 2019b; Zabl et al., 2019; Tejos et al., 2021b), as well as Mg II emission (Leclercq et al., 2022). Again, down-the-barrel measurements have found examples of infalling material (e.g. Rubin et al., 2012), and disk-like models have been used for X-ray emission from the CGM of the Milky Way (Kaaret et al., 2020) and absorption around NGC1097 (Bowen et al., 2016). Simulations also find that the cool CGM forms co-rotating and accreting flows near the galaxy major axis (e.g. DeFelippis et al., 2020; Ho et al., 2020).

Whilst these structures are common to most models and are deduced from a variety of observations, there remains uncertainty on several fronts. Firstly, Hopkins et al. (2021) add cosmic rays to the driving of outflows in the FIRE simulations, which allows them to reach megaparsec scales around $L_\star$ galaxies, whereas the outflow rates without cosmic rays, and those in Illustris for most stellar masses (Nelson et al., 2019), drop dramatically beyond 50 kpc. It is also unclear how much cool gas is contained within these winds, with some models suggesting primarily hot winds (e.g. Pandya et al., 2021), and others allowing cool winds to large scales (e.g. Fielding & Bryan, 2022).

The extent of the cool, co-rotating structures in the CGM is also not well-determined. The FIRE simulations suggest that gas infall onto galaxies is primarily hot at distances above ≈ 40 kpc for $L_\star$ (Hafen et al., 2022), and hot accretion is generally expected to dominate around such galaxies at low redshift (e.g. Faucher-Giguère et al., 2011; Fielding et al., 2017), yet predictions and detections of co-rotating cool gas (often in the form of Mg II) extend substantially further (e.g Zabl et al., 2019; Ho et al., 2020; French & Wakker, 2020).

Robustly determining whether absorption measurements are probing these struc-

tures is extremely difficult using single-sightline observations, with some studies selecting candidate outflow and disk absorbers based on galaxy inclination and absorber aziumthal angle (e.g. Bordoloi et al., 2011; Schroetter et al., 2015; Zabl et al., 2019; Schroetter et al., 2019). Improving upon this selection strategy will require multiple lines-of-sight probing a range of impact parameters around the same galaxy.

In this study we focus on the Q0107 system, a quasar triplet at z $\sim$ 1: LBQS 0107-025A, LBQS 0107-025B, and LBQS 0107-0232, hereafter denoted A, B, and C. QSOs A and B lie at z$\approx$0.96, with C at z$\approx$0.73, with co-ordinates given in Table 2.1. The three quasars have separations of $\approx$ 1 arcminute ($\approx$ 370 kpc at z=0.5), allowing multiple lines-of-sight to be probed through the CGM/IGM around galaxies in this field. Lyα absorption along these sightlines allows a combination of lower column densities and larger scales than most studies relying on gravitationally-lensed systems (arcs or multiply-lensed QSOs, e.g. Zahedy et al., 2016; Lopez et al., 2018; Mortensen et al., 2021; Okoshi et al., 2021; Tejos et al., 2021b).

Many studies have utilised this unique configuration to study the gas around galaxies. Dinshaw et al. (1997) observed QSOs A and B, using a maximum likelihood analysis to conclude that the data was best explained by randomly inclined disks approximately 1 Mpc in radius. A larger sample including the Q0107-A and B pair was analysed in D'Odorico et al. (1998), who concluded a disk-like or spherical geometry was possible, with radii $\approx$600 kpc. Young et al. (2001) complemented this by considering absorption systems appearing in multiple sightlines at similar redshifts, and found that matches involving stronger absorption tended to have smaller velocity separations. Such systems also occur more frequently among high-column-density absorbers, as found by Petry et al. (2006).

Crighton et al. (2010) used improved QSO spectra of all three lines-of-sight as well as galaxy spectra. They observed a highly-significant excess of absorption systems covering all three sightlines over an ensemble of randoms, providing clear evidence that gas and galaxies are associated on scales of hundreds of kpc. This field was also included in studies of galaxy–absorber cross-correlations in H I (Tejos et al., 2014, hereafter T14) and O VI (Finn et al., 2016).

Absorbers detected in more than one of these three lines-of-sight at a similar

redshift have also been studied in detail using ionization modelling. Muzahid (2014) detected both the warm and cool phase of the CGM around an $L_\star$ galaxy at z $\approx$ 0.2, whilst Anshul et al. (2021) detected multi-phase gas at z $\approx$ 0.4.

We built on these works in Paper 1, in which we showed that the excess absorption seen covering multiple lines-of-sight separated by hundreds of kpc is stronger both in high-column-density absorption and around star-forming galaxies, than in low-density absorption and around quiescent galaxies. We found a bimodality in the distribution of azimuthal angles of detected galaxy-absorber pairs, extending to $\approx$300 kpc. That absorbers near the major axis had line-of-sight velocities preferentially aligned with the galaxy rotation and that minor axis absorbers were more likely to exhibit O VI suggest that the higher detection rates near the major and minor axes are due to rotating and outflowing structures respectively.

In this paper we model the absorption around galaxies in the Q0107 field in order to test for these structures in the CGM. The presence of multiple lines-of-sight through the Q0107 field, alongside the extensive galaxy data, constrains the model absorption at multiple locations around the galaxy. We can therefore determine the CGM structures probed by our sightlines more confidently than in single-sightline observations.

At redshifts with multiple galaxies near to the lines-of-sight, we might expect tidal debris (e.g. Morris & van den Bergh, 1994), ram-pressure-stripped gas (e.g. Fumagalli et al., 2014; Fossati et al., 2019a), and other intra-group material (e.g. Stocke et al., 2014; Péroux et al., 2017; Bielby et al., 2017), as well as distortion of any disk or outflow structures in the CGM. We therefore consider only isolated galaxies here, deferring analysis of galaxies that are not isolated to a later work. For the purposes of this paper, we select galaxies with no detected companion within 500 kpc and 500 $\mathrm{km\,s^{-1}}$. This is substantially larger than the virial radius and velocity for the galaxies in our sample, allowing us to test for the presence of outflows near the CGM/IGM interface[1]. This rules out group interactions as far as possible given

[1]We only consider galaxies with spectroscopic redshifts, as deep imaging for this field consists of too few bands for estimating photometric redshifts. Completeness is discussed briefly in Section 2 of this work, and more thoroughly in Paper 1 and T14.

our detection limits, but does not rule out a contribution from faint undetected galaxies.

In Section 4.2 we discuss selection of the sub-sample of isolated galaxies considered in this work. Section 4.3 summarizes the toy models used in our attempts to reproduce the observed absorption, whilst Section 4.4 describes in detail three example galaxies and their surrounding absorption. We then discuss the results from our sample in Section 4.5, and finally summarize in Section 4.6. Details of the modelling process and the results from the remainder of our isolated galaxy sample are left to the Appendix (Section C.1).

We use the Planck 2018 cosmology (Planck Collaboration, 2020) throughout, with $\Omega_m = 0.315$ and $H_0 = 67.4$ km/s/Mpc, and quote physical sizes and distances unless otherwise stated.

4.2 Sample of isolated galaxies

This paper makes use of the absorber and galaxy catalogues used in Paper 1, built on those used in T14. The details of the reduction and analysis required to produce these catalogues are given in T14 and Chapter 2 of this thesis, so are not repeated here. We do discuss the selection of isolated galaxies that we attempt to model in this study.

The majority of the 72 galaxies with both position angle/inclination measurements and well-constrained redshifts lie in close proximity to multiple other galaxies. We use a 500 kpc and 500 $\mathrm{km\,s^{-1}}$ cut in order to select isolated galaxies, so that their CGM is less likely to be disturbed by interactions with other galaxies. This produces a sample of 12 galaxies which we model in this paper. We note that this does not rule out the possibility of fainter galaxies for which we could not estimate a redshift either directly contributing to the absorption (e.g. Ho et al., 2020), or disturbing the CGM of the detected galaxy, nor does it rule out previous mergers leaving a disturbed CGM.

Galaxies are shown in relation to the quasar sightlines and the observations in Figure 4.1, and several galaxy properties are listed in Table 4.1.

Figure 4.2 shows these galaxies on the stellar mass-SFR plane alongside the full galaxy survey of this field. Most of the galaxies considered in this work lie close to the main sequence of star-forming galaxies, with two non-star-forming galaxies well below this (A-30 and 25833), and one galaxy substantially above the main sequence (B-14). The selected galaxies are biased towards low stellar masses and high star-formation rates relative to the full sample. This because we only select galaxies within the HST field, which is the deepest part of the survey. The HST field also includes the MUSE data, from which faint emission-line galaxies can be detected.

4.3 Models

We use three basic toy models throughout this work: a biconical outflow, a rotating disk, and a power-law halo. Our models are described briefly here; further details are given in Appendix B.3. The parameters used to describe each of these models are listed in Table 4.2 and discussed here. These models are heavily dependent on the galaxy and sightline orientation, so impact parameter, galaxy inclination, and azimuthal angle are also inputs to these models, with values fixed by the observations rather than as free parameters.

All three model types require a reference density in order to set the strength of the model absorption. As the power-law profile is undefined at r = 0, we use the density at a radius of 1 kpc as the reference value (ρ_1) for both the halo and outflow models. The exponential density profile used for our model disk is well-defined at r=0, so we use this density ρ_0 to normalize our model densities. The three model types also all allow for a thermal or turbulent velocity component v_t that can further widen any absorption features. (We do not attempt to distinguish between broadening due to thermal or turbulent velocities.) This term makes no noticeable difference to the broad absorbers seen using FOS, but we adopt values of 20-40 $\mathrm{km\,s^{-1}}$ to help to improve the fit for some resolved absorbers in the COS spectra. This is consistent with the expected widths of IGM absorbers (e.g. Davé et al., 2010).

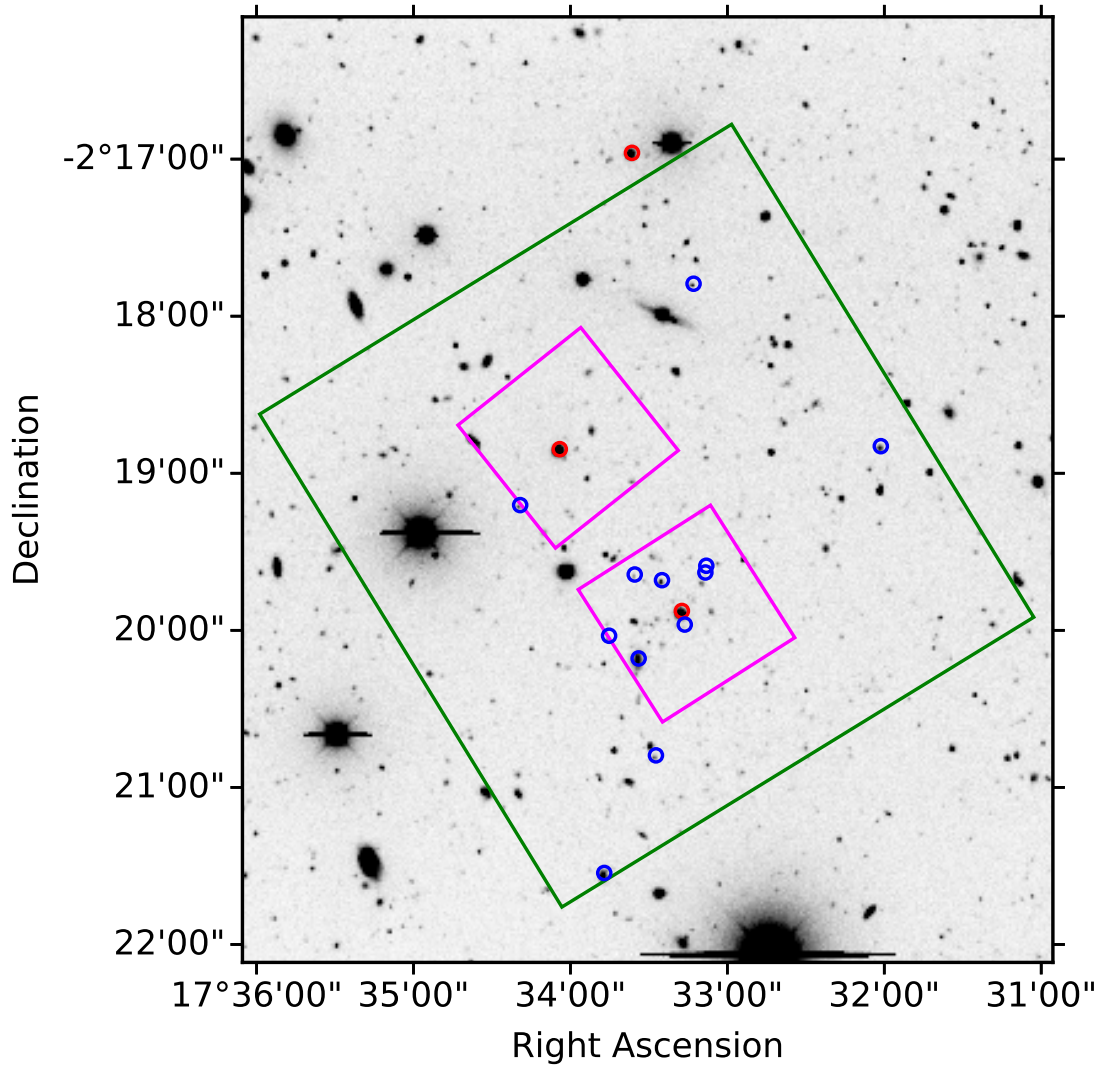

Figure 4.1: The layout of the surveys used in this study. The background image was taken with the Kitt Peak 4-metre Telescope. The solid green square shows the region covered by HST imaging, whilst the smaller magenta squares show the MUSE fields centered on QSOs A and B. The quasars are shown by red circles, with A the southernmost and C the northernmost. The twelve galaxies included in our 'isolated' sample are shown with blue circles.

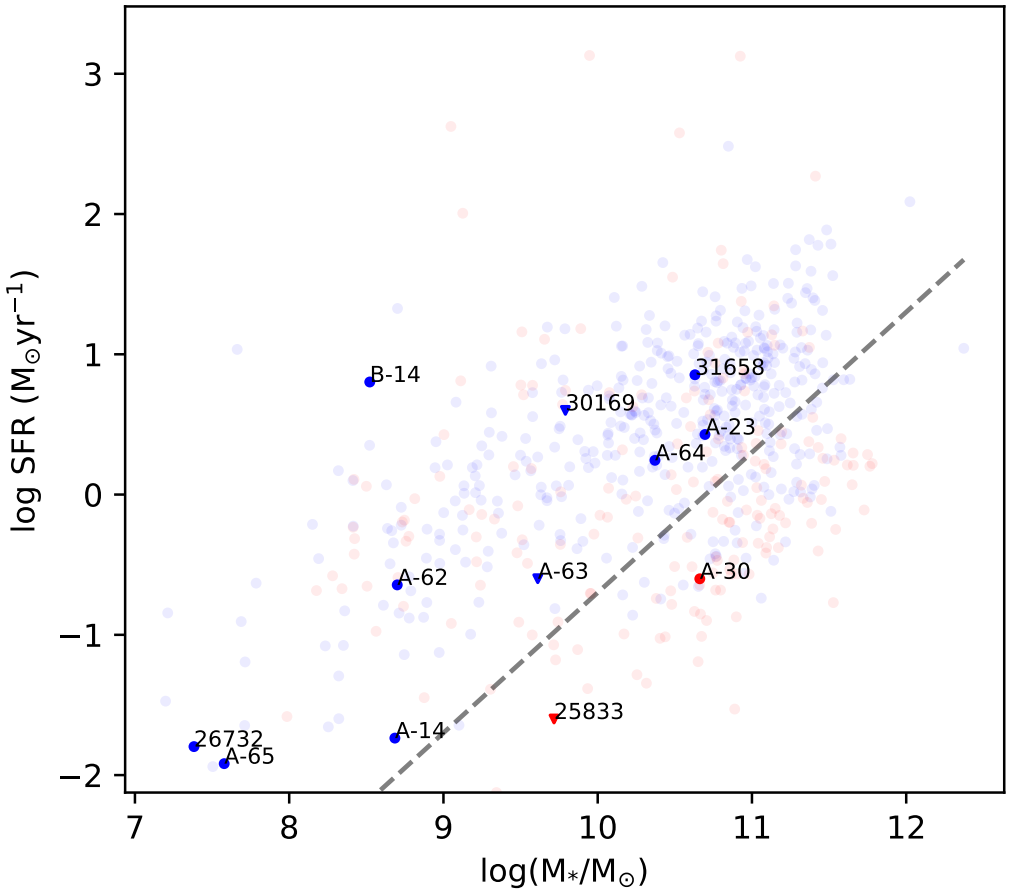

Figure 4.2: Stellar mass vs star-formation rate for galaxies in our sample. Faded points show the overall galaxy sample (identical to Figure 5 from Paper 1), whilst galaxies detailed in this work are bold and labelled with the galaxy MOS or MUSE ID as given in Table 4.1. Galaxies identified as star-forming are shown in blue, with non-star-forming galaxies in red. The grey dashed line indicates an sSFR of 0.02 Gyr^{-1}, an approximate match to the SF/non-SF designations that were made using template fitting. Masses are estimated using the formulae from Johnson et al. (2015) and star-formation rates estimated using the Hα or [OII] (3727 Å) luminosities. These measurements are detailed in Paper 1. Note that neither line is available for the three objects marked by triangles. They do not lie in the wavelength region covered by the spectra of A-63 and 30169, so the correlation between Hα/[OII] SFR and Hβ luminosity has been used, producing a large uncertainty. Galaxy 25833 is non-star-forming, so the noise in its spectrum has been used to generate an approximate upper limit.

Table 4.1: Summary of galaxy properties for our selected sample of isolated galaxies. Derivation of these properties is described in more detail in Paper 1. Column descriptions: (1) Galaxy ID used in this work (MUSE and MOS IDs were collated separately; MUSE ID is used for galaxies featuring in both MOS and MUSE catalogues); (2) Galaxy redshift (all galaxies in this subsample have redshift uncertainties smaller than 0.001); (3, 4) On-sky coordinates of galaxy; (5) Observed magnitude in the SDSS r-band; (6) Galaxy luminosity in SDSS r-band as a multiple of $L_\star$ ($L_\star$ estimate from Montero-Dorta & Prada (2009), uncertainties smaller than 0.005 $L_\star$ are omitted); (7) Stellar mass estimated as in Johnson et al. (2015) (for most galaxies the largest uncertainty is a scatter of 0.15 dex in their relation); (8) Halo mass estimated using the abundance matching technique from Behroozi et al. (2010); (9) Star-formation flag denoting a star-forming or non-star-forming galaxy; (10) Star-formation rate estimated from galaxy emission lines, using the Kennicutt (1998) and Kewley et al. (2004) calibrations for Hα and [O II] respectively (uncertainties are a combination of scatter in these relationships and uncertainty in the line fit); (11) Line used to estimate SFR (SFRs estimated from Hβ using the correlation between SFR estimated from Hα and Hβ line luminosity, generating a substantially larger uncertainty); (12) Note of whether emission-line kinematics from the MUSE data are available for this galaxy.

Galaxy	z	RA	Dec	r-band	Luminosity	$M_\star$	M_h	SF Flag	SFR	Line	Kinematics
		°	°		($L_\star$)	$\log_{10}(M_\odot)$	$\log_{10}(M_\odot)$		($M_\odot$/yr)		
(1)	(2)	(3)	(4)	(5)	(6)	(7)	(8)	(9)	(10)	(11)	(12)
A-14	0.053	17.5594	-2.3363	19.93 ± 0.01	0.02	8.7 ± 0.2	10.9 ± 0.3	SF	$0.018^{+0.009}_{-0.006}$	Hα	Yes
26732	0.087	17.5576	-2.3466	22.80 ± 0.02	0.01	7.4 ± 0.2	10.4 ± 0.3	SF	$0.016^{+0.007}_{-0.005}$	Hα	No
25833	0.123	17.5631	-2.3591	19.83 ± 0.01	0.10	9.7 ± 0.2	11.4 ± 0.3	non-SF	<0.06	Hα	No
A-62	0.178	17.5569	-2.3280	21.78 ± 0.01	0.04	8.7 ± 0.2	11.0 ± 0.3	SF	$0.23^{+0.16}_{-0.09}$	Hα	Poor
A-65	0.220	17.5522	-2.3265	26.06 ± 0.46	0.01	7.6 ± 0.7	10.5 ± 0.7	SF	$0.012^{+0.005}_{-0.003}$	Hα	No
B-14	0.261	17.5720	-2.3200	22.57 ± 0.02	0.05	8.5 ± 0.2	10.9 ± 0.3	SF	$6.3^{+3.3}_{-2.2}$	Hα	Yes
A-63	0.488	17.5598	-2.3274	23.38 ± 0.03	0.09	9.6 ± 0.2	11.5 ± 0.3	SF	$0.25^{+0.63}_{-0.18}$	Hβ	Yes
30169	0.584	17.5337	-2.3138	21.65 ± 0.01	0.68 ± 0.02	9.8 ± 0.2	11.6 ± 0.3	SF	$4.0^{+10.0}_{-2.9}$	Hβ	No
31658	0.728	17.5536	-2.2966	22.81 ± 0.03	0.40 ± 0.02	10.6 ± 0.2	12.4 ± 0.6	SF	$7.1^{+2.3}_{-1.8}$	[O II]	No
A-23	0.843	17.5626	-2.3339	23.86 ± 0.12	0.22 ± 0.03	10.7 ± 0.3	12.5 ± 0.7	SF	$2.7^{+0.9}_{-0.7}$	[O II]	Poor
A-30	0.850	17.5545	-2.3327	24.58 ± 0.21	0.12 ± 0.02	10.7 ± 0.3	12.5 ± 0.7	non-SF	$0.25^{+0.14}_{-0.09}$	[O II]	Poor
A-64	0.926	17.5523	-2.3272	24.58 ± 0.03	0.14 ± 0.03	10.4 ± 0.5	12.1 ± 0.8	SF	$1.8^{+0.6}_{-0.5}$	[O II]	Yes

Outflows

For our model outflows, we assume a constant velocity and constant flow rate, necessitating a r^{-2} density profile. An approximately constant outflow velocity (v_{out}) does appear to be justified by some simulations (e.g Mitchell et al., 2020b), although TNG50 outflows appear to slow somewhat at small scales (over the first $\approx$ 20 kpc, Nelson et al., 2019). This velocity can usually be well-determined using the observed galaxy inclination and galaxy–absorber line-of-sight velocity offset, and therefore has uncertainties comparable to those in these observations (usually $\lesssim 50$ km s^{-1}).

A well-defined opening angle is supported by observations, in nearby emission (Bland & Tully, 1988), transverse absorption (e.g Bordoloi et al., 2011), and down-the-barrel observations (Rubin et al., 2014), which we assume to be constant (we label the half-opening angle θ_{out}). We do allow for a hollow cone in which the centre of the outflow is further heated such that the neutral fraction is low and H I density is suppressed. Outside the cone (or in the centre of a hollow cone, where the polar angle $\theta < \theta_{in}$), we use a density of zero. With the relationship between gas density and distance from the galaxy fixed to a r^{-2} power law, the relative column densities at the three locations probed by the lines-of-sight are determined primarily by the outflow opening angle. This angle is therefore usually constrained to better than 10° accuracy. A hollow cone could be detected if a line-of-sight near the galaxy minor axis had a lower than expected column density relative to another absorber, or by the presence of two absorption components that may be resolved in the COS spectra.

Where multiple lines-of-sight probe an outflow, it may be possible to detect changes in velocity or opening angle with radius, but we do not attempt to quantify these in our toy models. Our galaxy observations cannot generally be used to distinguish which cone of the outflow is inclined away from us, so we use the S_{Nr} parameter, which has a value of +1 if the outflow cone to the north of the galaxy is moving redward along the line-of-sight or -1 otherwise, to allow either case to be modelled. The effect of changing this parameter is illustrated in Figure 4.3.

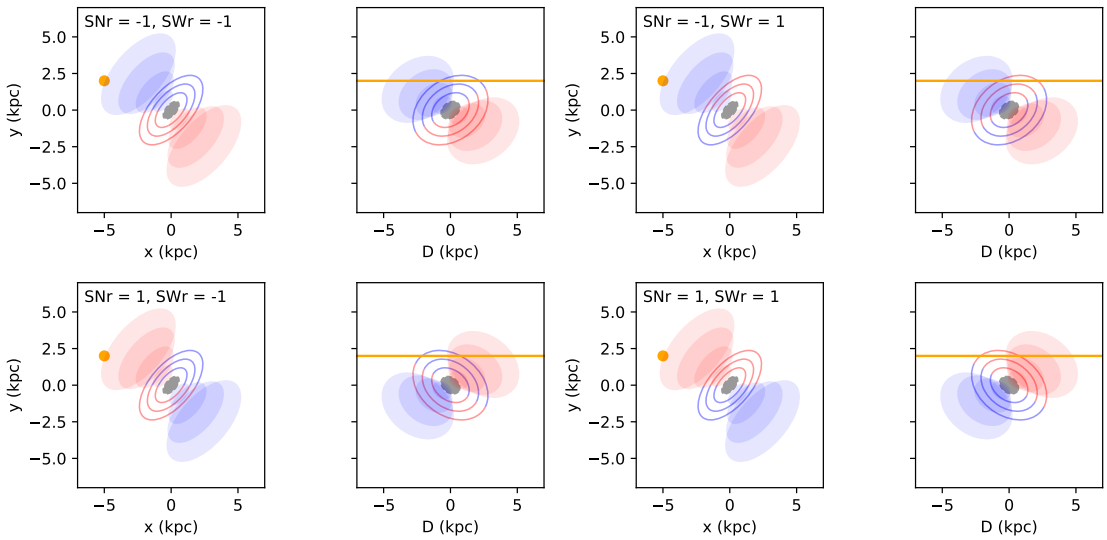

Figure 4.3: A schematic of the possible orientations of disk and outflow models possible around a single galaxy. In each panel, the grey ellipse indicates the galaxy disk, with the red and blue ellipses indicating model disk and outflow components with motion away from and towards the observer respectively (assuming the disk is dominated by rotational velocity rather than infall). Two panels are shown for each combination of S_{Wr} and S_{Nr}, the two model parameters denoting orientation. The leftmost of these shows the on-sky view, whilst the right panel shows a view along the example line-of-sight (shown by the orange dot and line in the two panels) with the quasar to the right of the image and observer to the left of the image. Model velocities and densities are evaluated at 10-parsec intervals along the line-of-sight, denoted by the 'D' coordinate in this figure.

Disks

Our model rotating disks are naturally constrained to the same direction as the galaxy kinematics (if visible), denoted by the S_{Wr} parameter which similarly has a value of ± 1 (and is illustrated in Figure 4.3).

They have exponential density profiles parallel and perpendicular to the major axis, with independent scale heights (h_r and h_z). A large vertical scale height would allow our models to be compatible with the thick disk suggested by Steidel et al. (2002), as well as the thick disk and 'wedge' seen in the simulated cool CGM by Ho et al. (2020) and DeFelippis et al. (2020), but we do not model any lag in velocity with height, as considered in Steidel et al. (2002). The scale heights determine how the model column densities change when probed at different locations by the sightlines. They have a complex degeneracy with the reference density, dependent on the locations of the sightlines. In most cases, the ratio of scale heights is somewhat constrained (although often only to within a factor of $\approx$3) by the relative column densities in the different lines-of-sight. However, the scale heights themselves remain mostly degenerate with the reference density, so we generally do not quote these in this work. Absorber widths can also provide some constraints, as a line-of-sight probing a thicker disk will feature absorption covering a wider range of line-of-sight velocities, but as absorption can be broadened by many other effects, this only provides a weak floor to the scale heights.

In addition to the rotational velocity (v_ϕ), an accreting component of velocity is allowed (v_r), as in Zabl et al. (2020). Where multiple absorption features are detected, the separate rotating and infalling velocity components can be constrained by differing velocity offsets at the locations of the lines-of-sight. However, where only one absorber is detected, only the sum or the difference of the two velocity components is well determined. Any constrained' velocity components have uncertainties originating from the galaxy and absorber redshift measurements, so usually $\lesssim 50\ \mathrm{km\,s^{-1}}$.

Table 4.2: List of parameters describing the toy models used in this work.

Symbol	Description	Unit
	Halo	
v_t	Thermal/turbulent velocity	$\mathrm{km\,s^{-1}}$
ρ_1	Reference H I density (1 kpc)	$\mathrm{cm^{-3}}$
α	Power law index (on H I density profile)	
v_δ	Galaxy-Halo velocity offset	$\mathrm{km\,s^{-1}}$
	Outflow	
v_t	Thermal/turbulent velocity	$\mathrm{km\,s^{-1}}$
ρ_1	Reference H I density (1 kpc)	$\mathrm{cm^{-3}}$
v_{out}	Outflow velocity (constant)	$\mathrm{km\,s^{-1}}$
θ_{out}	Half-opening angle	$^\circ$
θ_{in}	Inner half-opening angle	$^\circ$
S_{Nr}	Galaxy orientation	
	Disk	
v_t	Thermal/turbulent velocity	$\mathrm{km\,s^{-1}}$
ρ_0	Reference H I density (r=0)	$\mathrm{cm^{-3}}$
h_r	Disk-plane scale height	kpc
h_z	'Vertical' scale height	kpc
v_r	Infall velocity	$\mathrm{km\,s^{-1}}$
v_ϕ	Rotation velocity	$\mathrm{km\,s^{-1}}$
S_{Nr}	Galaxy orientation	
S_{Wr}	Direction of rotation	

Spherical Halos

We also model a spherical halo with a power-law density profile (index α), and allow a small velocity offset between the halo and galaxy (v_δ, allowing for actual peculiar velocity or the uncertainty on the redshift measurements). This requires absorbers at the same redshift with column densities that are larger in sightlines with smaller impact parameters.

Modelling process

We consider points at 10 pc intervals along the line-of-sight (shown as the D-coordinate in Figure 4.3), and apply the following process:

i) We convert the coordinates of these points from the observed (impact parameter, position angle and distance along LOS) into the relevant coordinates for

the proposed model around the galaxy using the inclination and position angle estimates from the HST image.

ii) Using the model parameters, we calculate the H I density and line-of-sight velocity component at each point. These values are applied to the entire 10-pc section centered at that point, from which we calculate the column density of that segment of the line-of-sight.

iii) We use the properties of the Lyα transition to calculate the optical thickness of each 10-pc column section from the column density. This is then convolved with a Gaussian of width v_t, and binned by line-of-sight velocity (using bins of 0.25 $\mathrm{km\,s^{-1}}$), producing model optical thickness as a function of velocity.

iv) For systems in which the proposed model consists of multiple components (e.g. a both a disk and an outflow), we calculate the optical thickness separately and then sum the models together.

v) Converting the optical thickness to transmission spectra and convolving with the relevant COS or FOS line-spread function produces our final model spectra.

Our model spectra can then be compared with the observations in all three lines-of-sight.

Ideally, an automated routine would be used to fit these synthetic spectra to the observations. A Monte-Carlo Markov Chain (MCMC) process could be used to explore the parameter space available, estimating the chi-squared surface and hence the best-fitting values and uncertainties on each parameter for each model type. The best fit to the data from each model type could then be compared to find the overall best fit.

Whilst an automated fitting routine for quantifying the goodness-of-fit between the model and observed spectra and tuning the model parameters to find the best fit for each model type would allow our results to be more reliably reproduced, creating such a routine presents several difficulties. Absorption features known to be due to transitions other than Lyα would need to be masked. However, identifying which absorption features are due to Lyα is itself uncertain, and will affect the fit.

This routine would need to account for blended features, where a physical model might only provide a good fit to a small number of pixels in the spectrum. The likelihood function used would need to allow for blends, probably by penalising model absorption that is weaker than observed to a lesser extent than model absorption that is stronger than that observed. Some form of weighting would also be needed to allow for the fact that absorbers with large velocity offsets and/or large impact parameters are more likely to be physically unconnected with the galaxy. Furthermore, models consisting of both disks and outflows would be difficult to constrain due to the much larger number of free parameters.

Tuning these weights in order to produce meaningful results would be arbitrary as well as time-consuming. For these reasons, we do not attempt an automated fit in this work, and instead vary the parameters manually until a reasonable fit is obtained.

For each galaxy we consider each model type and combination of orientations (S_{Nr} and S_{Wr}, defined above), producing seven possible models. In most cases the halo model can be ruled out, as it requires the closest sightlines to exhibit the strongest absorption, and all absorbers to have small and similar velocity offsets to the galaxy. Several combinations of orientation can also be ruled out from producing any identified absorption components because the direction of galaxy–absorber velocity offset produced by the model is opposite to that seen in the observed spectra. Additionally, the galaxy kinematics constrain the direction of rotation (S_{Wr}) if a velocity gradient is visible.

With the model types and orientations greatly limited, we then identify the model velocities required to reproduce the observed offset between galaxy and an absorber (this is strongly dependent on the galaxy inclination), and adjust the density parameter to provide an approximate fit to the absorber (the total model column density is then usually consistent with the catalogue value estimated by VPFIT). If it is clear that reproducing this absorber introduces inconsistency with absorption in the other lines-of-sight, then this model combination can also be discarded.

We then iteratively adjust the remaining parameters to improve the fit, matching the width of the absorber and ensuring that the model absorption in other sightlines

is consistent with the observations where possible (usually either by reducing it to a level not distinguishable from the noise, or by matching another absorber). The absorber width depends on both v_t and the combination of velocities and opening angle/scale height, so models can often be ruled out at this stage. In each iteration a single parameter is changed, with the size of each change reducing until it becomes difficult to judge whether the change is improving the fit (the level at which this occurs is generally determined by the noise levels in the observed spectra).

Note that we do not artificially limit the range of values any parameters can take at this stage, although velocities are limited by the 500 $\mathrm{km\,s^{-1}}$ cut.

This process leads to a small number of possible models that can reproduce each absorber, or rules out all of our toy models. As long as the orientations are compatible (e.g. a disk and outflow existing around the same galaxy must have the same S_{Nr}), these can then be combined to fit as many absorption components as possible.

For the reasons stated above, the best fit for each single model to an absorber is judged 'by-eye' rather than using a statistical measure. Where multiple differing combinations are possible, we list both in our results rather than choosing one based on a 'goodness-of-fit' statistic. In order to decide a preference in these cases, we use the model parameters and their consistency with the galaxy observations (e.g. rotation velocities similar to the galaxy rotation are preferred), as well as comparable disks and outflows in the literature. The reasons for any such preference are discussed in the relevant part of Section 4.4 or Appendix C.1.

4.4 Individual systems

Using the models described above, we can attempt to match the absorption observed in the multiple lines-of-sight around several galaxies. Whilst the models contain several free parameters, which will usually allow them to fit an individual component, the additional constraints from several sightlines enable us to determine the structures observed. Here we discuss some examples. We present galaxy and absorber properties, as well as illustrating the galaxy HST image, MUSE kinematics where

available, and the location of the lines-of-sight. We then compare the observed absorption with that produced by our toy models. Other galaxy-absorber systems are included in Appendix C.1, with the combination of results from our sub-sample discussed in Section 4.5. The tables show all galaxies within 1 Mpc of at least one line-of-sight and all absorbers within 500 $\mathrm{km\,s^{-1}}$ of the main galaxy considered.

4.4.1 Galaxy A-14

A-14 is a small galaxy with a mass $\sim 10^{8.5}\ M_{\odot}$ at redshift z $\approx$ 0.05, with details given in Table 4.3 and illustrated in Figure 4.4, yet with a low redshift that makes it the largest galaxy in the field on the sky. The galaxy shows a clear velocity gradient in [O III] emission[2], with strong absorption in sightline A at an impact parameter of $\approx$ 26 kpc. VPFIT has identified an additional weaker component blueward of the galaxy in LOS-A, and there may be a component in LOS-B that is blended with higher-order Lyman transitions from z $\approx$ 0.399, approximately 80 $\mathrm{km\,s^{-1}}$ redward of the galaxy (the $n = 17$ and $n = 16$ to $n = 1$ Lyman transitions are visible at ≈ 0 and ≈ 150 $\mathrm{km\,s^{-1}}$ from the systemic redshift of A-14). Note that the spectrum of LOS-C is blocked by a sub-DLA from redshift $\approx$ 0.56, so no absorption can be detected.

Our toy models can simultaneously fit the strong absorption feature in LOS-A and contribute to the unexplained component of absorption in LOS-B, using a single outflow. The position angles of the two sightlines necessitate a wide opening angle, as shown in the schematic in Figure 4.4. Both sightlines probe the edge of the conical outflow, so the geometry is not sensitive to the possibility of a hollow cone. An opening angle of $\approx 60°$ and an outflow velocity of ≈ 70 $\mathrm{km\,s^{-1}}$ are sufficient to produce the observed velocities and column densities of the two absorbers. Ideally we would consider the presence of metal lines for possible further evidence of warm, metal-enriched material. However, the low redshift of this galaxy means that our

[2]Because of a strong sky line in close proximity to Hα at this redshift, the fainter emission in the outer parts of the galaxy is vulnerable to being 'shifted' in wavelength by up to a few Å during the sky subtraction process (see Section 2 of Cantalupo et al., 2019). We therefore choose to present the [O III] emission from this galaxy, which is unaffected by sky lines.

COS data lack coverage of several metal lines, such as O VI, that might indicate outflows.

VPFIT finds that a weak, broad component at a very similar wavelength improves the fit on the wings of this strong absorption feature. Its width would suggest a hot component, but an outflow could not produce this width whilst also approximating the stronger component and a power-law halo would produce absorption in B that is not observed. A 'patchy' halo, or one with an extremely steep density profile, may be a plausible explanation. This could also be a detection of the warm-hot intergalactic medium (WHIM).

There is also a weak absorption component identified in LOS-A at 220 $\mathrm{km\,s^{-1}}$ blueward of the galaxy. This is only marginally above the uncertainty limit used to remove noise spikes masquerading as absorbers (described in T14). Although its velocity offset is in the same direction as the rotation of the galaxy ISM, it is far larger than both the detected rotation speed of the galaxy and its estimated virial velocity. We therefore consider it unlikely that this absorber originates from an extended gaseous disk around this galaxy, and its low column density and large velocity offset mean that it is doubtful whether this absorption is physically associated with this galaxy at all.

We can rule out a disk producing the strong absorption component in A, as this would generate absorption in B that is not consistent with the observations. Both sightlines probe the blueward portion of any model disk. If the rotating velocity component dominates, such a disk would produce absorption blueward of the galaxy, where it would be detectable. If the infall velocity dominates, the absorption in B could be 'hidden' under the blended system, but the velocity required is much larger than both the free-fall and virial velocities, so we deem this unlikely.

Of the toy models we consider, a bi-conical outflow is therefore the most likely explanation for the strong absorber seen around this galaxy in the spectrum of QSO-A, although a disk with low H I column density is not ruled out and may contribute to a weaker absorption feature.

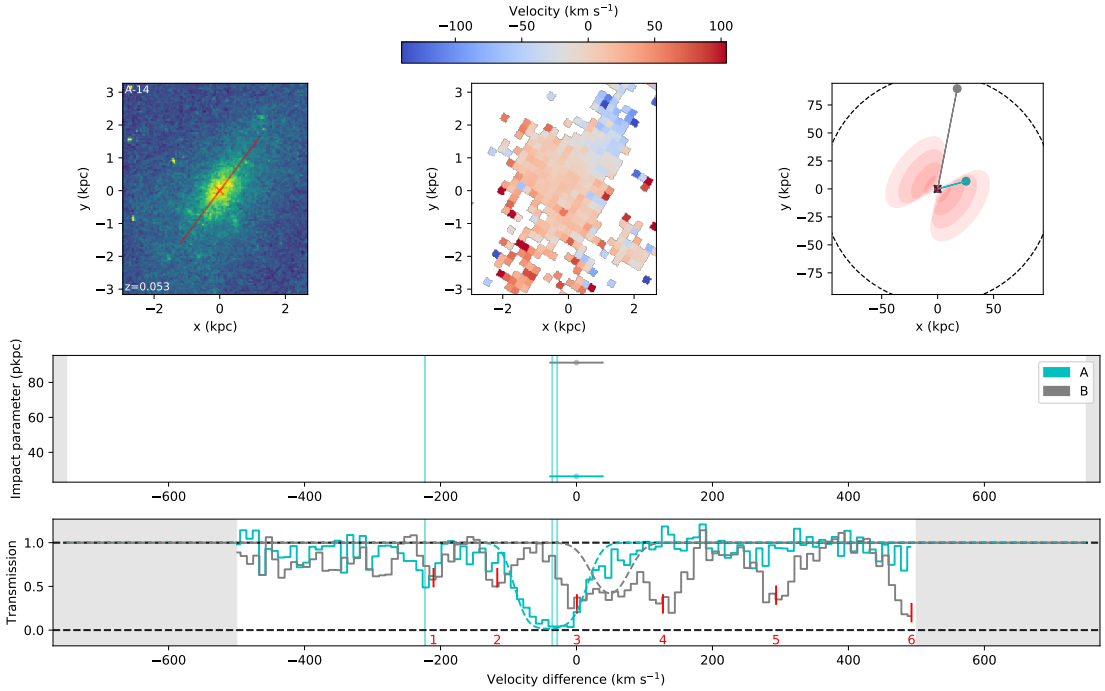

Figure 4.4: Details of the absorption and galaxy environment around MUSE galaxy A-14, using [O III] as observed in MUSE for the velocity map. Note that QSO-C (will be shown in orange throughout) is blocked by a sub-DLA at z ≈ 0.558, so is excluded from this figure. **Top-left**: HST white-light image of the galaxy. The overlaid red line shows the projected major axis as found by GALFIT. **Top-middle**: Line-of-sight velocity obtained from fitting to the [O III] emission line as observed in MUSE. **Top-right**: A wider view of the geometry of the system on the sky, showing the lines joining the centre of the galaxy to each QSO (A in cyan, B in grey, C in orange where present). The black dashed circle indicates the virial radius of the galaxy, whilst the putative outflow is shown by the red ellipses. Additional crosses (where present) show the locations of other galaxies at this redshift. **Central panel**: The location of galaxies around this redshift, indicated as a function of impact parameter from the QSO sight-lines and velocity difference from this galaxy (positive velocities showing galaxies redward of this primary galaxy). The bolded galaxy features in the upper panels, whilst any other galaxies are faded. The horizontal bars show the velocity error arising from the galaxy redshift measurement. Each galaxy appears multiple times, once for each QSO, coloured as in the upper panels. **Bottom panel**: The transmission of the three QSO spectra at the wavelength of Lyα at the redshift of this galaxy, using the continuum fits described in Section 2.1.1 to normalise the spectra. Dashed horizontal lines show full and zero transmission. Solid vertical lines passing through both panels show the locations of Lyα absorption as found using VPFIT. Dashed lines coloured as in the other panels show the predicted absorption profiles given the preferred toy model described in the text (in this case an outflow with a velocity of ≈ 70 km s^{-1} and half-opening angle of ≈ 60°). Additional absorption features intervening from other redshifts are labelled by red tick marks and numbered from blue to red. In this case all six are Lyman lines from the same redshift as the sub-DLA, with features labelled 1 to 6 resulting from the n=19 to n=14 transitions.

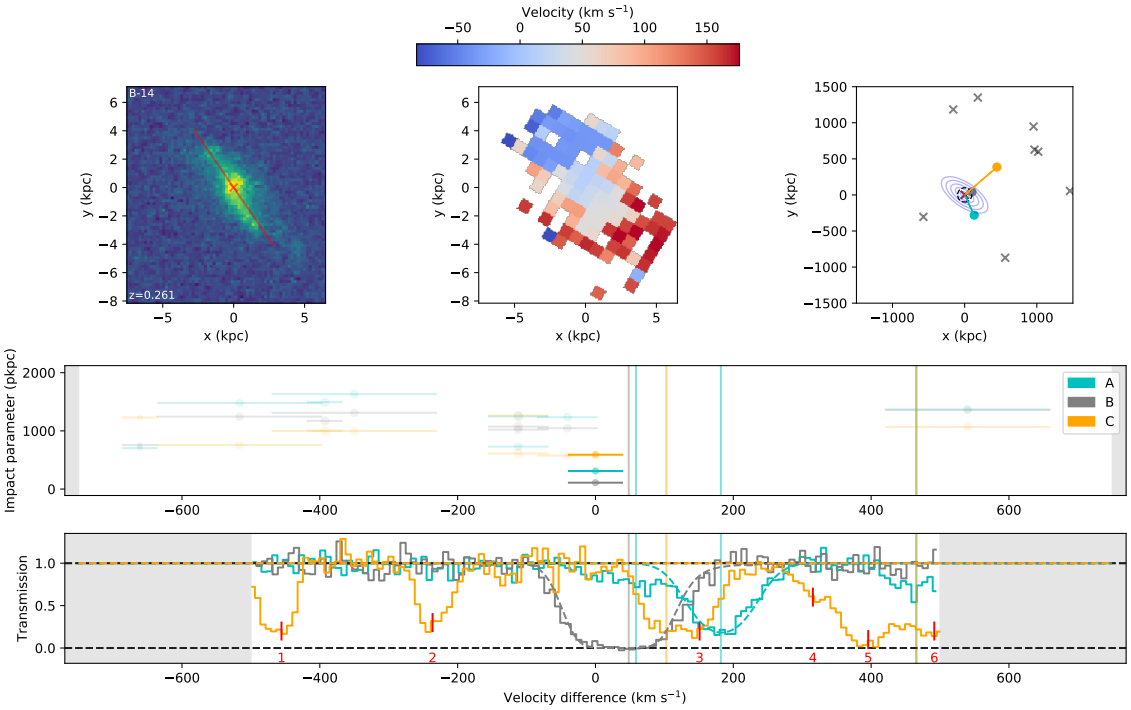

Figure 4.5: Details of the absorption and galaxy environment around MUSE galaxy B-14, a $\sim 0.05L_\star$ galaxy at z $\approx$ 0.26, using Hα as observed in MUSE. The layout is identical to that shown in Figure 4.4, with the model disk indicated by the blue ellipses. The model absorption is that produced by a disk with 270 km s^{-1} rotation velocity and 40 km s^{-1} infall velocity. Additional absorption features labelled are all identified as molecular H2 lines from the sub-DLA at z $\approx$ 0.558.

Table 4.3: Summary of galaxies and absorbers at z $\sim$ 0.053. Column descriptions: (1) Galaxy ID; (2) galaxy redshift; (3) galaxy luminosity as a multiple of $L_\star$; (4) galaxy inclination measured using GALFIT; (5) absorber line-of-sight; (6) impact parameter of absorber around galaxy; (7) azimuthal angle between absorber and galaxy major axis; (8) absorber column density; (9) absorber Doppler width; (10) velocity offset between galaxy and absorber (positive values denote absorbers 'redward' of the galaxy); (11) any detected transitions at this redshift other than neutral hydrogen.

Galaxy (1)	z (2)	Lum ($L_\star$) (3)	Inc (4)	LOS (5)	Imp (kpc) (6)	Azimuth (7)	log(N H I) (8)	b ($\mathrm{km\,s^{-1}}$) (9)	Δv ($\mathrm{km\,s^{-1}}$) (10)	Other ions (11)
A-14	0.053	0.02	62° ± 1°	A	26	38° ± 1°	13.67 ± 0.29	103 ± 50	-30 ± 60	
				A	26	38° ± 1°	14.36 ± 0.09	36 ± 7	-40 ± 60	
				A	26	38° ± 1°	13.31 ± 0.09	15 ± 6	-220 ± 60	
				B	91	29° ± 1°	(None, limit $\approx$ 12.9)			

Table 4.4: Summary of galaxy–absorber group at z $\sim$ 0.261. Additional galaxies and metal absorbers have velocities shown relative to the first galaxy (B-14). Column descriptions are given in Table 4.3.

Galaxy	z	Lum ($L_\star$)	Inc	LOS	Imp (kpc)	Azimuth	log(N H I)	b ($\mathrm{km\,s^{-1}}$)	Δv ($\mathrm{km\,s^{-1}}$)	Other ions
B-14	0.261	0.05	64° ± 8°	A	310	11° ± 13°	13.39 ± 0.05	44 ± 7	460 ± 60	
				A	310	11° ± 13°	14.15 ± 0.03	39 ± 2	180 ± 60	
				A	310	11° ± 13°	13.42 ± 0.09	67 ± 18	60 ± 60	
				B	110	76° ± 13°	14.82 ± 0.02	71 ± 4	50 ± 60	C III (0), O VI (+50)
				C	590	85° ± 13°	13.85 ± 0.04	42 ± 6	470 ± 60	
				C	590	85° ± 13°	13.97 ± 0.03	34 ± 3	100 ± 60	
(26595)		0.2		A	730				(-110)	
				B	1022					
				C	1262					
(36043)		0.2		A	1235				(-40)	
				B	1046					
				C	575					
(36413)		0.8		A	1249				(-110)	
				B	1074					
				C	611					

4.4.2 Galaxy B-14

B-14 is also a low-luminosity galaxy ($\sim 0.05L_\star$), although at a higher redshift of z $\approx$ 0.26, inclined at $\approx 60°$, illustrated in Figure 4.5 and with details given in Table 4.4. Absorption is visible in all three sightlines, seen in the lower panel. The strongest component appears in LOS-B (column density $10^{14.8}$ cm^{-2}), at an impact parameter of $\sim$ 100 kpc along the minor axis, with a velocity $\sim$ 50 km s^{-1} with respect to the galaxy. LOS-B exhibits O VI at the same velocity as this H I, as well as weak C III close to the galaxy redshift. The strongest H I component in LOS-A is 180 km s^{-1} redshifted relative to the galaxy ($10^{14.2}$ cm^{-2}), although there appears to be a much weaker component ($10^{13.4}$ cm^{-2}) with a smaller velocity offset. This lies $\sim$ 300 kpc away from the galaxy, and close to the major axis. No metals are detected in LOS-A, but the lower H I column density than in LOS-B means that the O VI to H I ratio of the gas in A could still be similar to that in B. The absorption in sightline C has column density $10^{14.0}$ cm^{-2}, 100 km s^{-1} and 600 kpc away along the minor axis. Several other features in LOS-C are visible, but these are transitions from molecular hydrogen in the sub-DLA at z $\approx$ 0.56.

The H I probed by LOS-A lies near the projected major axis, with a velocity offset in the same direction as the galaxy ISM emission, suggestive of co-rotating material. At first glance the absorption in B could be an outflow, with a higher Doppler parameter and O VI detection possibly indicating heated material along the minor axis. However, our toy models cannot reproduce the breadth and offset of the observed absorption without producing additional absorption in LOS-A or C that would be inconsistent with the observations. A disk model with both rotating and accreting velocity components can approximately reproduce the strongest absorption components in both the A and B sightlines. The model shown in the lower panel of Figure 4.5 uses velocities of 270 and 40 km s^{-1} respectively for these components. Although this absorber is broad (width $\approx$ 70 km s^{-1}), this is produced in our model with very little thermal/turbulent velocity, as the range of velocities probed as the line of sight passes through our model disk is sufficient. The required rotation velocity of $\approx$ 270 km s^{-1} is substantially larger than both the observed galaxy rotation and the galaxy virial velocity (both $\lesssim$ 100 km s^{-1}), so such rotation

and accretion is difficult to physically motivate.

This model also leaves the absorption in C and the weaker component in A unexplained. The absorption in C has other galaxies at a similar distance (faded orange points in the central panel), some of which are substantially larger than B-14, so may not be associated with this galaxy. An outflow model with narrow opening angle $\lesssim 20°$ could also explain this absorption in C without intersecting LOS-A or B, requiring an outflow velocity close to 150 $\mathrm{km\,s^{-1}}$. The weak component at +60 $\mathrm{km\,s^{-1}}$ in LOS-A is more likely to be associated with B-14, but still lies well beyond the virial radius. Any outflow wide enough to reach this line-of-sight would produce additional absorption in B, and is therefore ruled out. This absorption is broad, with a Doppler width ≈ 70 $\mathrm{km\,s^{-1}}$, so may be probing the WHIM at temperatures $\approx 10^5$ K.

None of our toy models can reproduce all absorption components identified as Lyα within 500 $\mathrm{km\,s^{-1}}$ of this galaxy. The disk model shown is the only model found to approximately match two of the four absorbers seen within 300 $\mathrm{km\,s^{-1}}$ of the galaxy, and is compatible with the addition of a narrow ouflow from LOS-C that would fit a third component of absorption.

An alternative model that can reproduce the strongest component in B is an outflow with $v_{out} \approx 100$ $\mathrm{km\,s^{-1}}$ and $\theta_{out} \approx 45°$. Such an outflow would produce additional absorption in C that is not observed. This better fits the expected parameter ranges than the rapidly-rotating disk, as well as the metal content of absorption in B, but does not replicate either absorber seen in LOS-A and does not match that in C, so can only fit a single component.

Given the inconsistency between a strong outflow and the observations in LOS-C, we primarily consider the disk model in our later discussion.

4.4.3 Galaxy 31658

31658 is a 0.4 $L_\star$ star-forming galaxy at z $\approx$ 0.728, detailed in Table 4.5 and Figure 4.6. This is slightly beyond the redshift of QSO-C, so no absorption can be detected in this sightline. Lyα absorption is visible in both of the remaining lines-of-sight, which at this redshift lies in the lower-resolution FOS spectra. The equivalent Lyβ

absorption does appear in COS, but this is blended with absorption features from multiple other redshifts, strongly affecting QSO-B. In A, the Lyβ absorption is clearly made up of two components, as identified by VPFIT, but its low signal-to-noise makes it difficult to fit. As the Lyα absorption has higher signal-to-noise and does not appear to be affected by blending with absorption from other redshifts, we prefer to model the absorption in Lyα.

The position angles of absorption in both A and B are near the minor axis, but the similar azimuthal angles would probe the same cone of any outflow, so this cannot reproduce the velocity difference between the absorption in the two sightlines.

They would probe a putative disk at different azimuthal angles. A disk with a very large rotation velocity (>500 $\mathrm{km\,s^{-1}}$) and comparatively small infall component (<30 $\mathrm{km\,s^{-1}}$) would be required to reproduce the velocity difference between the absorbers, and still leaves one of the absorption components in A without explanation. It would also have to be extremely thin in order to produce strong absorption at A, with a larger impact parameter and nearer to the major axis. This is the model shown in Figure 4.6. As the lines-of-sight would intersect such a disk at locations over 1 Mpc ($\approx 5r_{vir}$) from the galaxy, and the disk would have to be extremely thin and fast, it is unlikely to represent a physical structure in the IGM near this galaxy.

We therefore cannot produce a plausible model for the absorption around this galaxy using our simple disk and outflow models. Other possibilities include IGM absorption unassociated with a galaxy, and material associated with a galaxy that is fainter than the limit of our redshift survey.

All three absorbers have relatively large column densities for the IGM, above 10^{14} $\mathrm{cm^{-2}}$. Our Paper 1 results suggest that the probability of finding a pair of such absorbers within 500 $\mathrm{km\,s^{-1}}$ of a particular galaxy is $\approx 2\%$, and therefore that these absorbers are likely associated with a galaxy.

Outside the MUSE fields, our detection limit at this redshift is $\approx 0.1\ L_\star$, whilst inside the MUSE fields detections are limited to a luminosity $\approx 0.06\ L_\star$ or a star-formation rate of $\approx 0.1\ \mathrm{M_\odot\ yr^{-1}}$. This allows for an undetected galaxy (or multiple galaxies) that could be producing some of these absorption components. Given the fairly high column densities at large impact parameters, this could plausibly explain

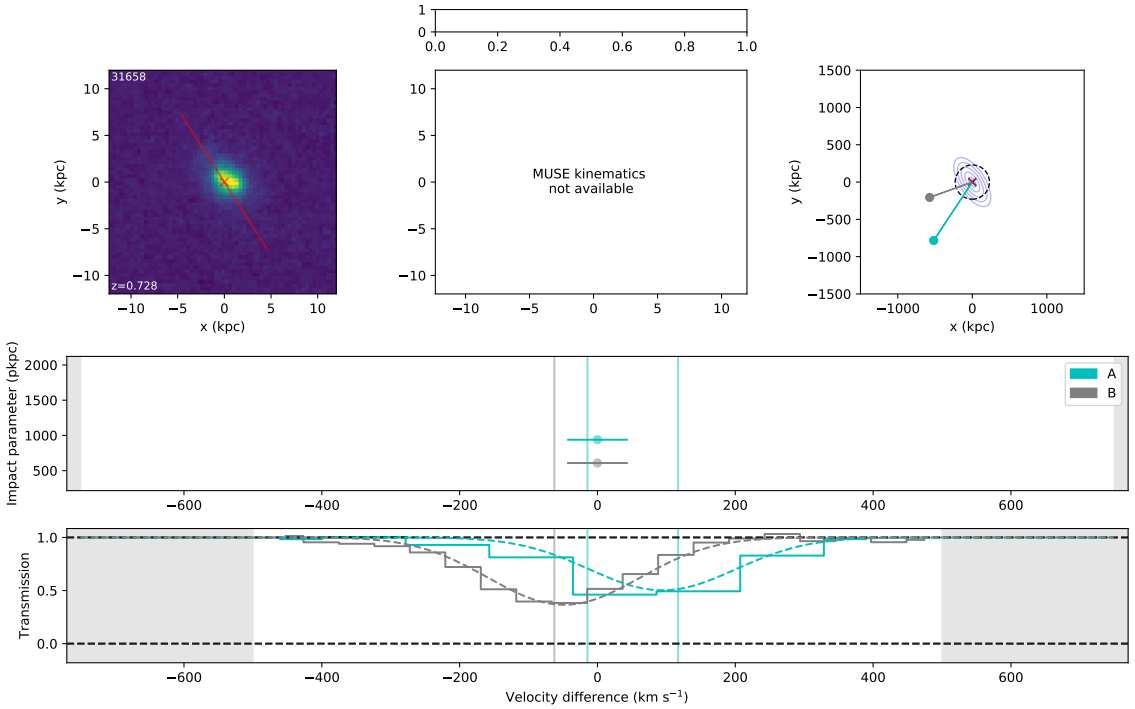

Figure 4.6: Details of the absorption and galaxy environment around galaxy 31658, a $\sim 0.4L_\star$ galaxy at z $\sim$ 0.73. The layout is identical to that shown in Figure 4.4, and the model shown in the lower panel is disk with rotation velocity ~ 550 km s^{-1}.

at least some of the absorption in the A and B sightlines.

The combination of similar column densities, similar azimuthal angles, and a notable velocity offset, leads to the conclusion that simple disk, halo and outflow models are not likely explanations for the absorption around this galaxy.

4.5 Discussion

In addition to the three example galaxies discussed above, a further nine isolated galaxies are described in Appendix C.1. More details on the models used are given in Appendix B.3. The best models found to fit each galaxy are summarized in Table 4.6.

We now discuss the results from our best-fitting models with regards to other studies using observational data and hydrodynamical simulations.

Table 4.5: Summary of galaxy–absorber group at z $\sim$ 0.728. Any additional galaxies and metal absorbers have velocities shown relative to the first galaxy (31658). Note that this galaxy is beyond the redshift of QSO-C, so no absorption could be detected. Column descriptions are given in Table 4.3.

Galaxy	z	Lum ($L_\star$)	Inc	LOS	Imp (kpc)	Azimuth	log(N H I)	b ($\mathrm{km\,s^{-1}}$)	Δv ($\mathrm{km\,s^{-1}}$)	Other ions
31658	0.728	0.40	63° ± 4°	A	939	66° ± 6°	14.20 ± 0.10	23 ± 4	-10 ± 40	
				A	939	66° ± 6°	14.14 ± 0.10	36 ± 7	120 ± 40	
				B	608	77° ± 6°	14.23 ± 0.01	134 ± 4	-60 ± 40	

Table 4.6: Summary of isolated galaxies and the best-fitting toy models.

Galaxy	z	Figure	Table	Text	Best model(s)
A-14	0.053	4.4	4.3	4.4.1	(2/3 absorbers) Outflow, θ=60°, v=70 $\mathrm{km\,s^{-1}}$, extent > 95 kpc
					(Good fit, remaining component is weak with a large velocity offset)
26732	0.087	C.1	C.1	C.1.1	(1/1 absorbers) Disk, height ratio ≈40, v_ϕ= 550 $\mathrm{km\,s^{-1}}$, v_r= 120 $\mathrm{km\,s^{-1}}$, extent > 100 kpc
					OR Outflow, θ=50°, v=440 $\mathrm{km\,s^{-1}}$, extent > 100 kpc
					(Only absorption component is weak with a large velocity offset)
25833	0.123	C.2	C.2	C.1.2	(1/2 absorbers) Disk, height ratio ≈100, v_ϕ= 700 $\mathrm{km\,s^{-1}}$, v_r= 20 $\mathrm{km\,s^{-1}}$, extent > 230 kpc
					(Both absorption components have ∼500 $\mathrm{km\,s^{-1}}$ velocity offset)
A-62	0.178	C.3	C.3	C.1.3	(2/2 absorbers) Outflow, θ=20°, v=150 $\mathrm{km\,s^{-1}}$, extent 70-260 kpc
					(could have larger extent if constant rate/velocity assumptions relaxed)
A-65	0.220	C.4	C.4	C.1.4	(2/2 absorbers) Outflow, θ=30°, v=120 $\mathrm{km\,s^{-1}}$, extent > 260 kpc
					AND Disk, height ratio ≈40, v_ϕ= 220 $\mathrm{km\,s^{-1}}$, v_r= 50 $\mathrm{km\,s^{-1}}$, extent > 90 kpc
B-14	0.261	4.5	4.4	4.4.2	(2/4 absorbers) Disk, height ratio ≈10, v_ϕ= 270 $\mathrm{km\,s^{-1}}$, v_r= 40 $\mathrm{km\,s^{-1}}$, extent > 330 kpc
					(adjusting disk scale heights and adding spherical halo may help produce 3rd absorber)
A-63	0.488	C.5	C.5	C.1.5	(1/3 absorbers) Outflow, θ=20°, v=650 $\mathrm{km\,s^{-1}}$, extent > 350 kpc
					(no good fit for this galaxy)
30169	0.584	C.6	C.6	C.1.6	(no good fit for this galaxy)
31658	0.728	4.6	4.5	4.4.3	(2/3 absorbers) Disk, height ratio ≈300, v_ϕ= 550 $\mathrm{km\,s^{-1}}$, v_r= 20 $\mathrm{km\,s^{-1}}$, extent > 1 Mpc
A-23	0.843	C.7	C.7	C.1.7	(1/1 absorbers) Disk, height ratio ≈300, v_ϕ= 350 $\mathrm{km\,s^{-1}}$, v_r= 30 $\mathrm{km\,s^{-1}}$, extent > 240 kpc
					(possible weak component also fit if extent > 550 kpc)
A-30	0.850	C.8	C.8	C.1.8	(1/2 absorbers) Outflow, θ=45°, v=250 $\mathrm{km\,s^{-1}}$, extent > 650 kpc
					AND Disk, height ratio ≈40, v_ϕ= 350-450 $\mathrm{km\,s^{-1}}$, v_r= 20-120 $\mathrm{km\,s^{-1}}$, extent > 40 kpc
					(disk explains possible unidentified weak component)
					(remaining absorber is weak with a large velocity offset)
A-64	0.926	C.9	C.9	C.1.9	(1/2 absorbers) Disk, height ratio ≈30, v_ϕ= 150-350 $\mathrm{km\,s^{-1}}$, v_r= 0-200 $\mathrm{km\,s^{-1}}$, extent > 180 kpc

Table 4.7: Model outflow properties around galaxies for which outflows can reproduce some of the observed absorption components. Column descriptions: (1)-(5) are from Table 4.1; (6) specific star-formation rate; (7) maximum extent at which absorption is detected (at the point of highest H I density along the sightline with the largest impact parameter); (8) galaxy virial radius; (9) model half-opening angle; (10) model outflow velocity; (11) escape velocity from the location of the sightline at the maximum observed extent. Note that, as discussed in the text, the constant flow rate assumption could be relaxed slightly and allow for the outflow around A-62 to reach 260 kpc in extent.

Galaxy	z	$M_\star$	M_h	SFR	sSFR	Extent	r_{vir}	θ_{out}	v_{out}	v_{esc}
		$\log_{10}(M_\odot)$	$\log_{10}(M_\odot)$	$(M_\odot/yr)$	Gyr^{-1}	(kpc)	(kpc)	(°)	$(km\,s^{-1})$	$(km\,s^{-1})$
(1)	(2)	(3)	(4)	(5)	(6)	(7)	(8)	(9)	(10)	(11)
A-14	0.053	8.7 ± 0.2	10.9 ± 0.3	$0.018^{+0.009}_{-0.006}$	$0.038^{+0.025}_{-0.015}$	95	90 ± 20	60	70	80 ± 20
A-62	0.178	8.7 ± 0.2	11.0 ± 0.3	$0.23^{+0.16}_{-0.09}$	$0.45^{+0.39}_{-0.21}$	70	90 ± 30	20	150	100 ± 30
A-65	0.220	7.6 ± 0.7	10.5 ± 0.7	$0.012^{+0.005}_{-0.003}$	$0.32^{+0.45}_{-0.30}$	260	70 ± 40	30	120	40 ± 20
A-30	0.850	10.7 ± 0.3	12.5 ± 0.7	$0.25^{+0.14}_{-0.09}$	$0.005^{+0.02}_{-0.004}$	650	290 ± 140	45	250	280 ± 140

4.5.1 Outflows

Our toy model outflows can reproduce at least some of the absorption in 4 galaxies from our sample of 12, which are listed in Table 4.7. These include three small, star-forming galaxies, with outflows requiring a range of half-opening angles 20-60°, velocities of 70-150 $\mathrm{km\,s^{-1}}$, and extents of $\lesssim$ 250 kpc. A-30 is a more massive, quiescent galaxy, which requires a much faster outflow with a much greater extent ($\sim$ 220 $\mathrm{km\,s^{-1}}$ and $>$ 600 kpc). The $\approx$ 2.5 Gyr required for the gas to travel this distance is sufficiently long that the galaxy's apparent quiescence on short timescales (based on lack of emission lines) does not rule out a stellar-feedback-driven outflow.

The extent of these outflows is comparable to the results from Paper 1, in which we showed a bimodality in the azimuthal angles of detected absorbers relative to galaxies extended to $\approx$ 300 kpc, and found evidence linking the major- and minor-axis absorbers with accretion and outflows. With one of the four putative outflows discussed here extending to approximately this distance, and another continuing substantially beyond that, the small sample from this work supports our conclusions from Paper 1.

Our outflow models are similar to those used in the MEGAFLOW survey (Schroetter et al., 2019), so we can compare our results directly. Both models allow for a hollow cone, but this is not necessary for any of the four galaxies for which outflows can match the observations. We also consider a constant velocity and r^{-2} density profile. However, their galaxy observations consist of a single MUSE field around each line-of-sight, limiting their impact parameters to generally $\lesssim$ 150 kpc, so we cannot judge the extent of their model outflows.

We use the same equation as in Veilleux et al. (2005) (their Section 4.6 and Equation 4 from Schroetter et al. 2019) to estimate the escape velocities of outflows from our galaxies. Of these four galaxies, the two with the higher sSFRs have outflows exceeding escape velocity (A-62 and A-65 have v_{out}/v_{esc} of $\approx$ 1.5 and 3 respectively), whilst those with lower sSFR do not (A-14 and A-30 have v_{out}/v_{esc} of 0.9 and 0.8). This is also consistent with outflows escaping more frequently from lower-mass galaxies, as suggested by Schroetter et al. (2019). However, uncertainties on the model parameters are difficult to estimate, and those on the escape velocity are

sufficiently large that these comparisons between the outflow and escape velocities are uncertain.

The model outflows from Schroetter et al. (2019) are also generally narrower than ours, with most half-opening angles $\approx 30°$ or smaller. The opening angles from our models are constrained by the need to intersect or avoid intersecting each of the three lines-of-sight, so the narrower outflows they propose could not fit our observations of A-14 or A-30. We also note that three of our galaxies have lower masses than most included in the MEGAFLOW survey, which could be contributing to the wider outflows, as outflow collimation is expected to be a 'path of least resistance' effect (e.g. Tomisaka & Ikeuchi, 1988; Nelson et al., 2019). Their geometric selection of likely outflows may also exclude outflows with wide opening angles.

There is disagreement between some of the largest numerical simulations on the extent of outflows, so our model results could in principle help to discriminate between the various feedback prescriptions included in these simulations. Although the strength of any conclusions drawn here is limited by a small sample, as well as model constraints motivated partially by simulations, it can still be useful to compare our models with outflows from simulations including EAGLE, Illustris and FIRE.

Hopkins et al. (2021) find that the addition of cosmic rays to the FIRE-2 simulations allows some outflows from $\sim L_\star$ galaxies to reach Mpc scales. The most massive galaxy that we find exhibiting a possible outflow does appear to reach at least 650 kpc, but the other three have much lower masses for which cosmic rays do not make a substantial difference (due to the relative reduction in cosmic-ray pressure). Three additional galaxies in our sample with $M_\star > 10^{10}$ $M_\odot$ do not produce absorption that is consistent with our model outflows, although the lines-of-sight do not probe their halos near the projected minor axis. Such a small sample size means that we cannot determine whether large-scale outflows are common around such galaxies, and therefore whether cosmic rays are important to consider in discussions of the IGM.

Mitchell et al. (2020a) and Nelson et al. (2019) discuss outflows in EAGLE and TNG50 respectively. As expected, these works find that differences in the feedback

prescriptions lead to different outflow characteristics. Mass flow rates in EAGLE remain approximately constant through concentric shells up to the virial radius of small galaxies, as is coded into our models, whilst mass flow rate drops in TNG50. We therefore cannot use the detection of outflows at large impact parameters to favour EAGLE over TNG50. However, two of our proposed outflows could produce an improved fit if the flow rate (and velocity) were allowed to decrease with radius. This would favour the TNG model, but small sample size means that we cannot claim strong evidence of such a reduction in flow rate or velocity. Neither study considers outflows much beyond the virial radius in any detail, although Mitchell et al. (2020b) note that outflows from low-mass halos must extend past the virial radius in order to explain metal enrichment in the IGM (e.g. Aguirre et al., 2001; Booth et al., 2012).

Both of these works include estimates of outflow velocity with galaxy mass in the inner CGM, generally producing outflows with velocities between 50 and 150 $\mathrm{km\,s^{-1}}$ for a wide range of halo masses, despite measuring outflows at different redshifts using different methods, although TNG50 outflows show a clearer increase in outflow velocity with halo mass. Our model outflow velocities are not significantly different from the predictions of these simulations, despite much larger impact parameters.

Opening angles are also discussed in both simulation papers, but they use different measures that make it difficult to compare directly. Our small number of outflows have a wide range of opening angles, so it is not surprising that the measures adopted by Mitchell et al. (2020a) and Nelson et al. (2019) both produce estimates within this range ($\approx 50^\circ$ and $\approx 25^\circ$ respectively).

The parameters of our proposed outflows are therefore mostly compatible with the models from MEGAFLOW, as well as the EAGLE and FIRE simulations, with slightly more disagreement between our models and TNG50 (possibly related to their measurements being taken at higher redshifts).

4.5.2 Disks

Our toy model disks can also reproduce some of the absorption around five of our galaxies, namely A-65, B-14, 31658, A-23 and A-64. The required parameters of

these disks are given in Table 4.8. The direction of rotation matches the stellar kinematics from MUSE for B-14 and A-64, whilst the MUSE data for A-23 does not exhibit a clear velocity gradient and no emission line fit was possible for A-65. Only the disk around B-14 is able to approximate multiple absorption components from the observations, whilst that around A-65 requires both an outflow and a disk in order to reproduce the data. The large extent and required velocity means that the absorption around galaxy 31658 is unlikely to represent a disk-like structure, so is not discussed further.

Our model disks are again similar to those used in MEGAFLOW, although tracing smaller column densities at larger impact parameters. In principle, the need to match absorption in the other lines-of-sight imposes constraints on the circular and infall components. The ratio of scale heights parallel and perpendicular to the disk are also constrained by the ratio of column densities at multiple azimuthal angles, or the need for absorption to remain weaker than our detection limit at certain azimuthal angles. The two scale heights and both components of velocity can therefore be treated as separate parameters that can be varied independently.

Unfortunately, most of the specific galaxies for which a model disk is compatible with the observations make only limited use of these constraints, as broad absorption in the other lines-of-sight can easily mask any absorption originating from our model disk, but cannot be fit by the disk (this applies to galaxies A-64, A-65 and 31658). The additional lines-of-sight therefore do not provide strong constraints on the disk parameters. B-14 is the only galaxy for which the absorption in multiple sightlines allows the rotating and infalling components to be determined separately.

We must therefore make assumptions on one component in order to determine the other. Purely circular orbits are not expected, especially at these large radii, and would require circular velocities larger than the virial velocity for all three model disks that are not well-constrained by multiple sightlines. Assuming free-fall for accreting material at large radii is incompatible with the constraints on A-23, and would still require velocities larger than virial for A-65.

Zabl et al. (2019) assume a value for $v_{in} = 0.6\ v_{vir}$, motivated by results from Goerdt & Ceverino (2015). This is comparable to the best-fit infall velocity for

Table 4.8: Model disk properties around galaxies for which disks can reproduce some of the observed absorption components. We include both velocity components under several assumptions of infall velocity. Where v_ϕ is left blank, this combination is not consistent with the observed absorption. Column descriptions: (1)-(4) are from Table 4.1; (5) model scale height ratio (i.e. relative disk thickness); (6) maximum observed disk extent (the 3-d distance from galaxy to the point on the line-of-sight where it intersects the disk plane, for the sightline with largest impact parameter with detected absorption); (7) virial radius; (8) virial velocity; (9) model circular velocity if infall assumed to be zero; (10), (12) model circular velocities if infall assumed to be 0.6 v_{vir} and the free-fall velocity at the maximum observed extent respectively; (11), (13) assumed infall velocities of 0.6 v_{vir} and the free-fall velocity at the maximum observed extent.

								$v_r = 0$	$v_r = 0.6\ v_{vir}$		$v_r = v_f$	
Galaxy	z	$M_\star$ $\log_{10}(M_\odot)$	M_h $\log_{10}(M_\odot)$	h_r/h_z	Extent (kpc)	r_{vir} (kpc)	v_{vir} ($km\,s^{-1}$)	v_ϕ ($km\,s^{-1}$)	v_ϕ ($km\,s^{-1}$)	v_r ($km\,s^{-1}$)	v_ϕ ($km\,s^{-1}$)	v_r ($km\,s^{-1}$)
(1)	(2)	(3)	(4)	(5)	(6)	(7)	(8)	(9)	(10)	(11)	(12)	(13)
A-65	0.220	7.6 ± 0.7	10.5 ± 0.7	40	90	70 ± 40	50 ± 30	400	360	30	360	35
B-14	0.261	8.5 ± 0.2	10.9 ± 0.3	10	330	90 ± 20	70 ± 20	-	270	41	270	47
31658	0.728	10.6 ± 0.2	12.4 ± 0.6	300	1070	220 ± 150	230 ± 150	530	-	137	-	200
A-23	0.843	10.7 ± 0.3	12.5 ± 0.7	300	240	230 ± 150	250 ± 160	300	270	151	-	330
A-64	0.926	10.4 ± 0.5	12.1 ± 0.8	30	180	160 ± 100	190 ± 120	340	160	113	20	280

B-14, and requires circular velocities comparable to v_{vir} for A-23 and A-64. This is preferred by our model fits, despite requiring a circular velocity of $\approx 7\ v_{vir}$ for A-65.

For the larger, higher-redshift halos A-23 and A-64, model disks with these assumed infall velocities and circular velocities $\lesssim v_{vir}$ can produce absorption that is consistent with the observations. For all assumed infall velocities onto A-65, and in order to fit the two strong absorption components around B-14, our model disks would require circular velocities $> 2\ v_{vir}$. Such a large velocity is not likely to physically represent a disk-like structure, and suggest that the gas may instead be associated with a different galaxy.

Several previous works have used disk-like models to study the rotating component of the CGM. Ho & Martin (2019) use the shape of galaxy spiral arms for a small sample of sightlines probing the inner CGM of low-z galaxies, in order to constrain the direction of the galaxy inclination, and therefore the line-of-sight component of any infall velocity. They find maximum infall velocities of 30-40 $\mathrm{km\,s^{-1}}$ for two of their five galaxy-quasar pairs, and ruling out infall for another pair. Steidel et al. (2002) also find that Mg II absorption kinematics in the inner CGM are likely dominated by rotation. Simple toy models underpredicted the co-rotation fractions seen in Lyα by French & Wakker (2020), but they used a tighter definition of co-rotation than our work by fitting a rotation curve to the galaxy spectrum. The rotating velocity component is substantially larger than the infall component for both of our galaxies with model disks probed at distances $\lesssim r_{vir}$, consistent with these previous results.

Rotating structures in the CGM are generally aligned with the central galaxy in most simulations, and this is supported by observations including our Paper 1. DeFelippis et al. (2020) find a 'wedge' of cool gas with angular momentum well-aligned with that of the galaxy, that extends to $\approx 1/2$ of the virial radius for small to medium-sized halos in Illustris. Both EAGLE (Huscher et al., 2021) and FIRE-2 (Hafen et al., 2022) find that cool gas is rotationally supported around $L_\star$ galaxies only on small scales (≈ 40 kpc). The results from our more massive halos are at much larger impact parameters than this, and require a substantial infalling component if they are bound within the halo, so are not rotationally supported. Probes with

smaller impact parameters (e.g. Tejos et al., 2021b, although they find primarily pressure support) would be needed to detect the rotational support expected in the inner CGM.

Ho et al. (2020) discuss the rotation of Mg II structures in EAGLE, finding that a thick rotating structure is typical. Whilst the ratio of scale heights in our models is constrained by the column densities seen in multiple lines-of-sight, the scale heights themselves are partially degenerate with the central density, so are not well-determined. The vertical scale heights of 5-20 kpc seen in Ho et al. (2020) and Steidel et al. (2002) can provide a reasonable fit for all four of our putative disks, but markedly different scale heights are also possible.

We only find two galaxies for which a rotating and/or accreting disk-like structure (with velocities $\lesssim v_{vir}$) can reproduce the observations, which therefore do not provide any substantial evidence for the extent or thickness of H I disks in the CGM.

4.5.3 Unattributed absorbers

There are also two galaxies around which all absorbing components have a large velocity offset (> 300 km s^{-1}), and a further two for which our disk/outflow models cannot reproduce any of the absorbing components. In both cases for which all absorption is at a large velocity offset, only the A and B sightlines are available, and neither pass within the virial radius. 26732 is the lowest-mass galaxy in the sample, whilst 25833 likely has the lowest sSFR (our given SFR estimate being an upper limit). It is therefore unsurprising that little absorption can be seen outside the virial radius of these galaxies.

The two galaxies for which our toy models could not reasonably match any of the absorption are A-63 and 30169. These both lie in the redshift range for which all three sightlines are usable, and are close to edge-on and face-on respectively. For A-63, all three sightlines are close to the minor axis, so a disk is required to be extremely large with very high infall velocity in order to produce substantial line-of-sight velocities. Due to the high inclination, an outflow would also need a large velocity (≈ 750 km s^{-1}) to match the absorption. For 30169, all three sightlines probe similar impact parameters, but have much larger differences in observed

column density and velocity, which our models cannot reproduce.

As we note in Section 4.3, the reality of the gas flows is likely far more complex than our toy models can capture. However, for both of these galaxies it seems unlikely that over-simplification of our toy models is the cause of their failure to match observations. For example, it is difficult to conceive of a plausible outflow model in which lines-of-sight in opposite directions near the minor axis produce the similar velocity offsets seen near A-63.

Whilst both appear isolated, the detection limits allow for the presence of an unseen companion galaxy ($\lesssim 0.06\ L_\star$ or $\lesssim 0.1\ \mathrm{M}_\odot\ \mathrm{yr}^{-1}$ SFR at 30169, $\lesssim 0.03\ L_\star$ or $\lesssim 0.05\ \mathrm{M}_\odot\ \mathrm{yr}^{-1}$ SFR at A-63). A companion to the east of 30169 could plausibly explain the absorption in both A and B, with a larger impact parameter to C matching the lack of observed absorption. An unseen companion would also seem to be a likely cause for the absorption in QSO-C at the redshift of A-63, as the impact parameter to A-63 is more than 1 Mpc.

Tidal interactions between galaxies can more easily affect the outer regions of the CGM, so the lack of any visible distortion in the stars or the ISM kinematics does not rule out such interactions distorting the CGM and leading to the observations that cannot be fit by our models (e.g. Fossati et al., 2019a; Dutta et al., 2020).

4.5.4 Reliability of attributing absorbers

As we describe when discussing each galaxy (Section 4.4 and Appendix C.1), for most galaxies we can rule out at least some of our toy models through the relative column densities and velocities of absorption components, and thereby constrain the origins of the absorbing material. To summarize, for four of our twelve galaxies we can rule out a disk or an outflow from producing the strongest absorber because such a model would be incompatible with the other lines-of-sight. For a further four galaxies, the additional sightlines provide substantial constraints on the model parameters without ruling out either model entirely. In addition, for almost all galaxies our halo models are ruled out due to absorbers with substantially different velocities along the different lines-of-sight and/or column densities inconsistent with the expected reduction in density with radius. Whilst single-sightline observations

can use results from simulations and other observations to prefer one model over another (using properties such as metallicity and azimuthal angle), the additional lines-of-sight used here are clearly useful in constraining the possible models.

However, even with this additional information, it can be difficult to determine the robustness of the models we assign to the galaxies and absorbers. For example, how much to weight parameters in a range consistent with other literature, against a slightly improved fit (e.g. B-14 in our sample).

As noted throughout this work, these toy models are simplified, and do not take into account the changing ionization state of the gas, any 'patchiness' of the structures in the CGM, changes in velocities with distance (either for outflows or disks), or changes in the state of the CGM with time (such as an intermittent outflow, e.g. Muratov et al. 2017). Our toy models could therefore appear to rule out a disk or outflow in cases where the failure to fit the observations is due to one of these scenarios. We attempt to include these possibilities in our discussion of each individual galaxy.

Robustly identifying absorbers with outflowing or accreting material is a consistent challenge for transverse line-of-sight studies. Studies of this nature have used a cut in position angle and inclination in order to split absorbers into outflows and inflows, most often when studying Mg II at small impact parameters (Bordoloi et al., 2011; Schroetter et al., 2015; Zabl et al., 2019; Schroetter et al., 2019). We show the cut used by MEGAFLOW, alongside our sample of absorbers and whether we identify them as possible disks or outflows, in Figure 4.7.

We find several absorbers that are best fit by a rotating structure at azimuthal angles close to the projected minor axis (similar to the single case found by Kacprzak et al. 2012a), and outflows relatively close to the major axis. Geometric cuts similar to those shown in the figure would therefore produce different identifications to the kinematic considerations we have included. This suggests that these cuts, whilst useful, are unlikely to be robust in determining whether an absorber is part of a disk or outflow.

Although disk-like absorption is found at all azimuthal angles, we do not see any evidence of outflowing H I within 25° of the major axis for these moderately inclined

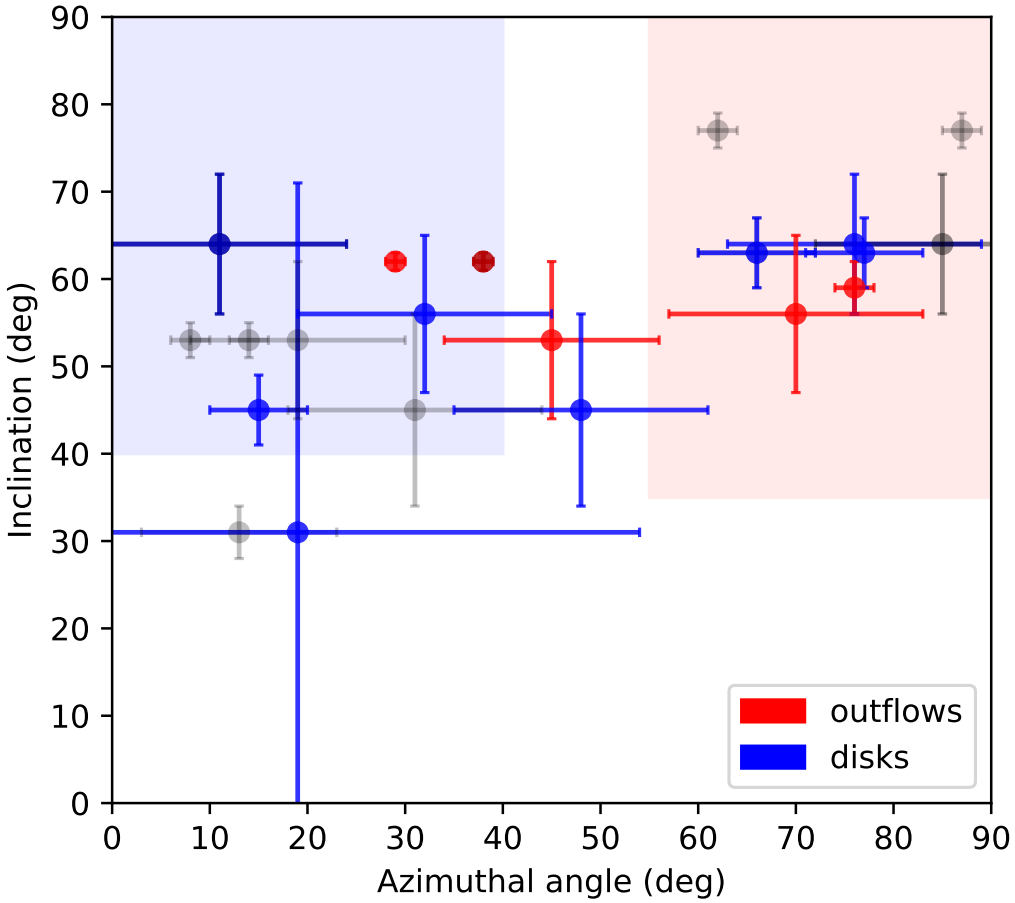

Figure 4.7: Azimuthal angle against inclination for galaxy-absorber pairs in our sample. Absorbers identified as probing a possible outflow are shown in red, with disks in blue and unattributed absorbers in grey. We also shade the regions used to identify the 'primary' disk and outflow subsamples in MEGAFLOW in blue and red repectively (Zabl et al., 2019; Schroetter et al., 2019).

galaxies. This matches expectations for these structures and suggests that outflows at z<1 do not fill a large majority of the solid angle.

Other observables that may aid in discriminating between infalling and outflowing material include column density (e.g. Kacprzak et al., 2019) and metallicity (e.g Péroux et al., 2020). However, we find no substantial difference between the column densities of absorbers identified as disks and outflows by our toy models or those that would be identified as such using geometric cuts. Some observations have failed to reproduce the expected metallicity difference between major- and minor-axis absorption (e.g Kacprzak et al., 2019; Pointon et al., 2019), possibly due to contamination where high-metallicity and low-metallicity material cannot be distinguished along the line-of-sight. We also detect metals in too few of our absorbers for this to be useful. Neither column density nor metallicity can therefore be used reliably to identify absorbers originating from disks and outflows in these observations.

With only two or three sightlines passing each galaxy in our sample, in most cases each proposed model is only probed by a single line-of-sight, with a few models probed by two. This means that the model parameters are often not well-constrained, with degenerate effects on the resulting absorption. If a larger number of sightlines were available for each galaxy, these model structures could be probed by multiple sightlines, providing stronger constraints on the model parameters or ruling out a larger range of models. More complex models including physical processes such as entrainment and changes in velocity, temperature and ionization state would require even more information to constrain. However, even using only the two or three sightlines in this field we are often able to rule out many simple models, providing a clear improvement over single-sightline observations.

4.5.5 Broad absorbers

The CGM/IGM around our sample of galaxies appears to contain a substantial number of broad Lyα absorbers (BLAs), with Doppler widths above 40 $\mathrm{km\,s^{-1}}$, expected to trace the warm-hot intergalactic medium (WHIM, e.g. Tepper-García et al., 2012; Pessa et al., 2018). Of the 27 absorbers identified as Lyα within 500 $\mathrm{km\,s^{-1}}$ of our isolated galaxies, 19 have widths above 40 $\mathrm{km\,s^{-1}}$, and 9 above 100

$\mathrm{km\,s^{-1}}$. This is substantially larger than the 20-50 $\mathrm{km\,s^{-1}}$ found to cover typical IGM absorbers (e.g Davé et al., 2010).

However, the low resolution of the FOS spectra appears to be the main contributor to this abundance of BLAs. Many of our galaxies and absorbers have redshifts above z $\approx$ 0.75, such that both Lyα and Ly β are in the FOS spectra and cannot provide constraints on the line width, and several others are sufficiently weak that Lyβ again fails to provide useful constraints on the Doppler width.

There are therefore only four BLAs near our isolated galaxies with b $>$ 50 $\mathrm{km\,s^{-1}}$ where the width is well-constrained by transitions appearing in the COS spectra (around A-14, A-62, and two near B-14, each discussed in the description of these galaxies), and five absorbers with widths of 40-50 $\mathrm{km\,s^{-1}}$. Of the four candidate BLAs, two are fit by our models without a large thermal component. The range of line-of-sight velocities that would be produced by our toy models in these cases is sufficient to explain the width of the absorption. The other two cannot be fit by a disk/outflow model or our power-law halos due to constraints from the multiple lines-of-sight, but may be produced by a more 'patchy' warm halo and/or the WHIM. The five 40-50 $\mathrm{km\,s^{-1}}$ absorbers are all at a large velocity offset ($>$ 350 $\mathrm{km\,s^{-1}}$), and have impact parameters larger than the virial radius of the nearby isolated galaxy, and are therefore consistent with probing the IGM at temperatures of $\approx 10^{4.7}$ K (e.g. Tepper-García et al., 2012).

4.6 Chapter summary & conclusions

In this work we model the absorption around twelve isolated galaxies in the Q0107 field in order to fit observations from the three lines-of-sight. This sample includes all galaxies with no detected companion within 500 kpc and 500 $\mathrm{km\,s^{-1}}$, and covers both star-forming and passive galaxies with stellar masses $10^{7.5} \lesssim \mathrm{M_\star(M_\odot)} \lesssim 10^{10.5}$ across the redshift range z $<$ 1. Motivated by results from Paper 1, as well as many other works, we focus in particular on whether co-rotating, disk-like structures and bi-conical outflows can reproduce the observed absorption. The use of three lines-of-sight provides additional constraints over previous works using QSO sightlines,

although a small sample limits the strength of our conclusions.

We find that:

(i) Disk and outflow models can approximately reproduce $\approx 50\%$ of absorption features seen within 500 $\mathrm{km\,s^{-1}}$ of isolated galaxies, rising slightly to $\approx 60\%$ of features within 300 $\mathrm{km\,s^{-1}}$. However, the parameters required for these structures to match observations, such as large extents and velocities, are not always consistent with those expected based on results in the literature, possibly suggesting that the actual incidence of these physical structures is smaller.

(ii) Either a disk or outflow model can be ruled out as an origin of the strongest absorber within 300 $\mathrm{km\,s^{-1}}$ of four of our twelve galaxies using the kinematics and column densities of absorption in the other lines-of-sight. The additional sightlines improve constraints on the model parameters around a further four galaxies. Multiple lines-of-sight therefore can be used to better determine the origins of absorption in the CGM/IGM.

(iii) Four of the twelve galaxies considered exhibit absorption consistent with a biconical outflow, which in three cases extend beyond the galaxy virial radius. Whilst only one of these produces clear absorption in multiple sightlines, the velocities found are consistent with the results from Schroetter et al. (2019), using Mg II to observe at smaller impact parameters. The two outflows around the galaxies with higher sSFR exceed escape velocity, whilst those with lower sSFR do not. We find two cases in which a substantial slowing or weakening of the outflow as it moves outwards can improve the fit over a constant-velocity outflow.

(iv) Five of the twelve galaxies exhibit absorption consistent with a rotating and infalling disk. Two of these fit the $\sim 0.6\ v_{vir}$ infall velocity found by Goerdt & Ceverino (2015) and assumed by Zabl et al. (2019). The others are constrained to have a circular velocity larger than v_{vir} under most plausible assumptions of inflow velocity. These are therefore not likely to form physical disk-like structures, despite the disk model fit.

(v) Two of the galaxies feature no identified absorption within 350 $\mathrm{km\,s^{-1}}$. These are the least massive galaxy and the least star-forming galaxy in our sample, consistent with expected dependencies on r/r_{vir} and sSFR.

(vi) Two of the galaxies do not have absorption that can be matched by a disk or outflow, despite a substantial star-formation rate. Whilst our toy models are over-simplified, this over-simplification is unlikely to be the reason for the failure of our models to reproduce the absorption around these two galaxies. These absorbers therefore have a different origin, possibly an undetected companion galaxy.

(vii) Only one galaxy requires both a disk and an outflow in order to reproduce the identified absorption components, although the existence of both structures is not ruled out for several others. We therefore cannot determine whether disks and outflows frequently exist simultaneously around the same galaxy, which could constrain the timescales required for gas recycling.

(viii) At moderate inclinations of $\approx$ 40-70°, some absorbers best fit by disk-like structures can be found close to the projected minor axis (e.g. Kacprzak et al., 2012a; Tejos et al., 2021b), and those best fit by outflows can be found down to 30° from the major axis. Geometric cuts using only azimuthal angle and inclination therefore do not appear sufficient to produce pure samples of disk and outflow absorbers.

The presence of multiple lines-of-sight near to individual galaxies clearly provides useful constraints on the structures in the CGM and IGM, providing estimates of outflow opening angles and velocities, and allowing rotating and in-falling velocity components of the expected accretion on to the galaxy to be separated. However, our study is limited by a small sample size. A larger sample would allow better exploration of the possible space of sightline configurations and galaxy properties. This would strengthen many of the tests we attempt here, as well as allowing us to determine how the model parameters vary with galaxy properties.

Constraining models of the structure of gas in the CGM/IGM is extremely difficult with single-sightline absorption measurements. Although the kinematics of

material at high column densities in the inner CGM are becoming easier to observe using emission lines in wide-field IFUs (e.g. Finley et al., 2017; Burchett et al., 2021; Zabl et al., 2021b; Leclercq et al., 2022), probing these structures at larger scales remains extremely challenging. Observing lower-column-density absorption in several locations around a single galaxy usually requires either a chance configuration of background QSOs or gravitationally-lensed galaxies, or deep and time-consuming observations of background galaxies. Building a statistical sample of such models is therefore unlikely for some time, although several instruments due to be used on the ELT and other upcoming 30m-class telescopes include IGM/CGM tomography in their science cases (e.g. Maiolino et al., 2013; Evans et al., 2015; Marconi et al., 2021). This would allow a large sample of similar model results to be constructed at high redshifts.

In upcoming work we will apply similar procedures to galaxies that are clearly not isolated. This will add to our sample size, but will also include those for which the CGM is likely to be affected by interactions with other galaxies.

CHAPTER 5

Modelling the gas around galaxy pairs and groups

In this chapter we utilize the simple disk, halo and outflow models discussed in Chapter 4 and attempt to determine the extent to which absorption in and around galaxy groups can be explained as a superposition of such structures around the individual galaxies. This work is presented in the form of a paper, which is (at the time of submitting this thesis) in preparation for submission to MNRAS, and referred to as 'Paper 3' throughout the thesis.

5.1 Background

The exchange of gas between galaxies and their surroundings plays a vital role in their evolution. Cool gas that provides fuel for star formation needs to be accreted from outside the galaxy in order to explain the observed star-formation rates and gas content of galaxies (e.g. Freundlich et al., 2013; Scoville et al., 2017). Cool gas is also ejected from galaxies by stellar-feedback- or AGN-driven winds, and models suggest that these processes are important in regulating its star formation (e.g. Lehnert et al., 2013; Somerville et al., 2015; Salcido et al., 2020). This reservoir of gas surrounding galaxies is known as the circumgalactic medium (CGM, e.g. Tumlinson

et al. 2017), and is usually defined as extending to the virial radius.

This material is difficult to observe in emission due in part to its low density (although emission-line maps of gas on CGM scales have become more common in recent years, e.g. Chen et al. 2019; Fossati et al. 2019a; Zabl et al. 2021b; Leclercq et al. 2022), so is most commonly detected using absorption features along the lines-of-sight to background sources, often quasars (e.g. Bahcall & Spitzer, 1969; Bergeron, 1986; Bergeron et al., 1994; Weymann et al., 1998; Adelberger et al., 2005; Chen et al., 2010; Prochaska et al., 2011; Rubin et al., 2018; Pointon et al., 2019; Wilde et al., 2021; Lehner et al., 2021). These absorption-based studies often discuss large numbers of galaxy-sightline pairs, whether as targeted surveys (e.g. Tumlinson et al., 2013; Bielby et al., 2019) or by utilizing other surveys and/or archival data (e.g. Wild et al., 2008), but are usually limited to a single line-of-sight through the gas around any galaxy or group. Some studies are able to utlilize quasar pairs or triplets (lensed or projected, e.g. Fossati et al., 2019b; Maitra et al., 2019), bright background galaxies (e.g. Zahedy et al., 2016; Péroux et al., 2018; Chen et al., 2020b; Okoshi et al., 2021) or gravitationally-lensed arcs (e.g. Lopez et al., 2018, 2020; Tejos et al., 2021a; Mortensen et al., 2021), but these are not common enough to produce statistically meaningful samples of galaxy-absorber pairs.

Many observations find evidence for disk-like accreting and rotating structures along the major axis of galaxies (e.g. Charlton & Churchill, 1998; Steidel et al., 2002; Bouché et al., 2016; Ho et al., 2017; Zabl et al., 2019; French & Wakker, 2020), and this is generally reproduced by simulations, with simulated CGM structures aligned with the galaxy major axis (e.g Ho et al., 2019; Mitchell et al., 2020b; DeFelippis et al., 2020; Hafen et al., 2022). Similarly, evidence for outflowing material is often found along the minor axis of galaxies (e.g. Bland & Tully, 1988; Heckman et al., 1990; Finley et al., 2017; Lan & Mo, 2018; Schroetter et al., 2019; Burchett et al., 2021; Zabl et al., 2021a), which are also reproduced by simulations (e.g Nelson et al., 2019; Mitchell et al., 2020a; Pandya et al., 2021). This leads to some observations finding a bimodality in the azimuthal angles of detected absorption (absorption is found primarily along the major and minor axes, e.g. Kacprzak et al., 2012b; Bouché et al., 2012; Kacprzak et al., 2015), as well as differences in flow rates and

metallicities along galaxy major and minor axes in simulations (e.g. Péroux et al., 2020).

However, gas flows around galaxy groups are likely far more complex. For example, in the nearby M81/M82 group, H I observations reveal a conical outflow structure on small scales, but clear distortion on larger scales due to the other group galaxies (e.g. Sorgho et al., 2019). Tidal interactions are expected to produce a significant fraction of Lyα absorbers in groups (e.g. Morris & van den Bergh, 1994), and likely contribute to other observed ions (e.g. Chen & Mulchaey, 2009). Some studies have identified possible tidal material in absorption, but this is usually difficult to distinguish from other origins (e.g. Chen et al., 2014; Guber et al., 2018). Ram-pressure stripping is also likely to affect the state of the CGM and any intra-group gas during interactions (e.g. Fumagalli et al., 2014; Fossati et al., 2019a). This removal of gas from galaxies and their CGM affects not only the gas itself, but also leads to 'quenching' of star formation in group galaxies (e.g. Peng et al., 2010; Wetzel et al., 2013; Jian et al., 2017; Kuschel et al., 2022)

There have been numerous case studies focusing on the gas in individual galaxy groups, using a variety of absorption features, but also emission lines in more recent cases. Some of these find material that can be associated with a particular galaxy, including some likely outflows and accretion (e.g. Péroux et al., 2017; Johnson et al., 2018), but also material that cannot be associated with a galaxy, and therefore forms an intra-group medium (e.g Bielby et al., 2017; Epinat et al., 2018), as well as suggestions of tidal material (e.g. Kacprzak et al., 2010; Chen et al., 2019). Where multiple absorption/emission components can be identified, material consistent with both disk/outflow structures and tidal/intra-group material can sometimes be seen in the same galaxy group (e.g. Nateghi et al., 2021; Leclercq et al., 2022).

Statistical studies utilizing large samples of galaxy groups are also used to determine the dominant processes in these systems. Bordoloi et al. (2011) found that Mg II absorption near galaxy groups could be due to a superposition of the halos around individual galaxies. In contrast, Nielsen et al. (2018) found that a superposition model could not match the absorber kinematics, and preferred a model in which most cool gas was associated with the group itself rather than any member

galaxy. More recently, Dutta et al. (2020) found Mg II absorption more extended around galaxy groups than isolated galaxies, but also a clear dependence on galaxy properties, suggesting that both the galaxy halos themselves and the interactions between galaxies contribute to the absorption.

If material stripped from galaxies contributes substantially to the gas content in groups, then we may expect gas in these groups to have a higher metal content (having passed through the galaxy and been enriched by cycles of star formation, e.g. Oppenheimer et al. 2016). However, this is not found by Pointon et al. (2019).

The distribution of gas in groups therefore remains unclear. Emission from the CGM remains difficult to detect due to a low density, which usually limits such studies to scales of $\lesssim$ 100 kpc (e.g. Burchett et al., 2021; Leclercq et al., 2022). There remains inconsistency in defining galaxy groups, which are subject to different algorithms, linking lengths, and detection limits in different studies. This makes direct comparisons between observations, or with simulations, difficult (e.g. Oppenheimer et al., 2021). The power of absorption studies is limited by the presence of sufficiently bright background sources, so in most cases the gas around any galaxy group is probed by only a single line-of-sight and we cannot measure gas properties elsewhere in the group.

It is this final difficulty which we seek to address in this paper. We study the Q0107 field, a quasar triplet at z $\sim$ 1 with separations of $\sim$ 1 arcminute ($\approx$ 400 kpc at z = 0.5), with basic quasar properties given by Table 2.1. The use of multiple lines-of-sight through a densely-surveyed field helps to constrain the gas structures and properties on CGM scales.

This field has been utilized in several previous studies, including early studies of the size scales of Lyα absorbers (e.g. Dinshaw et al., 1997; D'Odorico et al., 1998; Young et al., 2001), analysis of the coincidences between absorption in the different lines-of-sight (e.g. Petry et al., 2006; Crighton et al., 2010), construction of the 2D 2-point correlation functions of absorption in both H I and O VI (Tejos et al. 2014, hereafter T14, Finn et al. 2016), and detailed radiative transfer modelling of a small number of absorbers (e.g. Muzahid, 2014; Anshul et al., 2021). Improvements to the available data, such as higher-resolution spectra of the three quasars, high-resolution

imaging from the Hubble Space Telescope, and IFU observations of the field, have enabled our recent works extending these results.

This work continues to use the disk and outflow models from Paper 2, but extends coverage to galaxy pairs and groups in our sample. By combining disk/outflow models, we can examine the hypothesis in which most absorption in groups results from the CGM of the individual galaxies. We also search for signs of tidal material based on the kinematics of the gas relative to nearby galaxies.

In Section 5.2 we summarize the selection and properties of the sub-sample of galaxy groups considered in this work. Section 5.3 summarizes the toy models used in our attempts to reproduce the observed absorption (covered in more detail in Paper 2), whilst Section 5.4 describes in detail the absorption around each galaxy group, and the process of attempting to fit our models to that absorption. We then discuss the overall results in Section 5.5, and finally summarize in Section 5.6.

5.2 Sample of galaxy groups

Paper 2 considered only isolated galaxies, defined as those with no detected companion within 500 kpc and 500 $\mathrm{km\,s^{-1}}$, making it unlikely that the region within a galaxy's virial radius overlaps with that of another detected galaxy. In this work we consider galaxies that are not isolated.

This definition of 'group' requires only two galaxies, and also has a larger 'linking length' (maximum distance between galaxies for them to be considered in the same group) than many similar studies that define group galaxies (e.g. Bordoloi et al., 2011; Nielsen et al., 2018; Fossati et al., 2019b). However, we do use a smaller window than some other studies considering isolated galaxies (e.g. COS-halos, Tumlinson et al., 2013). Therefore all galaxies in our sample are considered as 'group' or 'isolated', but we include groups with larger galaxy separations than other works.

These 'group' galaxies make up the majority of our full sample, so it is impractical to model the absorption around all of these. As our models rely on position angle and inclination measurements obtained from the HST imaging, we selected our sample from groups that have at least two galaxies lying in the HST field. We

manually select a sample of nine groups that meet this restriction, and intentionally span a large range in group properties including redshift as well as number and mass of group galaxies. This range of redshifts and stellar masses is intended to be comparable to that seen in our isolated sample from Paper 2. The selection was made 'blindly' with respect to the nearby absorption, in order to avoid biasing our results.

We note that the definition of 'group' does vary substantially across our large redshift range, such that a group at low redshift would be seen as an isolated galaxy is it were at a higher redshift, with any satellite galaxies going undetected. However, this does not strongly affect our sample, as most of our groups have at least two members that could be detected up to z $\approx$ 1. G-517 is the only group likely to be classified as isolated if it lay at a different redshift, whilst G-383 (consisting of two faint galaxies) could appear isolated in a small redshift range but would more likely go undetected entirely.

The properties of the resulting group sample are listed in Table 5.1, with individual galaxy properties shown in Table 5.2, and their locations on the sky illustrated in Figure 5.1. Only galaxies within the HST field are shown (although we discuss the presence of more distant galaxies when modelling the absorption within these groups).

We note that star-formation rates of galaxies in groups and clusters tend to be lower than field galaxies for similar stellar masses (e.g. Larson et al., 1980; Wetzel et al., 2013). This is found for our full sample and group definitions used in Paper 1, with a K-S test on specific star-formation rates yielding a difference of $\approx 2.5\sigma$. The sample of group galaxies used in this work and the sample of isolated galaxies from Paper 2 are not large enough for a statistical comparison to produce meaningful results, but we do find our group sample to have slightly lower average sSFRs and lower proportion of SF galaxies (using our template classification detailed in Paper 1).

The stellar masses and SFRs of galaxies in our sample are shown in Figure 5.2, which can be directly compared to the similar figure in Paper 2 (Figure 4.2). These two subsamples span a similar range in mass and SFR. Both our Paper 2 and Paper

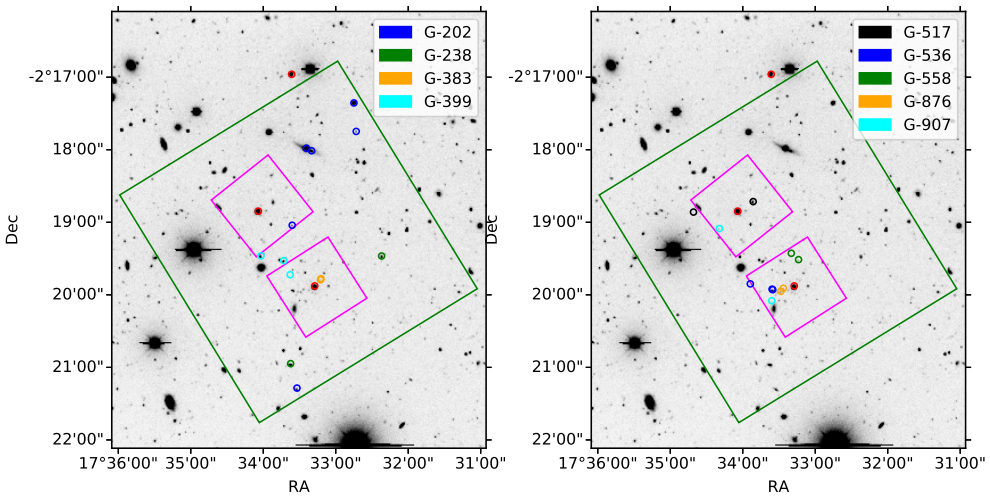

Figure 5.1: The layout of the surveys used in this study. The background image was taken with the Kitt Peak 4-metre Telescope. The solid green square shows the region covered by HST imaging, whilst the smaller magenta squares show the MUSE fields centered on QSOs A and B. The quasars are shown by red circles, with A the southernmost and C the northernmost. The galaxies within the HST field that are analysed in this work are spread across the two panels, with $z < 0.5$ galaxies in the left panel, and higher-redshift galaxies in the right panel. These are coloured by group and labelled by the group identifier listed in Table 5.1.

Table 5.1: Summary of group properties for our selected sample of galaxy groups. Columns are as follows: (1) Group reference used throughout the paper; (2) group central redshift; (3) number of detected galaxies within 500 $\mathrm{km\,s^{-1}}$of the central redshift and 1 Mpc of at least one QSO line-of-sight; (4) total stellar mass of detected galaxies ; (5) closest impact parameter of any galaxy to any line-of-sight; (6) minimum separation between two detected galaxies; (7) r-band luminosity ratio between brightest two galaxies; (8)-(10) estimated galaxy detection limits in the MOS and MUSE surveys, showing continuum estimates in terms of $L_\star$ and SFR limits on emission-line-only detections.

Group Ref	z	N gals	total $M_\star$ $\log_{10}(M_\odot)$	b_{min} (kpc)	Min Pair (kpc)	Lum Ratio	Det Lim (MOS) ($L_\star$)	Det Lim (MUSE) ($L_\star$)	Det Lim (Line-only) ($M_\odot$/yr)
(1)	(2)	(3)	(4)	(5)	(6)	(7)	(8)	(9)	(10)
G-202	0.202	25	11.9 ± 0.2	103	17	2.6	0.004	0.003	0.004
G-238	0.238	4	11.5 ± 0.2	236	42	1.5	0.006	0.004	0.005
G-383	0.383	2	9.7 ± 0.2	38	5	1.5	0.018	0.011	0.016
G-399	0.399	5	11.1 ± 0.2	122	71	3.3	0.020	0.013	0.018
G-517	0.517	2	10.3 ± 0.2	95	320	29.5	0.04	0.02	0.03
G-536	0.536	6	11.5 ± 0.4	120	4	1.4	0.04	0.03	0.04
G-558	0.558	7	11.1 ± 0.5	148	53	1.2	0.04	0.03	0.04
G-876	0.876	4	11.1 ± 0.4	75	26	2.1	0.13	0.08	0.12
G-907	0.907	2	10.7 ± 0.5	170	594	1.7	0.15	0.09	0.13

Table 5.2: Summary of galaxy properties for our selected sample of group galaxies. For each group only galaxies with position angle and inclination measurements are shown. Derivation of these properties is described in more detail in Paper 1. Column descriptions: (1) Group ID used in this work; (2) Galaxy ID (MUSE and MOS IDs were collated separately; MUSE ID is used for galaxies featuring in both MOS and MUSE catalogues); (3, 4) On-sky coordinates of galaxy; (5) Observed magnitude in the SDSS r-band; (6) Galaxy luminosity in SDSS r-band as a multiple of $L_\star$ ($L_\star$ estimate from Montero-Dorta & Prada (2009), uncertainties smaller than 0.005 $L_\star$ are omitted); (7) Stellar mass estimated as in Johnson et al. (2015) (for most galaxies the largest uncertainty is a scatter of 0.15 dex in their relation); (8) Halo mass estimated using the abundance matching technique from Behroozi et al. (2010); (9) Star-formation flag denoting a star-forming or non-star-forming galaxy; (10) Star-formation rate estimated from galaxy emission lines, using the Kennicutt (1998) and Kewley et al. (2004) calibrations for Hα and [O II] respectively (uncertainties are a combination of scatter in these relationships and uncertainty in the line fit); (11) Line used to estimate SFR (SFRs estimated from Hβ using the correlation between SFR estimated from Hα and Hβ line luminosity, generating a substantially larger uncertainty); (12) Note of whether emission-line kinematics from the MUSE data are available for this galaxy.

Group	Galaxy	RA	Dec	r-band	Luminosity	$M_\star$	M_h	SF Flag	SFR	Line	Kinematics
		°	°		($L_\star$)	$\log_{10}(M_\odot)$	$\log_{10}(M_\odot)$		($M_\odot$/yr)		
(1)	(2)	(3)	(4)	(5)	(6)	(7)	(8)	(9)	(10)	(11)	(12)
G-202	B-22	17.5600	-2.3173	22.86 ± 0.03	0.02 ± 0.01	8.4 ± 0.2	10.9 ± 0.3	non-SF	0.06 ± 0.04	Hα	Poor
	25962	17.5589	-2.3548	21.46 ± 0.01	0.07 ± 0.01	8.7 ± 0.1	11.0 ± 0.3	SF	0.5 ± 0.3	Hα	No
	31704	17.5453	-2.2958	22.58 ± 0.02	0.03 ± 0.01	8.2 ± 0.1	10.8 ± 0.3	SF	0.08 ± 0.05	Hα	No

Continued on next page

Continued from previous page

	31787	17.5556	-2.3002	21.35 ± 0.01	0.08 ± 0.01	9.7 ± 0.1	11.5 ± 0.2	SF	0.5 ± 0.2	Hα	No
	32497	17.5567	-2.3000	18.46 ± 0.01	1.10 ± 0.01	11.0 ± 0.1	13.1 ± 0.5	non-SF	2.3 ± 1.9	Hα	No
	32778	17.5458	-2.2893	19.59 ± 0.01	0.39 ± 0.01	10.2 ± 0.1	11.8 ± 0.3	SF	1.5 ± 0.5	Hα	No
G-238	26677	17.5604	-2.3491	20.59 ± 0.01	0.22 ± 0.01	9.7 ± 0.2	11.4 ± 0.3	SF	1.3 ± 0.4	Hα	No
	29214	17.5395	-2.3244	21.38 ± 0.01	0.11 ± 0.01	8.9 ± 0.1	11.1 ± 0.3	SF	0.4 ±0.1	Hα	No
G-383	A-48	17.5535	-2.3299	23.96 ± 0.09	0.03 ± 0.01	9.6 ± 0.2	11.5 ± 0.3	non-SF	<0.04	Hα	No
	A-49	17.5534	-2.3296	25.90 ± 0.51	0.02 ± 0.01	8.7 ± 0.6	11.1 ± 0.4	non-SF	<0.02	Hα	No
G-399	A-56	17.5605	-2.3287	25.17 ± 0.27	0.01 ± 0.01	8.5 ± 0.5	11.0 ± 0.3	SF	0.05 ± 0.01	Hα	No
	A-69	17.5620	-2.3255	22.06 ± 0.01	0.19 ± 0.01	9.8 ± 0.2	11.6 ± 0.3	SF	0.4 ± 0.2	Hα	Poor
	B-7	17.5672	-2.3244	21.37 ± 0.01	0.36 ± 0.01	10.6 ± 0.2	12.3 ± 0.5	non-SF	<0.1	Hα	No
G-517	B-34	17.5780	-2.3143	25.39 ± 0.26	0.02 ± 0.01	7.6 ± 0.6	10.7 ± 0.4	SF	<0.04	[O II]	No
	B-43	17.5643	-2.3119	21.50 ± 0.01	0.59 ± 0.01	10.3 ± 0.2	12.0 ± 0.4	SF	3.8 ± 1.5	[O II]	Yes
G-536	A-36	17.5598	-2.3322	21.30 ± 0.01	0.77 ± 0.01	10.9 ± 0.2	12.9 ± 0.7	SF	6 ± 3	[O II]	Yes

Continued on next page

Continued from previous page

	A-37	17.5599	-2.3320	22.30 ± 0.06	0.31 ± 0.02	10.6 ± 0.2	12.4 ± 0.6	SF	1.3 ± 0.4	[O II]	Poor
	A-40	17.5649	-2.3308	25.61 ± 0.27	0.02 ± 0.01	9.4 ± 0.4	11.4 ± 0.3	SF	0.03 ± 0.02	[O II]	No
G-558	A-72	17.5538	-2.3253	23.66 ± 0.13	0.10 ± 0.01	9.7 ± 0.5	11.6 ± 0.4	SF	0.7 ± 0.2	[O II]	Yes
	A-75	17.5555	-2.3238	25.02 ± 0.29	0.03 ± 0.01	8.3 ± 0.4	10.9 ± 0.4	SF	0.5 ± 0.1	[O II]	Yes
G-876	A-32	17.5580	-2.3325	23.61 ± 0.05	0.30 ± 0.01	10.6 ± 0.2	12.4 ± 0.6	SF	7 ± 2	[O II]	Yes
	A-38	17.5573	-2.3318	23.88 ± 0.13	0.24 ± 0.03	10.8 ± 0.3	12.6 ± 0.8	SF	4.7 ± 1.1	[O II]	Yes
G-907	A-16	17.5600	-2.3347	24.34 ± 0.18	0.17 ± 0.03	10.4 ± 0.5	12.2 ± 0.9	SF	2.3 ± 0.6	[O II]	Poor
	B-19	17.5721	-2.3181	24.88 ± 0.25	0.10 ± 0.03	10.4 ± 0.5	12.2 ± 0.8	SF	1.1 ± 0.3	[O II]	Poor

3 subsamples are biased towards low-mass and star-forming galaxies, as we focus on galaxies near to the sightlines, where the increased depth and easier detection of emission-line galaxies using MUSE has a larger impact on the sample.

5.3 Models

We use the same three basic models as in Paper 2/Chapter 4, namely a power-law halo, bi-conical outflow, and rotating disk. In that work we include a full description of the model parameters, the process of using the galaxy observations and model parameters to generate synthetic spectra, and the process of optimizing for the best-fit models (Section 4.3 and Appendix B.3).

To briefly summarize, the strength of absorption caused by a spherical halo with power-law density profile is determined by its index α and the distance between the galaxy and sightline, whilst its velocity is constant and may be offset from the galaxy by v_δ. An outflow has a constant radial velocity v_{out} and has non-zero density only within a polar angle θ_{out}. We assume a constant outflowing flux, leading to a density profile of r^{-2} within the cone of the outflow. A hollow cone, such that density is zero close to the galaxy minor axis (within θ_{in}), is allowed for, but not included in our initial estimate of model parameters. Disks have an exponential profile with scale heights h_r and h_z, alongside radial and azimuthal velocity components v_r and v_ϕ respectively. All three model types also have an allowed thermal or turbulent velocity v_t that broadens the absorption profile (we do not attempt to distinguish between thermal and turbulent velocities).

In addition to these free parameters, the measurements of galaxy position angle and inclination (from the GALFIT models applied to the HST image) are required as inputs to these models, alongside the chosen galaxy orientation (S_{Nr} and S_{Wr}, described in Paper 2). Both the direction of galaxy rotation and the direction along the minor axis that points away from the observer may be unconstrained, although the MUSE kinematics and the direction of any spiral arms can be used, if visible, to constrain these before modelling the absorption.

Model spectra are generated by combining 10pc segments along each line-of-sight.

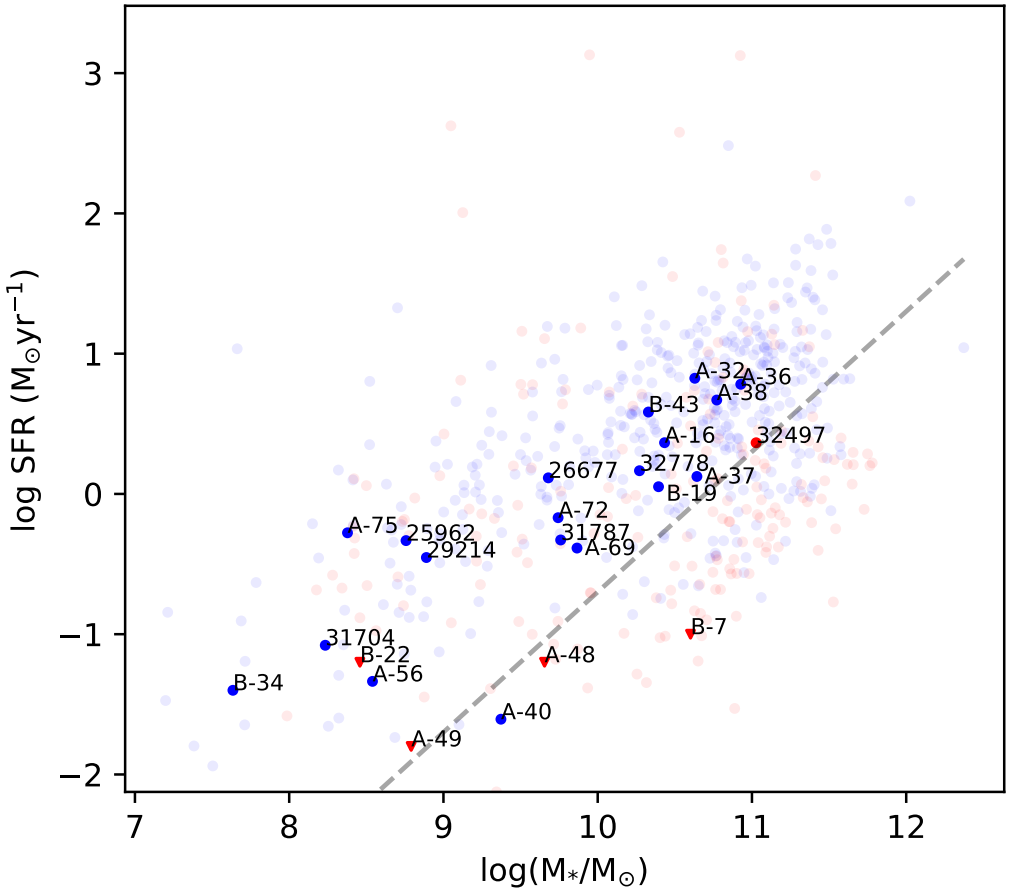

Figure 5.2: Stellar mass vs star-formation rate for galaxies in our sample. Faded points show the overall galaxy sample (identical to Figure 5 from Paper 1), whilst galaxies detailed in this work are bold and labelled with the galaxy MOS or MUSE ID as given in Table 5.2. Galaxies identified as star-forming are shown in blue, with non-star-forming galaxies in red. The grey dashed line indicates an sSFR of 0.02 Gyr^{-1}, an approximate match to the SF/non-SF designations that were made using template fitting. Masses are estimated using Equations 1 and 2 from Johnson et al. (2015) and star-formation rates estimated using the Hα or [OII] (3727 Å) luminosities. These measurements are detailed in Paper 1. The objects marked with triangles are upper limits where no clear emission line is detected. Note that the small number of non-star-forming galaxies with apparent extremely high SFRs are due to fringing effects in the VIMOS data (see T14 Section 3.1) being fit as emission lines. These erroneous measurements do not affect our results.

Each segment has a density determined by the distance and orientation between the sightline segment and the galaxy as well as the density profile of the model, and a line-of-sight velocity determined by the model outflow/infall/rotation velocities projected into the direction of the line-of-sight. Combining these yields a column density, and therefore optical thickness, as a function of velocity or wavelength. The model absorption profile is calculated by combining the optical thickness of all model components included (i.e. the total result from all disk and outflow models around galaxies in the group), converting this to a transmission spectrum, and then convolving with the instrumental line-spread function.

As we discuss in Paper 2, creating an automated routine to find the best-fit parameters of these models is complex and time-consuming, so is not considered for a small sample within a single field. Instead we consider each possible model (halo, disk or outflow for each galaxy with inclination and position angle measurements), and determine which absorption components could be fit by such a model without producing excess absorption in the synthetic spectrum over that seen in the observations, for any of the three lines-of-sight. This primarily concerns eliminating model combinations that do not produce velocity offsets in the correct direction, or match the relative column densities that would be produced in the different sightlines. We then iteratively adjust the model parameters to produce a reasonable fit, and finally find the combination of models that reproduces the maximum number of observed absorption components.

This method identifies the various models capable of reproducing each observed absorption feature, although it does not provide a quantitative measure of the best fit (which would likely depend substantially on the priors chosen on the parameter space). Throughout this work we therefore list the different model combinations found to produce a reasonable approximation of the observed spectra.

5.4 Absorption around galaxy groups

We now apply these models to the absorption in galaxy groups, and attempt to reproduce the H I absorption components visible in the QSO spectra at the group

redshift. Although Lyα is usually preferred, in some cases it is saturated, blended, or lies in the lower-resolution FOS spectra, so Lyβ provides better constraints on the models. Below we discuss our preferred combination of models some of these groups, including the model parameters and the reasons for rejecting alternative combinations. Additional groups are discussed in Appendix C.2.

5.4.1 G-238

Group G-238 consists of two star-forming galaxies (29214 and 26677) appearing in the HST field at z $\approx$ 0.24. These are the two nearest galaxies to the lines-of-sight at this redshift, although there are several others at larger impact parameters. The observations are detailed in Table 5.3 and Figure 5.3.

QSO-A features two absorption components at this redshift, with the redder absorber featuring O VI detected at a significant level. No significant absorption is detected in B or C, but some weak absorption in C could be hidden by molecular lines from the sub-DLA. Both of the absorbers are at very similar velocities to the two galaxies, but a simple halo model requires a steep density profile (much steeper than r^{-2}), otherwise it would produce absorption in B that is inconsistent with observations. QSO-A also lies close to the minor axis of 26677 and the major axis of 29214. A model consisting of an outflow and disk around the two galaxies respectively can approximately produce the results seen in the observations.

These galaxies are reasonably well-separated, lying outside of each others' virial radii, so it is not surprising that a superposition of disks and outflows can reasonably reproduce the observations. This model is also supported by the detection of O VI at a redshift matching the redder Lyα component that we identify as a likely outflow. The other absorber has O VI to H I ratio less than 1/5 of this, better fitting accretion from the IGM.

5.4.2 G-399

A-56, A-69 and B-7 are the three galaxies within the HST image at z $\approx$ 0.399. The state of the gas causing absorption in the sightlines at this redshift is modelled in

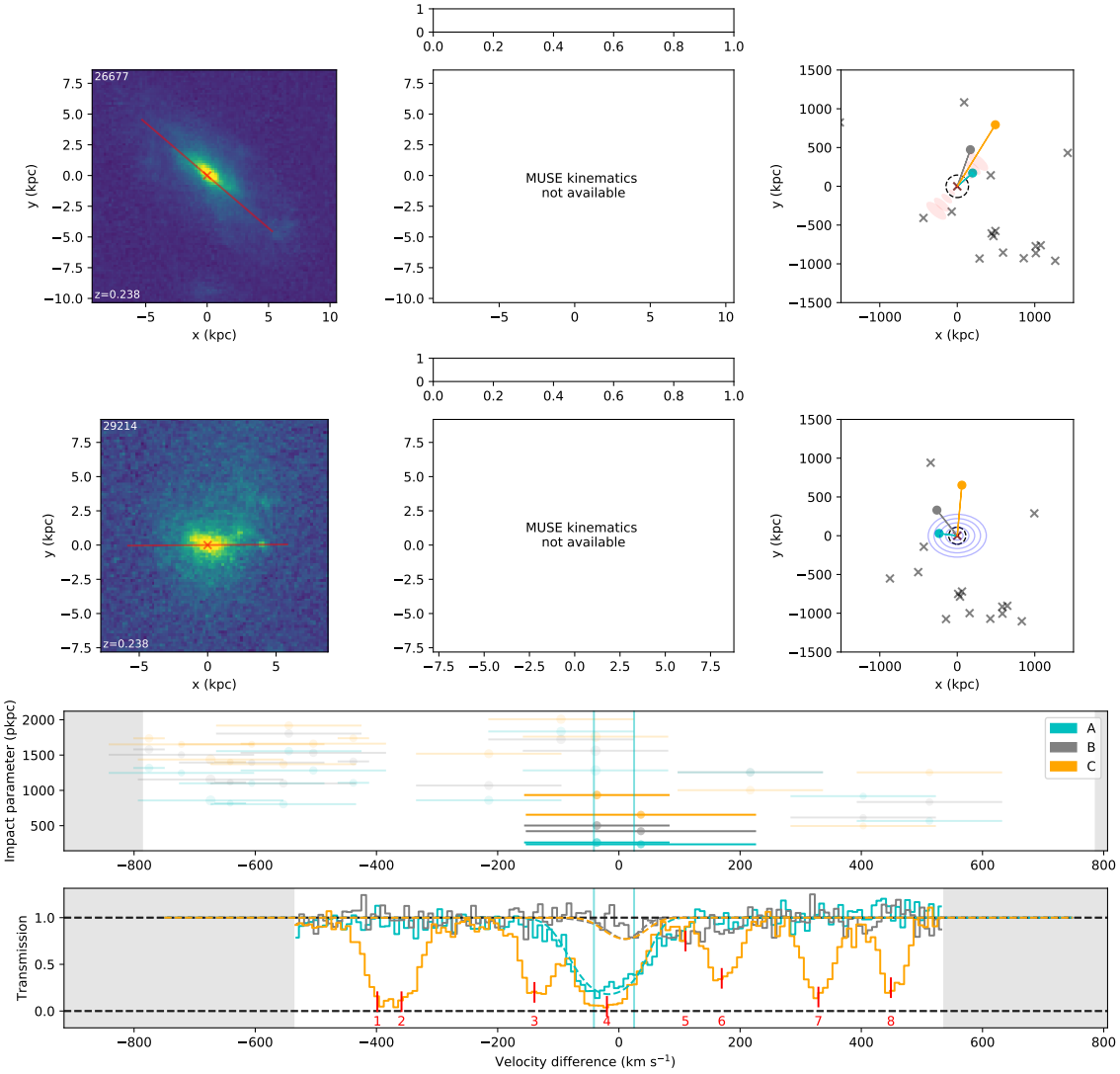

Figure 5.3: Details of the absorption and galaxy environment around group G-238. The upper two rows of panels illustrate the galaxies and the models used, whereas the lower panels indicate the location of the galaxies and absorption at the group redshift. Features are identical to those in Figure 4.4, but with the images of multiple group galaxies shown (and kinematics where available). The model shown in the lower panel is a disk with rotation velocity ~ 100 km s^{-1} around galaxy 29214, and an outflow with opening angle 20° and velocity 120 km s^{-1}. Additional absorbers identified by red ticks are mostly molecular lines at the redshift of the sub-DLA at z $\approx$ 0.56, except for the weak absorption in LOS-B (5), which is Lyβ from z $\approx$ 0.47.

Table 5.3: Summary of galaxy and absorber properties for group G-238. Any additional galaxies and metal absorbers have velocities shown relative to the first galaxy (26677). with columns as follows: (1) Group redshift; (2) Galaxy ID; (3) Galaxy luminosity (as a multiple of $L_\star$; (4) Galaxy inclination; (5) Line-of-sight identifier; (6) Impact parameter between galaxy and line-of-sight at the group redshift; (7) Azimuthal angle between galaxy major axis and the line-of-sight; (8) Absorber column density; (9) Absorber Doppler parameter; (10) Velocity offset between galaxy and absorber (Any additional galaxies and metal absorbers have velocities shown relative to the first galaxy, in this case B-22); (11) Any detected metal ions at the same redshift as this H I absorber.

z (1)	Galaxy (2)	Lum ($L_\star$) (3)	Inc (4)	LOS (5)	Imp (kpc) (6)	Azimuth (7)	log(N H I) (8)	b ($\mathrm{km\,s^{-1}}$) (9)	Δv ($\mathrm{km\,s^{-1}}$) (10)	Other ions (11)
0.238	26677	0.22	67° ± 1°	A	262	81° ± 1°	13.99 ± 0.20	43 ± 7	-10 ± 100	
				A	262	81° ± 1°	13.75 ± 0.35	54 ± 21	+60 ± 100	O VI
				B	502	69° ± 1°	(None, limit ∼12.8)			
				C	934	81° ± 1°	(None, limit ∼12.9)			
	29214	0.11	43° ± 3°	A	236	8° ± 5°			(+70)	
				B	422	52° ± 5°				
				C	654	84° ± 5°				
	(22676)	0.32		A	859				(-180)	
				B	1069					
				C	1519					
	(33195)	0.04		A	919				(+440)	
				B	616					
				C	495					

Anshul et al. (2021); both sightlines feature transitions from multiple metal ions. The details are given in Table 5.4 and illustrated in Figure 5.4. Note that the absorption features in QSO-C are identified with transitions from different redshifts.

B-7 is the largest galaxy in this group, and the closest to QSO-B, but is non-star-forming. The other two galaxies within the HST field are star-forming galaxies but also less massive. A-69 lies on the edge of the MUSE field, with the edge of the field running approximately along the major axis. There may be a velocity gradient across the galaxy, but this is not clear. A-56 lacks a well-determined orientation, as it is indistinguishable from a point source in the HST image.

An outflow around A-69 is capable of producing two absorption components in A, but not the factor of ≈ 10 difference in column density between the two components and the much stronger absorption in B. However, combining this outflow with a disk can reproduce the observed absorption in A whilst remaining consistent with B and C. An outflow with 30° half-opening angle and 160 $\mathrm{km\,s^{-1}}$ velocity, alongside an extended H I disk with 160 $\mathrm{km\,s^{-1}}$ rotation returns an approximate match. An outflow around B-7 is ruled out, as the large velocity offset required to match the absorption in A alongside the opening angle required to cover LOS-A would produce a substantially broader absorption feature.

No disk or outflow around any of the galaxies could produce the absorption in B without substantially exceeding the observed levels of absorption in A or C. The high column density in B is metal-enriched, exhibiting absorption from a range of metal ions, and has a line-of-sight velocity between the two larger galaxies in this group. This may suggest that this material has been stripped from one of the galaxies, or that an outflow from one of the galaxies has been distorted by interaction with the CGM of the other such that it can no longer be fit by our toy models.

Anshul et al. (2021) find that the absorption in QSO-A is consistent with solar metallicity in both components, that the low ions (H I and C III) are consistent with photoionization in the stronger component, and that the O VI in both components is consistent with collisionally ionized, $T \gtrsim 10^5$ K gas. This would appear to be consistent with the O VI resulting primarily from outflowing material in both components. They note that the material observed would likely have been ejected from

the central galaxy > 600 Myr ago. It therefore seems possible that the material we have modelled as a rotating disk has been recycled from this outflow, but only gas that has cooled efficiently is seen in this disk. In this scenario, the stronger absorption component consists of both the proposed cool disk and a warm outflow; the cool disk dominates this absorption component for the low ions, but less so for the O VI. This would explain the similar metallicity of both phases and components. Stripped material near the minor axis could also reproduce the observations in place of this possible outflow.

Anshul et al. (2021) also find multiple phases in the absorption in B, with a broad Lyα component alongside the O VI and a narrower component matching the low ions. They find that the low ions are consistent with photoionized gas at $\sim$1/10th solar metallicity, and that the O VI could be produced either by diffuse hot gas at similar metallicity, or by cooler collisionally-ionized gas with near-solar metallicity. They suggest that these could respectively trace either the diffuse, hot CGM or intra-group medium, or the interface between a low-ionization cloud and the hot-CGM (that cloud possibly originating from an outflow).

If this absorption in B is due to a hot and diffuse CGM or intra-group medium, it must either be distorted or patchy, as a spherical distribution cannot match the ratio of absorption strengths in the two sightlines. Similarly, our biconical outflow models cannot reproduce this ratio, suggesting (if an outflow exists) either a substantial change in outflow rate with time, a very patchy medium, or distortion due to the interaction between the two galaxies.

5.4.3 G-876

A-32 is an $\approx 0.3L_*$ galaxy at z $\approx$ 0.88, inclined at $\approx 30°$. It is paired with A-38, a galaxy of similar magnitude that is less than 30 kpc away. Neither galaxy shows any signs of morphological distortion in the HST image or any kinematic signatures of interaction between the two galaxies; both galaxies show a velocity gradient along their major axis that is likely due to rotation (with velocity ≈ 100 km s^{-1}). This system is detailed in Table 5.5 and Figure 5.5.

A-38 is redshifted by $\approx$ 50 km/s relative to A-32, and is therefore at the same

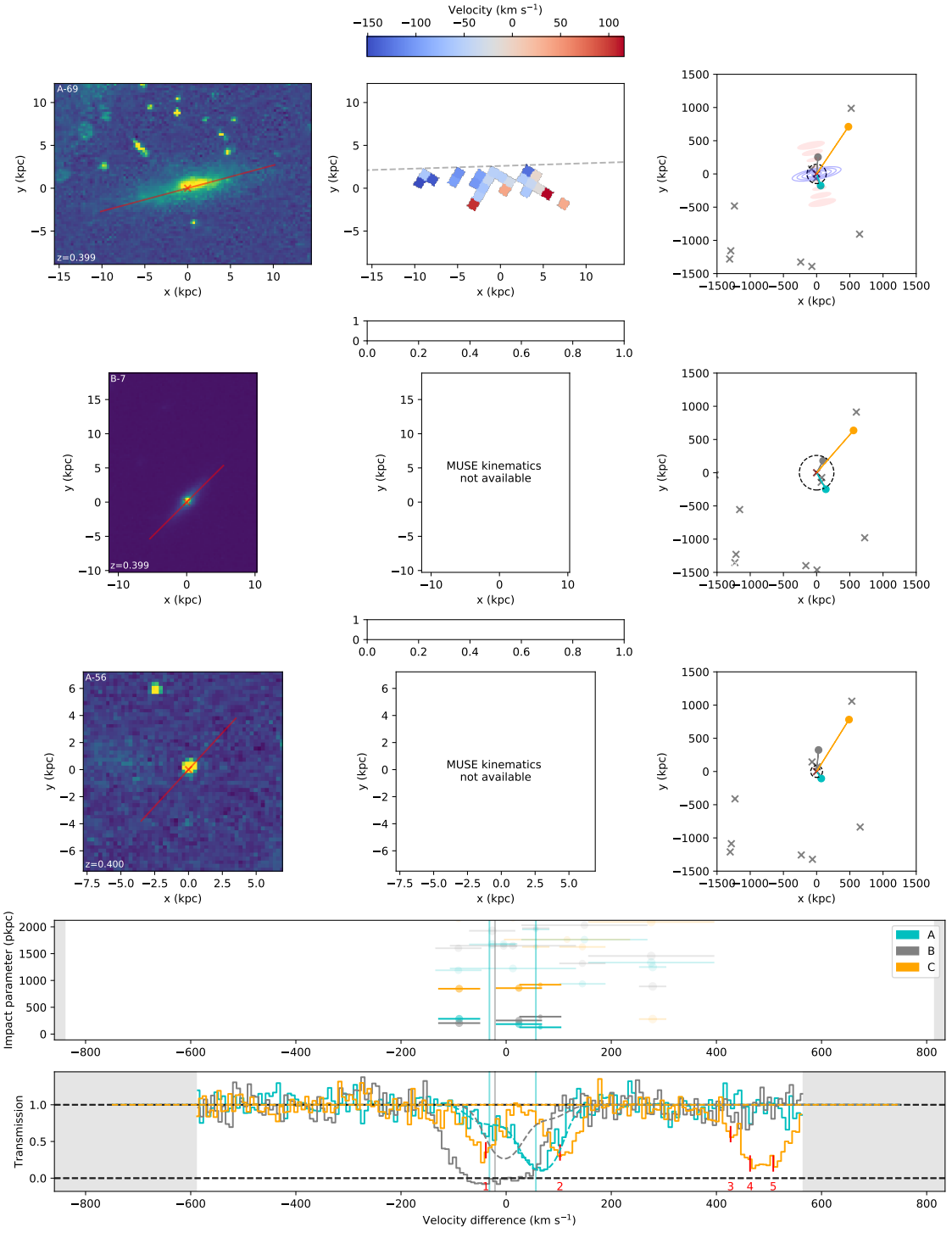

Figure 5.4: Details of the absorption and galaxy environment around group G-399. The layout is identical to that shown in Figure 4.4, with kinematics measured from the Hα emission line seen in the MUSE data, and the model shown in the lower panel combines an outflow with 25° half-opening angle and 160 km s^{-1} velocity with a disk with 150 km s^{-1} rotation and 50 km s^{-1} infall, both around galaxy A-69. All five absorption components labelled with red ticks are molecular lines associated with the sub-DLA at z ≈ 0.56. Note that galaxy A-69 lies at the edge of the MUSE field, so the velocity map is truncated approximately along the dashed grey line.

Table 5.4: Summary of galaxy–absorber group at z $\sim$ 0.399. Any additional galaxies and metal absorbers have velocities shown relative to the first galaxy (A-56). Columns are identical to those in Table 5.3.

z (1)	Galaxy (2)	Lum ($L_\star$) (3)	Inc (4)	LOS (5)	Imp (kpc) (6)	Azimuth (7)	log(N H I) (8)	b ($\mathrm{km\,s^{-1}}$) (9)	Δv ($\mathrm{km\,s^{-1}}$) (10)	Other ions (11)
0.399	A-56	0.01	35° ± 35°	A	122	76° ± 45°	13.15 ± 0.09	15 ± 6	-100 ± 40	C III, O VI
				A	122	76° ± 45°	14.14 ± 0.03	35 ± 2	-10 ± 40	C III, O VI
				B	325	38° ± 45°	16.77 ± 0.02	24.9 ± 0.5	-90 ± 40	C I, N III, Si III, O III, O VI
				C	921	11° ± 45°	(None, limit ≈ 13.0)			
	A-69	0.19	77° ± 2°	A	186	82° ± 2°			(-40)	
				B	254	74° ± 2°				
				C	857	44° ± 2°				
	B-7	0.36	82° ± 1°	A	285	70° ± 1°			(-150)	
				B	205	12° ± 1°				
				C	846	1° ± 1°				
	(26721)	0.2		A	937				(+80)	
				B	1318					
				C	1626					
	(34572)	1.2		A	1251				(+210)	
				B	889					
				C	280					

redshift as the absorption in sightline A, whilst sightline B is blueshifted by 100 $\mathrm{km\,s^{-1}}$ relative to this galaxy.

Sightline A lies at a distance of ≈ 100 kpc along the major axis of A-32 and 75 kpc at $\approx 20°$ to the major axis of A-38, with sightline B at ≈ 600 kpc along the minor axis. Both show absorption, with H I column densities $\sim 10^{15.8}$ and $10^{15.4}$ $\mathrm{cm^{-2}}$ and Doppler parameters 30 and 20 $\mathrm{km\,s^{-1}}$ respectively. Sightline A features O III and O IV absorption at this redshift, whilst sightline B does not show any metal absorption. However, the detection limit for these ions allows for the gas seen in LOS-B to have similar O III and O IV column densities to that in A. Note that as both Lyα and Lyβ lie in the FOS gratings at this redshift, the Doppler parameters are not resolved; higher-order lines appearing in COS constrain the Doppler widths but reveal no additional structure. These galaxies lie beyond the redshift of QSO-C, so no absorption can be detected in the third sightline.

The relatively similar column densities alongside a large difference in impact parameter prevents any of our models from simultaneously matching both absorbers. That the absorption in A is close to the major axis of both galaxies, whilst B is near the minor axis of both galaxies, would suggest that these could be a disk and outflow respectively.

If the absorption in sightline A is associated with A-32, it is co-rotating and could be part of an extended disk with rotation velocity ≈ 100 $\mathrm{km\,s^{-1}}$ (depending on any infall component). If associated with A-38, the absorption in A must have comparable rotation and infall velocities, in order to produce absorption with no clear line-of-sight velocity offset. Alternatively, a power-law halo around A-38 could reproduce this lack of velocity offset.

An outflow from either galaxy can also reproduce the absorption in B. In order to reproduce the velocity offset, these putative outflows would require velocities of ≈ 140 $\mathrm{km\,s^{-1}}$ (from A-32) or ≈ 210 $\mathrm{km\,s^{-1}}$ (from A-38). We note that A-38 cannot produce both a disk matching A and an outflow matching B, as the need for the disk velocity offsets to 'cancel' fixes the galaxy orientation, whilst an outflow matching B requires the opposite orientation.

This still leaves several possible combinations of models that can reproduce the

observations. A reasonable fit is shown in Figure 5.5, and combines an outflow with velocity 140 $\mathrm{km\,s^{-1}}$and opening angle 40° and a disk with rotation velocity 100 $\mathrm{km\,s^{-1}}$, both originating from A-32.

We also note that galaxy 26501 is substantially brighter than either A-32 or A-38, so may be contributing to the absorption in LOS-B. Furthermore, the velocity difference between the two galaxies and the location of each galaxy near the major axis of the other suggest orbital angular momentum with similar alignment to the rotation of both galaxies. Therefore the absorption that could be identified as a disk around one galaxy may also be tidal material resulting from their interaction, or larger-scale accretion into the group, rather than associated with one of the galaxies.

5.5 Discussion

The model fits shown above can now be discussed in the context of our previous works, especially the sample of isolated galaxies considered in Paper 2, as well as results from the literature. We summarize the best-fitting results for each galaxy group in Table 5.6.

5.5.1 Model success

Firstly, our disk and outflow models provide a plausible fit for 21 of the 28 detected H I components within 500 $\mathrm{km\,s^{-1}}$ and 500 kpc of our sample galaxies. This 75% success rate is somewhat higher than the ≈ 50-60% found for the isolated galaxy sample in Paper 2 (13 of 26 within 500 $\mathrm{km\,s^{-1}}$ and 12 of 20 within 300 $\mathrm{km\,s^{-1}}$).

It may be expected that for group galaxies with gravitational interactions, such forces would distort any structure in the CGM and reduce the rate at which these models can reproduce the absorption at large scales. This is seen in, for example, the M81 group, where 21 cm emission is seen tracing both a disk-like and biconical outflow structure around M82 on small scales, but distorted in the direction of M81 on larger scales (e.g. Sorgho et al., 2019). Such distortions would be expected to reduce the success rate of our models in galaxy groups, although in some circumstances our

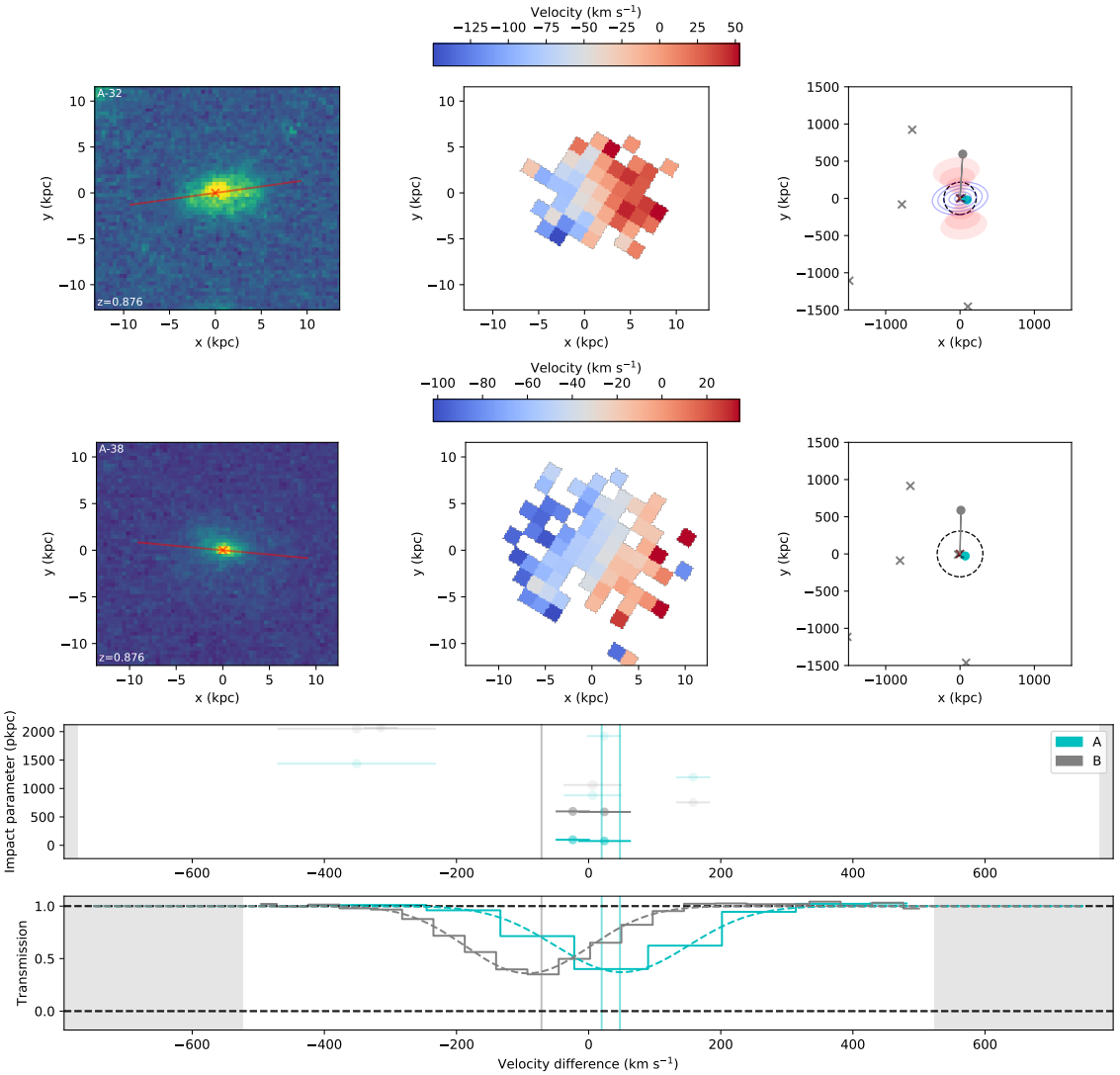

Figure 5.5: Details of the absorption and galaxy environment around group G-876. The layout is identical to that shown in Figure 5.3, with kinematics measured from the [O II] emission line seen in the MUSE data, and the model shown in the lower panel combines an outflow with velocity 160 $\mathrm{km\,s^{-1}}$and opening angle 40° and a disk with rotation velocity 100 $\mathrm{km\,s^{-1}}$.

Table 5.5: Summary of galaxy–absorber group G-876. Any additional galaxies and metal absorbers have velocities shown relative to the first galaxy (A-32). Note that this group is beyond the redshift of QSO-C, so no absorption could be detected. Columns are identical to those in Table 5.3.

z (1)	Galaxy (2)	Lum ($L_\star$) (3)	Inc (4)	LOS (5)	Imp (kpc) (6)	Azimuth (7)	log(N H I) (8)	b ($\mathrm{km\,s^{-1}}$) (9)	Δv ($\mathrm{km\,s^{-1}}$) (10)	Other ions (11)
0.876	A-32	0.30	55° ± 3°	A	97	19° ± 4°	15.78 ± 0.30	30 ± 5	40 ± 20	O IV (0), O III (-10)
				B	597	79° ± 4°	15.45 ± 0.47	22 ± 3	-50 ± 20	
	A-38	0.24	54° ± 5°	A	75	16° ± 5°			(+50)	
				B	588	86° ± 5°				
	(26501)	0.80		A	879				(+30)	
				B	1062					
	(29799)	0.38		A	1197				(+180)	
				B	755					

Table 5.6: Summary of galaxies in groups and the best-fitting toy models (ordered by redshift). Only galaxies with estimated position angles are shown in this table. Columns are as follows: (1) Group identifier; (2)-(4) Galaxy IDs, luminosities, and star-formation classes derived from template fitting, as given in Table 5.2; (5) Brief description of model combinations found to produce a reasonable fit.

Group	Galaxy	Lum ($L_\star$)	SF-Class	Model(s)
(1)	(2)	(3)	(4)	(5)
G-202	B-22	0.02	SF	(4/5 absorbers) B-22 outflow, θ=15°, v=250 $\mathrm{km\,s^{-1}}$, extent > 100 kpc
	25962	0.07	non-SF	AND 31787 outflow, θ=20°, v=50 $\mathrm{km\,s^{-1}}$, extent > 400 kpc
	31704	0.03	SF	AND 32778 disk, height ratio ≈10, v_ϕ= 120 $\mathrm{km\,s^{-1}}$, v_r= 0 $\mathrm{km\,s^{-1}}$, extent > 400 kpc
	31787	0.08	SF	(other options possible, e.g. 25962 disk, but less likely)
	32497	1.1	non-SF	
	32778	0.4	SF	
G-238	26677	0.2	SF	(2/2 absorbers) 26677 outflow, θ=20°, v=120 $\mathrm{km\,s^{-1}}$, extent > 260 kpc
	29214	0.1	SF	AND 29214 disk, height ratio ≈40, v_ϕ= 100 $\mathrm{km\,s^{-1}}$, v_r= 30 $\mathrm{km\,s^{-1}}$, extent > 240 kpc
				(29214 disk and halo possible instead, with similar disk parameters)
G-383	A-48	0.03	non-SF	(3/3 absorbers) A-48 outflow, θ=10°, v=600 $\mathrm{km\,s^{-1}}$, extent > 40 kpc
	A-49	0.01	SF	AND A-49 disk, height ratio ≈100, v_ϕ= 150 $\mathrm{km\,s^{-1}}$, v_r= 40 $\mathrm{km\,s^{-1}}$, extent > 400 kpc

Continued on next page

Continued from previous page

				(A-48 disk with v_ϕ= 320 km s^{-1}, v_r= 0 km s^{-1}also possible)
				(some parameters very uncertain due to edge-on galaxy pair)
G-399	A-56	0.01	SF	(2/3 absorbers) A-69 outflow, θ=25°, v=160 km s^{-1}, extent > 180 kpc
	A-69	0.19	SF	AND A-69 disk, height ratio ≈100, v_ϕ= 150 km s^{-1}, v_r= 50 km s^{-1}, extent > 200 kpc
	B-7	0.36	non-SF	(strongest absorber not fit by any toy model)
G-517	B-34	0.12	SF	(No detected absorption)
	B-43	0.6	SF	(Upper limit logN ≈13.3)
G-536	A-36	0.8	SF	(4/7 absorbers) A-36 outflow, θ=55°, v=140 km s^{-1}, extent > 120 kpc
	A-37	0.3	SF	AND A-40 disk, height ratio ≈100, v_ϕ= 110 km s^{-1}, v_r= 60 km s^{-1}, extent > 400 kpc
	A-40	0.02	SF	(other absorption may be due to stripping in galaxy interactions, A-37 disk also possible)
G-558	A-72	0.10	SF	(2/3 absorbers) A-72 outflow, θ=40°, v=150 km s^{-1}, extent > 500 kpc
	A-75	0.03	SF	OR A-75 outflow, θ=50°, v=70 km s^{-1}, extent > 350 kpc
	A-77	0.04	SF	AND
				A-75 disk, height ratio ≈70, v_ϕ= 90 km s^{-1}, v_r= 50 km s^{-1}, extent > 200 kpc

Continued on next page

Continued from previous page

				OR A-75 halo, $v_\delta \approx 0$, $\alpha \gtrsim 2$
				(sub-DLA not fit, absorber is likely due to a galaxy that is not detected)
G-876	A-32	0.30	SF	(2/2 absorbers) A-32 disk, height ratio ≈20, v_ϕ= 100 km s^{-1}, v_r= 0 km s^{-1}, extent > 100 kpc
	A-38	0.24	SF	OR A-38 disk, height ratio ≈10, v_ϕ= 100 km s^{-1}, v_r= 100 km s^{-1}, extent > 80 kpc
				AND
				A-32 outflow, θ=40°, v=160 km s^{-1}, extent > 600 kpc
				OR A-38 outflow, θ=35°, v=210 km s^{-1}, extent > 600 kpc
G-907	A-16	0.17	SF	(2/2 absorbers) A-16 disk, height ratio ≈20, v_ϕ= 100 km s^{-1}, v_r= 50 km s^{-1}, extent > 200 kpc
	B-19	0.10	SF	AND B-19 outflow, θ=60°, v=80 km s^{-1}, extent > 200 kpc
				OR
				A-16 outflow, θ=60°, v=150 km s^{-1}, extent > 180 kpc
				AND B-19 disk, height ratio ≈20, v_ϕ= 130 km s^{-1}, v_r= 40 km s^{-1}, extent > 180 kpc

disk and outflow models could appear successful even with these distortions present.

Our higher success rate for group galaxies over isolated galaxies could suggest that galaxy interactions are not having a significant impact on our sample. However, there are several effects that could counter any impact of group interactions.

Firstly, the larger number of galaxies near to each absorber increases the number of free parameters available for our models, and therefore the likelihood of obtaining a reasonable fit even if the models do not reflect the true physical state of the gas (or reflect the state of the gas poorly due to effects such as intermittent outflows and changes in ionization state, as well as distortions due to group interactions). However, the groups for which some H I absorption cannot be fit by our models appear to be those with the largest number of galaxies, whereas for those with 2-4 galaxies we have been able to find a plausible fit to all identified absorbers (a difference of $\approx 2\sigma$ in mean N_{gals}). This suggests that the increased number of free parameters, largest for groups with many galaxies, is not the primary reason for our high success rate.

We also search for other differences between the properties of the groups for which all absorbers were fit, and those with some absorption that could not be fit. No significant differences were found in their redshifts, total stellar masses, impact parameters to the nearest or most massive galaxy, ratios of stellar masses or luminosities of the brightest two galaxies, or the projected separations of the tightest pair of galaxies in each group. These tests therefore provide little indication of the likely origins of unexplained absorbers. We do find that individual absorbers that were not consistent with any of our models have higher H I column densities than those we could successfully fit, and discuss these in more detail in Sections 5.5.4 and 5.5.5.

Second, the larger number of galaxies, and resulting smaller impact parameters between the lines-of-sight and the nearest galaxy, may also contribute to the success of our models. With the known correlation between impact parameter and column density (e.g. Werk et al., 2014; Wilde et al., 2021), this contributes to generally higher H I column densities in our groups (median H I column densities of $10^{14.5}$ and $10^{13.8}$ cm^{-2} in absorbers associated with this work and our Paper 2 sample

respectively). These higher column densities also make successful fits more likely, as weak absorption produced by the toy models can more easily be 'hidden' under other absorbers, and column densities are less constrained once absorption begins to saturate. The smaller impact parameters also increase the likelihood of probing any inflowing or outflowing structures closer to the galaxy than any distortions caused by interactions within the group.

Third, it is possible that some absorption resulting from group interactions could be fit by our models regardless. This could include material along the plane of a galaxy interaction masquerading as an accreting disk, and stripped material near the galaxy minor axis appearing consistent with an outflow. These false fits are unlikely to occur where multiple absorbers are reproduced by a single model, due to the extra constraints, but may contribute to some of our model fits based on a single absorber.

Studies of cool CGM gas using Mg II absorption have come to differing conclusions on the origin of the more extended absorption in galaxy groups. Bordoloi et al. (2011) suggest that a superposition of CGM absorption from the constituent galaxies can reproduce the observed results, whereas Nielsen et al. (2018) prefer a model in which absorbers are generally associated with the intra-group medium rather than any individual galaxy. Using samples extending to slightly higher redshifts, Fossati et al. (2019b) suggest that this is material originating primarily from tidal interactions between group galaxies, whilst Dutta et al. (2020) support a model with contributions from individual halos and tidal interactions.

Our models cannot directly test for tidal material (although we do discuss this briefly in Section 5.5.4), but do produce a superposition of possible structures sometimes found in the CGM of isolated galaxies. However, this differs from the superposition model tested in Bordoloi et al. (2011), Nielsen et al. (2018) and Dutta et al. (2020) in that the covering fraction of these CGM structures in groups is not constrained to be the same as that around isolated galaxies.

Our high model success rate provides some support for a superposition model for groups using our definition and sample selection, but does not rule out a contribution from intra-group and tidal material. The apparent difference between

this conclusion and that of Nielsen et al. (2018) may in part result from our larger linking lengths, so our group sample contains some galaxy pairs with larger separations, which are less likely to be affected by group interactions. Our sample also features galaxies at large impact parameters that may explain weak absorbers seen in group environments, which are not satisfactorily explained under their superposition model. Dutta et al. (2020) found a similar result, ruling out superposition as the origin for their strongest and weakest absorbers. Nielsen et al. (2018) found that combining the expected galaxy-absorber velocity offsets (as observed around isolated galaxies) with the galaxy-galaxy offsets seen in groups produced a model absorber-absorber velocity distribution significantly wider than observed. However, possibly due to including faint MUSE galaxies near the lines-of-sight, our groups exhibit smaller galaxy-galaxy velocity differences than their sample, reducing this inconsistency.

We also note that our sample includes galaxies fainter than those included in the Bordoloi et al. (2011) sample. Their lack of faint galaxies likely leads to some interacting galaxies being classified as isolated, therefore making the absorption profiles of group and isolated galaxies more similar.

Our high success rate at reproducing absorption in our sample of galaxy groups suggests that this superposition of disk and outflow structures, similar to those sometimes found around isolated galaxies, may explain a substantial fraction of absorption found around these groups. The increase in parameter space due to the larger number of galaxies, effects due to the higher column densities and smaller impact parameters, and absorption from other sources (e.g. intra-group and tidal material) mis-identified as disk/outflow material, are all likely to contribute to the higher success rate found fitting these models to gas around groups than around isolated galaxies.

5.5.2 Model parameters

We briefly discuss the model parameters that produce the best fit for the absorption near these galaxy groups. In most cases these are similar to those found near isolated galaxies in Paper 2, where we discuss the parameters in more detail, but some

Table 5.7: Model outflow properties around galaxies for which outflows can reproduce some of the observed absorption components. Column descriptions: (1)-(5) are repeated from Table 5.2; (6) specific star-formation rate; (7) maximum impact parameter at which outflow is detected; (8) maximum extent at which absorption is detected (at the point of highest H I density along the sightline with the largest impact parameter); (9) galaxy virial radius; (10) model half-opening angle; (11) model outflow velocity; (12) escape velocity from the location of the sightline at the maximum observed extent. (Note that the starred escape velocities denote $r/r_{vir} > 2$, so escape velocity is calculated assuming the outflowing material lies beyond the galaxy halo, rather than within an isothermal halo.)

Galaxy	z	$M_\star$ $\log_{10}(M_\odot)$	M_h $\log_{10}(M_\odot)$	SFR ($M_\odot$/yr)	sSFR Gyr^{-1}	b_{max} (kpc)	Extent (kpc)	r_{vir} (kpc)	θ_{out} (°)	v_{out} ($km\,s^{-1}$)	v_{esc} ($km\,s^{-1}$)
(1)	(2)	(3)	(4)	(5)	(6)	(7)	(8)	(9)	(10)	(11)	(12)
B-22	0.202	8.4 ± 0.2	10.9 ± 0.3	0.06 ± 0.04	$0.22^{+0.19}_{-0.10}$	100	110 ± 10	90 ± 20	15	250	110 ± 30
31787	0.202	9.7 ± 0.1	11.5 ± 0.2	0.5 ± 0.2	0.08 ± 0.04	390	460 ± 10	130 ± 30	20	50	60* ± 30
A-48	0.383	9.6 ± 0.2	11.5 ± 0.3	< 0.04	< 0.01	40	40 ± 10	120 ± 30	10	600	210 ± 50
A-69	0.399	9.8 ± 0.2	11.6 ± 0.3	0.4 ± 0.2	0.06 ± 0.03	190	200 ± 10	130 ± 30	25	160	130 ± 40
A-36	0.536	10.9 ± 0.2	12.9 ± 0.7	6 ± 3	0.08 ± 0.05	120	140 ± 10	360 ± 190	55	140	650 ± 200
A-72	0.558	9.7 ± 0.5	11.6 ± 0.4	0.7 ± 0.2	$0.13^{+0.20}_{-0.08}$	430	530 ± 20	120 ± 60	40	150	60* ± 30
A-75	0.558	8.3 ± 0.4	10.9 ± 0.4	0.5 ± 0.1	2.3 ± 1.3	370	410 ± 20	80 ± 30	50	70	30* ± 10
A-32	0.876	10.6 ± 0.2	12.4 ± 0.6	7 ± 2	0.16 ± 0.11	600	740 ± 30	210 ± 100	40	160	50 ± 30
A-38	0.876	10.8 ± 0.3	12.6 ± 0.8	4.7 ± 1.1	0.08 ± 0.05	590	730 ± 40	250 ± 160	35	210	160 ± 100
B-19	0.907	10.4 ± 0.5	12.2 ± 0.8	1.1 ± 0.3	$0.05^{+0.10}_{-0.02}$	170	240 ± 20	170 ± 110	60	80	250 ± 160
A-16	0.907	10.4 ± 0.5	12.2 ± 0.9	2.3 ± 0.6	$0.09^{+0.18}_{-0.05}$	180	230 ± 30	170 ± 120	60	150	250 ± 170

differences are highlighted here.

Outflows

Table 5.7 lists the possible outflows that can reproduce some of the Lyα absorption seen near these groups of galaxies.

The possible outflows have model parameters that are generally consistent with our results from Paper 2, with a range of half-opening angles extending to $\approx 60°$ and velocities mostly between 50 and 250 $\mathrm{km\,s^{-1}}$ (excepting the proposed A-48 outflow, for which our best estimate is 600 $\mathrm{km\,s^{-1}}$ but much lower velocities of ~ 200 $\mathrm{km\,s^{-1}}$ lie within the 1σ range, as the galaxy is very close to edge-on). The larger number of possible outflows over our Paper 2 result is due to a larger number of galaxies in the vicinity of each absorber.

There is also very little difference in the extents of these outflows (median 200 kpc in groups, 180 kpc isolated; mean 280 and 270 kpc), whether or not these are normalized to the virial radius (mean extent $\approx 1.9\ r_{vir}$ and median $\approx 1.5\ r_{vir}$ for both samples). The median impact parameter to our putative outflows is similar to the median impact parameter between detected H I and the nearest galaxy (190 kpc). This supports the existence of outflows extending to at least the virial radius from isolated and group galaxies, more similar to those in the FIRE simulations with cosmic rays included (e.g. Hopkins et al., 2021), than other models suggesting outflows rarely extend past the virial radius.

Using our best-fit results, seven of the eleven possible outflows would exceed escape velocity were the galaxy isolated, comparable to the two of four outflows exceeding escape velocity in Paper 2. Although the very small sample in Paper 2 provided some suggestion of a correlation between sSFR and v/v_{esc}, we do not find a significant correlation using the larger sample here ($\approx 1\sigma$). Schroetter et al. (2019) note that the outflows they find using Mg II absorption tend to only exceed escape velocity from low-mass galaxies ($\mathrm{M_\star/M_\odot} \lesssim 10^{9.6}$). Whilst our two model outflows from galaxies with smaller masses than this do indeed appear to exceed escape velocity, several of our higher-mass galaxies also exhibit outflows exceeding their escape velocities. These outflows are probed at scales larger than the virial

radius, whereas our two outflows around large galaxies probed on scales $< r_{vir}$ do not achieve escape velocity. This appears to support the continued acceleration at large radii seen in the simulations by Hopkins et al. (2021) with cosmic rays included, although, as they discuss, only the material near or above the escape velocity would be capable of reaching these scales in the absence of additional acceleration.

In Paper 2, we noted that the model outflows in Schroetter et al. (2019) did not feature opening angles as wide as the 45-60° found in our isolated sample, possibly due to their stellar masses tending to be larger and resulting in an increased collimation effect. Our group sample includes a larger number of high-mass galaxies, especially at high redshifts, and our model half-opening angles remain large for these galaxies. However, our models suggest narrower outflows provide a better fit to the galaxies at lower redshift, which also tend towards lower masses, opposite to the trend expected due to collimation. This trend may be weaker than it appears, as some of the higher-redshift objects (in the A-16 and A-32 groups) are unresolved and the absorber width does not help to constrain the outflow opening angle.

If those relying on unresolved absorption are removed, our total (group and isolated) sample of outflows has opening angles much more similar to those seen in Schroetter et al. (2019), but still shows a trend of wider outflows at higher masses and redshifts. It is unclear whether the redshift or mass difference is contributing to the difference in opening angle, but there are observations suggesting that outflows at higher redshifts are closer to isotropic with respect to the galaxy (e.g. Chen et al., 2021).

Disks

We show the best-fitting parameters for absorption fit by our disk model in Table 5.8.

The successful disk-like structures also appear similar to our results from Paper 2, with scale height ratios from 10 to ∼300, and extents ranging from less than 100 kpc to more than 1 Mpc. The average extents (≈300 kpc) are also similar. However, we find substantially smaller circular velocities than around isolated galaxies (by $\approx$ 270 to 120 $\mathrm{km\,s^{-1}}$median, or 3 v_{vir} to 1), and also produce a better fit using

Table 5.8: Model disk properties around galaxies for which disks can reproduce some of the observed absorption components. Column descriptions: (1)-(4) are from Table 5.2; (5) model scale height ratio (i.e. relative disk thickness); (6) maximum impact parameter at which this structure is detected (7) maximum observed disk extent (the 3-d distance from galaxy to the point on the line-of-sight where it intersects the disk plane, for the sightline with largest impact parameter with detected absorption); (8) virial radius; (9) virial velocity; (10) model circular velocity; (11) model radial/infall velocity.

Galaxy	z	$M_\star$ $\log_{10}(M_\odot)$	M_h $\log_{10}(M_\odot)$	h_r/h_z	b_{max} (kpc)	Extent (kpc)	r_{vir} (kpc)	v_{vir} ($km\,s^{-1}$)	v_ϕ ($km\,s^{-1}$)	v_r ($km\,s^{-1}$)
(1)	(2)	(3)	(4)	(5)	(6)	(7)	(8)	(9)	(10)	(11)
32778	0.202	10.2 ± 0.1	11.8 ± 0.3	20	410	420 ± 10	170 ± 60	130 ± 50	150	< 20
29214	0.238	8.9 ± 0.1	11.1 ± 0.3	40	240	240 ± 10	100 ± 20	70 ± 20	100	30
A-49	0.383	8.7 ± 0.6	11.1 ± 0.4	200	410	410 ± 10	90 ± 50	80 ± 40	170	< 20
A-69	0.399	9.8 ± 0.2	11.6 ± 0.3	100	190	730 ± 300	130 ± 30	110 ± 30	150	40
A-40	0.536	9.4 ± 0.4	11.4 ± 0.3	100	400	460 ± 60	110 ± 40	100 ± 30	110	70
A-75	0.558	8.3 ± 0.4	10.9 ± 0.4	70	180	290 ± 60	80 ± 30	70 ± 20	90	50
A-32	0.876	10.6 ± 0.2	12.4 ± 0.6	20	100	110 ± 10	210 ± 100	230 ± 130	100	< 20
A-38	0.876	10.8 ± 0.3	12.6 ± 0.8	10	80	90 ± 10	250 ± 160	250 ± 160	80	90
B-19	0.907	10.4 ± 0.5	12.2 ± 0.8	20	170	250 ± 50	170 ± 110	190 ± 120	130	40
A-16	0.907	10.4 ± 0.5	12.2 ± 0.9	20	180	290 ± 70	170 ± 120	200 ± 130	100	50

smaller infall velocities for our group models. These infall velocities are often better constrained than for isolated galaxies (for which we generally assumed an infall velocity of $0.6v_{vir}$), as with more high-column density absorption in groups it is more likely that multiple absorbers can be fit by a single model.

Given the small sample size, especially around isolated galaxies, this $\approx 1.5\sigma$ difference in circular velocity may simply be due to the galaxy properties and sightline configurations that feature in the sample (although the extents and impact parameters are similar). The assumed infall velocity for isolated galaxies, and its effect on the rotational velocities required to fit the observed absorption, may also contribute, but changing this assumption will increase the rotation velocity for some models and decrease it for others.

A real difference between circular velocities of accreting material onto isolated and group galaxies may be detected here, but it is difficult to demonstrate when using absorption at only one or two locations around each galaxy. For example it is possible that, rather than seeing absorption due to gas falling onto one of the individual galaxies within our groups, we are seeing material falling into the group halo, which would likely extend further than the halo of an isolated galaxy of the same stellar mass as one of the group galaxies. Interaction between infalling material and group gas could slow its apparent velocity and contribute to the observed difference (as a similar interaction between the CGM and galaxy ISM appears to cause velocity lag in the ISM, Bizyaev et al. 2022). Alignment between the group galaxies and large-scale structure (e.g. Tempel & Libeskind, 2013; Zhang et al., 2015; Hirv et al., 2017) could lead to accretion at larger scales looking similar to accretion onto an individual galaxy (possibly supported by several of our groups featuring multiple galaxies with similar position angles, most noticeably G-383 and G-876). Accretion from large-scale structure into a galaxy group may also have been observed by Bielby et al. (2017).

Azimuthal angle dependency

We also briefly note that attempting to identify disks and outflows purely by cutting in position angle and inclination (as in e.g. Bordoloi et al., 2011; Zabl et al., 2019;

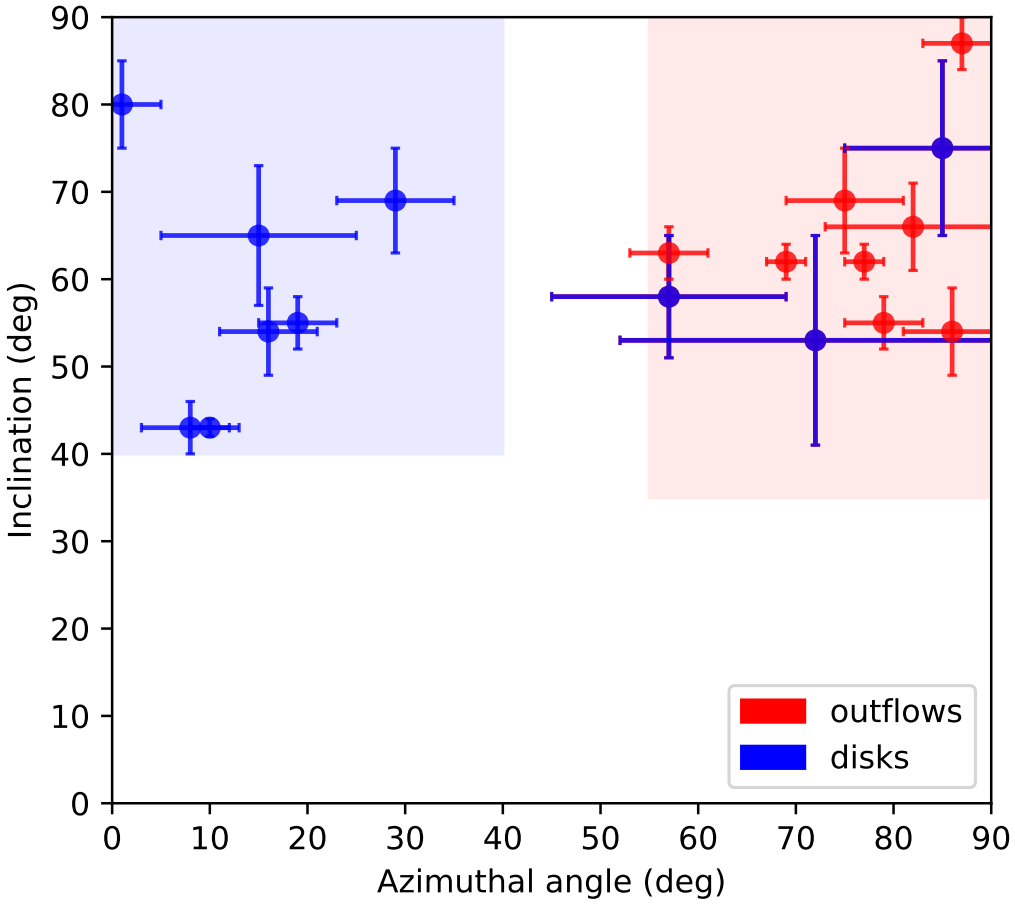

Figure 5.6: Azimuthal angle against inclination for galaxy-absorber pairs in our sample. Absorbers identified as probing a possible outflow are shown in red, with disks in blue. We also shade the regions used to identify the 'primary' disk and outflow subsamples in MEGAFLOW in blue and red respectively (Zabl et al., 2019; Schroetter et al., 2019).

Schroetter et al., 2019) produced results inconsistent with our models when applied to our Paper 2 sample of isolated galaxies, although our models were more likely to support disks and outflows near the major and minor axes respectively. We apply this same cut here, and show the results in Figure 5.6.

All of our model outflows lie in the region that would be identified as such using these geometric cuts, whilst our model disks spread over both regions. These results reinforce our conclusions from Paper 2, showing that these geometric cuts are useful but are unlikely to produce pure disk or outflow samples.

5.5.3 Correlations between group size and absorption

Whether the gas around galaxy groups results primarily from a superposition of the CGM of the individual galaxies, or from stripped material, increasing the number of galaxies in a group is expected to increase the column densities of gas seen around the group. It is therefore unsurprising that we find a correlation between the number of galaxies in a group, and the number of H I absorption features identified within a 500 $\mathrm{km\,s^{-1}}$ window. We also find a strong correlation between the column density of an absorber, and the number or total mass of nearby galaxies (using any combination of a 500 or 300 $\mathrm{km\,s^{-1}}$ window in redshift and 300, 500 or 1000 kpc in impact parameter), with Spearman co-efficients suggesting $> 95\%$ confidence in all of these cases. These correlations also persist if we consider only absorption in the COS spectra, or only that in the FOS spectra, so is present across our redshift range of $0 < z < 1$ and is not impacted by the presence or lack of faint galaxies and weak absorption visible only at low redshifts.

The total stellar mass of nearby galaxies to each H I absorber (using a 500 $\mathrm{km\,s^{-1}}$ velocity window and 1000 kpc impact parameter cut) is shown in Figure 5.7. There is no significant difference between the number or total mass of nearby galaxies surrounding absorbers identified as disks and those identified as outflows using our toy models (using any of the above cuts). As in Paper 2, we find no significant difference between the column densities of disk and outflow absorption. We do find a small difference in Doppler widths (outflows with median ≈ 50 $\mathrm{km\,s^{-1}}$, disks ≈ 40 $\mathrm{km\,s^{-1}}$), but large uncertainties due to unresolved absorption mean that this is also not significant.

The absorbers within these groups that could not be fit using either model have higher H I column densities and exist in more massive groups, although the significance is again limited by a small sample size. If these consist of material that has been ejected from galaxies and forms an intra-group medium, this would likely be more prevalent in denser, more massive groups with more interactions between galaxies, as is found here.

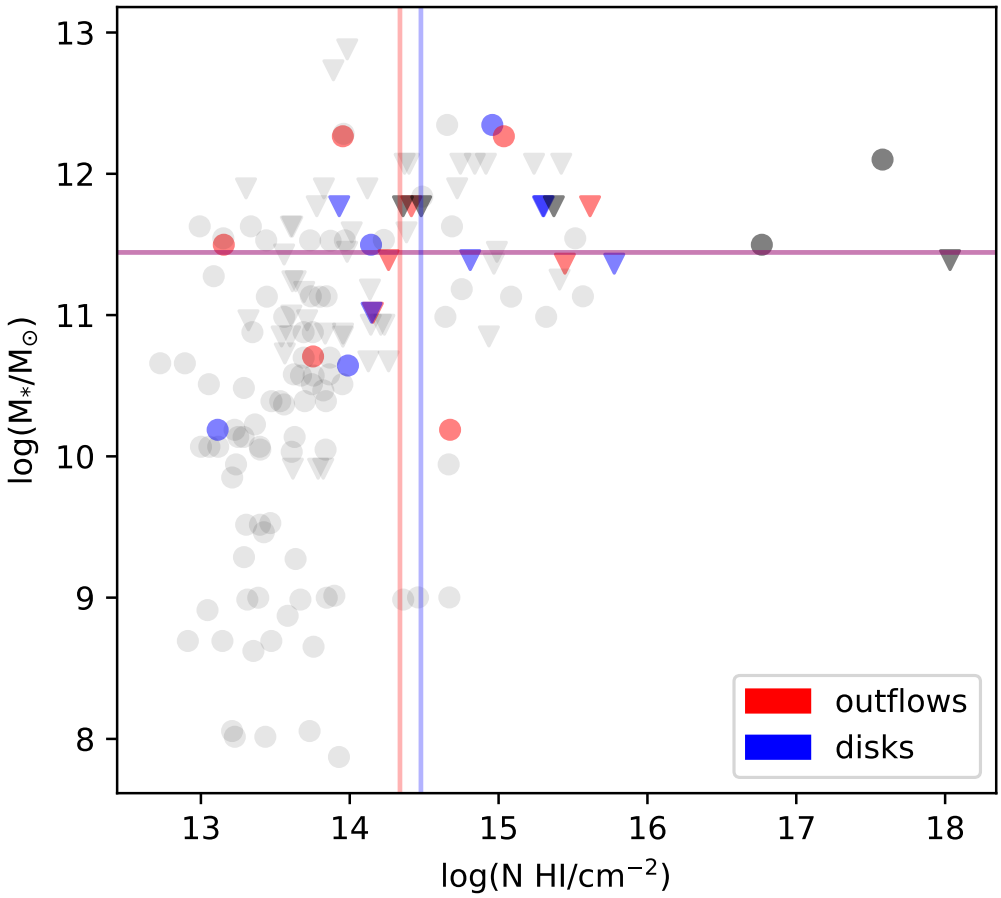

Figure 5.7: Column density against total galaxy stellar mass found within 500 km s^{-1} and 1 Mpc of H I absorbers. Faded points show our full sample of detected H I absorption, whilst bold points show absorbers within 500 km s^{-1} of the galaxy groups considered in this work. The bold points are also coloured by the best-fitting model type, with bold grey points showing absorption that could not reasonably be fit by our models. Faded lines show the median for each model type in both measurements. We have also split the sample by redshift, with absorption found in the FOS spectra shown with triangles, and those in the COS spectra with circles.

5.5.4 Galaxy interactions

Tidal interactions between galaxies in groups are expected to strip gas out of the galaxies, which should be detectable (e.g. Morris & van den Bergh, 1994). Streams of stars and gas attributed to tidal effects are seen around nearby galaxies (e.g. Majewski et al., 1996; Ibata et al., 2001; Foster et al., 2014; Sorgho et al., 2019), and there are suggestions of observed tidal material around more distant galaxies using emission lines (e.g. Epinat et al., 2018; Johnson et al., 2018). However, identifying this material in absorption is challenging. By considering absorption that could not be reproduced using our toy models, and by looking at close pairs of galaxies most likely to be interacting, we attempt to identify tidal material in our observations.

Although not included in the main sample due to the difficulty of fitting position angle and inclination measurements, the Q0107 field features a clear ongoing galaxy merger, denoted B-39 and illustrated in Figure 5.8. We do not attempt to fit our disk/outflow models to this merger. Additionally, the absorption at this redshift is blended with Lyβ from z $\approx$ 0.72, making it difficult to identify associated Lyα components.

The VPFIT results suggest two weak components in sightline A, one close to the merger systemic redshift and another $\approx$120 km s^{-1} redward, and one stronger component in sightline C, with a small blueshift relative to the systemic redshift. Based on the directions and velocities of the stellar arms/streams seen in the Figure, absorption from an extension of these streams would have the opposite velocity offset to that observed in both of these lines-of-sight.

However, given the lack of other nearby galaxies, it seems likely that at least some of the absorption observed can be attributed to the interaction between these galaxies, possibly on a previous pass between these galaxies such that their orbits have changed the line-of-sight velocity relative to the large-scale absorption. Simulations suggest stripped gas may be found opposing the direction of motion, depending on the orbital configuration (Rodríguez et al., 2022), so tidal material cannot be ruled out.

Several absorbers around the galaxy groups we consider in this work can not be reasonably approximated by our disk/outflow/halo toy models. If a large propor-

tion of these absorbers are due to tidal material, these would likely be found more frequently near to close galaxy pairs. However, we do not find any significant difference between the closest pair separations of groups with unexplained absorption, and those for which all absorbers can be fit by our models.

Despite the lack of evidence for absorption due to interactions between galaxies across the sample as a whole, we can still look individually at these unexplained absorbers and consider whether tidally-stripped material can provide a reasonable explanation.

The unexplained absorption in G-202 has a velocity offset close to our cut-off of 500 $\mathrm{km\,s^{-1}}$, and is therefore likely associated with other galaxies (its high column density making a physical association with at least one galaxy likely, see e.g. T14 and Paper 1). However, B-22 does appear distorted, with a tail of extended emission visible in the direction of LOS-B. Tidal material is therefore a possible explanation for some of the absorption in this sightline, but this absorption is reasonably approximated by our toy models.

The sub-DLA near G-558 could not be fit using our models, and likely has an undetected host galaxy much closer to the line-of-sight than the detected group of galaxies.

Strong, metal-enriched absorption in G-399 lies at a velocity between the two large galaxies in this group. As discussed in Anshul et al. (2021), this contains a warm component as well as a cooler gas phase. This is consistent with intra-group material, lying within r_{vir} of the largest group galaxy, and could be tidal in origin.

The galaxies A-36 and A-37 are close together ($<$ 10 kpc, with A-40 a more distant companion), and appear distorted in the HST image, suggesting that they are interacting. The unexplained absorption components all lie blueward of all three galaxies, but have a much larger velocity offset than the velocity difference between the galaxies. This would suggest that this absorption does not identify material ejected by the interactions between these two galaxies. This absorption may be associated with the more massive, but distant, galaxies with a smaller velocity offset.

Therefore, in the four galaxy groups with unexplained absorption, stripped material appears a reasonable hypothesis for two, only one of which contains a nearby

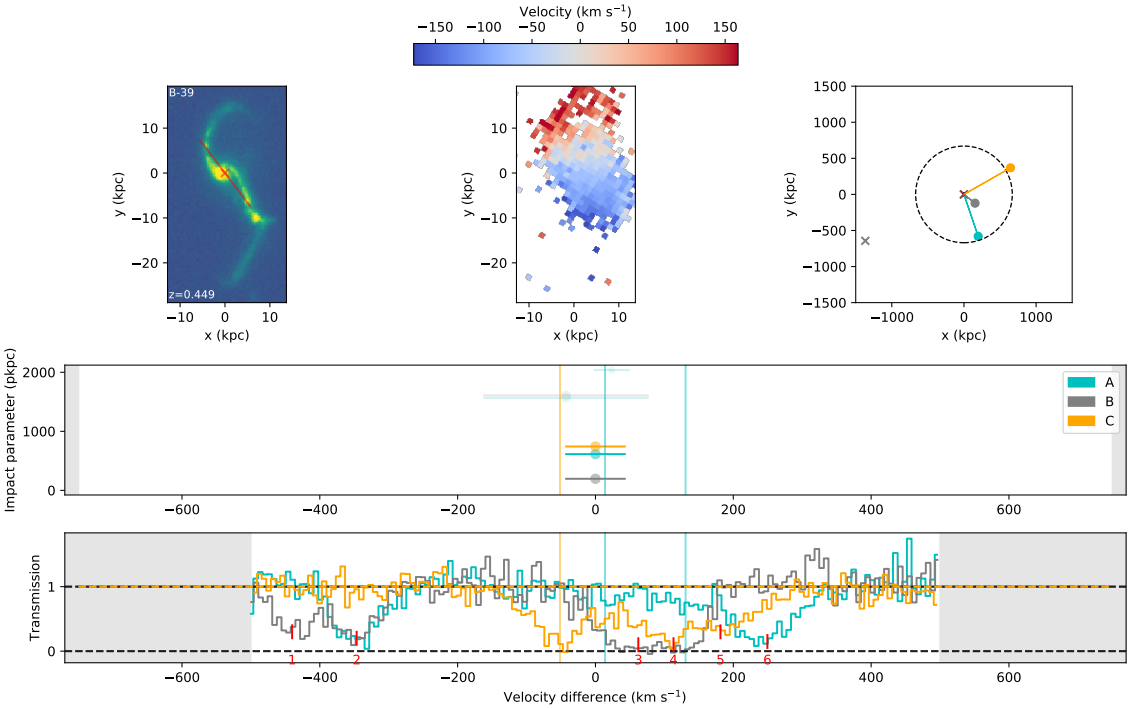

Figure 5.8: Details of the absorption and galaxy environment around the galaxy merger B-39 at z ∼ 0.45. The layout is identical to that shown in Figure 4.4, but no model is shown as the position angle and inclination of these galaxies could not be measured. The galaxy kinematics are measured from the [O III] emission line seen in the MUSE data. Tick marks (1) and (2) show the Lyman n=6 transition from z ≈ 0.88; whilst (3)-(6) show Lyβ from z ≈ 0.72.

pair of galaxies that is likely interacting.

Stronger evidence for tidal material could come from absorption in the direction of visible stellar streams, or material that lies between the interacting galaxies in velocity and in projection on the sky. This is not the case for the groups in this study, so whilst tidally-stripped gas may be the most likely explanation for a small fraction of absorbers, we do not have good evidence of its detection in this work.

5.5.5 Metal absorption

Around the twelve isolated galaxies in Paper 2, only two of the H I absorbers also featured metal absorption around the same galaxy. However, many of the absorbers detected here in galaxy groups do feature metal lines, most commonly C III and O VI, despite similar coverage and signal-to-noise ratio. This is consistent with our results from Paper 1, with O VI detections only appearing at impact parameters <

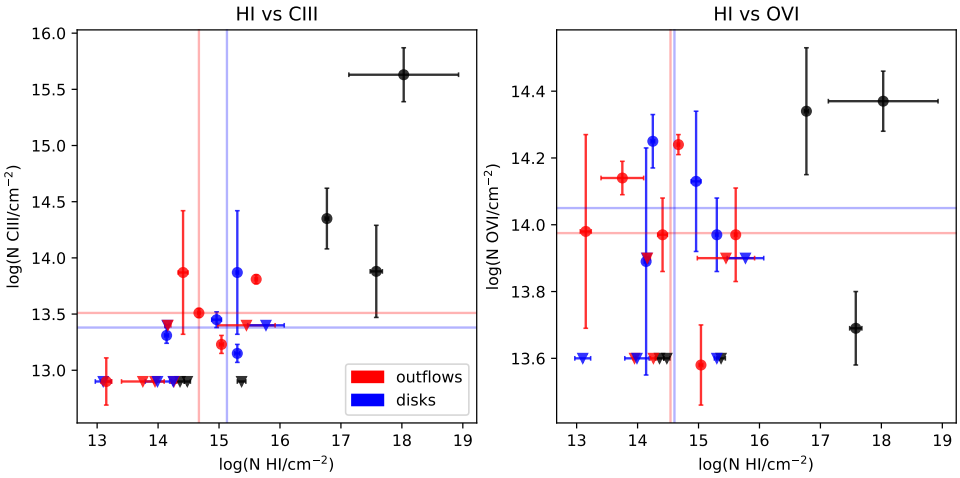

Figure 5.9: Column densities of H I, C III and O VI absorption found within 500 km s^{-1} of our group galaxies. Only metals within 30 km s^{-1} of detected H I are included. Upper limits where metals are not detected are shown by downward-pointing triangles. Points are coloured by best-fitting model type (disk, outflow or none). The median column densities of absorbers with detected metals are shown along each axis.

350 kpc from non-group galaxies [1], whereas O VI was found to be more extended in group environments (e.g. Johnson et al., 2015; Tchernyshyov et al., 2021).

Figure 5.9 shows the column densities of C III and O VI associated with H I absorbers around our galaxy groups, coloured by the type of model that provides the best fit to that absorber. In both cases there is no significant difference in either the H I or metal column densities between the two models. This would suggest that, if our simplified models are indeed indicative of outflow cones and accreting disks around these galaxies, the accreting material does not have significantly different metal content than the outflowing material.

With its lower ionization stage, it is unsurprising that C III correlates more strongly with H I than O VI. We find with $> 99\%$ confidence (using a Spearman rank with non-detections included or excluded) that the column densities of H I

[1]Note that this uses the friends-of-friends algorithm to discriminate between group and non-group galaxies as described in Paper 1. This differs from the definitions of 'isolated' and 'group' galaxies used in Paper 2 and this work in that the linking lengths used in Paper 1 vary with redshift in order to correct for the changing detection limit with redshift, and exclude MUSE galaxies in order to achieve consistent detection limits across the field. The average linking lengths are comparable to the 500 km s^{-1} and 500 kpc used here.

and C III are correlated, although we note that this correlation is not significant if absorbers that could not be fit by our toy models are excluded. There is not a significant correlation with O VI column density. The CGM/IGM is known to be multi-phase (e.g. Tripp et al., 2008; Werk et al., 2014; Concas et al., 2019; Anshul et al., 2021; Nateghi et al., 2021), and hence O VI likely probes a warmer phase of material than H I and C III, with warm outflows and halos often proposed (e.g Werk et al., 2016; Oppenheimer et al., 2016; Ng et al., 2019).

In isolated systems, accreting material would be expected to have a lower metallicity than that in outflows, due to enrichment of outflows through stellar evolution within the galaxy (e.g. Péroux et al., 2020). However, observations have often failed to detect a relationship between azimuthal angle and metallicity (e.g. Péroux et al., 2016; Kacprzak et al., 2019), possibly in part due to the mixing by azimuthal angle discussed in Paper 2 (and briefly in Section 5.5.2 of this work). Our sample from Paper 2 has too few metal detections to test this effect, but the numbers of O VI absorbers found along the major and minor axes using our full galaxy sample (Section 4.2 of Paper 1) do suggest higher metal content for minor-axis absorbers. It seems possible that, due to interactions between galaxies, metal enriched gas is more common around group galaxies, and therefore accreting material in group environments has metal content more similar to outflowing material than gas accreting onto isolated galaxies. However, other studies have found suggestions that low-metallicity gas can be masked by the presence of higher-metallicity gas in the line-of-sight (e.g. Pointon et al., 2019), which would allow our H I to be dominated by low-metallicity accretion despite strong metal detections with a different origin (e.g. warm halo, stripped material, intra-group gas).

We also note several high-column-density, metal-enriched absorbers that are not identified as disks or outflows. However, one of these is the sub-DLA in LOS-C, which likely has an undetected host galaxy and may not be strongly affected by the larger-scale environment. Another is close to 500 $\mathrm{km\,s^{-1}}$ offset from the galaxy group considered, and is therefore more likely to be associated with other galaxies at smaller velocity offsets. The third lies within the velocity ranged spanned by the nearby group, and could plausibly form part of an intra-group medium.

5.6 Chapter summary & conclusions

In this study we use multiple lines-of-sight to constrain the origins of H I absorption seen around 9 pairs and groups of galaxies at z < 1. By fitting simple disk, halo and outflow models around these galaxies we attempt to determine to what extent the absorption features seen in galaxy groups could be attributed to a superposition of the CGM around the individual galaxies, an extended intra-group medium, or material stripped from the CGM of the galaxies by interactions within the group. We model the absorption around nine galaxy groups in the Q0107 field, probed by three lines-of-sight, and find that:

i) Our disk and outflow models reproduce a slightly larger fraction of the identified H I absorbers where multiple galaxies are present ($\approx 75\%$) than around the isolated galaxies we consider in Paper 2 ($\approx 60\%$). This supports a model for which a superposition of absorption from the group galaxies results in the observed spectra. Sample variance and a larger parameter space (due to multiple nearby galaxies) appear to be plausible contributors to this higher success rate.

ii) Our 'group' sample includes systems with larger separations and lower masses than many previous works considering absorption around group and isolated galaxies. The larger number of galaxies also leads to a smaller impact parameter between absorption and the closest galaxy. Both effects may also contribute to our high success rate and resulting preference towards the superposition model.

iii) The best-fitting parameters for our model outflows are generally similar to those seen for isolated galaxies in our previous work (Paper 2, submitted), including several that appear to extend beyond the virial radius. However, a larger number of putative outflows have smaller opening angles; these galaxies preferentially have lower masses and redshifts than those with apparent wider outflows. This means our overall sample has parameters more similar to Schroetter et al. (2019), who use similar models for Mg II absorption.

iv) Our model disks have smaller rotation velocities than those around isolated galaxies (120 to 270 $\mathrm{km\,s^{-1}}$, $\approx 1.5\sigma$), despite similar impact parameters. This

may be due to interactions between infalling material and the extended group halo, but could also be due to the galaxy/sightline configurations sampled in this field. In order to constrain the rotation velocities, we have also had to assume an infall velocity in some cases, which may be distorting the results.

v) We do not detect any difference in the column densities of absorbers identified as likely disks and outflows, and their Doppler widths do not differ significantly. This matches our results from isolated galaxies in Paper 2. There does not appear to be a difference in the number or total stellar mass of galaxies in groups hosting these possible disks and outflows, although high-column-density absorbers do tend to be seen in denser galaxy environments (both in galaxy number and mass).

vi) Absorption that cannot be fit by our models does not occur more frequently in groups with a close pair of galaxies, and therefore does not provide evidence of material stripped by galaxy interactions. Tidally-stripped material is a plausible explanation for two of the four groups hosting these unexplained absorbers, but is not supported by additional evidence such as the absorption matching the velocity offsets between galaxy pairs or lying in the directions of possible tidal stellar features seen in the HST images.

vii) There is no significant difference between the C III or O VI contents of absorbers identified as disks and outflows. Whilst outflowing material is generally expected to be warmer and more metal-enriched, material accreting onto a group galaxy may have been recently stripped or ejected from another nearby galaxy, and thus be more enriched than accretion from the IGM onto an isolated galaxy. We do not find a significant correlation between H I and O VI column densities, which fits expectations of these ions tracing different gas phases.

This paper, alongside our previous works using the galaxy and QSO data covering the Q0107 field, demonstrates some advantages of using multiple lines-of-sight probing the gas around galaxies. In addition to being a highly-efficient way to build large samples of galaxy-absorber pairs, which we utilized to detect both a bimodality

in the azimuthal angle of these pairs and a preference for aligned angular momentum between gas and galaxies in Paper 1, these sightlines also provide some constraints on the possible CGM structures seen in absorption, and therefore the origins of absorbing material.

Through kinematic and column density considerations, we are able to rule out simple disk and outflow models for some absorption seen in the three sightlines, and tentatively identify some absorption as likely originating from disk or outflow structures. However, the large number of model parameters available when considering possible models in galaxy groups makes this identification yet more uncertain.

Searching for significant correlations between model parameters and galaxy/group properties will require a larger sample of such observations, probing a wider space of sightline configurations and group properties. Constraining more complex models encompassing a wider range of physical processes (entrainment of gas, changing ionization states, etc.) and therefore with a larger range of free parameters, will require a larger number of sightlines for each galaxy or group.

Obtaining datasets with such a large number of background sources will likely have to await future instruments able to utilize much fainter objects, such as those planned for the ELT. This CGM tomography is included in the science case for several of these (e.g. Maiolino et al., 2013; Evans et al., 2015; Marconi et al., 2021). Our work studying the Q0107 system therefore serves as a useful test case for techniques that can be applied to much larger samples (especially at higher redshifts) in the near future.

CHAPTER 6

Summary & Conclusions

This thesis describes a range of tests for the gas flows and structures seen around galaxies in different environments, using absorption measurements along multiple lines-of-sight alongside spectroscopic galaxy surveys. In this chapter we summarise the results of these tests as applied to the Q0107 system, and describe ongoing and future projects that can make use of these tests in order to improve our understanding of the CGM and IGM across a wider range of environments.

6.1 Summary of presented work

The gas around galaxies, incorporating both the CGM and IGM, has long been known to be a complex, multi-phase medium (e.g. Tripp et al., 2008; Werk et al., 2013; Mathes et al., 2014; Péroux et al., 2019; Chen et al., 2020a). Although emission-line maps are improving in sensitivity, it remains the case that most observations of this gas are made through absorption, covering only a pencil-beam through the gas around any individual galaxy, so the location and velocity of any absorption along the line-of-sight remain uncertain. In this thesis we have used multiple closely-spaced lines-of-sight alongside a wide and deep spectroscopic galaxy survey

to test several models of the gas distribution, taking advantage of constraints from observations at several locations around the galaxy.

Much of this work has focused on attempting to detect CGM structures, seen on small scales of $\lesssim$ 100 kpc, at larger distances, and constrain their properties and dependence on galaxy properties and environment as far as possible using absorption spectroscopy. This has involved both statistical tests of a large sample of galaxy-absorber pairs in the Q0107 field (described in Chapter 3), and more detailed modelling of disks and outflows around a smaller subset of isolated and group galaxies (Chapters 4 and 5 respectively). The main results of these works are summarized as follows:

i) H I absorption is found in multiple lines-of-sight at the same redshift in the Q0107 system than in a randomised ensemble of absorbers, indicating that the gas forms structures several hundred kpc in extent. Gas with high column densities ($> 10^{14}$ cm^{-2}) in multiple sightlines frequently appears at the same redshift as galaxies, whereas we do not find evidence that low-column-density absorption appears in structures reaching this extent. Absorption across multiple sightlines is also seen more frequently around star-forming galaxies, suggesting that stellar feedback may be producing some of these structures.

ii) Galaxy-absorber pairs (for H I absorption) exhibit a bimodality in position angle extending to $\approx$ 300 kpc, a little larger than the virial radius for most of the galaxies in our sample. This suggests that outflows and accreting flows reaching these scales are somewhat common. That a bimodality is also seen in O VI absorption, more heavily weighted towards galaxy minor axes, appears to support this, as does a tendency for major-axis absorption to exhibit angular velocity in the same direction as the galaxy.

iii) A sample consisting of only star-forming galaxies in our catalogue does not exhibit the bimodality in position angle that could be indicative of accreting and outflowing material, but this may in part be due to the smaller sample size. This bimodality once again becomes apparent when using a more restrictive 'strongly-star-forming' sample (using a threshold between $\approx$ 0.05 and

0.1 Gyr^{-1}). This suggests that this inflow/outflow dichotomy contributes to the overall bimodality seen on scales $\lesssim 300$ kpc, but is not ubiquitous among star-forming galaxies. The excess absorption seen on larger scales may also be partially due to these outflows, although we note that our star-forming galaxies are biased towards higher redshifts than the passive galaxies. Therefore any evolution in the state of the CGM/IGM with redshift could contribute to this excess absorption around star-forming galaxies, although any such evolution is expected to be small (e.g. Chen, 2012).

iv) Simple disk and outflow models (assuming constant velocities, simple geometries, and covering fraction of unity) can approximately reproduce $\approx 50\%$ of absorption features seen within 500 $\mathrm{km\,s^{-1}}$ of isolated galaxies, rising slightly to $\approx 60\%$ of features within 300 $\mathrm{km\,s^{-1}}$. The use of multiple lines-of-sight enables stronger constraints on the model parameters than would be possible using a single sightline, as the absorber column densities and kinematics are constrained at multiple locations. This allows us to better determine the origins of absorption in the CGM/IGM.

v) These models reproduce a slightly larger fraction of the identified H I absorbers where multiple galaxies are present ($\approx$75%). This supports a model in which a superposition of absorption from the group galaxies results in the observed spectra, but allows for a substantial contribution from tidal and intra-group material. Sample variance and a larger parameter space (due to multiple nearby galaxies) appear to be plausible contributors to this higher success rate, but our models are more successful among groups with fewer galaxies, suggesting that the increased parameter space is not the largest contribution. Impact parameters between absorption and the closest galaxy tend to be smaller around galaxy groups, which may also contribute to the success of our models.

vi) Four of the twelve isolated galaxies considered exhibit absorption consistent with a bi-conical outflow, of which at least two must extend beyond the virial radius in order to fit the observed absorption. The four putative outflows primarily have velocities ~ 100 $\mathrm{km\,s^{-1}}$, with those around the galaxies with higher

sSFR exceeding escape velocity, whereas those with lower sSFR do not. For two of these outflows, allowing the velocity or flow rate to decrease as the outflow extends further from the galaxy would likely improve the fit over our toy models (which constrain both of these values to be constant). The best-fitting model parameters for outflows around group galaxies are generally similar to those around isolated galaxies. However, putative outflows in groups often appear to have smaller opening angles; this effect is primarily driven by galaxies with low masses and redshifts.

vii) Our disk models, incorporating rotation and infall, can reproduce absorption features around five of our isolated galaxies, but must sometimes extend beyond the virial radius to do so. Three of the disk models are constrained to have a circular velocity larger than v_{vir} under most plausible assumptions of inflow velocity. These are therefore not likely to form physical disk-like structures, despite the disk model fit. We note that the disk model features a larger number of free parameters than the outflow and halo models, so 'coincidental' fits are more likely, but we cannot rule out absorption due to an unseen companion galaxy contributing around these galaxies. In groups, our model disks have smaller rotation velocities (120 to 270 $\mathrm{km\,s^{-1}}$, $\approx 1.5\sigma$), despite similar impact parameters. This may be due to interactions between infalling material and the extended group halo, but could also be due to the galaxy/sightline configurations sampled in this field.

viii) Two of the isolated galaxies feature no identified absorption within 350 $\mathrm{km\,s^{-1}}$. These are the least massive galaxy and the least star-forming galaxy in our isolated sample, consistent with correlations found between column density or covering fraction and r/r_{vir} or sSFR (e.g. Werk et al., 2014; Wilde et al., 2021; Huang et al., 2021). Our disk and outflow models fail to reproduce the absorption around a further two galaxies, despite substantial star formation. Whilst our toy models are over-simplified, relaxing some of the simplifying constraints (e.g. constant velocities, constant outflow rates) does not allow a plausible fit. These absorbers therefore have a different origin, possibly an undetected

companion galaxy.

ix) Only one of our isolated galaxies requires both a disk and an outflow in order to reproduce the identified absorption components. However, for several other galaxies the configuration of sightlines means that we would only probe one of these structures, so the CGM of these galaxies could features both a substantial disk and outflow. We therefore cannot determine whether disks and outflows frequently exist simultaneously around the same galaxy, which could constrain the timescales required for gas recycling. In galaxy groups, there are often several combinations of disk and outflow models that can fit any absorption feature, so we cannot determine whether both a disk and an outflow exist around the same galaxy.

x) As expected, absorbers found near the minor axis of a galaxy are more likely to be identified as outflows, and those near the major axis as disks, whether or not the galaxy is isolated. However, at moderate inclinations of $\approx$ 40 - 70°, some absorbers best fit by disk-like structures can be found close to the projected minor axis, and those best fit by outflows can be found down to 30° from the major axis. Geometric cuts using only azimuthal angle and inclination therefore do not appear sufficient to produce pure samples of disk and outflow absorbers.

xi) We do not detect any difference in the column densities of absorbers identified as likely disks and outflows, and their Doppler widths do not differ significantly. This is true for both our 'group' and 'isolated' samples. There does not appear to be a difference in the number or total stellar mass of galaxies in groups hosting these possible disks and outflows, although high-column-density absorbers do tend to be seen in denser galaxy environments (both in galaxy number and mass).

xii) Absorption that cannot be fit by our models does not occur more frequently in groups with a close pair of galaxies, and therefore does not provide evidence of material stripped by galaxy interactions. Tidally-stripped material is a plausible explanation for two of the four groups hosting these unexplained absorbers, but is not supported by additional evidence such as the absorption matching the

velocity offsets between galaxy pairs or lying in the directions of possible tidal stellar features seen in the HST images.

xiii) Only two of the H I absorbers near isolated galaxies feature detected metals at the same redshift, whereas a large fraction of absorbers in groups do show detected metals. There is no significant difference between the C III or O VI contents of absorbers identified as disks and outflows. Whilst outflowing material is generally expected to be warmer and more metal-enriched, material accreting onto a group galaxy may have been recently stripped or ejected from another nearby galaxy, and thus be more enriched than accretion from the IGM onto an isolated galaxy. We do not find a significant correlation between H I and O VI column densities, which fits expectations of these ions tracing different gas phases.

These results suggest that disks and outflows, although not ubiquitous, contribute substantially to H I absorption seen in the CGM out to ≈ 300 kpc. Alongside the bimodality in position angle seen in Chapter 3/Paper 1, minor axis O VI excess, major axis rotation, and the increased bimodality around 'strongly-star-forming' galaxies, we find disk and outflow models provide a reasonable fit to a substantial fraction of absorption around both isolated and group galaxies. The presence of both of these structures, likely evidence of gas recycling from galaxies into the CGM and back onto galaxies, is well-supported by observations of cool gas (e.g. Kacprzak et al., 2012b; Bouché et al., 2012; Tejos et al., 2021b) and predictions from simulations (e.g. Péroux et al., 2020; DeFelippis et al., 2020) on scales $\lesssim 100$ kpc.

However, in order to find a significant bimodality, we are currently forced to use large bins in impact parameter and galaxy samples covering a wide range of properties. We therefore cannot determine how this estimated extent varies when considering galaxies with different properties, at different redshifts, in different environments. Observations combining our current sample with archival data or new observations (where high-resolution imaging is available around quasar sightlines) would increase the sample size and allow us to better address this question.

In our results, both the excess absorption in multiple lines-of-sight around star-forming galaxies over non-star-forming galaxies, and some outflow models matching absorption at large scales, provide tentative support for models in which galaxy outflows extend substantially beyond the virial radius and into the IGM. Although large-scale outflows are thought to be necessary in order to explain the metal enrichment of the IGM (e.g. Aguirre et al., 2001; Booth et al., 2012), some simulations find that the effects of cosmic rays need to be included in order to produce such outflows with detectable levels of cool gas (e.g. Hopkins et al., 2021). However, even in this case the effects are dependent on the properties of the cosmic ray transport model included in the simulations (e.g. Butsky & Quinn, 2018). Further studies of gas properties and kinematics at these large scales will be required to determine whether such cosmic-ray effects have a substantial impact on the IGM.

We also find evidence of gas and galaxies featuring aligned angular momenta on scales larger than r_{vir}. Whilst simulations often predict co-rotating structures with substantial thickness (e.g. Ho et al., 2020; DeFelippis et al., 2020), the lack of location information on absorption along a line-of-sight makes it difficult to determine the geometry of such structures from observations. Our models assuming a disk-like geometry are often successful, and the use of the additional sightlines can provide some constraint on the disk thickness. However, the resulting properties vary substantially, for example the ratio between 'disk plane' and 'vertical' scale heights can be as small as 10 or as large as several hundred. We are not able to rule out alternative geometries, such as the 'wedge' predicted by (e.g. DeFelippis et al., 2020), filamentary structures with much lower covering fraction than a complete disk (e.g. Martin et al., 2019a), or tidal interactions near the plane of the galaxy rotation. Further work is needed to increase the significance with which large-scale co-rotation is detected and determine its origin and geometry, most likely requiring wide-field IFU observations around quasar sightlines in order to produce large samples with galaxy kinematics at large impact parameters.

However, we do not see any difference between the column densities or Doppler parameters of absorbers identified as disks and outflows by our toy models. This also holds if we were to use cuts in inclination and azimuthal angle similar to those

in MEGAFLOW (e.g. Schroetter et al., 2019; Zabl et al., 2019). Although metal content (in our work, mostly traced by O VI) was clearly generally higher along the minor axis, and absorbers near the minor axis were indeed best fit by our outflow models (and those near the major axis by disks), we found metal-bearing absorption also along the major axis and absorption near the minor axis was often best fit by a disk. These results emphasise the difficulty of robustly attributing absorption to infalling and outflowing material.

As we note in Chapter 4, the use of multiple lines-of-sight can greatly limit the allowed models, and therefore further sightlines would likely increase the confidence with which we can determine the origin of absorbing gas. This would allow further progress towards both estimating the fraction of absorption arising from these disk and outflow structures (possibly 50-75% based on the results in Chapters 4 and 5 of this thesis), and more accurately determining the properties of these structures (e.g. disk thickness and outflow opening angle). The prospects for obtaining such observations are discussed in Section 6.2.

6.2 Future prospects

The primary limitations on using and extending these techniques include the relatively small number of fields with such closely-spaced background lines-of-sight, and the extensive datasets required (high-resolving-power spectra, wide-field IFU kinematics, and high-resolution imaging). However, it is also the case that a small sample size limits the strength of any conclusions we can draw from our toy model results.

The first of these difficulties will remain so for some time, especially at low redshifts. Serendipitous alignment of multiple UV-bright background sources in projection is sufficiently rare that large samples of such sources are unlikely to be found without telescopes with substantially improved sensitivity. Unfortunately, missions proposed in this direction (e.g. the Large Ultraviolet Optical Infrared Surveyor, LUVOIR) are unlikely to be active until the mid-2030s or later. At higher redshifts, where Lyα transitions into the visible portion of the spectrum, quasars are

also more common, although deep galaxy surveys require far longer exposure times. As such, there are currently few fields with both galaxy and quasar data, with one example being the MUSE Ultra-Deep Field (MUDF, e.g. Lusso et al., 2019; Fossati et al., 2019b). Such fields are of great interest, due to the possibility of studying how the gas extent, position angle distribution, and success and parameters of disk and outflow models evolve with redshift.

This situation will be dramatically improved with the completion of 30m-class telescopes such as the Extremely Large Telescope (ELT) currently under construction. Not only will these telescopes be able to observe much fainter foreground galaxies, providing a more complete picture of the galaxy environment of observed absorption, but will also be able to use much fainter objects as background sources. This will greatly increase the number of fields with closely-spaced lines-of-sight. CGM/IGM tomography features strongly in the science case for several instruments being prepared for the ELT (e.g. Maiolino et al., 2013; Evans et al., 2015; Marconi et al., 2021), and will result in a large improvement over the relatively low-resolution studies using IGM tomography so far (e.g. Lee et al., 2018; Newman et al., 2020), which typically use sightlines separated by a few Mpc.

Furthermore, using fainter sources improves prospects of finding galaxies whose CGM is probed by an larger number of sightlines. This would allow more disk and outflow structures (as well as any other proposed models) to be observed in more locations, providing stronger constraints on model parameters and allowing more complex models, with more free parameters, to be tested.

The second difficulty, namely the extensive (and expensive) datasets required for such tests, can also be reduced by future telescopes and instruments. For example, BlueMUSE (Richard, 2019) will provide better spectral resolution over a larger field than MUSE, and will thereby offer galaxy kinematics more efficiently. It will also extend Lyα coverage to lower wavelengths, increasing the redshift range across which these studies can be conducted. BlueMUSE will also have improved sensitivity, and may allow the IGM to be detected using emission lines.

In the meantime, progress can be made by collecting data complementary to already existing observations. For example, our proposal for HST/COS UV obser-

vations of a z $\approx$ 1 QSO pair in the field of the Galaxy and Mass Assembly (GAMA) survey takes advantage of the fact that a wide, deep spectroscopic galaxy survey has already been conducted, so less observing time is needed to complete a galaxy-absorber dataset in this field. A similar view could be taken towards new galaxy surveys around fields containing background sources for which high-resolution archival spectra are already available.

The final difficulty we note would also be reduced somewhat by new observations, but also by improvements to the modelling process used. Increasing the level of automation in this process was not practical when producing this thesis, but would improve the rate at which galaxy-absorber groups could be modelled in future, and therefore allow a larger sample of such groups to be modelled. Ideally, this would involve a fitting routine that explores the model parameter space and finds the best model fit. However, as we discuss in Section 4.3, the large number of parameters and the complexity of dealing with blended absorption in multiple sightlines makes this challenging. A partial automation that can rule out some combinations of models may still provide some improvement and allow larger samples of galaxy-absorber groups to be modelled than the samples included in this thesis.

6.3 Final word

It is clear that the gas surrounding galaxies plays a vital role in how galaxies evolve, but its low density, complex structure, multiple phases, and the wide range of scales influencing its behaviour, have made it difficult to gain a complete understanding of the physics at play.

Studies using CGM emission are improving in sensitivity, especially in recent years, but the consistently high sensitivity across a large redshift interval enabled by absorption-line studies will likely remain an important tool for studying the CGM and IGM for some time. The inherent difficulty in determining the location of any absorption along the line-of-sight in turn leads to challenges in discriminating between its possible origins. Simulations also struggle to resolve the wide range of scales needed to model the various phases of the CGM and IGM; both sub-pc-

scale effects such as supernova feedback, and kpc- and larger-scale influences such as location within the cosmic web, are required to accurately simulate the CGM. The sub-grid models used in simulations to parameterise small-scale effects require tuning in order to match observed results.

Several important questions therefore remain unanswered, including the timescales required for gas recycling, the likelihood of outflows escaping galaxy halos (versus those recycled back onto the galaxy), the processes involved in the quenching of galactic star formation, the fraction of cool gas in outflows, the location of gas in galaxy groups, and any changes in these due to galaxy properties, large-scale environment or cosmic time. Understanding of these and other aspects of the CGM through absorption measurements will require some form of discrimination between infalling and outflowing material. Cuts in inclination and azimuthal angle are useful in this, but are unlikely to produce pure samples of disk and outflow absorbers.

The work in this thesis provides some evidence of large-scale rotating and outflowing structures in the CGM, suggesting that these structures can extend beyond the virialized halos of galaxies and supporting their existence in some galaxy groups. We also show that, where multiple sightlines are available, the kinematics and column densities can be used to rule out simple models, and thereby provide an alternative method for identifying such outflowing and rotating material. This work therefore represents a modest but valuable step towards understanding the gas flows and properties in the CGM and IGM, but for a more complete understanding we await future results.

APPENDIX A

Examples of GALFIT results

A.1 GALFIT results

Here we include some examples of our GALFIT results, in order to illustrate the utility of the modelling and the use of the quality flags described in Section 2.2.1. As illustrated in the Figures A.1 and A.2, the quality flags are based on the goodness of fit, not on the uncertainty in position angle or inclination. The flag 1 objects have no clear structure remaining in their residuals, flag 2 objects have minor structures, flag 3 objects may have major structures in the residuals that could indicate a poor estimate of position angle and inclination, and flag 4 objects are clearly a poor fit. Our tests in Section 3.3 are run using objects with flags 1-2 and 1-3, with similar results obtained in each case.

Figures A.3 and A.4 show all non-group galaxies with reasonable GALFIT results (at least flag 3) that exhibit O VI absorption within 500 $\mathrm{km\,s^{-1}}$. These illustrate the tendency for O VI absorption to be detected along the minor axis, as discussed in Section 3.3.2.

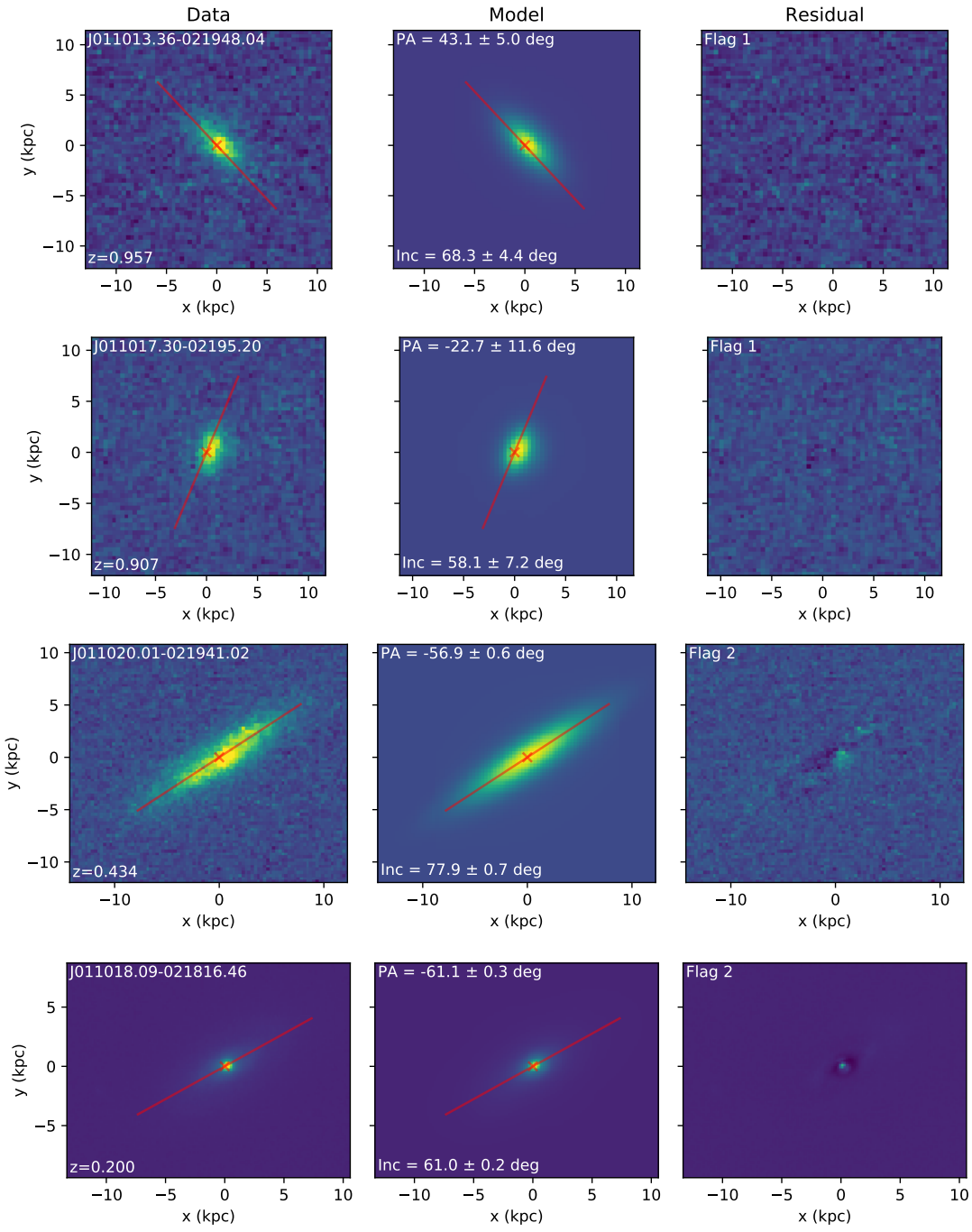

Figure A.1: Several examples of galaxy cut-outs resulting from our GALFIT modelling. Each row shows a single galaxy, with all three panels on an identical flux scale. The left panel illustrates the data from HST, the middle panel the best fit GALFIT model, and the right the residual. The galaxy ID and redshift, as well as the resulting position angle (relative to the HST image, which is not aligned with north), inclination and quality flag, are shown in the panels. The projected major axis, as determined by GALFIT, is shown by the red line.

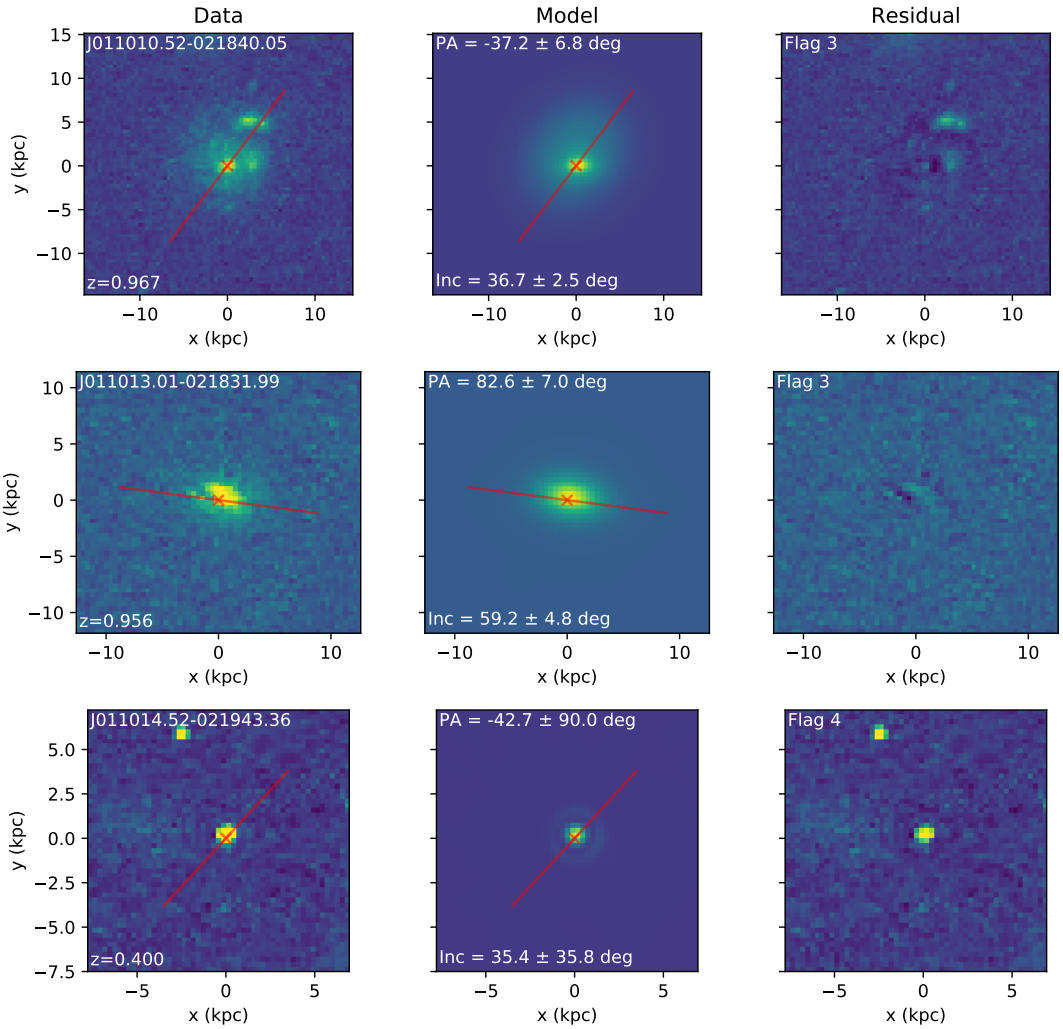

Figure A.2: Further examples of galaxy cut-outs resulting from our GALFIT modelling, as in Figure A.1

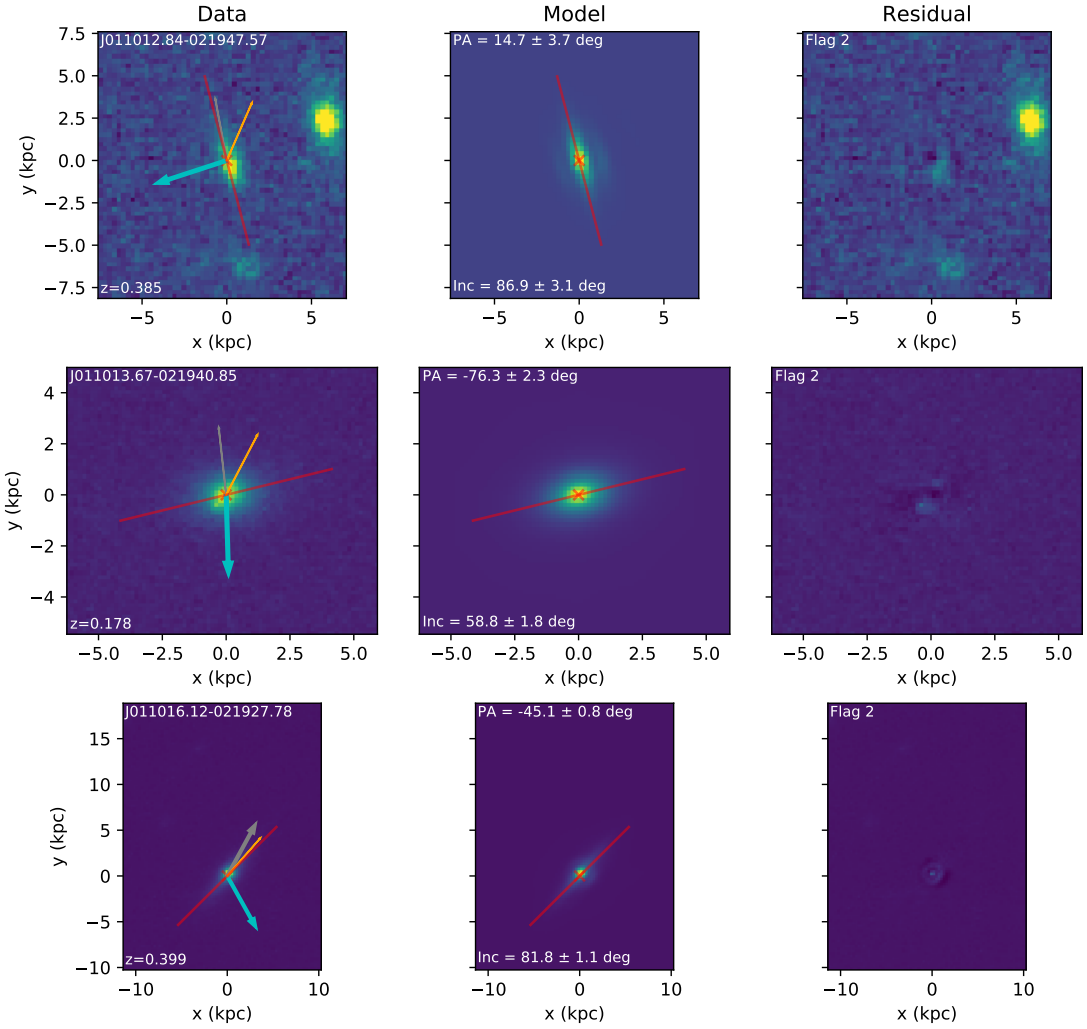

Figure A.3: Galaxy cut-outs resulting from our GALFIT modelling, showing galaxies not in groups, but with observed O VI absorption (as discussed in Section 3.3.2). Each row shows a single galaxy, with all three panels on an identical flux scale. The left panel illustrates the data from HST, the middle panel the best fit GALFIT model, and the right the residual. The galaxy ID and redshift, as well as the resulting position angle (relative to the HST image, which is not aligned with north), inclination and quality flag, are shown in the panels. The projected major axis, as determined by GALFIT, is shown by the faded red line. The three coloured stubs in the left-hand panel point the direction of the three QSOs, with cyan towards A, grey towards B, and orange towards C. The thick stubs with arrowheads indicate that that sightline exhibits detected O VI absorption within 500 $\mathrm{km\,s^{-1}}$, whilst the thin stubs without arrowheads inidcate non-detections of O VI.

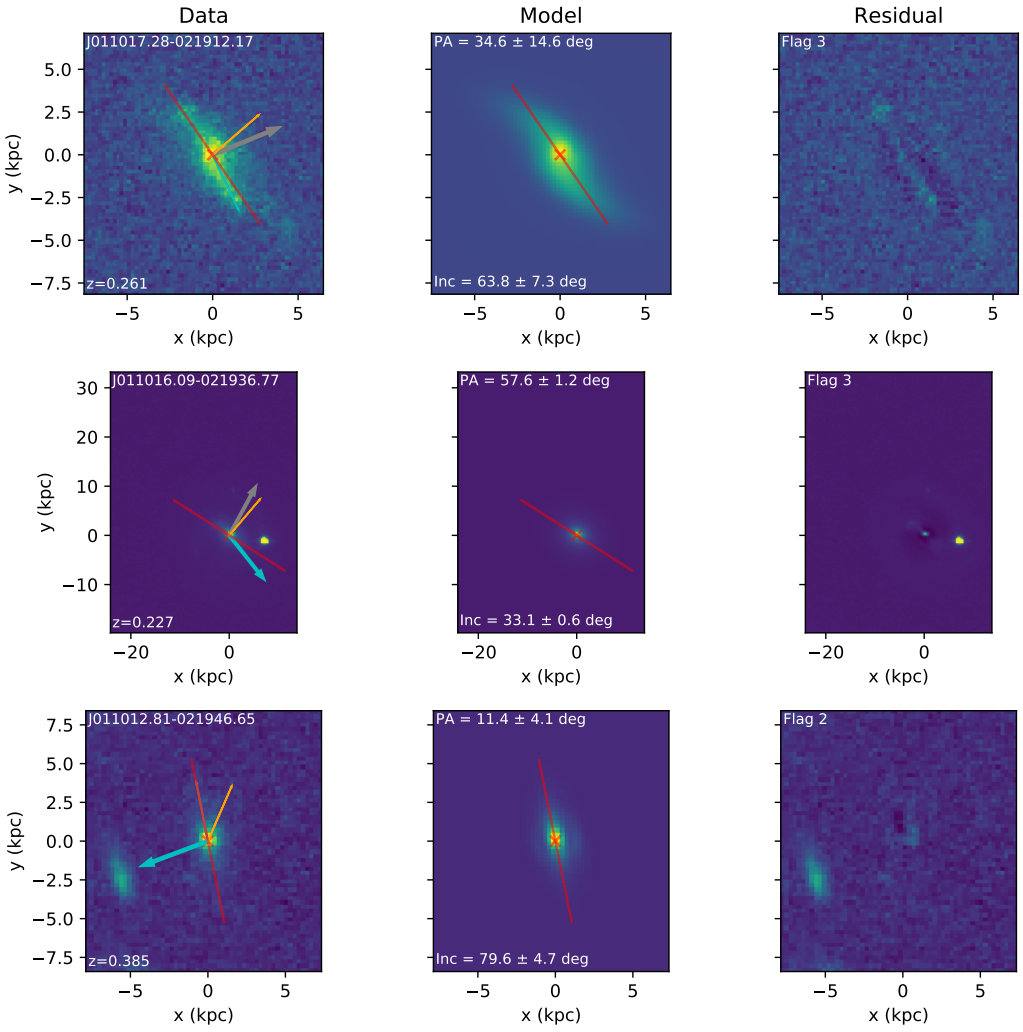

Figure A.4: Further examples of galaxy cut-outs of objects with O VI absorption detected within 500 $\mathrm{km\,s^{-1}}$, as in Figure A.3.

APPENDIX B

Model Details

Throughout the work described in this thesis, several of the processes we describe require involved computations that are too lengthy to include in the main text. These are detailed here.

B.1 Friends-of-Friends algorithm

In this section we describe the friends-of-friends algorithm used to find galaxy groups, and the calculations required to determine the linking lengths used. We use the analysis and results from Duarte & Mamon (2014) to motivate our choices.

For physical linking lengths $D_\perp$ and $D_\parallel$, any pair of galaxies at redshifts z_1 and z_2 (with d_c the comoving distance to that redshift), separated by an angle θ on the sky, are 'friends' if both of the following conditions are satisfied:

$$\frac{d_c(z_1) + d_c(z_2)}{2}\,\theta \;\leq\; D_\perp \tag{B.1.1}$$

$$\mid d_c(z_2) - d_c(z_1) \mid \leq\; D_\parallel \tag{B.1.2}$$

We scale the constant linking lengths – taken from Duarte & Mamon (2014) and

denoted b – by observed galaxy density, $D = b\,n^{-\frac{1}{3}}$, in order to account for the changing magnitude limit with redshift. In order to ensure that large groups do not bias the estimated density, we use large bins with a redshift width 0.2. Note that the angular diameter distance could be used in place of the comoving distance, and it could be argued that d_A should be used since galaxy groups are expected to be virialized. However, this also requires the line-of-sight linking length to be reduced by a factor of (1+z), and most studies do not apply this.

The comoving volume is calculated by integrating a conic section with an half-opening angle of 0.15°, through comoving distance between the redshift limits. This is approximately the radius of the DEIMOS data. MUSE galaxies are not counted in this process, as the greater depth of the MUSE data would bias the selection of groups in and around the MUSE fields (by adding galaxies to groups that would be undetected if they lay outside of the MUSE fields, and potentially joining groups together that would otherwise remain separate). By excluding these galaxies, the depth of VIMOS, DEIMOS and GMOS coverage throughout this aperture is close to constant.

$$V = \int_{d_c(z_{min})}^{d_c(z_{max})} \pi(\theta d_c)^2 \, d(d_c) \tag{B.1.3}$$

In each redshift bin, the number of observed galaxies is divided by the volume of the cone, to give the galaxy number density, which is converted to a linking length as above. Whilst the physical linking length is constant within a single bin, the angular separation and redshift difference are both affected by the galaxy redshift itself.

This algorithm is implemented by assigning each galaxy a group identifier. We then loop through each galaxy pair, and assign both galaxies the lower identifier if they are 'friends'. This is repeated until the sum of all identifiers converges (usually 3 to 5 iterations). All galaxies with the same identifier form a single galaxy group. Absorbers and the MUSE galaxies are associated with galaxy groups if they are 'friends' with any galaxy in that group.

Duarte & Mamon (2014) list three pairs of linking lengths, from which we use the larger, completeness-optimizing, values ($b_\perp = 0.2$, $b_\parallel = 3$). This results in

linking velocity differences of $\approx 800 - 1500$ km s^{-1} and transverse linking lengths of $\approx 800 - 1200$ pkpc. These linking lengths are large enough to allow a reasonable sample size of galaxy groups, as well as approximately matching the distance scales separating the three lines-of-sight. Such large linking lengths ensure that our non-group sample excludes any galaxies whose CGM is likely to be affected by ongoing group interactions.

We do repeat most analyses in Chapter 3 (those that require separation between group and non-group galaxies) whilst using the 'medium' linking lengths from Duarte & Mamon (2014), and this does not reveal any significant differences. Using the shortest linking lengths, we do not find enough groups to draw any conclusions.

B.2 Generating random absorbers

In Section 3.2, we test the excess of galaxy-absorber associations within a series of different constraints. Here we describe the process of generating the random sets of absorbers used in these tests, in which any physical association between gas and galaxies is removed.

We generated 5000 sets of randomly distributed absorbers similar to the method used in T14, as follows:

1. Calculate the signal-to-noise per resolution element for QSO spectrum
2. Convert this to minimum rest-frame equivalent width for the absorption feature as a function of redshift (see Figure 3.1)
3. For each real absorption feature, find the allowed region in redshift space for which the EW of the progenitor is larger than the minimum, and is not covered by galactic absorption
4. Distribute absorbers randomly through the allowed region, giving the random absorber the same properties as the observed progenitor

The signal-to-noise per resolution element is estimated by dividing the continuum value of the QSO spectrum by the uncertainty in the value of that pixel, and then

convolving with the line-spread function of the instrument. In order to improve execution time we use a box car of the correct FWHM as an approximation to the line-spread function.

The minimum observable equivalent width for an unresolved transition observed at wavelength λ is:

$$W_{min}(\lambda) = S\frac{FWHM}{\langle SNR\rangle_\lambda} \tag{B.2.4}$$

where FWHM is the width of the line-spread of the instrument, S is the significance required of the detection in units of sigma (where a value of 3 best matches the distribution of observed absorbers), and $\langle SNR\rangle_\lambda$ is the mean signal-to-noise per resolution element. If the resolution R = $\frac{\lambda}{FWHM}$ is constant:

$$W_{min}(\lambda) = \frac{S\lambda}{R\langle SNR\rangle_\lambda} = \frac{S\lambda_0(1+z)}{R\langle SNR\rangle_\lambda} \tag{B.2.5}$$

where λ_0 is the rest-frame wavelength of the transition. This gives a rest-frame equivalent width:

$$W_{min,r}(z) = \frac{S\lambda_0}{R\langle SNR\rangle_z} \tag{B.2.6}$$

We note that the lines in the COS spectra are usually resolved, with a median width b $\approx$ 30km s^{-1}. For these lines a more representative equivalent width limit can be found using the prescription given in Keeney et al. (2012), in which the optimal integration window is found using a convolution of the COS line-spread-function and the absorption line profile, rather than just the resolution of the instrument. However, many of the absorption features are narrower than this, so we continue to use the COS FWHM as a limiting value. This only has a notable effect on absorbers that are both weak and narrow, so only four absorbers of the 184 across the three COS spectra would have their allowed redshift ranges reduced by more than 15% if the Keeney et al. (2012) prescription were used.

From the absorption line catalogue (taken directly from T14), the best fit column density and Doppler parameter are given for each absorber. This can be robustly converted to an equivalent width via optical depth using the approximation given

in Draine (2011) (eqn 9.8, assuming negligible stimulated emission):

$$\tau_0 = \sqrt{\pi}\frac{e^2}{m_e c}\frac{n f_{osc}\lambda_0}{b} \tag{B.2.7}$$

where n and b are the column density and Doppler parameter of the absorber, λ_0 the rest-frame wavelength, and f_{osc} the oscillator strength. Draine then provides an approximation for equivalent width:

$$W = \sqrt{\pi}\frac{b}{c}\frac{\tau_0}{1+(\tau_0/2\sqrt{2})}(\text{for } \tau_0 < 1.25393) \tag{B.2.8}$$

$$W = \sqrt{\frac{4b^2}{c^2}ln(\frac{\tau_0}{ln2}) + \frac{b}{c}\frac{\gamma\lambda_0}{c}\frac{\tau_0 - 1.25393}{\sqrt{\pi}}}(\text{for } \tau_0 > 1.25393) \tag{B.2.9}$$

γ is the damping term of the Lorentzian component of the Voigt profile, which becomes non-negligible for high-column-density systems.

This value of equivalent width can then be compared with the minimum equivalent width detectable in the spectrum as a function of redshift, shown for QSO-A in Figure 3.1. We mask out the regions where the absorber would be undetectable due to insufficient equivalent width, as well as regions within 200 km/s of galactic absorption (as in T14, using C II, N V, O I, Si II, S II and Fe II). The region less than 3500 km/s blueward of the QSO is also masked, in order to remove most associated absorption. As found by Wild et al. (2008), $\approx 40\%$ of C IV absorption out to 3000 km/s is associated with outflows from the QSO, although absorption from outflows can extend beyond 10,000 km/s. The velocity cut used is therefore a compromise between excluding most absorption associated with the QSO, whilst excluding minimal intervening IGM absorption. This cut is also much larger than the region within which the proximity effect is significant (e.g Scott et al., 2002). Absorbers in this set that have already been placed are also masked using a window of 35 km/s (approximately the median width of H I absorption systems) so that systems that would not be resolved due to blending are not generated by this process. The absorber is then randomly assigned a redshift within the unmasked region.

B.3 Halo, disk and outflow models

Here we discuss in more detail the toy models used in Chapters 4 and 5 of this thesis, and how the observations and model parameters are used to derive the model absorption.

To derive the angles and distances required to work with toy models of the gas distribution, we define axes relative to the galaxy, such that $\hat{\boldsymbol{z}}$ lies along the galaxy minor axis, with $\hat{\boldsymbol{x}}$ and $\hat{\boldsymbol{y}}$ along the major axis, such that $\hat{x}$ is in the plane of the sky. If $\hat{\boldsymbol{z}}$ is defined to always have a northward component, $\hat{\boldsymbol{x}}$ and $\hat{\boldsymbol{y}}$ have westward and redward components, using the usual right-hand convention. (Note that these do not correspond to the x- and y-axis labels in the figures throughout this thesis.)

We measure relative to the centre of the galaxy O, considering the point where the line-of-sight intersects the plane of the sky (B) and the points A(D) a distance D along the LOS from B. $|\vec{OB}| = b$ for b the observed impact parameter. Therefore

$$\begin{aligned}\vec{OB} = S_W\, b\cos(p)\,\hat{\boldsymbol{x}} - S_N\, S_{Nr}\, b\sin(p)\cos(i)\,\hat{\boldsymbol{y}} \\ +S_N\, b\sin(p)\sin(i)\,\hat{\boldsymbol{z}}\end{aligned} \tag{B.3.10}$$

As both position angle p and inclination i are recorded as between 0 and 90 degrees, sign terms are needed to differentiate the possible orientations. S_W and S_N are 1 if the LOS lies west of the galaxy minor axis and north of the major axis respectively, and -1 otherwise (calculated from the coordinates of the galaxy and quasar). S_{Nr} is positive if the galaxy is inclined such that an outflow from the northern part of the galaxy would be travelling away from the observer. This is not constrained by the observations (although it is possible for one or two of our galaxies to constrain this through the direction of spiral arms, as in Ho & Martin 2019), but must be identical for different model structures around the same galaxy.

We then decompose the direction along the line of sight from B to A, a distance D along the LOS ($|\vec{BA}| = D$). Whether redward motion along the line of sight moves northward along the minor axis depends on the direction of the galaxies inclination:

$$\vec{BA} = D\sin(i)\,\hat{\boldsymbol{y}} + S_{Nr}\, D\cos(i)\,\hat{\boldsymbol{z}} \tag{B.3.11}$$

This gives the total displacement from the centre of the galaxy to a point a distance D along the line of sight from the galaxy:

$$\begin{aligned}\vec{OA} = (S_W\, b\cos(p))\,\hat{\boldsymbol{x}} + (D\sin(i) - S_N\, S_{Nr}\, b\sin(p)\cos(i))\,\hat{\boldsymbol{y}} \\ +(S_N\, b\sin(p)\sin(i) + S_{Nr}\, D\cos(i))\,\hat{\boldsymbol{z}}\end{aligned} \tag{B.3.12}$$

This is the relevant vector for determining the density at each point along the line-of-sight.

B.3.1 Halo model

The halo model density as a function of position depends only on the distance from the galaxy centre. The displacement in Equation B.3.12 correctly reduces to:

$$R = \sqrt{b^2 + D^2} \tag{B.3.13}$$

We consider a power law halo, with a density profile:

$$\rho = \rho_1 \left(\frac{R}{R_1}\right)^{-\alpha} \tag{B.3.14}$$

There is no line-of-sight velocity component, except that introduced in thermal/turbulent velocity components and the instrumental line-spread-function. The reference density ρ_1 is defined at $R_1 = 1$ kpc. We also allow the halo to be offset from the galaxy redshift by a velocity v_δ, accounting for any redshift uncertainty or real peculiar velocity. The halo model therefore has four free parameters:v_t, v_δ, ρ_0 and α.

B.3.2 Outflow model

The outflow model has the same density profile as the isothermal halo ($\alpha = -2$) if the polar angle is within the cone defined by θ_{in} and θ_{out}. This maintains a constant flow rate with distance from the galaxy (equivalent to a constant rate of mass-loading from the galaxy). This constant flow rate is consistent with results form EAGLE

(e.g. Mitchell et al., 2020a), but is not found in all simulations. We also do not consider any change in velocity due to gravitational or entrainment effects, or any change in the ionization state of the gas.

The projection of $\vec{OA}$ in the galaxy plane is given by:

$$r = \sqrt{(b\cos(p))^2 + (D\sin(i) - S_N\, S_{Nr}\, b\sin(p)\cos(i))^2} \tag{B.3.15}$$

and its projection along the galaxy minor axis is given by:

$$z = S_N\, b\sin(p)\sin(i) + S_{Nr}\, D\cos(i) \tag{B.3.16}$$

Note that z can be negative whilst r cannot.

The polar angle as a function of distance along the line-of-sight $\theta(D)$ is then given by $\tan(\theta) = r/z$.

For outflows, the bulk velocity of the gas is assumed to be entirely radial, so the velocity at the point A is along the vector $\vec{OA}$, and can easily be projected into the line of sight using $\vec{OA}.\vec{BA}$.

The outflow model therefore has parameters v_t, ρ_1, v_{out}, θ_{in} and θ_{out}, whilst S_{Nr} also affects the resulting model absorption.

B.3.3 Disk model

For disk structures, we also define the azimuthal angle in the disk plane, such that $\tan(\phi) = y/x$ (with y and x the components of $\vec{OA}$ in the disk plane). By construction, this means that ϕ is measured anticlockwise from y=0. This means that $v_y = \pm\, v_{circ}\cos(\phi)$ (the x component is perpendicular to the line-of-sight and the z-component is zero). This is positive if the line of sight is on the 'red' side of the galaxy minor axis, so can be stated as $v_y = S_W\, S_{Wr}\, v_{circ}\cos(\phi)$. We also allow a radial infall component within the plane of the disc, which must therefore have a y-component $v_y = -S_W\, v_r\sin(\phi)$. We add these components and project into the line-of-sight:

$$v_{LOS} = S_W\sin(i)\,(S_{Wr}\, v_\phi\cos(\phi) - v_r\sin(\phi)) \tag{B.3.17}$$

We note that setting z = 0, identifying the point at which the line-of-sight intersects the plane of the galaxy (and therefore the putative disk), reproduces the result given in Zabl et al. (2019) for their model thin disks:

$$R(z=0) = b\sqrt{1+\sin^2(p)\tan^2(i)} \tag{B.3.18}$$

This value (for the line-of-sight with largest b in which absorption is detected) is the disk extent given for model disks throughout the main text. The effect of the 'direction' of the galaxy inclination (S_{Nr}) is included in the calculation of ϕ.

We use an exponential model for the density profile (as used for velocity models in e.g. Steidel et al., 2002), with scale heights h_r and h_z along the major and minor axes respectively:

$$\rho = \rho_0 e^{\left(\frac{-r}{h_r}\right)} e^{\left(\frac{-|z|}{h_z}\right)} \tag{B.3.19}$$

This leaves our disk model with free parameters v_t, ρ_0, v_ϕ, v_r, h_r and h_z, one more than the outflow model. A disk may also have the additional degeneracy of the direction of rotation, if it is not determined by emission-line kinematics.

APPENDIX C

Modelling additional galaxies and groups

We have attempted to fit the absorption around several galaxies and groups using our 'toy' disk, halo and outflow models. In order to improve the readability of this work, only a small number have been included in detail in the main text (Chapters 4 and 5). The remainder of these modelled galaxy–absorber systems are discussed here.

C.1 Additional isolated galaxies

We detail here the modelling and results from additional isolated galaxies not included in the main paper (Paper 2, Chapter 4 of this thesis).

C.1.1 Galaxy 26732

Galaxy 26732 is a small (0.01 $L_\star$) galaxy at z $\approx$ 0.087. It is star-forming and lies $\sim$ 1 Mpc away from a pair of larger galaxies. There is weak absorption in LOS-A substantially blueward of the galaxy and slightly beyond the virial radius, and no detected absorption in B. (Note that C is not available due to the Lyman limit of a sub-DLA at z $\approx$ 0.56.)

The large impact parameter makes it unlikely that the absorption in LOS-A originates from either of the larger galaxies. Both available lines-of-sight lie near the major axis, suggesting a disk as the more likely model. However, this would require a remarkably large rotational velocity for such a small galaxy, in the region of 550 $\mathrm{km\,s^{-1}}$. (This can be varied by adding a substantial infall velocity component, but reducing the circular velocity to near the virial velocity would require a much faster infall than v_{vir}.) This galaxy lies outside the MUSE fields so galaxy kinematics are not available. Such a disk can approximately reproduce the absorption in A, without producing significant absorption in B.

Similarly, a wide, fast outflow with opening angle $\approx 50°$ could also produce the absorption in A whilst remaining consistent with the noise in B, but the velocity required is close to 450 $\mathrm{km\,s^{-1}}$. This is larger than all but one of the outflows proposed in Schroetter et al. (2019), and faster than the 90th-percentile velocities of outflowing gas in EAGLE outflows (Mitchell et al., 2020a). Given the weak absorption and large velocity offset, neither model is convincing and it seems more likely that this absorption is not physically associated with the galaxy. The line width of ≈ 50 $\mathrm{km\,s^{-1}}$ is larger than most IGM absorbers. If primarily due to thermal velocities, this indicates gas hotter than most detected absorbing gas, suggesting that this could be a WHIM detection.

C.1.2 Galaxy 25833

Galaxy 25833 is a small, non-star-forming galaxy at z $\approx$ 0.12, at the same redshift as two smaller galaxies $\sim$ 1 Mpc away. This is detailed in Table C.2 and Figure C.2. The only visible absorption lies close to 500 $\mathrm{km\,s^{-1}}$ blueward of the galaxy, and is relatively weak in both lines-of-sight. (The drop in transmission visible in the figure at +500 $\mathrm{km\,s^{-1}}$ is due to C III 977 Å from redshift z $\approx$ 0.4.)

Position angles and inclinations for the other galaxies are not measured, so outflows and disks around these objects cannot be modelled. Despite a smaller impact parameter, the absorption in A is weaker than that in B. A is also marginally closer to the minor axis, so an outflow with a sufficiently wide opening angle to produce the absorption in B would produce stronger absorption in A, so this cannot reproduce

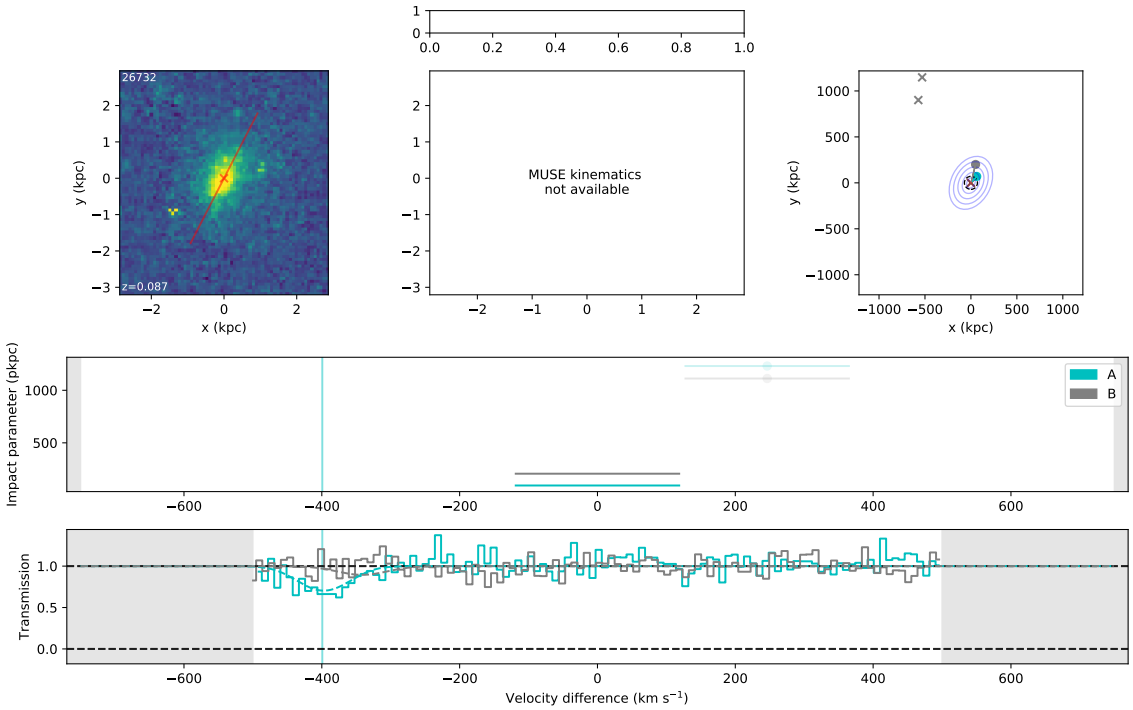

Figure C.1: Details of the Lyα absorption and galaxy environment around galaxy 26732, a $\sim 0.01L_\star$ galaxy at z $\sim$ 0.09. The layout is identical to that shown in Figure 4.4, and the model shown in the lower panel is a disk with rotation velocity ~ 550 km s^{-1}.

Table C.1: Summary of galaxy–absorber group at z $\sim$ 0.087. Any additional galaxies and metal absorbers have velocities shown relative to the first galaxy (26732). Note that this group is affected by the sub-DLA in the spectrum of QSO-C, so no absorption could be detected. Column descriptions are given in Table 4.3.

Galaxy	z	Lum ($L_\star$)	Inc	LOS	Imp (kpc)	Azimuth	log(N H I)	b ($\mathrm{km\,s^{-1}}$)	Δv ($\mathrm{km\,s^{-1}}$)	Other ions
26732	0.087	0.01	45° ± 4°	A	94	15° ± 5°	13.47 ± 0.07	49 ± 11	-400 ± 100	
				B	207	13° ± 5°	(None, limit ≈ 13.2)			
(37993)		0.4		A	1231				(+250)	
				B	1112					
(34203)		0.04		A	1282				(0)	
				B	1212					

the observations.

A disk also struggles to produce these absorber strengths, with an extremely thin disk required, as well as a rotation velocity that is not often found in such low-mass galaxies. The model shown in Figure C.2 is a disk with rotation velocity of 700 $\mathrm{km\,s^{-1}}$ and scale height ratio of 100:1. An outflow producing the absorption in A would also require a large velocity of $\approx 550\ \mathrm{km\,s^{-1}}$. Therefore neither is a likely explanation for this absorption.

C.1.3 Galaxy A-62

A-62 is a star-forming galaxy, with details given in Table C.3 and illustrated in Figure C.3. Absorption is seen in QSO-A but not in B, although there may be a weak Lyα feature in B that is not significant enough to be included in our line list. Their position angles are very similar on opposite sides of the galaxy, with A at much smaller impact parameter. Two components seen with similar column densities along the minor axis, along with O VI absorption, are consistent with a hollow-cone outflow. QSO-C is not available due to a saturated Lyman line from the sub-DLA, and the absorber at -400 $\mathrm{km\,s^{-1}}$ in LOS-A is a higher-order Lyman line from a strong absorption system at z $\approx$ 0.54.

Given the position angles and metal detection in the strong absorption feature in LOS-A, an outflow model would be preferred. An outflow with a velocity of $\approx 150\ \mathrm{km\,s^{-1}}$ and a half-opening angle of $\approx 30^{\circ}$ does approximately reproduce the absorption in LOS-A. However, in this case our models produce some absorption in LOS-B due to the constant velocity and constant flow rate conditions imposed. If this condition were relaxed, representing outflow material slowing due to a combination of gravity and interaction with the intergalactic medium, such an outflow may be consistent with the possible weak absorber seen near in LOS-B near the systemic redshift of the galaxy.

An alternative model could be material accelerating towards the galaxy along the line of sight, reaching $\approx 120\ \mathrm{km\,s^{-1}}$ at the location of LOS-A. Due to the position angles close to the minor axis, any rotation of an extended disk cannot be determined. Emission lines from MUSE also lack any clear rotation. If this infall

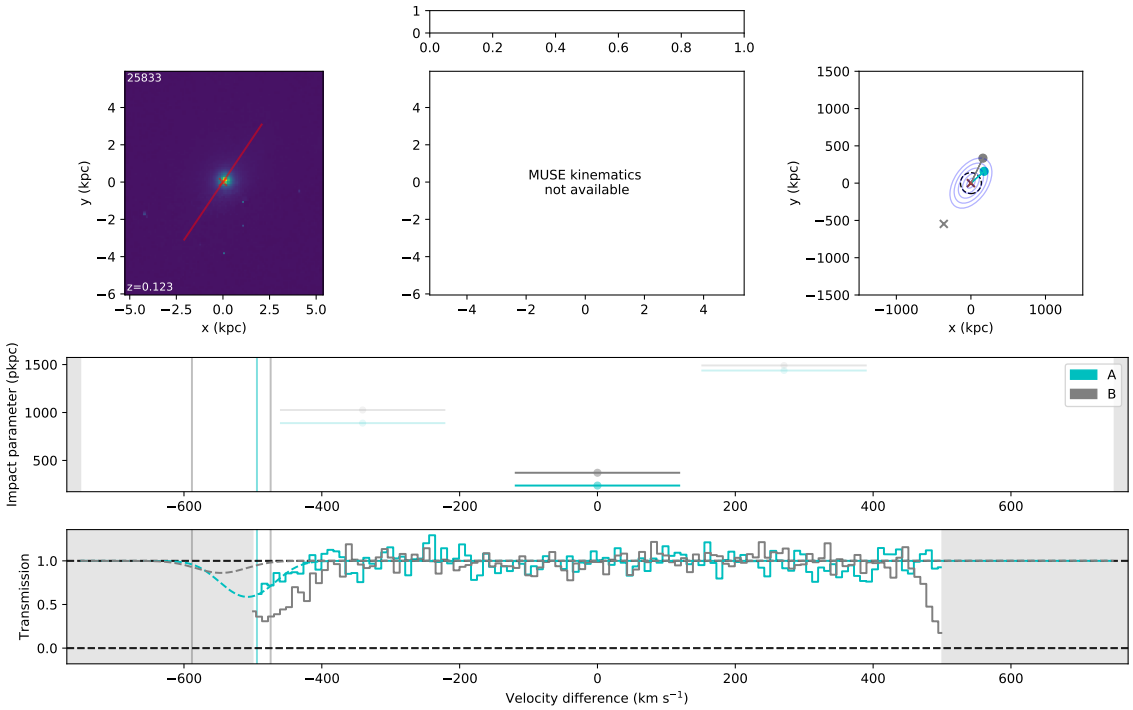

Figure C.2: Details of the Lyα absorption and galaxy environment around galaxy 25833, a $\sim 0.1L_\star$ galaxy at z $\approx$ 0.12. The layout is identical to that shown in Figure 4.4, and the model shown in the lower panel is a disk with rotation velocity $\approx$ 700 km s^{-1}.

Table C.2: Any additional galaxies and metal absorbers have velocities shown relative to the first galaxy (25833). Note that this group is affected by the sub-DLA in the spectrum of QSO-C, so no absorption could be detected. Column descriptions are given in Table 4.3.

Galaxy	z	Lum ($L_\star$)	Inc	LOS	Imp (kpc)	Azimuth	log(N H I)	b ($\mathrm{km\,s^{-1}}$)	Δv ($\mathrm{km\,s^{-1}}$)	Other ions
25833	0.123	0.10	53° ± 2°	A	238	14° ± 2°	13.40 ± 0.06	48 ± 8	-490 ± 100	
				B	372	8° ± 2°	13.84 ± 0.03	45 ± 4	-470 ± 100	
(17099)		0.04		A	890				(-340)	
				B	1026					
(34624)		0.04		A	1438				(+270)	
				B	1490					

formed a disk-like structure, the physical distance would be substantially larger than that for an outflow, so an outflow is the preferred model.

We note that despite the line fitting procedure generating two absorption components in LOS-A, a hollow cone does not help to improve the fit of the outflow model. The second component found in the fitting is substantially narrower than the COS line-spread-function and than most IGM absorbers (e.g. Davé et al., 2010), so may simply be a consequence of the changing physical distance (and therefore column density) along the line of sight. The stronger component is broad, and could be classified as a BLA, but this width is matched by the range of velocities produced by the outflow and does not require a large thermal component.

C.1.4 Galaxy A-65

A-65 is a small (0.02 $L_\star$), star-forming galaxy at z $\approx$ 0.22, with details in Table C.4 and illustrated in Figure C.4. The A and B sightlines both feature absorption, with A lying close to the major axis and B close to the minor axis. The absorption in A is weaker and has a large velocity offset. The galaxy is faint so the signal-to-noise ratio of the emission lines is not sufficient to obtain coherent kinematics (from Hα or O III). Note that the absorption seen at -400 $\mathrm{km\,s^{-1}}$ is Si III from a strong absorber at a slightly higher redshift of z $\approx$ 0.23, and the absorption feature visible in LOS-C at $\approx$ -120 $\mathrm{km\,s^{-1}}$ is identified with Lyβ at z $\approx$ 0.45.

The position angles of absorption suggest that a model consisting of a disk and outflow could explain the two components. However, the near-identical position angles of B and C mean that any outflow producing the strongest absorption component in B would also produce absorption well above the detection limit in LOS-C, which is not observed. Any outflow wide enough and fast enough to produce the observed absorption in A will produce two absorption components in B that are clearly separated, unlike the observations.

Similarly, whilst an extended H I disk could be the origin of the absorption in A, requiring a rotation velocity of 200-400 $\mathrm{km\,s^{-1}}$ (depending on any radial velocity component), the difference in impact parameter means that such a disk could not also cause the absorption seen in LOS-B.

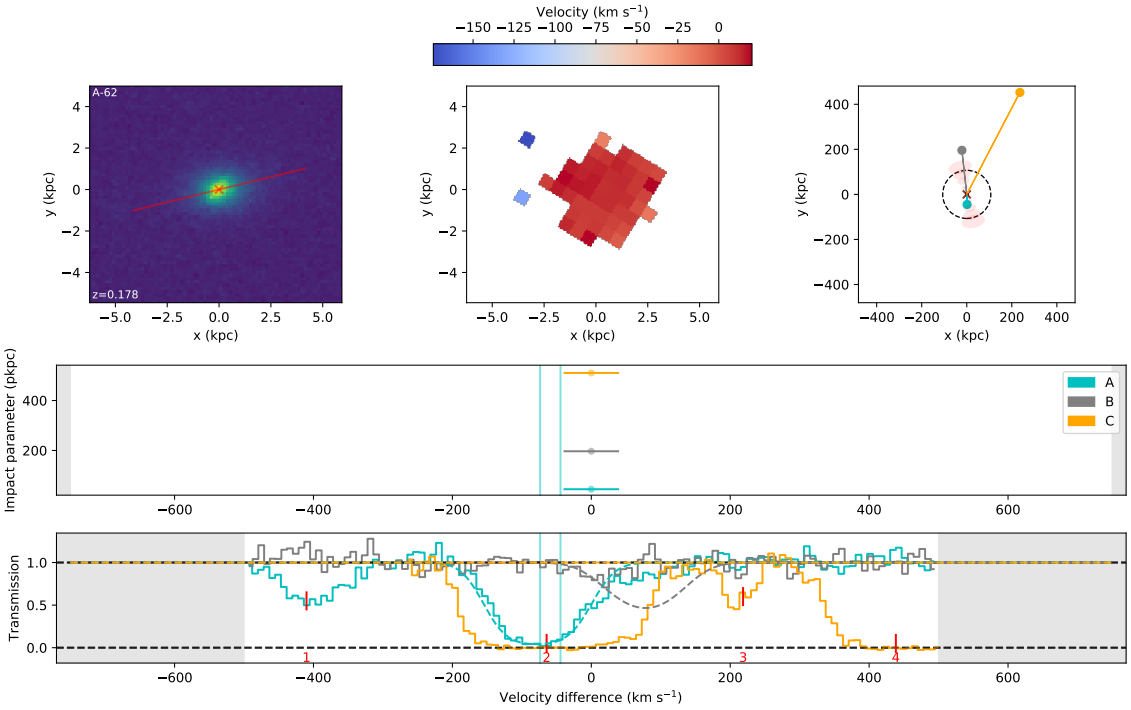

Figure C.3: Details of the Lyα absorption and galaxy environment around galaxy A-62, using Hα as observed in MUSE. The layout of the panels is identical to that in Figure 4.4. The model shown is an outflow with a velocity of ≈ 150 km s^{-1} and a half-opening angle of $\approx 30°$. Additional absorption features that are not due to Lyα at this redshift are labelled with red tick marks as follows: (1) Lyman n=7 from z = 0.536; (2) Lyman n = 11 from z = 0.558; (3) H2 molecular line from z = 0.558; (4) Lyman n = 10 from z = 0.558.

Table C.3: Summary of galaxy–absorber group at z ≈ 0.178. Non-MUSE galaxies and metal absorbers have velocities shown relative to the first galaxy (A-62). Column descriptions are given in Table 4.3. Note that column density upper limits for non-detections are approximations in the absence of absorption from other redshifts.

Galaxy	z	Lum ($L_\star$)	Inc	LOS	Imp (kpc)	Azimuth	log(N H I)	b ($\mathrm{km\,s^{-1}}$)	Δv ($\mathrm{km\,s^{-1}}$)	Other ions
A-62	0.178	0.04	59° ± 3°	A	45	76° ± 2°	14.46 ± 0.03	57 ± 2	-70 ± 60	C III, O VI
				A	45	76° ± 2°	14.67 ± 0.04	9 ± 4	-40 ± 60	
				B	197	80° ± 2°	(None, limit ≈ 12.9)			
				C	510	47° ± 2°	(None, limit ≈ 13.0)			

Table C.4: Summary of galaxy–absorber group at z ∼ 0.220. Non-MUSE galaxies and metal absorbers have velocities shown relative to the first galaxy (A-65). Column descriptions are given in Table 4.3.

Galaxy	z	Lum ($L_\star$)	Inc	LOS	Imp (kpc)	Azimuth	log(N H I)	b ($\mathrm{km\,s^{-1}}$)	Δv ($\mathrm{km\,s^{-1}}$)	Other ions
A-65	0.220	0.01	56° ± 9°	A	73	32° ± 13°	13.21 ± 0.05	33 ± 6	240 ± 40	
				B	262	70° ± 13°	13.74 ± 0.04	35 ± 4	-70 ± 40	
				C	589	69° ± 13°	(None, limit ≈ 12.9)			

We therefore cannot reproduce both observed absorption components using our simple disk/outflow models, without producing additional unobserved absorption. A model in which any cool clumps in the putative outflow are heated in the IGM, or one in which the outflow velocity is insufficient to escape to larger scales, could explain the absorption observed in B yet lacking in C.

In conjunction with the extended disk fitting the absorption in A, a slowing or heating outflow could then reasonably match all observed absorption around this galaxy.

C.1.5 Galaxy A-63

A-63 is a $\sim 0.1L_\star$ galaxy at z ≈ 0.488, with details in Table C.5 and illustrated in Figure C.5. It is isolated and highly inclined. A velocity gradient is visible in the MUSE data, but none of the three sightlines lie near the major axis.

The redshift is such that any associated Lyα lies in the FOS spectra, and therefore has much poorer spectral resolution than the COS spectra. Whilst VPFIT has identified absorption in sightlines B and C, it does not identify absorption in A, although the spectrum visible in the figure suggests possible weak, broad absorption. Lyβ is visible at this redshift, but is too weak to provide a model fit.

Both A and B lie close to the galaxy minor axis, but the absorption in both is blueward of the galaxy. An outflow therefore cannot explain both simultaneously. Similarly, no substantial component of the line-of-sight velocity offset to the absorber in B can come from rotation, and enough accretion to match that would produce a substantial redward component in A that is not observed.

An outflow can approximately match the absorption in B, but requires a very large outflow velocity of $\gtrsim 600$ km s^{-1} and a small opening angle of $\lesssim 20^\circ$ in order to produce the large velocity offset observed and avoid producing clear absorption in LOS-A. This is the model illustrated in Figure C.5. We note that this is much larger than typical stellar-feedback driven outflows, which typically have velocities of 100-200 km s^{-1} (e.g Concas et al., 2019; Schroetter et al., 2019)

Our models cannot match the absorption in LOS-C in addition to the other sightlines, due to its much larger impact parameter yet similar column density.

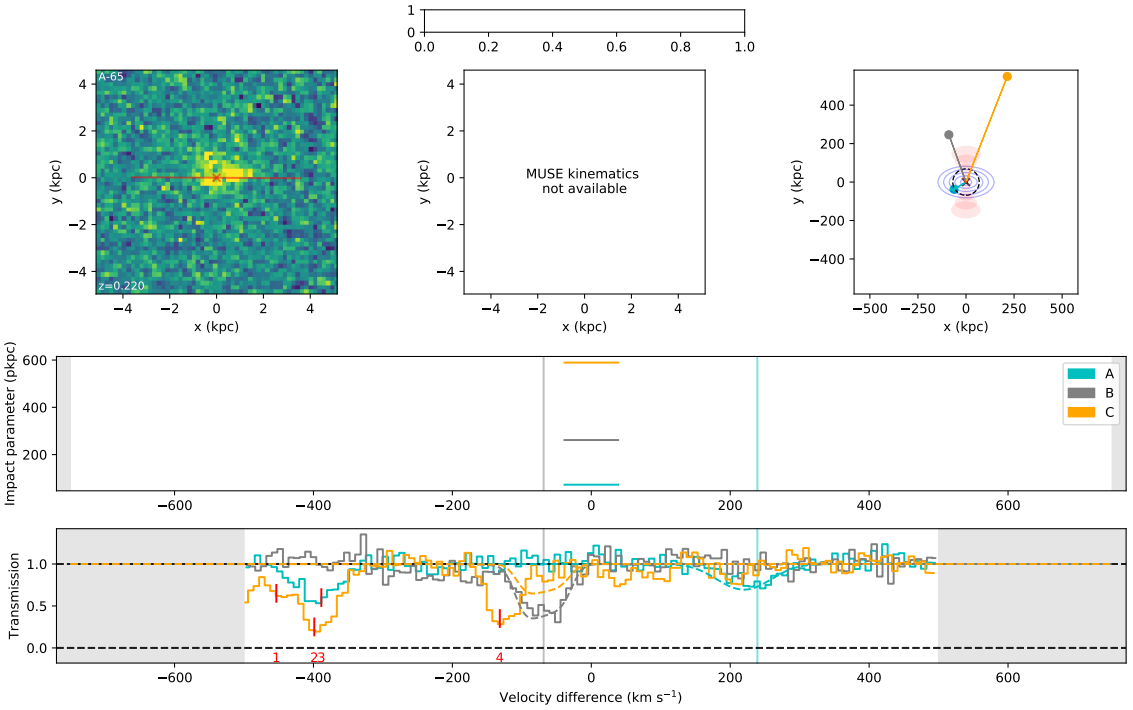

Figure C.4: Details of the Lyα absorption and galaxy environment around galaxy A-65. The layout of the panels is identical to that in Figure 4.4. The model shown combines a disk and an outflow. The putative outflow has a velocity of $\approx$ 120 km s^{-1} and a half-opening angle of $\approx 30°$, whilst the disk has a rotation velocity of 220 km s^{-1} and an infall velocity of 50 km s^{-1}. Absorbers originating from other redshifts are identified by the red ticks as follows: (1) Lyman n = 6 transition from z = 0.579; (2) and (3) Si III from z = 0.227; (4) Lyβ from z = 0.445.

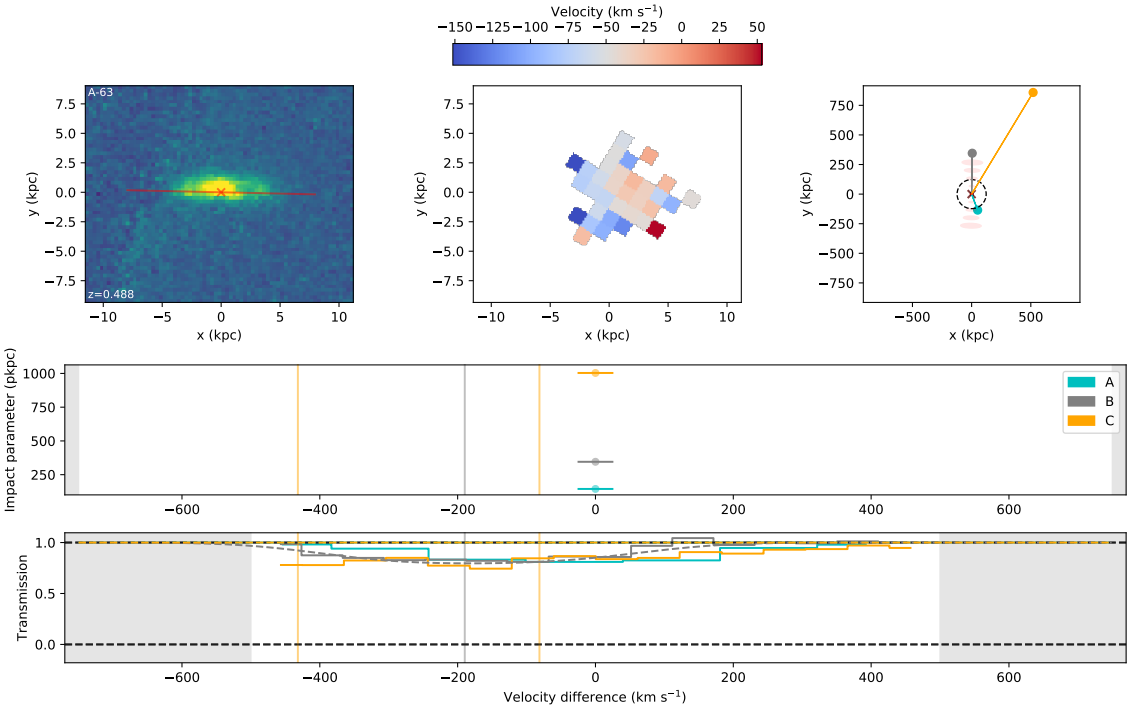

Figure C.5: Details of the absorption and galaxy environment around galaxy A-63, a $\sim 0.09L_\star$ galaxy at z $\approx$ 0.49, using [OII] as observed in MUSE. The layout is identical to that shown in Figure 4.4, and the model shown in the lower panel is an outflow with opening angle $\sim 20°$ and velocity of 650 km s^{-1}.

The low column densities and large velocity offsets of the detected absorbers allow for the possibility that they are unassociated with the galaxy, and the lack of constraints on the absorber width allow for the possibility that these may be WHIM detections. The large velocities required to reproduce any of the absorption components do not support the existence of disk/outflow structures around this galaxy.

C.1.6 Galaxy 30169

Galaxy 30169 is a near-face-on spiral galaxy outside of the MUSE fields (so no kinematics are available) at z $\approx$ 0.584 (see Table C.6 and Figure C.6). Absorption is visible in LOS-B, whilst features in A and B are identified with Lyman-β at z $\approx$ 0.88, and no clear features are seen in the spectrum of QSO-C. Therefore only the blue wing visible in the absorber in LOS-B is likely Lyα. One other galaxy lies within 1 Mpc of QSO-C, but does not have a well-determined position angle and no

Table C.5: Summary of galaxy–absorber group at z ≈ 0.488. Any additional galaxies and metal absorbers have velocities shown relative to the first galaxy (A-63). Column descriptions are given in Table 4.3.

Galaxy	z	Lum ($L_\star$)	Inc	LOS	Imp (kpc)	Azimuth	log(N H I)	b ($\mathrm{km\,s^{-1}}$)	Δv ($\mathrm{km\,s^{-1}}$)	Other ions
A-63	0.488	0.09	77° ± 2°	A	144	66° ± 2°	(None, limit ≈ 13.5)			
				B	345	87° ± 2°	13.79 ± 0.05	230 ± 30	-190 ± 30	
				C	1003	62° ± 2°	13.8 ± 0.2	260 ± 140	-80 ± 60	
				C	1003	62° ± 2°	13.6 ± 0.2	130 ± 40	-430 ± 40	

Table C.6: Summary of galaxy–absorber group at z ≈ 0.584. Any additional galaxies and metal absorbers have velocities shown relative to the first galaxy (30169). Column descriptions are given in Table 4.3.

Galaxy	z	Lum ($L_\star$)	Inc	LOS	Imp (kpc)	Azimuth	log(N H I)	b ($\mathrm{km\,s^{-1}}$)	Δv ($\mathrm{km\,s^{-1}}$)	Other ions
30169	0.584	0.68	31° ± 3°	A	672	52° ± 10°	(None, limit ≈ 13.4)			
				B	834	13° ± 10°	13.67 ± 0.16	70 ± 30	-280 ± 30	
				C	1002	38° ± 10°	(None, limit ≈ 13.5)			
(35758)		0.2		A	2035				(0)	
				B	1673					
				C	879					

other galaxies are within 500 $\mathrm{km\,s^{-1}}$ and 2 Mpc of the sightlines.

As the galaxy is close to face-on, a disk model cannot produce the large velocity offset to the absorber in LOS-B, without an extremely large velocity (> 600 $\mathrm{km\,s^{-1}}$). A conical outflow would be capable of generating such an offset, but would also produce absorption in the other two sightlines (as their impact parameters differ by less than a factor of two and position angle has only a weak effect at this inclination). An example of this is shown in the lower panel of Figure C.6.

Therefore neither the disk nor outflow model can reproduce the absorption component seen near this galaxy in LOS-B.

C.1.7 Galaxy A-23

A-23 lies at a redshift of z $\approx$ 0.843, and is detailed in Table C.7 and Figure C.7. The small apparent size of this galaxy makes it difficult to obtain any kinematic gradient, and the uncertainty in position angle is large.

Absorption is detected in LOS-B with a substantial blueshift in comparison to the galaxy. There is also a possible weak feature in LOS-A, although this was not identified by VPFIT as it lies marginally below the significance threshold.

If the possible absorber in A is included, an outflow cannot simultaneously fit both absorbers, as they lie in opposite sides of the major axis (and hence probe opposing outflow cones) yet have the same direction of velocity offset.

A thin disk requires a large rotation velocity (≈ 350 $\mathrm{km\,s^{-1}}$) in order to match the velocity offset to the absorber in LOS-B. Due to B lying closer to the major axis, a thinner disk increases the column density of B in comparison to A and can produce a similarly strong absorber despite its larger impact parameter. The infall velocity is also constrained by the apparent absorption in LOS-A, as both sightlines have a similar line-of-sight velocity component from disk rotation, but opposite line-of-sight components from infall.

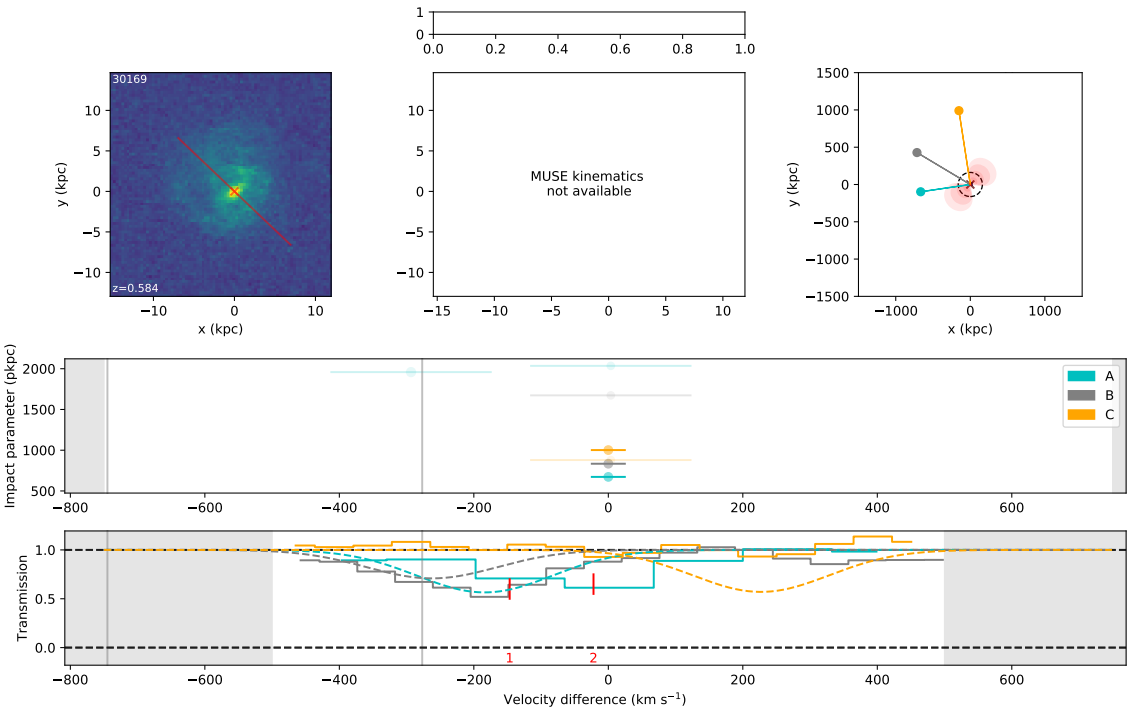

Figure C.6: Details of the absorption and galaxy environment around galaxy 30169, a $\sim 0.7L_\star$ galaxy at z $\approx$ 0.58, using [OII] as observed in MUSE. The layout is identical to that shown in Figure 4.4, and the model shown in the lower panel is an outflow with velocity ≈ 280 km s^{-1} and opening angle 40°. Absorption originating from another redshift is marked by red ticks, with both components here identified as Lyβ originating from z = 0.876.

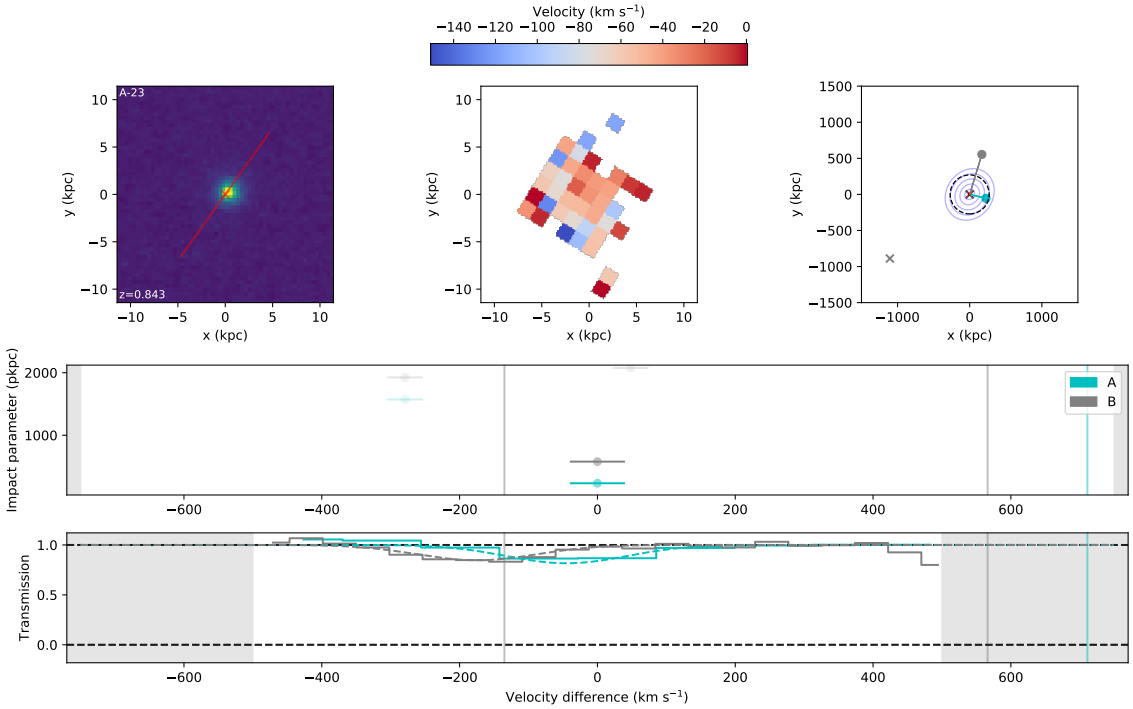

Figure C.7: Details of the absorption and galaxy environment around galaxy A-23, a $\sim 0.2L_\star$ galaxy at z $\approx$ 0.84, using [OII] as observed in MUSE. The layout is identical to that shown in Figure 4.4, and the model shown in the lower panel is disk with rotation velocity $\approx$ 350 km s^{-1}.

C.1.8 Galaxy A-30

A-30 lies at z$\sim$0.85, and is detailed in Figure C.8 and Table C.8. It is a non-star-forming galaxy, so lacks the emission lines necessary to produce kinematics. Strong absorption features in the spectrum are sufficient to provide a well-constrained redshift measurement.

Weak absorption is visible in LOS-B at $\approx$ 200 km s^{-1} redward of the galaxy, with a potential weak absorber at $\approx$ 400 km s^{-1} in LOS-A. Additional absorption identified as Lyα is visible in both sightlines around 500 km s^{-1} blueward of the galaxy. No other galaxy comes within 1.5 Mpc of any of the QSOs within 750 km s^{-1} of this galaxy. The absorbers lie in the low-resolution FOS spectra, but are too weak for Lyβ to provide a better fit.

Due to its much smaller impact parameter, any disk cannot match the absorption in B without producing much stronger absorption in A, but a sufficiently narrow outflow can cause absorption in B without producing absorption in LOS-A. A half-

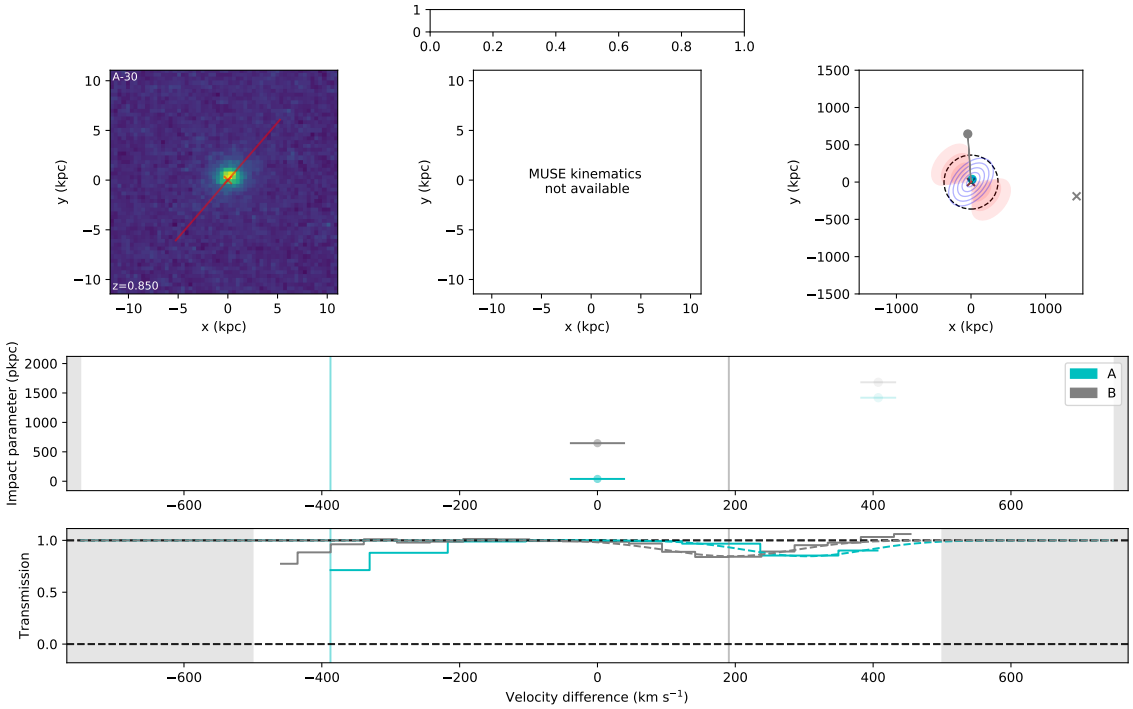

Figure C.8: Details of the absorption and galaxy environment around galaxy A-30, a $\sim 0.1L_\star$ galaxy at z $\approx$ 0.85, using [OII] as observed in MUSE. The layout is identical to that shown in Figure 4.4, and the model shown in the lower panel is disk with rotation velocity $\approx$ 450 km s^{-1} and outflow with velocity $\approx$ 250 km s^{-1}.

opening angle of $\sim 45°$ and an outflow velocity of $\sim$ 250 km s^{-1} can reproduce the observed absorption.

If the possible weak absorber in A is real, then a disk can produce a reasonable fit, but the required velocities are quite large. The small impact parameter means that a disk fitting the absorption in A will not produce any detectable absorption in B, making the rotating and infalling velocities degenerate. The rotation velocity can vary between $\sim$ 350 km s^{-1} (if 0.6 v_{vir} infall) and $\sim$ 450 km s^{-1} (if no infall), or could be made smaller with larger infall velocities.

The absorption at -400 km s^{-1} may be due to another galaxy outside the 750 km s^{-1} window shown.

C.1.9 Galaxy A-64

A-64 is another $\sim 0.1L_\star$, isolated, star-forming galaxy. Some kinematics are available, showing a clear velocity gradient across the galaxy, although the signal-to-noise

Table C.7: Summary of galaxy–absorber group at z ≈ 0.843. Any additional galaxies and metal absorbers have velocities shown relative to the first galaxy (A-23). Note that this galaxy is beyond the redshift of QSO-C, so no absorption could be detected. Column descriptions are given in Table 4.3.

Galaxy	z	Lum ($L_\star$)	Inc	LOS	Imp (kpc)	Azimuth	log(N H I)	b ($\mathrm{km\,s^{-1}}$)	Δv ($\mathrm{km\,s^{-1}}$)	Other ions
A-23	0.843	0.2 ± 0.02	31° ± 40°	A	233	68° ± 35°	(None, limit ≈ 13.5)			
				B	578	19° ± 35°	13.61 ± 0.08	130 ± 30	-140 ± 40	

Table C.8: Summary of galaxy–absorber group at z ≈ 0.850. Any additional galaxies and metal absorbers have velocities shown relative to the first galaxy (A-30). Note that this galaxy is beyond the redshift of QSO-C, so no absorption could be detected. Column descriptions are given in Table 4.3.

Galaxy	z	Lum ($L_\star$)	Inc	LOS	Imp (kpc)	Azimuth	log(N H I)	b ($\mathrm{km\,s^{-1}}$)	Δv ($\mathrm{km\,s^{-1}}$)	Other ions
A-30	0.850	0.12 ± 0.02	53° ± 9°	A	39	19° ± 11°	13.71 ± 0.02	106 ± 6	-390 ± 40	
				B	647	45° ± 11°	13.32 ± 0.14	70 ± 30	190 ± 40	

Table C.9: Summary of galaxy–absorber group at z ≈ 0.926. Any additional galaxies and metal absorbers have velocities shown relative to the first galaxy (A-64). Note that this galaxy is beyond the redshift of QSO-C, so no absorption could be detected. Column descriptions are given in Table 4.3.

Galaxy	z	Lum ($L_\star$)	Inc	LOS	Imp (kpc)	Azimuth	log(N H I)	b ($\mathrm{km\,s^{-1}}$)	Δv ($\mathrm{km\,s^{-1}}$)	Other ions
A-64	0.926	0.14 ± 0.03	45° ± 11°	A	140	48° ± 13°	14.13 ± 0.13	170 ± 60	140 ± 40	
				B	587	31° ± 13°	14.26 ± 0.08	320 ± 70	130 ± 40	

ratio is poor. This is detailed in Table C.9 and illustrated in Figure C.9.

Similar absorbers are seen in the A and B sightlines, with comparable strengths and velocity offsets, neither lying close to the major or minor axis of the galaxy. As LOS-A lies at a smaller impact parameter and closer to the galaxy minor axis than LOS-B, an outflow cannot reproduce two absorbers with similar densities.

Any rotation in a putative disk would generate a substantial line-of-sight velocity difference between the absorption in the two sightlines, which is not observed. Additionally, a disk would have to be extremely thin ($\sim$ 1000:1) for the position angle difference (B nearer the major axis) to counter the impact parameter difference (A nearer the galaxy) and produce similar-strength absorbers. A thicker disk (height ratio $\sim$ 30:1) could, however, produce the absorber in A only, with any weak absorption in B remaining consistent with the observations. This is the model shown in Figure C.9, with a rotation velocity of ≈ 350 km s^{-1}. Reducing the circular velocity and increasing the infall velocity can produce more reasonable estimates, with 0.6 v_{vir} infall allowing rotation velocities of ≈ 150 km s^{-1}.

Therefore, whilst the absorption in A can be successfully fit with our toy models, we cannot match the major components in A and B simultaneously.

C.2 Additional galaxy groups

The following tables and figures describe the properties and model fitting process for additional galaxy groups not included in the main thesis. These are reproduced from the Appendix of Paper 3.

C.2.1 G-202

G-202 is the largest group of galaxies in this field (both in number of galaxies and total stellar mass), at z $\approx$ 0.2. B-22, the only galaxy in the group that lies in the MUSE field, is a small galaxy with a distorted shape, possibly due to tidal interactions within this group. Our estimate of the galaxy's position angle may be slightly affected, but we have taken the orientation of the bright central component (having a larger uncertainty but less likely to be distorted). An additional 5 galaxies

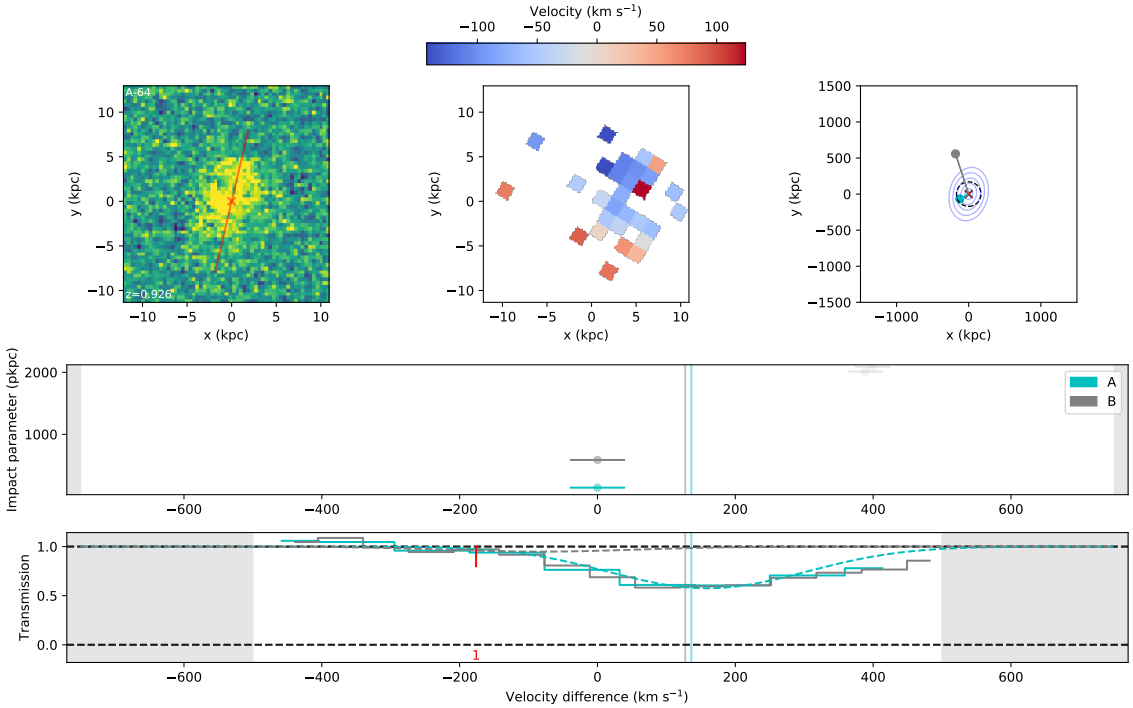

Figure C.9: Details of the absorption and galaxy environment around galaxy A-64, a $\sim 0.1L_\star$ galaxy at z $\sim$ 0.93, using [OII] as observed in MUSE. The layout is identical to that shown in Figure 4.4, and the model shown in the lower panel is a disk with rotation velocity $\sim$ 350 km s^{-1}. The absorption marked in the blue wing in both sightlines is identified as C III from z=0.227.

at this redshift have estimated position angles, and an further 19 lie within 1 Mpc of at least one of the lines-of-sight.

Absorption is visible in all three lines-of-sight, although several of the absorption components visible in Figure C.10 are due to features other than Lyα, including Lyman lines and molecular hydrogen lines from the sub-DLA at z = 0.558. The five absorption components we have attempted to fit are listed in Table C.10, alongside another strong absorber in LOS-B which is close to 500 $\mathrm{km\,s^{-1}}$ blueward of the galaxy. This large velocity offset makes it unlikely to be associated with any of the galaxies in the HST field, and more likely associated with one of the galaxies with slightly lower redshift.

Despite the relatively dense galaxy environment, a combination of disks and outflows provides a good approximation to four of the five components, and there may be a contribution to the fifth from a molecular line. The model shown in the Figure is an outflow with half-opening angle $\approx 15°$ and velocity ≈ 250 $\mathrm{km\,s^{-1}}$ from galaxy B-22 (matching the bluer component in B), an outflow with half-opening angle $\approx 20°$ and velocity ≈ 50 $\mathrm{km\,s^{-1}}$ from galaxy 31787 (matching the absorption in A), and a disk with rotation of 150 $\mathrm{km\,s^{-1}}$ and negligible infall around galaxy 32778 (matching the strong absorption in C and redder component of absorption in B).

Stripped material is expected in groups of interacting galaxies (e.g Morris & van den Bergh, 1994), and the distortion in B-22 may be due to this. However, a 'tail' of gas extending out along the path of this apparent stream would not intersect any of the three lines-of-sight. All absorbers identified have widths $\lesssim$50 $\mathrm{km\,s^{-1}}$, so we also do not clearly identify any hot intra-group gas.

Two components of absorption in LOS-B are also seen in C III and O VI, with redshifts matching the two Lyα components. No metals are detected in the A or C sightlines, imposing 1σ upper limits of $10^{12.9}$ and $10^{13.6}$ $\mathrm{cm^{-2}}$ on C III and O VI respectively in sightline A, whilst these lines could not be detected in LOS-C due to the sub-DLA. With the metals in C unconstrained, the absorbers in B and C could have similar C III/Lyα and O VI/Lyα ratios, consistent with both probing rotating/accreting material associated with the same galaxy. The C III and O VI

content of the bluer absorption component in B (identified as an outflow in our best model result) is lower than that of the redder component (identified as accretion).

It is possible that the accreting material has been stripped or ejected from other group galaxies, rather than accreted from the IGM, leading to a higher metal content. However, the increased strength of metal absorption may also be due to photo-ionization from the group galaxies.

We also note that B-22, with a proposed strong outflow, has a lower SFR (and sSFR) than most galaxies in this group. Therefore this putative outflow is either sustained by a very low star-formation rate, or the galaxy has quenched in the past $\approx$ 300 Myr. The disk model also requires angular momentum aligned on scales of $\approx$ 400 kpc, larger than seen in most models. Despite these difficulties, we cannot rule out a superposition of disk/outflow models fitting the absorption seen around this group.

C.2.2 G-383

A-48 and A-49 are a close pair of small, star-forming galaxies near to the line-of-sight to QSO-A, at z $\approx$ 0.38. They are separated by $\approx$ 5 kpc and aligned such that they lie approximately along each other's minor axis. A-48 is larger and closer to the QSO. They are illustrated in Figure C.11 and detailed in Table C.11. Other larger galaxies exist 1-1.5 Mpc from the sightlines, but outside the HST image so do not have measured position angles. Whilst emission-line velocities are measurable from the MUSE data for both galaxies, neither show a clear velocity gradient.

Strong absorption exists in LOS-A, near the minor axis of both galaxies and well within the virial radius, featuring C III and O VI absorption. Both indicate warm, metal-enriched material that would be consistent with a galactic wind (although, as the Lyα column densities of the other absorbers are small, their C III and O VI fractions are not constrained, and could be higher). As both galaxies are very close to edge on, the required outflow velocity in order to produce the 20 or 40 $\mathrm{km\,s^{-1}}$ line-of-sight velocity difference is massively affected by both the uncertainty in the velocity offset itself and the galaxy inclination. Using the measured values of both requires a fast outflow of $\sim 500\ \mathrm{km\,s^{-1}}$ to reproduce the observations, but any value

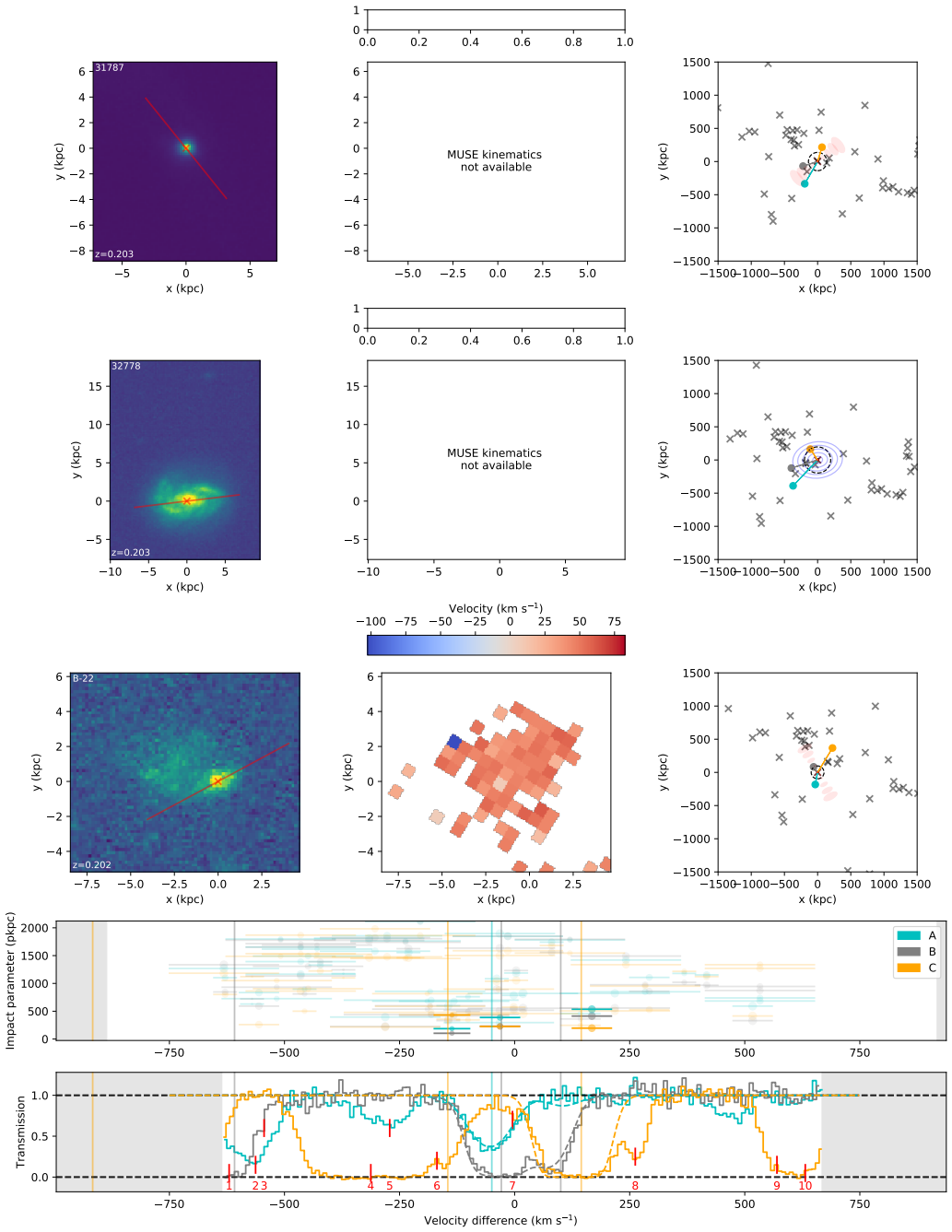

Figure C.10: Details of the Lyα absorption and galaxy environment around group G-202. Features shown are identical to those in Figure 4.4, with kinematics measured from Hα in the MUSE data. Three components make up the model shown in the lower panel: an outflow with half-opening angle $\approx 15°$ and velocity ≈ 250 km s^{-1} from galaxy B-22; an outflow with half-opening angle $\approx 20°$ and velocity ≈ 50 km s^{-1} from galaxy 31787; and a disk with rotation velocity ≈ 150 km s^{-1} and infall of $\lesssim 20$ km s^{-1} around galaxy 32778. Absorbers other than Lyα are marked with red ticks and identified as follows: (1) and (2) as the Lyman n = 5-0 transition from z = 0.536 in LOS-B and LOS-A respectively; (3) as Lyδ from z = 0.500 in LOS-B; (4) and (5) as the Lyman n=6 transition from z = 0.558 in LOS-C and LOS-A; (6) as Lyβ from z = 0.425; and (7)-(10) as molecular lines from the sub-DLA.

Table C.10: Summary of galaxy and absorber properties for G-202. Columns are labelled as in Table 5.3, although details of galaxies outside the HST field are shown more briefly.

z	Galaxy	Lum ($L_\star$)	Inc	LOS	Imp (kpc)	Azimuth	log(N H I)	b ($\mathrm{km\,s^{-1}}$)	Δv ($\mathrm{km\,s^{-1}}$)	Other ions
(1)	(2)	(3)	(4)	(5)	(6)	(7)	(8)	(9)	(10)	(11)
0.202	B-22	0.02	66° ± 5°	A	186	51° ± 9°	13.95 ± 0.02	52 ± 3	90 ± 40	None
				B	103	82° ± 9°	17.58 ± 0.10	16 ± 1	-470 ± 40	C II-III, O VI, Si II-III
				B			15.03 ± 0.03	43 ± 2	+110 ± 40	C III, O VI
				B			14.96 ± 0.08	18 ± 1	+240 ± 40	C III, O VI
				C	431	30° ± 9°	13.96 ± 0.05	43 ± 6	-10 ± 40	None
				C			14.65 ± 0.05	64 ± 3	+280 ± 40	None
	25962	0.07	81° ± 1°	A	295	65° ± 1°			(+100)	
				B	516	42° ± 1°				
				C	895	53° ± 1°				
	31704	0.03	41° ± 4°	A	457	16° ± 8°			(+280)	
				B	360	20° ± 8°				
				C	246	79° ± 8°				

Continued on next page

Continued from previous page

	31787	0.08	62° ± 2°	A	387	69° ± 2°			(+100)	
				B	230	69° ± 2°				
				C	226	56° ± 2°				
	32497	1.1	85° ± 2°	A	394	62° ± 1°			(-150)	
				B	226	77° ± 1°				
				C	215	54° ± 1°				
	32778	0.4	43° ± 1°	A	535	40° ± 2°			(+300)	
				B	412	10° ± 2°				
				C	195	63° ± 2°				
				Impact params (kpc)						
				A	B	C				
	(24419)	0.01		628	719	1118			(-430)	
	(27581)	0.03		724	930	1048			(-380)	
	(28913)	0.02		679	536	814			(-50)	
	(30488)	0.1		848	973	949			(+420)	

Continued on next page

Continued from previous page

	(31439)	1.0		1082	889	1036			(+100)	
	(31978)	0.1		697	439	478			(-50)	
	(32021)	0.1		678	415	438			(0)	
	(32308)	0.8		597	331	355			(-10)	
	(32591)	0.03		856	598	586			(-50)	
	(32755)	0.7		784	531	572			(+130)	
	(33166)	0.03		759	493	344			(+30)	
	(33268)	0.9		820	556	505			(+350)	
	(33496)	0.1		1100	844	799			(-490)	
	(34292)	0.03		895	809	500			(-320)	
	(34719)	0.3		834	590	259			(-420)	
	(34992)	2.9		818	551	456			(+150)	
	(35102)	0.5		1163	1132	861			(-330)	
	(36229)	0.1		1106	856	528			(+430)	
	(38978)	0.1		1488	1305	903			(-310)	

of outflow velocity $\lesssim 1000$ km s^{-1} can approximate the observations within the 1σ region of i and Δv.

Weak absorption in QSO-B is apparent at ≈ 320 km s^{-1} blueward of the galaxy pair, as well as 150 km s^{-1} redward. Possible absorbers in A at -320 and -150 are attributed to higher-order Lyman lines from higher redshift gas (Ly-β from z ≈ 0.64, and Lyγ from z ≈ 0.73). All apparent transitions in C are attributed to molecular lines from the sub-DLA at z ≈ 0.56.

Neither of the absorbers in B can be reproduced using a reasonable outflow, as it would need a very large opening angle to get close to the major axis, and this would produce a very large velocity spread on the absorption in A. As the absorbers lie near the major axis, a disk-like structure could be considered. This could be invoked for either or both absorbers in B, with potentially the two galaxies rotating in different directions producing the -320 and +150 km s^{-1} absorbers. Such a disk could not fit the absorption in A in addition to that in B, as a disk thick enough to produce strong absorption along the minor axis would also cover a wide range of line-of-sight velocities along LOS-B, and therefore wider absorption than is observed.

Given the uncertainties in inclination and velocity offset, an outflow fitting the absorption in A alongside a disk from either galaxy matching the redward component of absorption in B seems plausible. The large velocity offset required to match the blue component in B would require a larger disk velocity than the virial velocity of either galaxy. It is therefore more likely to be associated with the more distant galaxies, or not physically associated with any of the galaxies in this group.

C.2.3 G-517

Group G-517 is made up of only two galaxies. B-43 is a $\approx 0.6L_*$ spiral galaxy at z ≈ 0.52, with a far smaller ($\approx 0.02L_*$) companion galaxy B-34, illustrated in Table C.12 and Figure C.12. A large group exists at the same redshift, but this is more than 1.5 Mpc from the lines-of-sight. B-34 is sufficiently faint that it is difficult to obtain a position angle. The uncertainty on the B-43 position angle may also be underestimated as the flux in the spiral arms dominates over the disk that we use to measure the position angle.

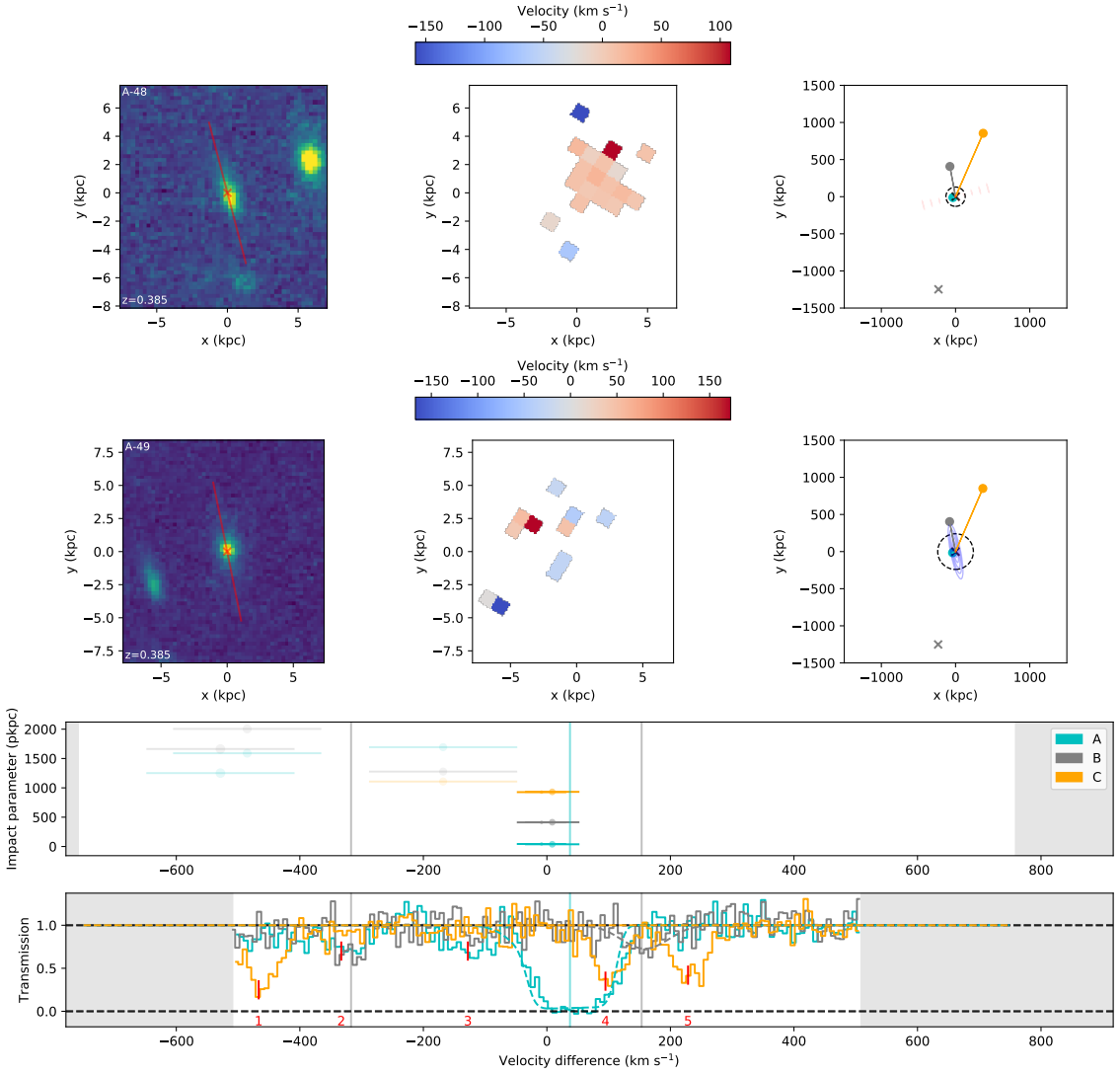

Figure C.11: Details of the absorption and galaxy environment around group G-383, a galaxy pair at z $\sim$ 0.39, with kinematics taken from the Hα emission line seen in the MUSE data. The layout is identical to that shown in Figure 4.4, and the model shown in the lower panel combines an outflow with 600 km s^{-1}velocity and 10° half-opening angle, and a rotating disk around A-49 with rotation velocity 180 km s^{-1}. Additional absorbers indicated by red ticks are identified as follows: (1), (4) and (5) are H2 molecular lines from the sub-DLA at z $\approx$ 0.56; (2) is Lyδ from z = 0.73; and (3) is Lyβ from z = 0.64. Note that the close separation between the galaxies in both velocity and projection makes them difficult to distinguish in the central panel.

Table C.11: Summary of galaxy and absorber properties of group G-383. Any additional galaxies and metal absorbers have velocities shown relative to the first galaxy (A-48). Columns are identical to those in Table 5.3.

z (1)	Galaxy (2)	Lum ($L_\star$) (3)	Inc (4)	LOS (5)	Imp (kpc) (6)	Azimuth (7)	log(N H I) (8)	b ($\mathrm{km\,s^{-1}}$) (9)	Δv ($\mathrm{km\,s^{-1}}$) (10)	Other ions (11)
0.383	A-48	0.03	87° ± 3°	A	38	87° ± 4°	14.67 ± 0.02	53 ± 2	+40 ± 40	C III, O VI
				B	414	4° ± 4°	13.22 ± 0.09	20 ± 7	-320 ± 40	(None)
				B	414	4° ± 4°	13.11 ± 0.13	24 ± 11	+150 ± 40	(None)
				C	932	38° ± 4°	(None, limit $\sim$ 13.0)			
	A-49	0.02	80° ± 5°	A	43	81° ± 4°			(-20)	
				B	411	0° ± 4°				
				C	927	35° ± 4°				

There is no significant absorption in any of the lines-of-sight. This is somewhat surprising for LOS-B, as it lies near the minor axis at a small impact parameter to a fairly large star-forming galaxy. This either indicates that such outflows are not ubiquitous around SF galaxies, that these outflows are 'patchy' (with covering factor <1), or that any outflow around this galaxy is heating the gas enough that no H I absorption is visible. Coverage of several metal species including C III and O VI is provided by our observations at this redshift, but no metals are detected.

C.2.4 G-536

A-36 and A-37 are a close pair of galaxies that are likely interacting (given the asymmetry in A-36), with A-40 a more distant third galaxy. Details are given in Table C.13 and Figure C.13. A substantial number of galaxies exist at similar redshifts with larger impact parameters. All three MUSE galaxies are star-forming, and the interacting pair have measurable kinematics. Strong absorption is visible along all three lines of sight. In galaxy A-36, the bright bulge appears to be off-centre with respect to the disk, likely indicating interaction with A-37. However, GALFIT is able to fit both galaxies reasonably well using a simple disk that is not strongly distorted.

In Figure C.13, we show the Lyβ transition in absorption at the redshift of this group. This is due to the Lyα lying in the lower-resolution FOS spectra, whilst Lyβ produces strong absorption in the COS spectra, so more structure in the Lyβ can be discerned.

Given several galaxies, there are multiple ways of generating the absorption features in the observed spectra. A wide outflow around A-36 can approximately reproduce the saturated Lyβ absorption in LOS-A, or a narrower outflow could explain the redmost component of this absorption. An outflow from galaxy A-37 with sufficient velocity to cover the galaxy-absorber offset seen to the absorbing components in LOS-B produces absorption that is too broad and therefore inconsistent with the observations. Depending on the orientation of the galaxy, an outflow around A-40 can also reasonably match either the blue or red end of the broad saturated absorption in LOS-A.

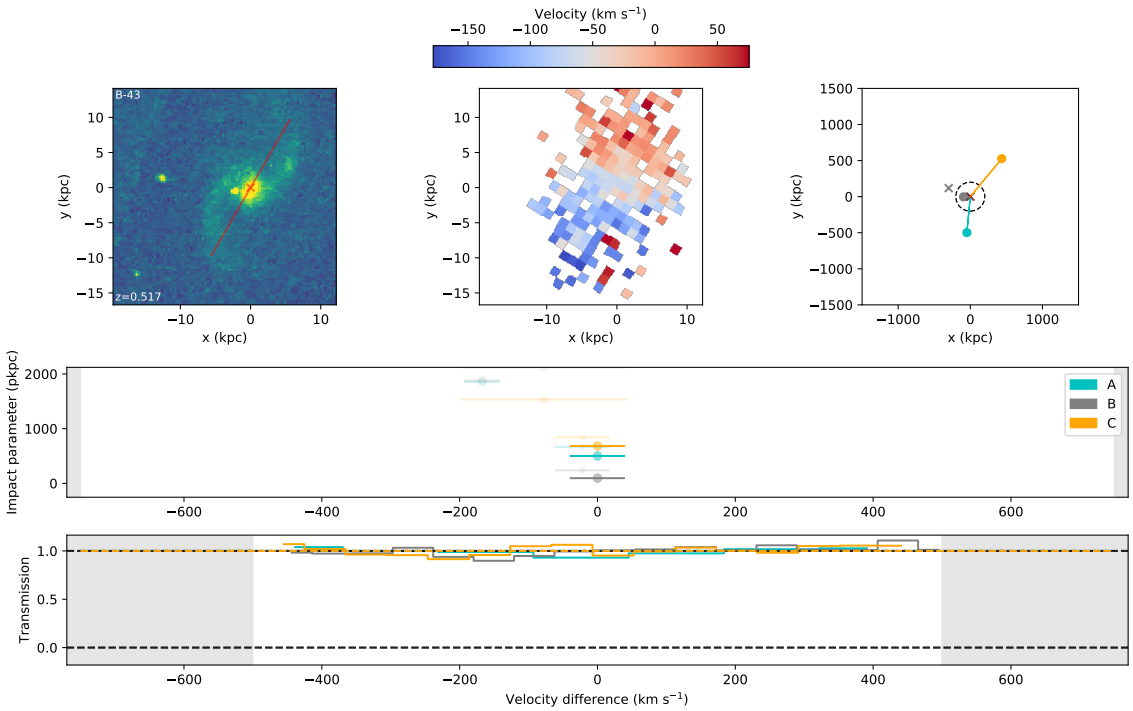

Figure C.12: Details of the absorption and galaxy environment of group G-517, with kinematics from [O III] as seen in the MUSE data. The layout is identical to that shown in Figure 4.4, except that no model is shown.

Table C.12: Summary of galaxy and absorber properties for group G-517. Any additional galaxies and metal absorbers have velocities shown relative to the first galaxy (B-43). Columns are identical to those in Table 5.3.

z (1)	Galaxy (2)	Lum ($L_\star$) (3)	Inc (4)	LOS (5)	Imp (kpc) (6)	Azimuth (7)	log(N H I) (8)	b ($\mathrm{km\,s^{-1}}$) (9)	Δv ($\mathrm{km\,s^{-1}}$) (10)	Other ions (11)
0.517	B-43	0.6	66° ± 1°	A	501	3° ± 6°	(None, limit ≈13.3)			
				B	95	86° ± 6°	(None, limit ≈13.3)			
				C	683	37° ± 6°	(None, limit ≈13.4)			
	(B-34)	0.02		A	666				(-20)	
				B	238					
				C	841					

Disk models may also contribute. A disk around A-36 will intersect both the A and B sightlines, and the galaxy velocity gradient acts in the direction such that any co-rotating disk cannot match the absorption found blueward of the galaxy. Given the saturation in A, such a disk cannot reproduce any substantial fraction of this absorption without also being detected in LOS-B redward of the galaxy. The observations therefore rule out this scenario. A disk around A-37 can fit a part of the absorption in A, most likely the blue end based on the galaxy kinematics, whilst a disk around A-40 can reproduce the strong absorption in B and a portion of the absorption in A.

The model shown in Figure C.13 includes this disk around A-40, with a rotation velocity of ≈ 110 km s^{-1}. An outflow from galaxy A-36 produces the other two components in A. However, the absorption in A could instead be produced by a disk-like structure around A-37 or an outflow around A-40 in combination with a weaker outflow from A-36.

Several metal features are detected at this redshift in sightlines A and B. LOS-A exhibits C III, O IV and O VI, whilst LOS-B features O II alongside C II, C III and C IV. The metals in A appear to form two components, rather than the three components detected in H I, and these two components feature similar column densities in each of the three detected ions. This is consistent with the two components being part of the same structure, an outflow from A-36 being our best model fit. The absorption in LOS-B has a lower C III content and a wider range of low ions detected, which also seems consistent with our models suggesting that this is primarily accretion onto A-40 (although the presence of some metals requires that this accretion is not pristine).

We therefore cannot rule out a superposition of disks and outflows in this group, although some combinations are ruled out. Given their close proximity and the distortions visible in the HST image, we would expect substantial interactions in the CGM of these galaxies, likely including tidal stripping, but cannot show this using the current observations of these galaxies. The absorption that is blueshifted by 300-500 km s^{-1} is not fit by our models, and may originate from these galaxies or some of the more distant galaxies at this redshift.

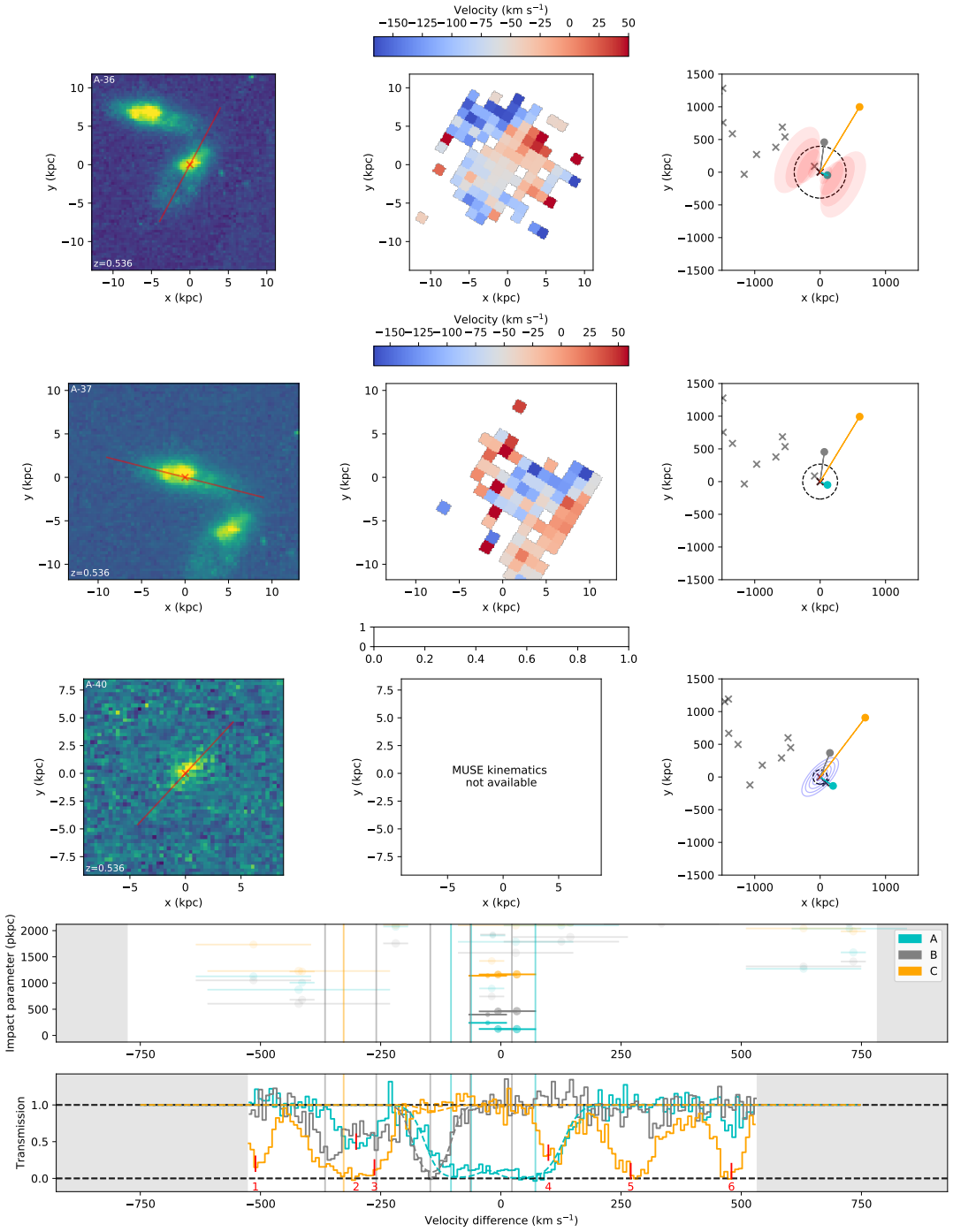

Figure C.13: Details of the absorption and galaxy environment around G-536. The layout is identical to that shown in Figure 4.4, although the lower panel shows the relevant Lyβ absorption, and kinematics shown are from the [O II] emission line seen in the MUSE data. The model shown in the lower panel combines an outflow with velocity 140 $\mathrm{km\,s^{-1}}$and half-opening angle 55° around A-36 and a disk with rotation velocity 110 $\mathrm{km\,s^{-1}}$around A-40. Absorption originating from another redshift is labelled with red ticks. Component (2) is Lyα from z ≈ 0.295, whilst all of the other labelled components are molecular lines originating from the sub-DLA in LOS-C.

Table C.13: Summary of galaxy–absorber group G-536. Non-MUSE galaxies and metal absorbers have velocities shown relative to the first galaxy (A-36). Columns are identical to those in Table 5.3.

z (1)	Galaxy (2)	Lum ($L_\star$) (3)	Inc (4)	LOS (5)	Imp (kpc) (6)	Azimuth (7)	log(N H I) (8)	b ($\mathrm{km\,s^{-1}}$) (9)	Δv (km/s) (10)	Other ions (11)
0.536	A-36	0.77	62° ± 2°	A	120	77° ± 2°	15.61 ± 0.02	39 ± 2	40 ± 60	O IV & C III(40 & -110)
				A	120	77° ± 2°	15.30 ± 0.02	67 ± 4	-90 ± 60	O VI (0 & -120)
				A	120	77° ± 2°	14.41 ± 0.08	290 ± 50	-140 ± 60	
				B	463	28° ± 2°	15.30 ± 0.04	24 ± 2	-180 ± 60	C II(-150, -230), O II (-140)
				B	463	28° ± 2°	14.36 ± 0.07	39 ± 7	-290 ± 60	C III(-180), C IV (0)
				B	463	28° ± 2°	14.48 ± 0.05	28 ± 3	-400 ± 60	
				C	1166	5° ± 2°	15.37 ± 0.07	53 ± 5	-360 ± 40	(No metals)
	A-37	0.31	72° ± 3°	A	123	31° ± 2°			(-40)	
				B	459	75° ± 2°				
				C	1163	52° ± 2°				
	A-40	0.02	65° ± 8°	A	240	63° ± 10°			(-60)	
				B	398	15° ± 10°				
				C	1140	30° ± 10°				
	(29364)	1.1		A	874				(-450)	
				B	606					
				C	1229					
	(29521)	0.4		A	1007				(-450)	
				B	681					
				C	1220					

C.2.5 G-558

This group of galaxies lies at the redshift of the sub-DLA at z = 0.558 in the spectrum of QSO-C. Whilst the three galaxies lying in the MUSE field (A-72, A-75 and A-77) are the closest to QSO-A, there are several other galaxies at this redshift at similar impact parameters to QSOs B and C. As neither the high-resolution imaging nor the IFU data cover QSO-C, no host galaxy has been identified for the sub-DLA. A-77 is a very low-surface-brightness galaxy, making it difficult for GALFIT to fit, so the position angle and inclination are not well-determined. The details are given in Table C.14and the galaxies and absorption at this redshift are shown in Figure C.14. The three closest galaxies are separated by $\approx$ 50 kpc. There may be some distortion visible in the light from these galaxies (they do not appear to be smooth disks), but this cannot be clearly attributed to interactions between the galaxies.

We use Ly-β for the fitting, as unlike Ly-α it lies in the higher-resolution COS wavelength range, and can therefore better constrain the models. The absorption in C is saturated across a large range of wavelengths, even in Ly-β, but absorption is also visible in both the A and B sightlines.

We note that the absorption in B at this redshift in both Lyα and Lyβ is a blend of H I absorption lines from other redshifts, making it difficult to identify which of the absorption features seen in Figure C.14 are Lyβ and therefore should be considered in our fitting. In particular, the absorption component identified at $\approx$ -100 $\mathrm{km\,s^{-1}}$ in LOS-B and marked with a vertical line in the figure is apparent in Lyα but not clearly visible in Lyβ. The absorption in LOS-B that is clearly visible at the wavelength of Lyβ was not clearly identified as such, and appears to be a blend of Lyα from z $\approx$ 0.32, Lyβ from this redshift, and Lyδ from z $\approx$ 0.64. However, the Lyβ does contribute, as the column densities estimated for the other H I systems making up this blend are not sufficient to produce the observed absorption.

Note that the velocity offset to galaxy 30142 is $\approx$ 300 $\mathrm{km\,s^{-1}}$, such that any outflow with sufficient velocity to match this would also produce a larger range of line-of-sight velocities than seen in the observed absorption. This also applies to galaxy 29812, despite a somewhat smaller velocity offset (as A and B lie nearer the minor axis). A disk around 30142 also fails to reproduce the column density ratio

between the two lines-of-sight, as the smaller impact parameter to LOS-B leads to absorption stronger than observed. Although a disk around 29812 is possible and can reproduce the absorption in LOS-B, such a disk would need a radius of ≈ 1 Mpc in order to reach the sightline. The absorption near this group of galaxies is therefore likely due to the trio of galaxies closest to the sightlines. A-77 does not have position angle and inclination measurements, so we can only model these structures around A-72 and A-75.

Neither a disk nor an outflow can simultaneously match both of the clear absorption components seen in sightlines A and B. For both galaxies with measured position angles, A lies at a smaller impact parameter and nearer to the major axis, so our disk models produce much larger column densities at A than at B (even accounting for the other contributors to the blended absorption in B). Any outflow with large enough opening angle to cover LOS-A and fast enough velocity to match the galaxy-absorber offset will also produce much wider absorption in B than is observed. A combination of models is therefore required.

We find that the absorption in A can be approximately reproduced by a halo or disk around A-75, whilst the absorption in B could be attributed to an outflow from A-72 or A-75 (or a disk from 29812, but this is less likely due to the larger extent required). We do detect O VI absorption in LOS-A but not in LOS-B. However, our detection limits allow the absorption in B to have a similar O VI to H I ratio to that in A. We therefore do not consider this non-detection to make an outflow origin for the absorption in B any less plausible.

The orientation (which side of the disk is inclined away from the observer, denoted by the S_{Nr} parameter) required of A-75 for an outflow to reach the absorption in B is not consistent with the disk model that fits A, so the combination of A-75 disk and outflow is not able to fit the observations. As A-72 is the most luminous and has the highest SFR of the two galaxies, we prefer the combination of outflow from A-72, and a disk or halo from A-75. A combination of outflow and halo from A-75 is also consistent with the observations and, as we note throughout this work, stripped material is difficult to rule out using these observations.

The model shown in Figure C.14 consists of an outflow around galaxy A-72

and a disk around A-75. The outflow has half-opening angle $\approx 40°$ and velocity 150 $\mathrm{km\,s^{-1}}$, whilst the disk has rotational velocity of 100 $\mathrm{km\,s^{-1}}$and an infall component of ≈ 50 $\mathrm{km\,s^{-1}}$.

C.2.6 G-907

A-16 and B-19 are both small, star-forming galaxies at z $\sim$ 0.9, illustrated in Table C.15 and Figure C.15. Both lines-of-sight show moderately strong absorption slightly blueward of both galaxies. The galaxies have sufficient signal-to-noise for kinematics to be measured, but are not well-resolved by MUSE so do not show a clear velocity gradient. They are separated by $\approx$ 600 kpc, so it is unsurprising that there is no sign of interaction in the HST image.

There are no clear constraints from the kinematics, and the absorption features in the FOS spectra are unresolved. Lyβ also lies in FOS at this redshift, so cannot be used to resolve these features. Each galaxy lies $\approx$ 200 kpc from one sightline, and $\approx$ 700 kpc from the other. Our models therefore cannot produce both absorption features with near-identical strengths and velocities using a disk and outflow from the same galaxy. However, the parameters can easily be tuned such that a disk or outflow from each galaxy can reproduce the absorption in the nearest line-of-sight.

In Figure C.15 we show an outflow with velocity 150 $\mathrm{km\,s^{-1}}$ and half-opening angle 60° from A-16, and a disk with scale height ratio 20:1 with circular and inward velocities of 130 and 30 $\mathrm{km\,s^{-1}}$ respectively around B-19. However, an outflow from B-19 and disk around A-16 can similarly reproduce the observations. In this case, the outflow would require only 80 $\mathrm{km\,s^{-1}}$ velocity, and a similar opening angle, and the disk would require $v_\phi \approx 150$ $\mathrm{km\,s^{-1}}$ and $v_r \approx 50$ $\mathrm{km\,s^{-1}}$. This scenario also produces more model absorption in the more distant sightline than the A-16 outflow, which better constrains the two disk velocity components and the outflow opening angle. Either scenario is possible with parameters within the bounds suggested by Paper 2 and other works.

Although our models cannot easily discriminate between these two scenarios, we find that the absorption around these galaxies is consistent with plausible CGM structures around the individual galaxies. Tidal material is not ruled out, but given

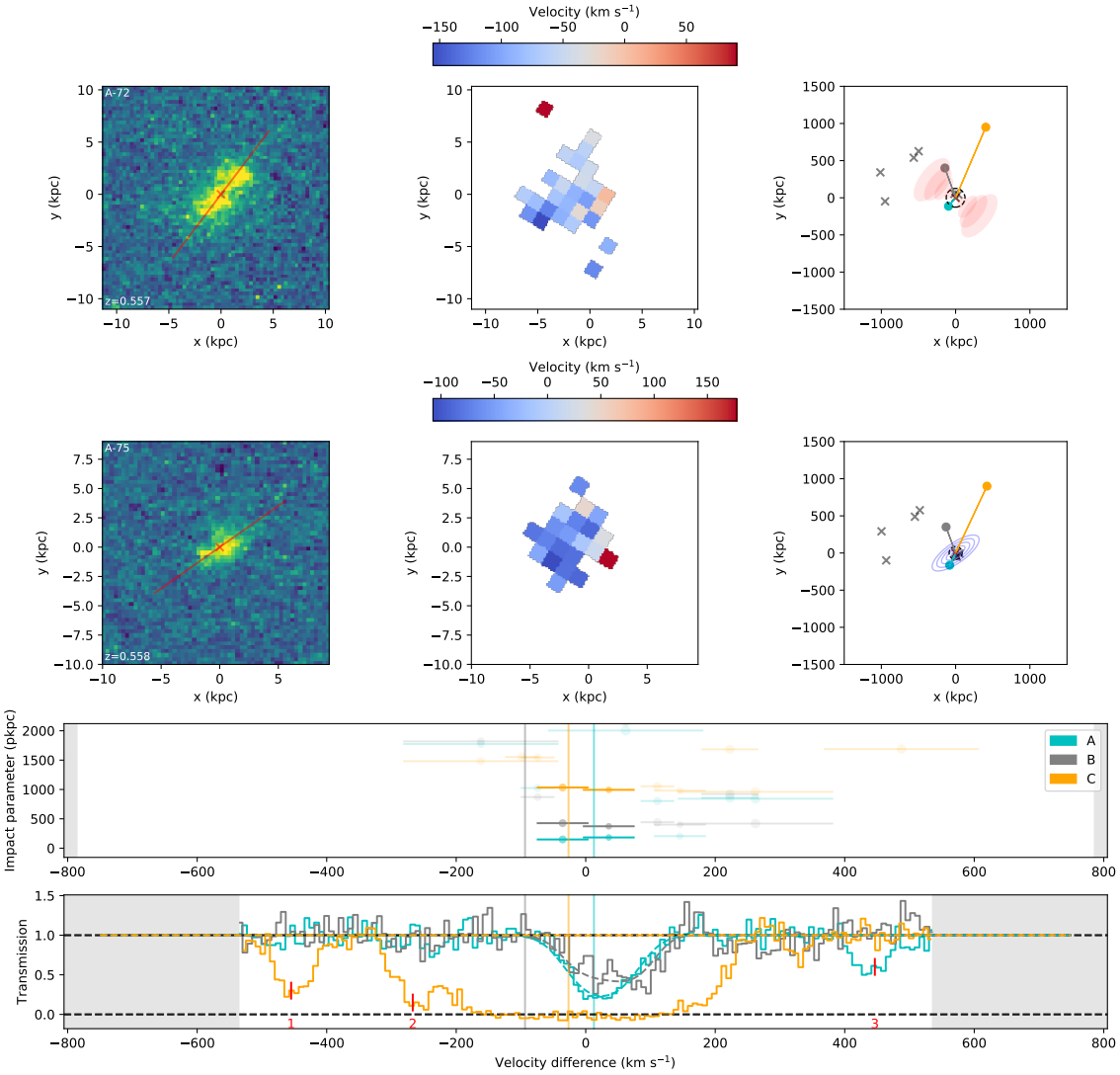

Figure C.14: Details of the Lyβ absorption and galaxy environment around group G-558 at the redshift of the sub-DLA. The layout is identical to that shown in Figure 4.4. The model shown is an outflow around galaxy A-72 (with half-opening angle $\approx 40°$ and velocity 150 km s^{-1}) and a disk around A-75 (with a rotational velocity of 100 km s^{-1}and an infall component of ≈ 50 km s^{-1}). Additional features labelled (1) and (2) are H2 molecular lines at the same redshift as the sub-DLA (z≈0.558), whilst (3) is the Lyman 7-0 transition from z=0.718.

Table C.14: Summary of galaxy–absorber group G-558. Any additional galaxies and metal absorbers have velocities shown relative to the first galaxy (A-72). Columns are identical to those in Table 5.3.

z (1)	Galaxy (2)	Lum ($L_\star$) (3)	Inc (4)	LOS (5)	Imp (kpc) (6)	Azimuth (7)	log(N H I) (8)	b ($\mathrm{km\,s^{-1}}$) (9)	Δv ($\mathrm{km\,s^{-1}}$) (10)	Other ions (11)
0.558	A-72	0.10	63° ± 3°	A	148	3° ± 4°	14.81 ± 0.03	37 ± 2	+50 ± 40	O VI
				B	426	57° ± 4°	14.26 ± 0.05	260 ± 40	-60 ± 40	None
				C	1033	14° ± 4°	18.0 ± 0.9	64 ± 12	+10 ± 40	C II,III, N III, O VI, Si II,III
	A-75	0.03	69° ± 6°	A	183	29° ± 6°			(+70)	
				B	373	75° ± 6°				
				C	994	30° ± 6°				
	A-77	0.04		A	205				(+180)	
				B	401					
				C	980					
	(27894)	0.1		A	1025				(-40)	
				B	871					
				C	1544					
	29812	0.2	78° ± 12°	A	804	83° ± 8°			(+150)	
				B	442	47° ± 8°				
				C	1054	6° ± 8°				
	30142	0.6	74° ± 2°	A	842	6° ± 2°			(+300)	
				B	419	35° ± 2°				
				C	960	87° ± 2°				

a separation between the galaxies that is substantially larger than the virial radius, this is unlikely to dominate the observed absorption.

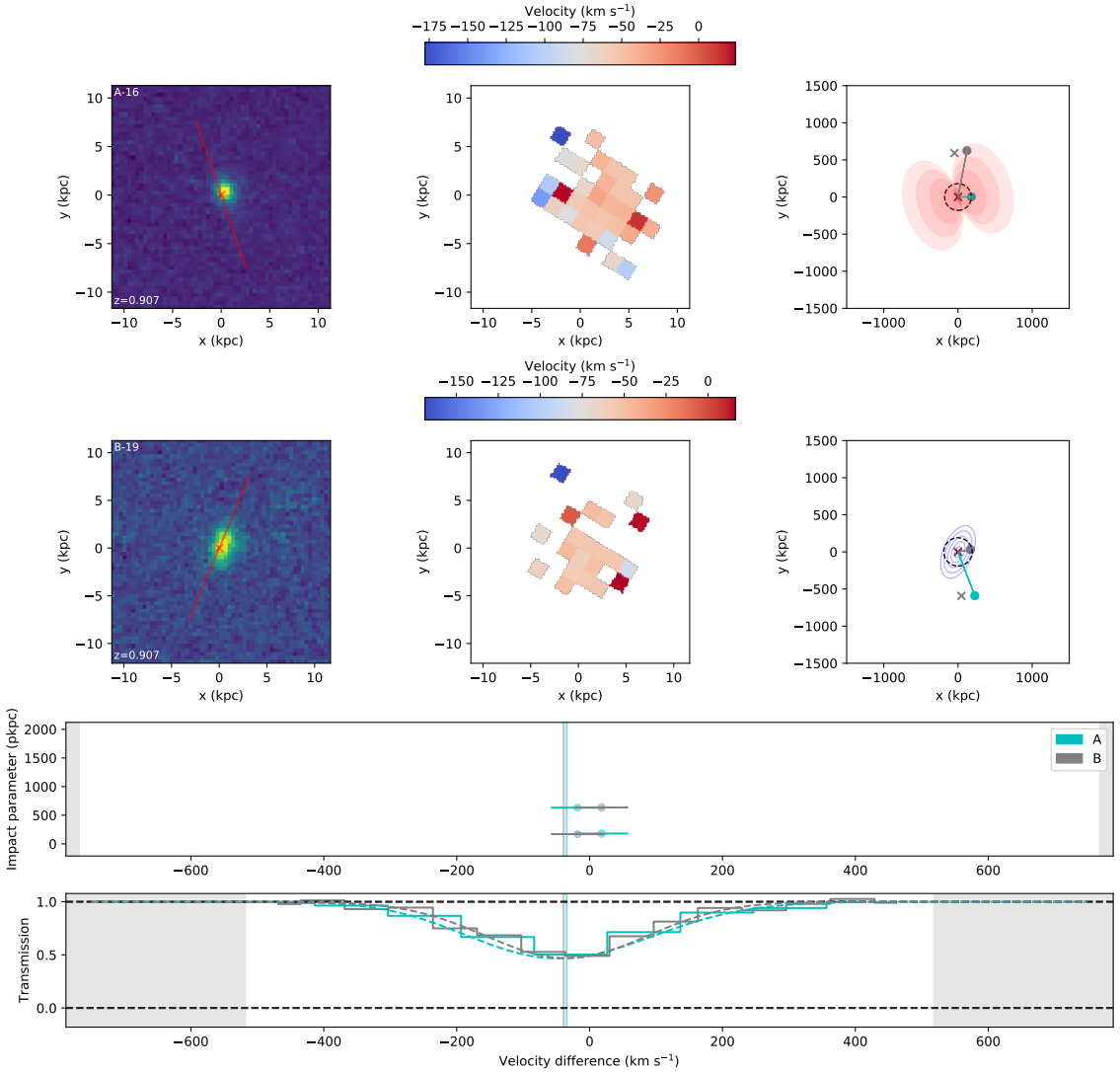

Figure C.15: Details of the absorption and galaxy environment around G-907, a galaxy pair at z $\sim$ 0.91. The layout is identical to that shown in Figure 4.4, with kinematics from the [O II] emission line seen in the MUSE data, and the model shown in the lower panel combines an outflow with velocity 150 km s^{-1} and half-opening angle 60° around A-16 and a disk with rotation velocity 130 km s^{-1} around B-19.

Table C.15: Summary of galaxy–absorber group G-907. Any additional galaxies and metal absorbers have velocities shown relative to the first galaxy (A-16). Note that this group is beyond the redshift of QSO-C, so no absorption could be detected. Columns are identical to those in Table 5.3.

z (1)	Galaxy (2)	Lum ($L_\star$) (3)	Inc (4)	LOS (5)	Imp (kpc) (6)	Azimuth (7)	log(N H I) (8)	b ($\mathrm{km\,s^{-1}}$) (9)	Δv ($\mathrm{km\,s^{-1}}$) (10)	Other ions (11)
0.907	A-16	0.17	53° ± 12°	A	180	72° ± 20°	14.16 ± 0.05	170 ± 20	-50 ± 40	
				B	635	30° ± 20°	14.15 ± 0.03	157 ± 11	-60 ± 40	
	B-19	0.10	58° ± 7°	A	631	44° ± 12°			(-40)	
				B	170	57° ± 12°				

Bibliography

Abbott B. P., et al., 2016, Physical Review Letters, 116, 221101 1.1.1

Adelberger K. L., Steidel C. C., Shapley A. E., Pettini M., 2003, ApJ, 584, 45 3.1

Adelberger K. L., Shapley A. E., Steidel C. C., Pettini M., Erb D. K., Reddy N. A., 2005, ApJ, 629, 636 3.1, 4.1, 5.1

Aguirre A., Hernquist L., Schaye J., Katz N., Weinberg D. H., Gardner J., 2001, ApJ, 561, 521 4.5.1, 6.1

Albareti F. D., et al., 2017, ApJS, 233, 25 2.2

Andernach H., Zwicky F., 2017, English and Spanish Translation of Zwicky's (1933) The Redshift of Extragalactic Nebulae, doi:10.48550/arXiv.1711.01693, `http://arxiv.org/abs/1711.01693` 4

Anshul P., Narayanan A., Muzahid S., Beckett A., Morris S. L., 2021, MNRAS, 503, 3243 3.3.2, 4.1, 5.1, 5.4.2, 5.4.2, 5.5.4, 5.5.5

Astropy Collaboration et al., 2018, AJ, 156, 123 3.4

Babcock H. W., 1939, Lick Observatory Bulletin, 498, 41 1.4.1

Bacon R., et al., 2010, SPIE, 7735, 773508 1.2.2, 2.1.2

Bacon R., et al., 2017, A&A, 608, A1 2.1.2

Bahcall J. N., Salpeter E. E., 1966, ApJ, 144, 847 1.3

Bahcall J. N., Spitzer Jr. L., 1969, ApJL, 156, L63 1.3, 4.1, 5.1

Baldwin J. A., Phillips M. M., Terlevich R., 1981, Publ. Astron. Soc. Pac., 93, 5 1.2.2

Baumgardt H., Hilker M., 2018, MNRAS, 478, 1520 1.2

Beckett A., Morris S. L., Fumagalli M., Bielby R., Tejos N., Schaye J., Jannuzi B., Cantalupo S., 2021, MNRAS, 506, 2574 1.6, 2, 3, 4.1

Behroozi P. S., Conroy C., Wechsler R. H., 2010, ApJ, 717, 379 1.4.1, 3.1, 4.1, 5.2

Bell E. F., McIntosh D. H., Katz N., Weinberg M. D., 2003, ApJS, 149, 289 1.2.2

Bergeron J., 1986, A&A, 155, L8 1.3.4, 3.1, 4.1, 5.1

Bergeron J., Boissé P., 1991, A&A, 243, 344 3.1

Bergeron J., et al., 1994, ApJ, 436, 33 3.1, 4.1, 5.1

Berlind A. A., Weinberg D. H., 2002, ApJ, 575, 587 1.4.1

Berta S., Lutz D., Genzel R., Förster-Schreiber N. M., Tacconi L. J., 2016, A&A, 587, A73 1.2.1

Bertin E., Arnouts S., 1996, ApJS, 117, 393 2.1.2

Bielby R., Crighton N. H. M., Fumagalli M., Morris S. L., Stott J. P., Tejos N., Cantalupo S., 2017, MNRAS, 468, 1373 3.1, 4.1, 5.1, 5.5.2

Bielby R. M., et al., 2019, MNRAS, 486, 21 3.1, 3.3.2, 5.1

Bielby R. M., et al., 2020, MNRAS, 493, 5336 2.1.2

Bizyaev D., Walterbos R. A. M., Chen Y.-M., Drory N., Lane R. R., Brownstein J. R., Riffel R. A., 2022, MNRAS, 515, 1598 5.5.2

Bland J., Tully B., 1988, Nature, 334, 43 3.1, 4.1, 4.3, 5.1

Blumenthal G. R., Faber S. M., Primack J. R., Rees M. J., 1984, Nature, 311, 517 1.4.1

Bond J. R., Kofman L., Pogosyan D., 1996, Nature, 380, 603 1.4.2, 3.1

Booth C. M., Schaye J., Delgado J. D., Dalla Vecchia C., 2012, MNRAS, 420, 1053 4.5.1, 6.1

Bordoloi R., et al., 2011, ApJ, 743, 10 3.3, 4.1, 4.3, 4.5.4, 5.1, 5.2, 5.5.1, 5.5.2

Bordoloi R., et al., 2014, ApJ, 794, 130 3.3

Bouché N., Murphy M. T., Péroux C., Csabai I., Wild V., 2006, MNRAS, 371, 495 3.1

Bouché N., Hohensee W., Vargas R., Kacprzak G. G., Martin C. L., Cooke J., Churchill C. W., 2012, MNRAS, 426, 801 4.1, 5.1, 6.1

Bouché N., et al., 2016, ApJ, 820, 121 3.4, 4.1, 5.1

Bowen D. V., Chelouche D., Jenkins E. B., Tripp T. M., Pettini M., York D. G., Frye B. L., 2016, ApJ, 826, 50 3.1, 4.1

Brook C. B., Stinson G., Gibson B. K., Roškar R., Wadsley J., Quinn T., 2012, MNRAS, 419, 771 4.1

Bruzual G., Charlot S., 2003, MNRAS, 344, 1000 1.2.2, 1.2.2, 2.1.2, 2.2

Bruzual A. G., 1983, ApJ, 273, 105 1.2.2

Burchett J. N., Elek O., Tejos N., Prochaska J. X., Tripp T. M., Bordoloi R., Forbes A. G., 2020, ApJ, 891, L35 3.2.3

Burchett J. N., Rubin K. H. R., Prochaska J. X., Coil A. L., Rickards Vaught R., Hennawi J. F., 2021, ApJ, 909, 151 1.5.1, 3.1, 4.1, 4.6, 5.1

Butsky I. S., Quinn T. R., 2018, ApJ, 868, 108 6.1

Calzetti D., Armus L., Bohlin R. C., Kinney A. L., Koornneef J., Storchi-Bergmann T., 2000, ApJ, 533, 682 2.2

Cantalupo S., Lilly S. J., Haehnelt M. G., 2012, Monthly Notices of the Royal Astronomical Society, 425, 1992 1.2

Cantalupo S., et al., 2019, MNRAS, 483, 5188 2.1.2, 2

Carswell R. F., Webb J. K., 2014, Astrophysics Source Code Library, p. ascl:1408.015 2.1.1

Casuso E., Beckman J. E., 2004, A&A, 419, 181 3.1

Cen R., Tripp T. M., Ostriker J. P., Jenkins E. B., 2001, ApJL, 559, L5 3.1

Chabrier G., 2003, Publ. Astron. Soc. Pac., 115, 763 1.2.2

Charlot S., Kauffmann G., Longhetti M., Tresse L., White S. D. M., Maddox S. J., Fall S. M., 2002, MNRAS, 330, 876 2.2

Charlton J. C., Churchill C. W., 1998, ApJ, 499, 181 3.1, 4.1, 5.1

Chen H.-W., 2012, MNRAS, 427, 1238 3.1, 3.3.1, iii

Chen H.-W., Mulchaey J. S., 2009, ApJ, 701, 1219 3.2.3, 5.1

Chen H.-W., Lanzetta K. M., Webb J. K., Barcons X., 1998, ApJ, 498, 77 3.1

Chen H.-W., Wild V., Tinker J. L., Gauthier J.-R., Helsby J. E., Shectman S. A., Thompson I. B., 2010, ApJL, 724, L176 5.1

Chen H.-W., Gauthier J.-R., Sharon K., Johnson S. D., Nair P., Liang C. J., 2014, MNRAS, 438, 1435 3.1, 5.1

Chen H.-W., Zahedy F. S., Johnson S. D., Pierce R. M., Huang Y.-H., Weiner B. J., Gauthier J.-R., 2018, MNRAS, 479, 2547 3.1

Chen H.-W., Boettcher E., Johnson S. D., Zahedy F. S., Rudie G. C., Cooksey K. L., Rauch M., Mulchaey J. S., 2019, ApJ, 878, L33 5.1

Chen H.-W., et al., 2020a, MNRAS, 497, 498 3.1, 4.1, 6.1

Chen Y., et al., 2020b, MNRAS, 499, 1721 1.5.1, 3.2.3, 3.5, 5.1

Chen Y., et al., 2021, MNRAS, 508, 19 5.5.2

Chevalier R. A., Clegg A. W., 1985, Nature, 317, 44 3.1

Clowe D., Bradac M., Gonzalez A. H., Markevitch M., Randall S. W., Jones C., Zaritsky D., 2006, ApJ, 648, L109 1.4.1

Concas A., Popesso P., Brusa M., Mainieri V., Thomas D., 2019, A&A, 622, A188 3.1, 4.1, 5.5.5, C.1.5

Conroy C., et al., 2007, ApJ, 654, 153 1.4.1

Cooke J., O'Meara J. M., 2015, ApJL, 812, L27 3.1

Crighton N. H. M., Morris S. L., Bechtold J., Crain R. A., Jannuzi B. T., Shone A., Theuns T., 2010, MNRAS, 402, 1273 (document), 2.1, 3.1, 3.2, 4.1, 5.1

Croxall K. V., Zee L. v., Lee H., Skillman E. D., Lee J. C., Côté S., Kennicutt R. C., Miller B. W., 2009, ApJ, 705, 723 3.1

D'Odorico V., Cristiani S., D'Odorico S., Fontana A., Giallongo E., Shaver P., 1998, A&A, 339, 678 4.1, 5.1

Danovich M., Dekel A., Hahn O., Ceverino D., Primack J., 2015, MNRAS, 449, 2087 3.4

Das S., Sardone A., Leroy A. K., Mathur S., Gallagher M., Pingel N. M., Pisano D. J., Heald G., 2020, ApJ, 898, 15 1.5.1

Davé R., Oppenheimer B. D., Katz N., Kollmeier J. A., Weinberg D. H., 2010, MNRAS, 408, 2051 4.3, 4.5.5, C.1.3

Davé R., Finlator K., Oppenheimer B. D., 2012, MNRAS, 421, 98 3.1

Davies R. L., et al., 1997. pp 1099–1106, doi:10.1117/12.268996, `http://adsabs.harvard.edu/abs/1997SPIE.2871.1099D` 2.1.2

Davies J. J., Crain R. A., Pontzen A., 2021, MNRAS, 501, 236 1.5.2

DeFelippis D., Genel S., Bryan G. L., Fall S. M., 2017, ApJ, 841, 16 4.1

DeFelippis D., Genel S., Bryan G. L., Nelson D., Pillepich A., Hernquist L., 2020, ApJ, 895, 17 3.1, 3.2.3, 3.3, 3.4, 3.4, iv, 4.1, 4.3, 4.5.2, 5.1, 6.1

Dekel A., Silk J., 1986, ApJ, 303, 39 1.4.1

Diamond-Stanic A. M., Coil A. L., Moustakas J., Tremonti C. A., Sell P. H., Mendez A. J., Hickox R. C., Rudnick G. H., 2016, ApJ, 824, 24 3.4

Dinshaw N., Weymann R. J., Impey C. D., Foltz C. B., Morris S. L., Ake T., 1997, ApJ, 491, 45 3.1, 3.2, 4.1, 5.1

Draine B. T., 2011, Physics of the Interstellar and Intergalactic Medium. Princeton University Press, http://adsabs.harvard.edu/abs/2011piim.book.....D 1.3.3, B.2

Duarte M., Mamon G., 2014, MNRAS, 440, 1763 B.1, B.1, B.1

Dutta R., et al., 2020, MNRAS, 499, 5022 3.1, 3.3, 4.5.3, 5.1, 5.5.1

Dutta R., et al., 2021, MNRAS, 508, 4573 4.1

Dyson F. W., Eddington A. S., Davidson C., 1920, Philosophical Transactions of the Royal Society of London. Series A, Containing Papers of a Mathematical or Physical Character, 220, 291 1.1.1

Efstathiou G., Eastwood J. W., 1981, MNRAS, 194, 503 1.5.2

Einstein A., 1905, Annalen der Physik, 322, 891 1.1.1

Einstein A., 1915, Sitzungsber. preuss.Akad. Wiss, 47, 831 1.1.1

Einstein A., 1916, Annalen der Physik, 354, 769 1.1.1

Epinat B., et al., 2018, A&A, 609, A40 5.1, 5.5.4

Evans C., et al., 2015, Technical report, The Science Case for Multi-Object Spectroscopy on the European ELT, https://ui.adsabs.harvard.edu/abs/2015arXiv150104726E. https://ui.adsabs.harvard.edu/abs/2015arXiv150104726E 4.6, 5.6, 6.2

Event Horizon Telescope Collaboration et al., 2019a, ApJ, 875, L1 1.1.1

Event Horizon Telescope Collaboration et al., 2019b, ApJ, 875, L5 1.1.1

Faber S. M., et al., 2003. pp 1657–1669, doi:10.1117/12.460346, http://adsabs.harvard.edu/abs/2003SPIE.4841.1657F 2.1.2

Falanga M., Bozzo E., Lutovinov A., Bonnet-Bidaud J. M., Fetisova Y., Puls J., 2015, A&A, 577, A130 1.1.1

Faucher-Giguère C.-A., Kereš D., Ma C.-P., 2011, MNRAS, 417, 2982 4.1

Ferland G. J., et al., 2017, Revista Mexicana de Astronomia y Astrofisica, 53, 385 1.3.4

Fielding D. B., Bryan G. L., 2022, ApJ, 924, 82 4.1

Fielding D., Quataert E., McCourt M., Thompson T. A., 2017, MNRAS, 466, 3810 4.1

Finley H., et al., 2017, A&A, 605, A118 1.5.1, 3.1, 4.1, 4.6, 5.1

Finn C. W., et al., 2016, MNRAS, 460, 590 2.1.1, 3.1, 4.1, 5.1

Forbes D. A., Kroupa P., 2011, Publications of the Astronomical Society of Australia, 28, 77 1.2

Fossati M., Fumagalli M., Gavazzi G., Consolandi G., Boselli A., Yagi M., Sun M., Wilman D. J., 2019a, MNRAS, 484, 2212 3.1, 3.3.2, 4.1, 4.5.3, 5.1

Fossati M., et al., 2019b, MNRAS, 490, 1451 2.1.2, 3.1, 4.1, 5.1, 5.2, 5.5.1, 6.2

Foster C., et al., 2014, MNRAS, 442, 3544 5.5.4

French D. M., Wakker B. P., 2020, ApJ, 897, 151 3.1, 3.4, 4.1, 4.5.2, 5.1

Freundlich J., et al., 2013, A&A, 553, A130 3.1, 5.1

Friedman A., 1999a, General Relativity and Gravitation, 31, 31 2

Friedman A., 1999b, General Relativity and Gravitation, 31, 1991 2

Friedmann A., 1922, Zeitschrift fur Physik, 10, 377 1.1.1

Friedmann A., 1924, Z. Physik, 21, 326 1.1.1

Fukugita M., Hogan C. J., Peebles P. J. E., 1998, ApJ, 503, 518 3.1

Fumagalli M., Fossati M., Hau G. K. T., Gavazzi G., Bower R., Sun M., Boselli A., 2014, MNRAS, 445, 4335 3.1, 4.1, 5.1

Fumagalli M., Cantalupo S., Dekel A., Morris S. L., O'Meara J. M., Prochaska J. X., Theuns T., 2016, MNRAS, 462, 1978 2.1.2

Fumagalli M., Haardt F., Theuns T., Morris S. L., Cantalupo S., Madau P., Fossati M., 2017, MNRAS, 467, 4802 1.3.4, 2.1.2

Gabasch A., et al., 2006, A&A, 448, 101 3.12

Gatkine P., Veilleux S., Cucchiara A., 2019, ApJ, 884, 66 1.5.1

Girelli G., Pozzetti L., Bolzonella M., Giocoli C., Marulli F., Baldi M., 2020, A&A, 634, A135 1.4.1

Gnat O., Sternberg A., 2007, ApJS, 168, 213 1.3.4

Gnat O., Sternberg A., 2009, ApJ, 693, 1514 1.3.4

Goerdt T., Ceverino D., 2015, MNRAS, 450, 3359 4.5.2, iv

Grand R. J. J., et al., 2017, MNRAS, 467, 179 1.5.2

Green J. C., et al., 2012, ApJ, 744, 60 2.1.1

Grimes J. P., et al., 2009, ApJS, 181, 272 3.1

Groves B., Brinchmann J., Walcher C. J., 2012, MNRAS, 419, 1402 1.2.1

Guber C. R., Richter P., Wendt M., 2018, A&A, 609, A85 5.1

Guzik J., Seljak U., 2002, MNRAS, 335, 311 1.4.1

Hafen Z., et al., 2019, MNRAS, 488, 1248 3.1

Hafen Z., et al., 2020, MNRAS, 494, 3581 3.1

Hafen Z., et al., 2022, arXiv:2201.07235 [astro-ph] 4.1, 4.5.2, 5.1

Harrison C. M., Costa T., Tadhunter C. N., Flütsch A., Kakkad D., Perna M., Vietri G., 2018, Nat Astron, 2, 198 1.4.1

Hartigan J. A., Hartigan P. M., 1985, Ann. Statist., 13, 70 3.3

Heckman T. M., Armus L., Miley G. K., 1990, ApJS, 74, 833 3.1, 4.1, 5.1

Heckman T. M., Norman C. A., Strickland D. K., Sembach K. R., 2002, ApJ, 577, 691 1.3.4

Heckman T., Borthakur S., Wild V., Schiminovich D., Bordoloi R., 2017, ApJ, 846, 151 3.1

Hinton S. R., Davis T. M., Lidman C., Glazebrook K., Lewis G. F., 2016, Astronomy and Computing, 15, 61 2.1.2

Hirv A., Pelt J., Saar E., Tago E., Tamm A., Tempel E., Einasto M., 2017, A&A, 599, A31 5.5.2

Ho S. H., Martin C. L., 2019, ApJ, 888, 14 4.5.2, B.3

Ho S. H., Martin C. L., Kacprzak G. G., Churchill C. W., 2017, ApJ, 835, 267 3.1, 3.4, 4.1, 5.1

Ho S. H., Martin C. L., Turner M. L., 2019, ApJ, 875, 54 5.1

Ho S. H., Martin C. L., Schaye J., 2020, ApJ, 904, 76 4.1, 4.2, 4.3, 4.5.2, 6.1

Hopkins P. F., Kereš D., Oñorbe J., Faucher-Giguère C.-A., Quataert E., Murray N., Bullock J. S., 2014, MNRAS, 445, 581 1.5.2

Hopkins P. F., Chan T. K., Ji S., Hummels C., Keres D., Quataert E., Faucher-Giguere C.-A., 2021, MNRAS, 501, 3640 1.5.2, 3.1, 3.2.3, 3.3, 4.1, 4.5.1, 5.5.2, 6.1

Huang Y.-H., Chen H.-W., Shectman S. A., Johnson S. D., Zahedy F. S., Helsby J. E., Gauthier J.-R., Thompson I. B., 2021, MNRAS, 502, 4743 3.1, 3.3, viii

Hubble E., 1929, Proceedings of the National Academy of Science, 15, 168 1.1.1, 1.2

Huscher E., Oppenheimer B. D., Lonardi A., Crain R. A., Richings A. J., Schaye J., 2021, MNRAS, 500, 1476 3.4, 3.4, iv, 4.5.2

Ibata R., Irwin M., Lewis G. F., Stolte A., 2001, ApJ, 547, L133 5.5.4

Jacoby B. A., Cameron P. B., Jenet F. A., Anderson S. B., Murty R. N., Kulkarni S. R., 2006, ApJ, 644, L113 1.1.1

Japelj J., et al., 2019, A&A, 632, A94 3.5

Jian H.-Y., et al., 2017, ApJ, 845, 74 1.4.2, 5.1

Johnson S. D., Chen H.-W., Mulchaey J. S., 2015, MNRAS, 449, 3263 1.2.2, 2.2, 4.2, 4.1, 5.2, 5.2, 5.5.5

Johnson S. D., et al., 2018, ApJL, 869, L1 3.1, 5.1, 5.5.4

Kaaret P., et al., 2020, Nature, 4, 1072 4.1

Kacprzak G. G., Murphy M. T., Churchill C. W., 2010, MNRAS, 406, 445 5.1

Kacprzak G. G., Churchill C. W., Steidel C. C., Spitler L. R., Holtzman J. A., 2012a, MNRAS, 427, 3029 4.5.4, viii

Kacprzak G. G., Churchill C. W., Nielsen N. M., 2012b, ApJ, 760, L7 4.1, 5.1, 6.1

Kacprzak G. G., Muzahid S., Churchill C. W., Nielsen N. M., Charlton J. C., 2015, ApJ, 815, 22 3.3.2, 3.3.3, 5.1

Kacprzak G. G., Pointon S. K., Nielsen N. M., Churchill C. W., Muzahid S., Charlton J. C., 2019, ApJ, 886, 91 3.1, 3.3.3, 4.5.4, 5.5.5

Kauffmann G., et al., 2003, MNRAS, 341, 33 1.2.2

Keeney B. A., Danforth C. W., Stocke J. T., France K., Green J. C., 2012, Publ. Astron. Soc. Pac., 124, 830 2.1.1, B.2

Keeney B. A., Stocke J. T., Rosenberg J. L., Danforth C. W., Ryan-Weber E. V., Shull J. M., Savage B. D., Green J. C., 2013, ApJ, 765, 27 3.1

Keeney B. A., et al., 2017, ApJS, 230, 6 3.3.1

Kennicutt J., 1998, ARA&A, 36, 189 1.2.2, 2.2, 4.1, 5.2

Kereš D., Katz N., Weinberg D. H., Davé R., 2005, MNRAS, 363, 2 3.1

Kewley L. J., Geller M. J., Jansen R. A., 2004, AJ, 127, 2002 1.2.2, 2.2, 4.1, 5.2

Kewley L. J., Nicholls D. C., Sutherland R. S., 2019, ARA&A, 57, 511 1.2.2

Kim T.-S., et al., 2020, MNRAS 3.2.3

Klypin A. A., Shandarin S. F., 1983, MNRAS, 204, 891 3.1

Komatsu E., et al., 2011, ApJS, 192, 18 1.4.1

Koyama K., 2016, Reports on Progress in Physics, 79, 046902 1.4.1

Krishnendu N. V., Ohme F., 2021, Universe, 7, 497 1.1.1

Kuschel M., et al., 2022, Technical report, Investigating the Dominant Environmental Quenching Process in UVCANDELS/COSMOS Groups, https://ui.adsabs.harvard.edu/abs/2022arXiv220512169K. https://ui.adsabs.harvard.edu/abs/2022arXiv220512169K 1.4.2, 5.1

Laha S., Reynolds C. S., Reeves J., Kriss G., Guainazzi M., Smith R., Veilleux S., Proga D., 2021, Nature, 5, 13 1.4.1

Lan T.-W., Mo H., 2018, ApJ, 866, 36 3.1, 4.1, 5.1

Lanzetta K. M., Bowen D. V., Tytler D., Webb J. K., 1995, ApJ, 442, 538 3.1

Larson R. B., Tinsley B. M., Caldwell C. N., 1980, ApJ, 237, 692 5.2

Le Fevre O., Crampton D., Felenbok P., Monnet G., 1994, A&A, 282, 325 2.1.2

LeFevre O., et al., 2003, in Instrument Design and Performance for Optical/Infrared Ground-based Telescopes. International Society for Optics and Photonics, pp 1670–1681, doi:10.1117/12.460959, https://www.spiedigitallibrary.org/conference-proceedings-of-spie/4841/0000/Commissioning-and-performances-of-the-VLT-VIMOS/10.1117/12.460959.short 2.1.2

Leavitt H. S., Pickering E. C., 1912, Harvard College Observatory Circular, 173, 1 1.2

Leclercq F., et al., 2022, A&A, 663, A11 1.5.1, 4.1, 4.6, 5.1

Lee K.-G., et al., 2018, ApJS, 237, 31 3.5, 6.2

Lehner N., et al., 2021, Technical report, KODIAQ-Z: Metals and Baryons in the Cool Intergalactic and Circumgalactic Gas at 2.2, https://ui.adsabs.harvard.edu/abs/2021arXiv211203304L. https://ui.adsabs.harvard.edu/abs/2021arXiv211203304L 5.1

Lehnert M. D., Heckman T. M., Weaver K. A., 1999, ApJ, 523, 575 3.1, 4.1

Lehnert M. D., Le Tiran L., Nesvadba N. P. H., van Driel W., Boulanger F., Di Matteo P., 2013, A&A, 555, A72 1.3.4, 3.1, 4.1, 5.1

Lemaître G., 1931, MNRAS, 91, 483 1.1.1

Lofthouse E. K., et al., 2020, MNRAS, 491, 2057 2.1.2

Lopez S., et al., 2018, Nature, 554, 493 1.5.1, 3.1, 4.1, 5.1

Lopez S., et al., 2020, MNRAS, 491, 4442 1.5.1, 3.1, 4.1, 5.1

Lusso E., et al., 2019, MNRAS, 485, L62 6.2

Lynden-Bell D., Lynden-Bell R. M., 1995, MNRAS, 275, 429 1.4.2

Macquart J.-P., et al., 2020, Nature, 581, 391 1.5.1, 3.1

Madau P., Dickinson M., 2014, ARA&A, 52, 415 2.2

Maiolino R., et al., 2013, Technical report, A Community Science Case for E-ELT HIRES, https://ui.adsabs.harvard.edu/abs/2013arXiv1310.3163M. https://ui.adsabs.harvard.edu/abs/2013arXiv1310.3163M 4.6, 5.6, 6.2

Maitra S., Srianand R., Petitjean P., Rahmani H., Gaikwad P., Choudhury T. R., Pichon C., 2019, MNRAS, 490, 3633 4.1, 5.1

Majewski S. R., Munn J. A., Hawley S. L., 1996, ApJ, 459, L73 5.5.4

Mandelbaum R., Seljak U., Kauffmann G., Hirata C. M., Brinkmann J., 2006, MNRAS, 368, 715 1.4.1

Marconi A., et al., 2021, The Messenger, 182, 27 4.6, 5.6, 6.2

Martin C. L., Shapley A. E., Coil A. L., Kornei K. A., Bundy K., Weiner B. J., Noeske K. G., Schiminovich D., 2012, ApJ, 760, 127 1.5.1, 3.1

Martin D. C., et al., 2019a, Nature Astronomy, 3, 822 6.1

Martin C. L., Ho S. H., Kacprzak G. G., Churchill C. W., 2019b, ApJ, 878, 84 3.1, 3.3.1, 4.1

Mathes N. L., Churchill C. W., Kacprzak G. G., Nielsen N. M., Trujillo-Gomez S., Charlton J., Muzahid S., 2014, ApJ, 792, 128 3.1, 4.1, 6.1

Mathewson D. S., Cleary M. N., Murray J. D., 1974, ApJ, 190, 291 1.4.2, 3.1

Matthews T. A., Sandage A. R., 1963, ApJ, 138, 30 1.3

Michelson A. A., Morley E. W., 1887, American Journal of Science, 34, 333 1.1.1

Mitchell P. D., Schaye J., Bower R. G., Crain R. A., 2020a, MNRAS, 494, 3971 3.1, 3.2.3, 3.3, 3.3.1, 4.1, 4.5.1, 5.1, B.3.2, C.1.1

Mitchell P. D., Schaye J., Bower R. G., 2020b, MNRAS, 497, 4495 3.1, 4.3, 4.5.1, 5.1

Montero-Dorta A. D., Prada F., 2009, MNRAS, 399, 1106 3.12, 4.1, 5.2

Morris S. L., Jannuzi B. T., 2006, MNRAS, 367, 1261 2.1.2

Morris S. L., van den Bergh S., 1994, ApJ, 427, 696 3.1, 3.3.2, 3.4, 4.1, 5.1, 5.5.4, C.2.1

Morris S. L., Weymann R. J., Savage B. D., Gilliland R. L., 1991, ApJL, 377, L21 3.1

Mortensen K., Keerthi Vasan G. C., Jones T., Faucher-Giguère C.-A., Sanders R. L., Ellis R. S., Leethochawalit N., Stark D. P., 2021, ApJ, 914, 92 4.1, 5.1

Moster B. P., Somerville R. S., Maulbetsch C., van den Bosch F. C., Macciò A. V., Naab T., Oser L., 2010, ApJ, 710, 903 1.4.1

Muratov A. L., et al., 2017, MNRAS, 468, 4170 4.5.4

Muzahid S., 2014, ApJ, 784, 5 3.1, 3.3.2, 4.1, 5.1

Muzahid S., et al., 2021, MNRAS, 508, 5612 1.5.1

Nateghi H., Kacprzak G. G., Nielsen N. M., Muzahid S., Churchill C. W., Pointon S. K., Charlton J. C., 2021, MNRAS, 500, 3987 5.1, 5.5.5

Neeleman M., Prochaska J. X., Ribaudo J., Lehner N., Howk J. C., Rafelski M., Kanekar N., 2016, ApJ, 818, 113 3.1

Nelson D., et al., 2019, MNRAS, 490, 3234 3.1, 4.1, 4.3, 4.5.1, 5.1

Newman J. A., et al., 2013, ApJS, 208, 5 2.1.2

Newman A. B., et al., 2020, ApJ, 891, 147 6.2

Ng M., Nielsen N. M., Kacprzak G. G., Pointon S. K., Muzahid S., Churchill C. W., Charlton J. C., 2019, ApJ, 886, 66 5.5.5

Nicastro F., et al., 2018, Nature, 558, 406 3.1

Nidever D. L., Majewski S. R., Burton W. B., 2008, ApJ, 679, 432 3.1

Nielsen N. M., Churchill C. W., Kacprzak G. G., Murphy M. T., 2013, ApJ, 776, 114 3.1

Nielsen N. M., Kacprzak G. G., Pointon S. K., Churchill C. W., Murphy M. T., 2018, ApJ, 869, 153 5.1, 5.2, 5.5.1

Okoshi K., et al., 2021, AJ, 162, 175 4.1, 5.1

Oppenheimer B. D., et al., 2016, MNRAS, 460, 2157 3.3.2, 5.1, 5.5.5

Oppenheimer B. D., Babul A., Bahé Y., Butsky I. S., McCarthy I. G., 2021, Universe, 7, 209 5.1

Pandya V., et al., 2021, MNRAS, 508, 2979 4.1, 5.1

Peng C. Y., Ho L. C., Impey C. D., Rix H.-W., 2002, AJ, 124, 266 2.2.1, 3.3

Peng Y.-j., et al., 2010, ApJ, 721, 193 1.4.2, 5.1

Péroux C., et al., 2016, MNRAS, 457, 903 5.5.5

Péroux C., et al., 2017, MNRAS, 464, 2053 3.1, 4.1, 5.1

Péroux C., Rahmani H., Arrigoni Battaia F., Augustin R., 2018, Monthly Notices of the Royal Astronomical Society, 479, L50 5.1

Péroux C., et al., 2019, MNRAS, 485, 1595 1.5.1, 3.1, 4.1, 6.1

Péroux C., Nelson D., van de Voort F., Pillepich A., Marinacci F., Vogelsberger M., Hernquist L., 2020, MNRAS, 499, 2462 4.1, 4.5.4, 5.1, 5.5.5, 6.1

Persic M., Salucci P., Stel F., 1996, MNRAS, 281, 27 1.4.1

Pessa I., et al., 2018, MNRAS, 477, 2991 4.5.5

Petry C. E., Impey C. D., Fenton J. L., Foltz C. B., 2006, AJ, 132, 2046 2.1.1, 3.1, 4.1, 5.1

Phillips M. M., 1993, ApJL, 413, L105 1.2

Pichon C., Pogosyan D., Kimm T., Slyz A., Devriendt J., Dubois Y., 2011, MNRAS, 418, 2493 3.1

Pillepich A., et al., 2018, MNRAS, 473, 4077 1.5.2

Pisano D. J., 2014, AJ, 147, 48 1.5.1

Planck Collaboration 2020, A&A, 641, A6 1.1.1, 1.4.1, 3.1, 4.1

Pointon S. K., Kacprzak G. G., Nielsen N. M., Muzahid S., Murphy M. T., Churchill C. W., Charlton J. C., 2019, ApJ, 883, 78 3.1, 4.1, 4.5.4, 5.1, 5.5.5

Popping A., Meyer M., Staveley-Smith L., Obreschkow D., Jozsa G., Pisano D. J., 2015, Advancing Astrophysics with the Square Kilometre Array (AASKA14), p. 132 3.5

Press W. H., Schechter P., 1974, ApJ, 187, 425 1.4.1

Prochaska J. X., Weiner B., Chen H.-W., Mulchaey J., Cooksey K., 2011, ApJ, 740, 91 4.1, 5.1

Rakic O., Schaye J., Steidel C. C., Rudie G. C., 2011, MNRAS, 414, 3265 2.2

Rakic O., Schaye J., Steidel C. C., Booth C. M., Dalla Vecchia C., Rudie G. C., 2013, MNRAS, 433, 3103 3.1

Rauch M., Sargent W. L. W., Barlow T. A., Simcoe R. A., 2002, ApJ, 576, 45 3.1

Rees M. J., Ostriker J. P., 1977, MNRAS, 179, 541 1.4.1

Richard J., 2019, A Blue MUSE for the VLT, doi:10.5281/zenodo.3356260. , `https://ui.adsabs.harvard.edu/abs/2019vltt.confE..24R` 6.2

Riess A. G., et al., 1998, AJ, 116, 1009 1.2

Roberts-Borsani G. W., Saintonge A., Masters K. L., Stark D. V., 2020, MNRAS, 493, 3081 1.5.1

Robertson H. P., 1936, ApJ, 83, 257 1.1.1

Rodríguez S., Lambas D. G., Padilla N. D., Tissera P., Bignone L., Dominguez-Tenreiro R., Gonzalez R., Pedrosa S., 2022, Technical Report arXiv:2205.06886, Satellite galaxies in groups in the CIELO Project I. Gas removal from galaxies and its re-distribution in the intragroup medium, http://arxiv.org/abs/2205.06886. arXiv, doi:10.48550/arXiv.2205.06886, http://arxiv.org/abs/2205.06886 5.5.4

Rosswog S., 2009, New Astronomy Reviews, 53, 78 1.5.2

Rubin V. C., Ford Jr. W. K., Thonnard N., 1978, ApJ, 225, L107 1.4.1

Rubin K. H. R., Prochaska J. X., Koo D. C., Phillips A. C., 2012, ApJL, 747, L26 1.5.1, 3.1, 4.1

Rubin K. H. R., Prochaska J. X., Koo D. C., Phillips A. C., Martin C. L., Winstrom L. O., 2014, ApJ, 794, 156 4.3

Rubin K. H. R., Diamond-Stanic A. M., Coil A. L., Crighton N. H. M., Moustakas J., 2018, ApJ, 853, 95 3.1, 4.1, 5.1

Ryden B., 2003, Introduction to cosmology. https://ui.adsabs.harvard.edu/abs/2003itc..book.....R 1.1.1

Ryon J. E., 2019, Advanced Camera for Surveys HST Instrument Handbook 2.2.1

Salcido J., Bower R. G., Theuns T., 2020, MNRAS, 491, 5083 3.1, 4.1, 5.1

Salpeter E. E., 1955, ApJ, 121, 161 1.2.2

Sarazin C. L., 1986, Reviews of Modern Physics, 58, 1 1.4.2

Schaye J., et al., 2010, MNRAS, 402, 1536 3.1

Schaye J., et al., 2015, MNRAS, 446, 521 1.5.2

Schramm D., 1998, Space Science Reviews, 84, 3 1.4.1

Schroetter I., Bouché N., Péroux C., Murphy M. T., Contini T., Finley H., 2015, ApJ, 804, 83 4.1, 4.5.4

Schroetter I., et al., 2016, ApJ, 833, 39 3.1, 3.3, 3.3.1

Schroetter I., et al., 2019, MNRAS, 490, 4368 1.4.1, 3.1, 4.1, 4.5.1, 4.5.4, 4.7, iii, 5.1, 5.5.2, 5.6, 5.5.2, iii, 6.1, C.1.1, C.1.5

Scodeggio M., et al., 2005, Publ. Astron. Soc. Pac., 117, 1284 2.1.2

Scott J., Bechtold J., Morita M., Dobrzycki A., Kulkarni V., 2002, ApJ, 571, 665 B.2

Scoville N., et al., 2017, ApJ, 837, 150 3.1, 5.1

Shull J. M., Smith B. D., Danforth C. W., 2012, ApJ, 759, 23 3.1

Smette A., Surdej J., Shaver P. A., Foltz C. B., Chaffee F. H., Weymann R. J., Williams R. E., Magain P., 1992, ApJ, 389, 39 3.1

Somerville R. S., Popping G., Trager S. C., 2015, MNRAS, 453, 4337 3.1, 4.1, 5.1

Sorgho A., Foster T., Carignan C., Chemin L., 2019, MNRAS 1.4.2, 3.1, 5.1, 5.5.1, 5.5.4

Springel V., et al., 2005, Nature, 435, 629 3.1

Stairs I. H., 2003, Living Reviews in Relativity, 6, 5 1.1.1

Steidel C. C., Kollmeier J. A., Shapley A. E., Churchill C. W., Dickinson M., Pettini M., 2002, ApJ, 570, 526 3.1, 4.1, 4.3, 4.5.2, 5.1, B.3.3

Steidel C. C., Erb D. K., Shapley A. E., Pettini M., Reddy N., Bogosavljević M., Rudie G. C., Rakic O., 2010, ApJ, 717, 289 1.5.1, 3.1

Stewart K. R., et al., 2017, ApJ, 843, 47 3.1, 3.4, 4.1

Stocke J. T., et al., 2014, ApJ, 791, 128 4.1

Strömgren B., 1939, ApJ, 89, 526 1.2.2

Swinbank A. M., et al., 2017, MNRAS, 467, 3140 4.1

Tanabashi M., et al., 2018, Phys. Rev. D, 98, 030001 1.4.1

Tchernyshyov K., et al., 2021, arXiv:2110.13167 [astro-ph] 5.5.5

Tejos N., et al., 2014, MNRAS, 437, 2017 2.1.1, 3.1, 4.1, 5.1

Tejos N., et al., 2021a, arXiv e-prints, p. arXiv:2105.01673 5.1

Tejos N., et al., 2021b, MNRAS, 507, 663 1.5.1, 4.1, 4.5.2, viii, 6.1

Tempel E., Libeskind N. I., 2013, ApJL, 775, L42 3.3.1, 5.5.2

Tepper-García T., Richter P., Schaye J., Booth C. M., Dalla Vecchia C., Theuns T., 2012, MNRAS, 425, 1640 4.5.5

Tomisaka K., Ikeuchi S., 1988, ApJ, 330, 695 4.5.1

Tripp T. M., Savage B. D., 2000, ApJ, 542, 42 3.1

Tripp T. M., Sembach K. R., Bowen D. V., Savage B. D., Jenkins E. B., Lehner N., Richter P., 2008, ApJS, 177, 39 4.1, 5.5.5, 6.1

Tumlinson J., et al., 2011, Science, 334, 948 3.1

Tumlinson J., et al., 2013, ApJ, 777, 59 3.1, 5.1, 5.2

Tumlinson J., Peeples M. S., Werk J. K., 2017, ARA&A, 55, 389 1.4.1, 3.1, 4.1, 5.1

Turner M. L., Schaye J., Steidel C. C., Rudie G. C., Strom A. L., 2014, MNRAS, 445, 794 3.1

Turner M. L., Schaye J., Steidel C. C., Rudie G. C., Strom A. L., 2015, MNRAS, 450, 2067 3.1

Veilleux S., Cecil G., Bland-Hawthorn J., 2005, ARA&A, 43, 769 3.1, 4.5.1

Walker A. G., 1937, Proceedings of the London Mathematical Society, s2-42, 90 1.1.1

Wang B., Heckman T. M., Zhu G., Norman C. A., 2020, ApJ, 894, 149 4.1

Weinberger R., et al., 2017, MNRAS, 465, 3291 1.5.2

Werk J. K., Prochaska J. X., Thom C., Tumlinson J., Tripp T. M., O'Meara J. M., Peeples M. S., 2013, ApJS, 204, 17 3.1, 4.1, 6.1

Werk J. K., et al., 2014, ApJ, 792, 8 3.1, 3.3.2, 5.5.1, 5.5.5, viii

Werk J. K., et al., 2016, ApJ, 833, 54 3.1, 5.5.5

Wetzel A. R., Tinker J. L., Conroy C., van den Bosch F. C., 2013, MNRAS, 432, 336 1.4.2, 3.2.3, 5.1, 5.2

Weymann R. J., et al., 1998, ApJ, 506, 1 4.1, 5.1

Wijers N. A., Schaye J., Oppenheimer B. D., 2020, MNRAS, 498, 574 3.3.2

Wild V., et al., 2008, MNRAS, 388, 227 5.1, B.2

Wilde M. C., et al., 2021, ApJ, 912, 9 1.4.1, 3.3.1, 4.1, 5.1, 5.5.1, viii

Wolfe A. M., Gawiser E., Prochaska J. X., 2005, ARA&A, 43, 861 1.3.3

Young P. A., Impey C. D., Foltz C. B., 2001, ApJ, 549, 76 2.1.1, 3.1, 4.1, 5.1

Younsi Z., Psaltis D., Özel F., 2021, Technical report, Black Hole Images as Tests of General Relativity: Effects of Spacetime Geometry, `https://ui.adsabs.harvard.edu/abs/2021arXiv211101752Y`. `https://ui.adsabs.harvard.edu/abs/2021arXiv211101752Y` 1.1.1

Zabl J., et al., 2019, MNRAS, 485, 1961 3.1, 3.3.1, 3.3.1, 1, 3.4, 3.4, 4.1, 4.5.2, 4.5.4, 4.7, iv, 5.1, 5.5.2, 5.6, 6.1, B.3.3

Zabl J., et al., 2020, MNRAS, 492, 4576 3.1, 4.1, 4.3

Zabl J., et al., 2021a, arXiv e-prints, p. arXiv:2105.14090 5.1

Zabl J., et al., 2021b, MNRAS, 507, 4294 4.1, 4.6, 5.1

Zahedy F. S., Chen H.-W., Rauch M., Wilson M. L., Zabludoff A., 2016, MNRAS, 458, 2423 3.1, 4.1, 5.1

Zhang Y., Yang X., Wang H., Wang L., Luo W., Mo H. J., van den Bosch F. C., 2015, ApJ, 798, 17 3.3.1, 5.5.2

Zwicky F., 1933, Helvetica Physica Acta, 6, 110 1.4.1

de Blok W. J. G., et al., 2014, A&A, 569, A68 1.5.1

van de Hulst H. C., Raimond E., van Woerden H., 1957, Bulletin of the Astronomical Institutes of the Netherlands, 14, 1 1.4.1

van de Voort F., Schaye J., Booth C. M., Dalla Vecchia C., 2011, MNRAS, 415, 2782 3.1

van de Voort F., Springel V., Mandelker N., van den Bosch F. C., Pakmor R., 2019, MNRAS, 482, L85 1.5.2